A Thesis Submitted for the Degree of PhD at the University of Warwick

Permanent WRAP URL:

http://wrap.warwick.ac.uk/157408

Correlative Investigations into Advanced Silicon and Silicon Hybrid Anode Microstructures for High Capacity Li-ion Batteries

Romeo Malik

Submitted in part fulfilment of the requirements for the degree of
Doctor of Philosophy in Engineering

Warwick Manufacture Group

University of Warwick

February 2020

TABLE OF CONTENTS

ACKNOWLEDGEMENT

This doctoral experience would not have been so mesmerising without the remarkable people I've met along this journey. First and foremost, I would like to thank my supervisors Professor Rohit Bhagat and Dr Melanie Loveridge, for the opportunity to study for a PhD at the Electrochemical Engineering group at WMG. Throughout this journey, your tireless support, guidance and trust have nurtured me to get a long way to where I am now. I would like to convey my earnest gratitude to my supervisor Dr Melanie Loveridge, for her critical technical advice during my PhD and immense patience in revising every single piece of writing, has been invaluable. I would also like to express my gratitude to Professor Paul Shearing from University College London, for his expert advice I've needed during this work.

I'm grateful towards my former supervisors during my B.Tech and M.Tech at Indian Institute of Technology-Kharagpur, Professor Sudipto Ghosh and Dr Basab Chakraborty for providing me constant support and guidance, which led to my pursuit of a PhD.

I would like to acknowledge all my collaborators for their kind support. Special thanks to Professor Richard Walton and Luke Williams from Department Of Chemistry (University Of Warwick), with the synthesis of the metal-organic frameworks used in this research work. Also, for the many constructive and brainstorming sessions about my research. I'm grateful to David Walker of the University of Warwick X-ray diffraction facility for assisting with data collection. Thanks to Dr Vittorio Pellegrini, Dr Laura Silvestri and Dr Francesco Bonacorso at Graphene Labs (Italian Institute of Technology) for the opportunity to work with them, for all their help and inputs with the silicon-graphene experiments. Thanks to Dr Shashi Paul and Dr Krishna Manjunatha for the support with silicon-tin research work. Also, I am grateful to Dr Mike Lain and Dr Alexander Roberts, who always gave me their useful experimental tips and for always making time for me whenever needed. I would also like to extend my thanks to Dr Donal Finegan, Dr Dami Taiwo, Dr Francesco Iacoviello and Joshua Bailey from University College London who were excellent hosts and co-workers throughout. I would like to express my appreciation for the tremendous help in with X-ray CT scanning and image reconstruction by Dr Francesco Iacoviello from University College London and Dr Geoff West of the University of Warwick for his support and advice with FIB-SEM.

I would like to acknowledge funding from AMorpheuS project (Grant Reference EP/NO01583/1), the Faraday Institution Degradation Fast Start project (Grant Reference RG94392) and High Value Manufacturing Catapult at WMG (University Of Warwick). Also, the funding from the European Union's Horizon 2020 research and innovation programme under the grant agreement No. 696656 – GrapheneCore2.

A big thanks to all current and previous members of Electrochemical Engineering group from different parts of the world who made my time at WMG memorable. Thanks to Dr Daniel Gonzalez, Dr Anup Barai, Dr Carlos Pastor, Jayendra Bhalodiya, Yashraj Tripathy, Upender Rao Koleti, Muinuddin Maharun, Joko Triwibowo, Ganesh Mukilan, Conor Dean, Dr Ahmed Abaza, Dr Michael Brunell, Dr Raul Chinchilla Adell, Dr Chaou Tan and Dr Nasrin Shahed Khah for sharing their valuable

inputs and experiences contributing to the progress of the research work. Additionally, I am particularly grateful to Dr Qianye Huang and Dr Ronny Genieser, who are just more than any colleagues, for helping me throughout this doctoral journey through all technical inputs and their great cooking to mention the least.

It’s been a privilege to share my stay with Arunava Sengupta, James Mathew and Dr Ashwin Rajan, who are more than just a friend. They gave me a lot of support through the ups and downs in the last few years. Every time I was down in confidence, they had always been there for me and of course to the countless trips we had together would always be there in my memory lane. I am very thankful to Anand Mohan, Sumit Sinha, Anubhav Singh, and Dr Prakash Srirangam for all the cricketing and badminton sessions we had together. Also, representing WMG in cricket and winning the 2018 interdepartmental cup for the first time in WMG’s history, has been a real privilege.

Last but not least, I would like to thank my family, who has always supported me. Maa (Lipika Malik) and baba (Kalyan Kumar Malik), without you this PhD experience would have been just a mere dream without all your sacrifices and tireless care. To my wife, Suparna, thank you for patience, support, understanding and most importantly, your love. My deepest gratitude goes to my uncles, aunties, cousins, in-law’s family and grandparents. All, thank you so much!

DECLARATIONS

I, Romeo Malik, confirm that the work presented in this thesis is my own. It has been written and complied by myself and has not been submitted anywhere else. I have undertaken the work in this thesis except where otherwise stated.

Romeo Malik

February 2020.

PUBLISHED WORK

Publication directly related to this thesis:

Chapter 5: **Romeo Malik**, Melanie. J. Loveridge, Luke J. Williams, Qianye Huang, Geoff West, Paul R. Shearing, Rohit Bhagat and Richard I. Walton. Porous Metal–Organic Frameworks for Enhanced Performance Silicon Anodes in Lithium-Ion Batteries. *Chemistry of Materials.* 2019, 31, 11, 4156-4165.

Chapter 6: **Romeo Malik**, Qianye Huang, Laura Silvestri, Danqing Liu, Vittorio Pellegrini, Luigi Marasco, Eleonora Venezia, Francesco Bonaccorso, Michael J. Lain, David Greenwood, Geoff West, Paul R. Shearing and Melanie J. Loveridge. Synthesis of Layered Silicon-Graphene Hetero-structures by Wet Jet Milling for High Capacity Anodes in Li-ion Batteries. (Submitted).

Chapter 7: Melanie J. Loveridge, **Romeo Malik**, Shashi Paul, Krishna N. Manjunatha, Serena Gallanti, Chaou Tan, Michael Lain, Alexander J. Roberts and Rohit Bhagat. Binder-free Sn–Si heterostructure films for high capacity Li-ion batteries. *RSC Advances*, 2018, 8, 16726-16737.

Other peer-reviewed publications:

1. Donal P. Finegan, Eric Darcy, Matthew Keyser, Bernhard Tjaden, Thomas M. M. Heenan, Rhodri Jervis, Josh J. Bailey, **Romeo Malik**, Nghia T. Vo, Oxana V. Magdysyuk, Robert Atwood, Michael Drakopoulos, Marco DiMichiel, Alexander Rack, Gareth Hinds, Dan J. L. Brett and Paul R. Shearing. Characterising thermal runaway within lithium-ion cells by inducing and monitoring internal short circuits. *Energy & Environmental Science*, 2017, 10, 1377

2. Upender Rao Koleti, Cheng Zhang, Quang Truong Dinh, **Romeo Malik**, Tazdin Amietszajew and James Marco. A new concept to improve the lithium plating detection sensitivity in lithium-ion batteries. *International Journal of Smart Grid and Clean Energy*. (Accepted, under print).

3. Upender Rao Koleti, Cheng Zhang, **Romeo Malik**, Truong Quang Dinh, James Marco. The development of optimal charging strategies for lithium-ion batteries to prevent the onset of lithium plating at low ambient temperatures. *Journal of Energy Storage*, 2019, 24, 100798.

GRAPHICAL ABSTRACT

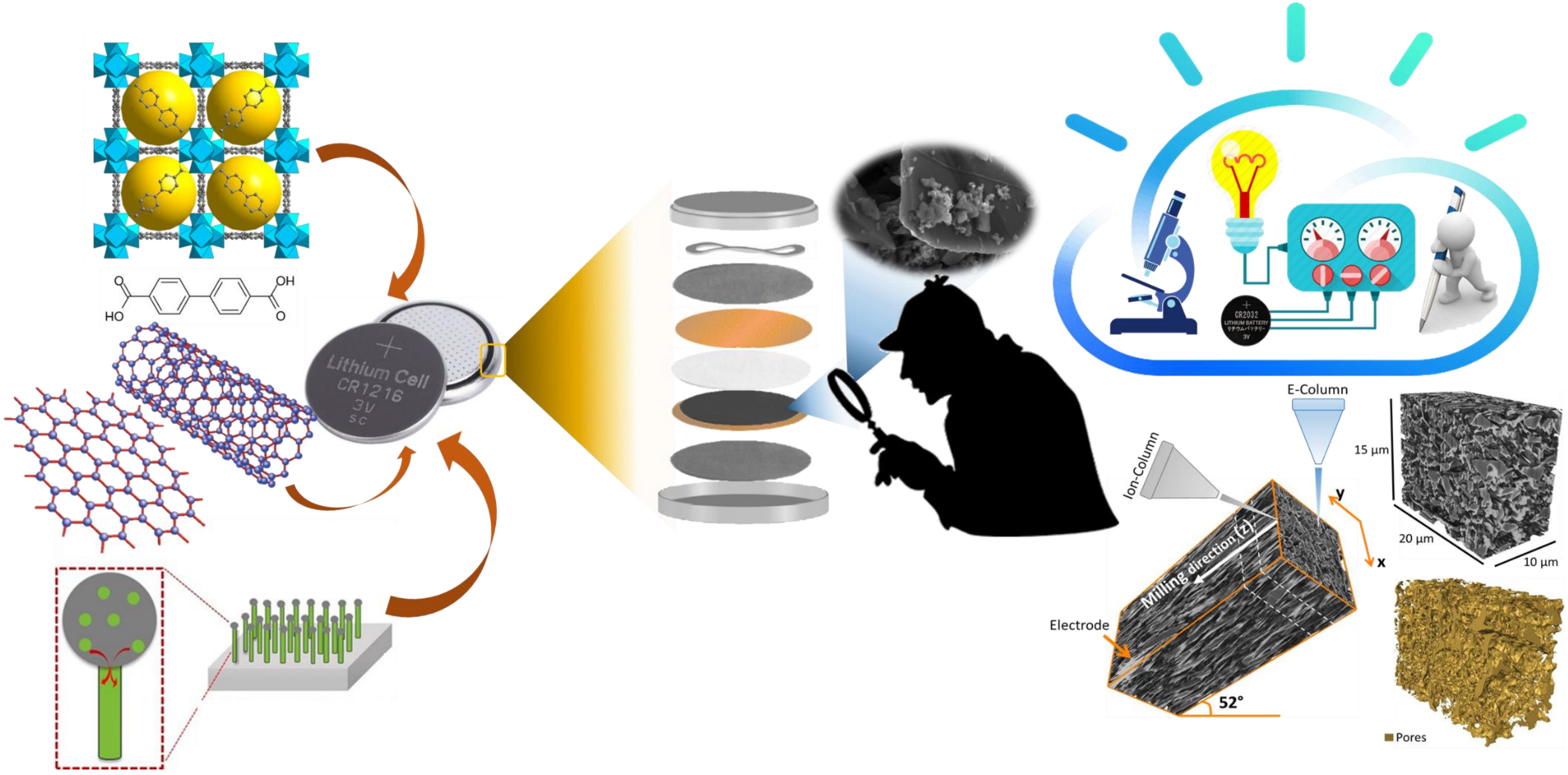

ABSTRACT

There is a continuing need for global attention to focus on further development of devices to enable efficient energy storage. This must align with a new and stringent renewable energy target of 32 % for the European Union by 2030. Present materials used within Li-ion batteries currently have a limitation on the amount of energy they can store and for a specified duration.

In order to advance the capacity of their most advanced cylindrical cells, Tesla, Samsung, LG and Sony at present use a small fraction of silicon in graphite-dominant anodes to overcome issues around volume expansion and to extend operational life. However, to date, no successful commercial product has been reported that contains silicon as the predominant lithium host material. The solutions offered so far in literature involve complex chemical synthesis or intricate processing routes, which are not realistic solutions to produce practical or cost-effective devices. The thesis core is based on innovative approaches to stabilising silicon-based anodes via additives, which can be conveniently synthesised or commercially available and are chemically compatible with the electrode components.

This research work reports on the use of metal-organic frameworks, namely UiO-66 and UiO-67, to enhance the electrochemical performance of high-capacity silicon anodes in lithium-ion batteries. This research work also studied other hybrid anode systems, based on silicon-graphene and silicon-tin powders, using conventional formulation approaches to compare with an advanced electrode manufacturing technique. This study demonstrates that certain additives improve the flexural capability and mechanical integrity of electrode materials. These additives extend the durability of silicon anodes to enable extended reversible transfer of Li-ions, and hence enable a longer lifespan of the battery.

This study reports the use of high-quality physicochemical characterisation from a variety of experimental techniques to correlate the anode's microstructure, dynamics and atomic-scale structure with the maintained performance of the battery. Focused ion beam-scanning electron microscopy (FIB-SEM) tomography, in conjunction with impedance spectroscopy and associated physical characterisation, has been employed to capture and quantify key aspects of the evolution of internal morphology and resistance build up within anodes. FIB-SEM tomography has been employed to explore the hierarchical structure of battery electrodes and for diagnosing battery failure mechanisms with high-resolution imaging. This approach will enable us to observe and quantify failures in Li-ion batteries at the electrode level. It is anticipated that this study will influence major improvements in the design of Li-ion battery materials and their processing which in turn positively impact cell performance.

LIST OF SYMBOLS AND ABBREVIATIONS

Symbol	**Definition**
ρ	Density (kg m^{-3})
R_{series}	Series resistance (Ω)
R_{SEI}	SEI resistance (Ω)
R_{CT}	Charge Transfer resistance (Ω)
Ws	Warburg Impedance (Ω)
t	Time (s or h)
T	Temperature (˚C)
Si	Silicon
Sn	Tin
Li^+	Lithium ion
Li_xSi_y	Amorphous lithiated silicon
Cu	Copper
Al	Aluminium
Z	Atomic number
Z'	Impedance real value (Ω)
$-Z''$	Impedance imaginary value (Ω)
C	Carbon
N	Nitrogen
O	Oxygen
Ga^+	Gallium ion
dQ	Differential capacity (mAh g^{-1})
dV	Differential voltage (V)
ΔG	Change in Gibbs free energy
n	Number of electrons per mole of product
F	Faraday's constant(9.65×10^4 C mol^{-1})
E	Electromotive force (V)
τ	Tortuosity factor
I	Beam intensity (W m^{-2})
I_o	Incident beam intensity (W m^{-2})
μ	Linear attenuation coefficient (m^{-1})

Abbreviations	**Definition**
1D	One-dimensional
2D	Two-dimensional
3D	Three-dimensional
BSE	Backscattered electrons
CC-CV	Constant current-constant voltage
CMC	Carboxymethyl cellulose
CNT	Carbon nanotube
C-rate	Current rate based on cell capacity
CT	Computed tomography
CVD	Chemical vapour deposition
DMC	Dimethyl carbonate
EC	Ethylene carbonate
EDS	Energy dispersive spectra
EECs	Electrical equivalent circuits
EIS	Electrochemical impedance spectroscopy
ETD	Everhart thornley detector
EV	Electric vehicle
FEC	Fluoroethylene carbonate
FIB	Focused ion beam
FIB-SEM	Focused ion beam-scanning electron microscopy
FLG_{WJM}	Graphene powder prepared via wet-jet milling
FOV	Field of View
GNPs	Few layer graphene nanoparticles
HRTEM	High-resolution transmission electron microscopy
ICE	Ion conversion and electron detector
LCO	Lithium cobalt oxide
LFP	Lithium iron phosphate
LIB	Lithium ion battery
LMIS	Liquid metal ion source
MCMB	Mesocarbon mesobeads
MOFs	Metal-organic frameworks

Na-PAA	Partially neutralized PAA with 70 mol % sodium hydroxide
NMC	Nickel manganese cobalt
NMP	N-Methyl-2-pyrrolidone
NMR	Nuclear magnetic resonance
NW	Nanowire
PAA	Polyacrylic acid
PE	Polyethylene
PECVD	Plasma-enhanced chemical vapour deposition
PEIS	Potentio electrochemical impedance spectroscopy
PEO	Polythene oxide binder
PP	Polypropylene
PPE	Polyphenylene ether
PVA	Polyvinyl alcohol
PVdF	Polyvinylidene fluoride
RVE	Representative volume element
SBR	Styrene-butadiene rubber
SE	Secondary electron
SEI	Solid electrolyte interphase
SEM	Scanning electron microscopy
SG	Stocastic grid model
$Si\text{-}FLG_{WJM}$	Si-graphene powder prepared via wet-jet milling
SiNP	Silicon nanoparticle
SnO	Tin (II) oxide
TEM	Transmission electron microscopy
TGA	Thermogravimetric analysis
UiO-66	1,4-Benzenedicarboxylic acid, 1.19 g, and zirconium(IV) chloride
UiO-67	4,4'-Biphenyldicarboxylic acid, 1.082 g, and zirconium(IV) chloride
VACNT	Vertically aligned carbon nanotube
VC	Vinylene carbonate
VLS	Vapour-liquid-solid

WJM	Wet-jet milling
XRD	X-ray Diffraction

LIST OF TABLES

LIST OF FIGURES

THESIS OUTLINE

Limited energy and power density, as well as lifespan of lithium-ion batteries still remains a major challenge at present in the realms of energy storage. Yet the correlation of microstructural degradation mechanisms with performance needs a deeper understanding. This is essential in material and component design to improve capacity retention over the lifetime. This PhD thesis focuses on understanding this microstructure-performance relationship in lithium-ion battery's anode system. The context of the research conducted is organised in the following eight chapters:

An introductory *Chapter 1* provides a background behind the rationale to study lithium-ion batteries. The underlying factors motivating the current research towards silicon-based anode systems and the research objectives are outlined here.

To address and expand upon the research objectives, *Chapter 2* comprehensively reviews higher capacity advanced anode materials and their respective electrode failure modes. Further, the strategies that have been employed to improve silicon's electrochemical performance are discussed.

Chapter 3 reviews the working principle of tomographic techniques and their potential application towards lithium-ion batteries. The reliability and appropriateness of three-dimensional tomographic analysis for studying battery electrode microstructure is reviewed. This chapter also reports the advantages and limitations of individual tomographic techniques to characterise the battery electrode's performance and degradation.

Chapter 4 presents the electrode and cell manufacturing procedure for silicon-based electrodes and methodology followed for physicochemical evaluation to investigate microstructural changes. The characterisation approach is discussed in this chapter to analyse the dynamic interactions between microstructure and electrochemical conditioning.

Chapter 5 demonstrates an evolved 3D microstructure of silicon-based anode systems with an associated array of characterisation. Specifically, the influence of incorporating MOFs on stability and pore network of silicon-based anodes was investigated.

Chapter 6 presents the use of hybrid anode materials, encompassing silicon nanoparticles embedded onto graphene, synthesised via a scalable wet-jet milling method. Tomography and impedance along with other physicochemical characterisations were employed to investigate the microstructural evolution under electrochemical cyclic aging.

Chapter 7 outlines an investigation of a silicon-tin hybrid system as an anode and also proposes an advanced manufacturing technique for scalable co-deposited silicon and tin.

Chapter 8 concludes the study by providing main understating of the knowledge developed to address the research question's underlying hypothesis. In closing, further scope of investigations and improvements are presented.

CHAPTER 1. INTRODUCTION

It is believed that a minimised dependency on fossil fuels and natural gas would diminish greenhouse gases, such as CO_2, in the atmosphere, which contribute to global warming. Lately, the efficiency of energy generation via renewable sources has improved, but to store this harvested energy, the need for reliable, high capacity energy storage devices have become crucial. In vehicle electrification, one of the major challenges is to determine the most suitable energy storage devices. Since their commercialisation in 1991, lithium-ion batteries (LIBs), have attracted broad attention as an energy storage solution. The primary challenge for LIBs concerning vehicle electrification or as an energy storage device is due to its limited capacity performance. The electrode materials inside the battery, and the way they are processed, dictates the quality of its performance. Therefore, to understand the co-relationships between material properties, microstructure and battery performance, a systematic characterisation approach is critical. However, relatively little attention has been focussed on the study of battery material microstructures, instead has focussed on active material chemistries and electrolytes. This study investigates the relationship between electrochemical performances to electrode materials microstructure for a high capacity LIB. To begin, this chapter provides an overview of the rationale behind the high capacity material and presents the research objectives.

1.1 MOTIVATION FOR THE THESIS

Historically the world has mostly functioned on power supplied with the support of fossil fuels. Finding alternative systems with which to store electricity has not seriously been made into any kind of mandate or national / global directive. Power stations across regional electrical grids have burned merely more fossil fuel whenever there is a surplus of energy demand. As a result, there is a rise in greenhouse gases in the atmosphere and with rising temperature arguably affecting the climate in a significant way[1]. Also, the transportation sector has a severe impact on the environment[2] and constitutes one of the significant sources of greenhouse gas emissions. It is estimated in the U.S. about 27 % of the greenhouse gas emission is from transportation and in some regions, the percentage could be even higher[2]. Within the transportation sector, light-duty vehicles (counting passenger cars and light-duty trucks) were the highest contributor of greenhouse gases by 60 % in 2015[2]. During the last decade, a notable incentive has grown to develop alternative sources of energy to phase out the existing hydrocarbon powered systems. In 2018, the World Energy Outlook stressed on an alternative energy source for the transportation sector to aid the climate changes from greenhouse gases and limited reserves of fossil fuels and natural gas[3]. Recently, a pledge was made for the "Decarbonisation of the global economy over the course of this century", taken at the U.N. Climate Change Conference, Paris 2015[4].

With the current scenario of rising global warming with an increase in CO_2 content in the atmosphere and its adverse effect on the climate, there is a huge motivation to strive for an alternative and cleaner source of energy for the existing conventional fossil fuel powered vehicles. Large-scale energy storage suggests itself to be a game-changer, set to emancipate alternative energy from the intermittence constraints. This means that wind, wave, solar and other renewable energy sources are at the forefront of a drive to reduce carbon emissions, and result in having an efficient way of storing energy. Hence a greater part of the energy "trilemma" could be addressed with renewable energy storage devices, with lithium-ion batteries (LIBs) being the most likely technology.

Rechargeable batteries have advanced a long way since the discovery that lithium ions can reversibly intercalate into the structures of transition-metal dichalcogenides[5]. Before the research community understood the essential safety attributes associated with LIBs, lithium metal was used as anode due to its high gravimetric density and volumetric energy density[7]. Molicel first launched their lithium batteries, with MoS_2 as cathode and lithium metal as the anode[7]. However, this lithium battery technology had to be recalled from the market due to significant safety concerns[8]. This paved the way for the evolution of LIB technology, where the lithium metal was replaced with graphite.[4] Ever since, researchers have explored numerous materials aimed at achieving higher energy density, lower cost, and safer rechargeable LIB technology[9–11].

Today, LIBs have been accredited for transforming communications and transportation, making it possible for the super-slim electronic devices and electric vehicles with a practical range to be a reality. The main reason that these innovations became possible was because LIBs can be much smaller and lighter in comparison to the previous generation storage devices namely, nickel-cadmium batteries, nickel-metal hydride batteries, lead-acid batteries and alkaline batteries. At the same time they are providing the same power and energy density. The added advantages of LIBs are that they can retain the charge for a more extended time period, and are composed of much less toxic materials (except nickel and cobalt as a lithium compound). As lithium is the lightest metal on the periodic table, and the one with greatest tendency to give up an electron, it remains the ideal ingredient to make robust, portable energy storage systems[12].

The LIB demand and market has been growing gradually ever since Sony launched its first commercial cells in 1991[13,14]. The commercialisation of LIBs has facilitated the initial move towards vehicle electrification. Subsequently the uptake of electric vehicles have also increased by 40 % over the last few years[15]. The total number of electric vehicles on the road is projected to be 18.7 million by 2030, up from 1 million at the 2018 year end[16]. To improve on the range performance of these EVs, there is a need for further improvement in material's energy density from 250 Wh Kg^{-1} towards a new and stringent target of 500 Wh Kg^{-1} by 2035[17]. Therefore, to make LIBs as the preferred method of energy storage, further technological advancement and optimisation of the materials is still needed.

The active and inactive materials inside the battery play a dominant role in dictating its performance. Tremendous efforts have been developed to refine the active battery materials and thus gain a better understanding of the complex processes that occur during their charge and discharge. Generally, battery electrodes are porous composites of active materials, conductive materials and a binding polymer. These functional porous composite materials have complex microstructures, playing a vital role in the electrochemical reactions taking place inside the battery. The performance of the LIBs is a correlative of these porous composites. The microstructures of functional electrode material influence LIB's charge-discharge behaviour, safety, capacity retention and life span.

1.2 CURRENT CONCERN WITH LITHIUM-ION BATTERY

With the growing application spectrum of LIBs, there is still a need to understand the microstructural evolution under cyclic aging. In recent years, LIBs in electric vehicles (*i.e.* Tesla Model S, Chevrolet Bolt, and Nissan Leaf) are continually exposed to inevitable stresses such as mechanical, thermal and electrochemical stresses. Despite the growing market share of electric vehicles, several incidents have shown that electrochemical characterisation alone doesn't provide adequate information to relate to their performance in the real world. One of the common issues is the discrepancy in driving range estimation[15]. Capacity loss of Nissan Leaf battery packs has been reported in numerous states in the USA between 2012-2018[18]. The drop in the battery capacity below the predicted capacity demands an enhanced understanding at the electrode material level. Hence, with the demand growing for LIBs, continued emphasis should be given in studying and understanding the correlations of electrochemical behaviour with property and structure.

Understanding the electrode microstructural evolution is vital for better material design and scalability. In recent years, researchers have been trying to track these structural changes using a variety of techniques such as optical microscopy[19], scanning electron microscopy (SEM)[20], transmission electron microscopy (TEM)[21], atomic-force microscopy[22], nuclear magnetic resonance spectroscopy (NMR)[23], and X-ray powder diffraction (XRD)[24]. However, the results from these characterisation techniques only provide two-dimensional (2D) information, which is insufficient for accurately analysing the representative three-dimensional (3D) structural evolution of the porous microstructures of electrodes[25–35].

Additionally, the macro-homogeneous model for predicting the electrochemical performance and transport behaviour of the porous electrode require electrode's porosity and thickness along with particle radius as the input parameters[36,37]. Otherwise it is assumed that the electrode material is homogeneous, isotropic and one-dimensional (1D) material made of mono-dispersed spherical particles[37,38]. While this macro-homogeneous model has been utilised to optimise and study the electrode design, it has a limited application towards studying the battery degradation or failure, owing to the restricted accountability of microstructural heterogeneity[36]. Models considering the actual three-dimensional (3D) microstructural information of the electrode contributed to a better understanding of the battery dynamics during operation[39]. Therefore, the real-life LIB microstructural data would provide better modelling accuracy and act as a validation step for the assumptions made (e.g. idealised microstructure from spherical particles)[28] on in the basic battery electrode models.

1.3 RESEARCH AIM AND OBJECTIVES

With a growing demand for high capacity LIBs, graphite (the most popular commercial anode material) poses a significant limitation with a maximum theoretical specific capacity of 372 mAh g^{-1} [40,41]. In recent years, a number of studies have shown that lithium-alloying materials offer significantly increased energy density as an anode[9,10,42–44]. Crystalline silicon (Si) and tin (Sn) are promising negative electrode candidates, with a specific capacity of 3579 mAh g^{-1} and 991 mAh g^{-1}, respectively[42]. Si lithiated at a higher voltage in comparison to graphite[44] that which reduces the probability for lithium plating thereby it is a much safer technology. Additionally, its availability in abundance in the nature makes it a sustainable material of choice. Therefore, Si anodes materials have attracted wide attention to replacing carbon-based anodes for application in high capacity LIBs[42–44].

Despite the higher specific capacity obtained, Si anodes still have major performance issues associated with them. This in turn has limited their commercialisation in LIBs[45,46]. These alloying materials undergo microstructural changes which are yet to be quantified accurately and comprehensively, and correlated with performance. During the lithiation and delithiation process, Li^+ ions alloy with electrode active materials. As a result of this alloying, the anode materials experience huge volume expansion during lithiation anywhere from 200 % to 280 % [9,43,44]. This volume alteration adversely affects the active particle's shape and size, and in particle arrangement resulting in mechanical stresses within the electrode architecture. In addition, Si has lower electrical conductivity since it is a semi-conductor[47] and lower solid-electrolyte interphase (SEI) stability from the volume changes during cycling[48]. Therefore, there is a need to understand electrode microstructure dynamics during operation and failure, as these structural evolutions ultimately culminate in the deterioration of battery performance, longevity and efficiency over time[49].

To address structural degradation issues in Si-based electrodes, various approaches have been adopted, which, in general, can be broadly categorised into the following two principal categories:

(i) Modifying silicon's morphology to better accommodate the volume changes, such as reduced particle sizes[50], macro porous structures[51] or nanostructuring[52].

(ii) Composite silicon-based anode formulations, including carbonaceous materials (carbon black, graphite, graphene)[53], hybrid active materials (composed of Si and other materials)[54], incorporating different binder chemistries (*i.e.* PVdF, CMC, PAA)[55–57], with different formulation ratios (of active material, conductive additive, binder, and solvents)[58].

Both approaches are widely applied to optimise the electrode performance, including extending cycle life. In the morphological modification, nano-structuring has attracted wide attention as an effective approach in accommodating mechanical strain as a result of volume changes[50]. However, the inherent large surface area also allows a large site for side reactions, which increases the impedance of the cell and results in capacity fade with aging[59]. Also, the morphological modification approach is usually based on highly complex synthesis methods, along with the excessive manufacturing cost of these materials, thus still posing practical questions for real applications[9]. Compared with this approach, optimising the electrode formulation and microstructure is relatively realistic and scalable. Therefore, this method incorporates and drives the core theme of this study. In this study, a commonly used method for formulating a variety of composite anodes is based on hybridising with carbonaceous materials (*i.e.* graphene), metals (*i.e.* Sn), and use of other additives *i.e.* metal-organic frameworks.

Although the battery electrode's microstructural study is essential from a post-mortem forensic perspective, the characterisation necessary for studying this microstructural changes is relatively less explored. Tomography techniques provide 3D information and enable quantitative analysis of microstructural parameters. There are various 3D imaging characterisation techniques such as atom probe tomography, electron tomography, X-ray computed tomography (CT), neutron tomography, scanning transmission electron microscopy (STEM) tomography and focused ion beam in conjunction with SEM (FIB-SEM) tomography. Commonly used imaging techniques for LIBs are FIB-SEM tomography[25,26,28–31] and X-ray CT[27,32–35]. X-ray CT and FIB-SEM tomography techniques provides a high-quality dataset of 3D images at multiple length scales. They enable high-resolution imaging in 3D at the nano-scale to micron-scales. In particular, statistically representable volumes of the electrode from these advanced characterisation techniques is important, to ensure accuracy and reproducibility, which minimises any uncertainty. Also, there lies a possibility to interpret the test results in a different approach for high capacity electrodes (i.e. Si-based or similar p-block element based electrodes) compared with commercially used carbon-based anodes.

Although many previous studies have been carried out on Si-based anodes, they have not considered current density and its influence on microstructure. There still exists a considerable need to evaluate the microstructural evolution to different current loading conditions under the presence of various additives in long term performance. Therefore, this study is focused on addressing the aim of developing a comprehensive understanding via advanced characterisation techniques, to pursue the following research question motivating this work:

- How do different additives to Si-based electrodes for LIBs influence the microstructure and performance at various current densities?

Therefore, the key objectives to pursue the above research question are mentioned below:

- Determine, experimentally, the influence of different additives on the performance of Si-based battery anode.
- Investigate the degree of battery degradation with such additives and establish the extent of influence these additives on geometrical parameters (*i.e.* porosity, pore surface area, electrode thickness, and tortuosity).
- Examine the evolution of impedance characteristics of these electrodes during cycling, which may, in turn, give further insights into understanding the overall electrode degradation.
- Establish an understanding between the microstructural evolution and electrochemical performance.

CHAPTER 2. LITERATURE REVIEW: SILICON ANODE AND MICROSTRUCTURE

A battery is the sum total of multiple electrochemical cells that are coupled in series and/or in parallel to provide the required voltage and capacity, respectively. The components of a typical LIB cell are a positive electrode (cathode) and a negative electrode (anode) separated by a porous separator soaked in an ionically conducting liquid electrolyte, enabling ion transfer between the two electrodes. Ever-increasing demands are challenging the current commercially available LIBs to deliver the energy and power requirements for hybrid and pure electric vehicles. The amount of energy a LIB can store is directly dependent on the active materials from which it is made. Therefore, advanced electrode materials with higher specific capacities (Ah kg^{-1}) and volume energy densities (Ah L^{-1}) are required. The current commercially used negative electrode material is a carbon allotrope, of the form graphite, has by now reached its performance limitations. Ongoing research efforts aimed at finding a carbon alternative are at the forefront of energy storage research in LIBs. New potential anode materials, typically p-block metals or metalloids, exhibit very high reversible capacities due to higher stoichiometric alloying with lithium compared to the current commercial graphite intercalation material. The latter display reversible cycling via an intercalation based storage mechanism. Therefore, there are several levels of possibility with elements and alloy systems for the p-block metals or metalloids (such as silicon) as negative electrodes for LIBs.

2.1 OPERATING PRINCIPLES AND COMPONENTS OF LIBs

Chemical energy stored inside batteries is electrochemically converted into electrical energy. During charging, current is passed to the cathode. The current oxidizes the cathode material, and positively charged lithium ions are extracted from the interstitial positions of the cathode. They diffuse into the electrolyte and travel through the separator towards the anode. At the same time, the generated electrons at the cathode flow through the external circuit towards the anode and result in reduction. After the completion of charging, the external circuit is left open so that the charge can be stored within the cell and stop the reverse flow of electrons towards the cathode. During discharging, the external circuit is closed, so that the electrons can flow back towards the cathode and reduce it. Lithium ions are de-intercalated or de-alloyed from the anode, and they diffuse back into the electrolyte and move back to the interstitial positions of the cathode (see Figure 2.1).

The maximum energy that can be drawn from battery depends on the Gibbs free energy (ΔG) of the materials inside the battery as is represented by the following equation:

$$\Delta G = -nFE \tag{2.1}$$

where n represent the number electrons, F represents Faraday's constant (magnitude of electric charge per mole of electrons) and E represents electromotive force (potential difference). It must be noted that not all the chemical energy is converted into electrical energy as an inevitable part is lost due to polarization effects, activation and a portion attributable to the concentration gradient in the electrode material. Most of these energy losses are in the form of heat. However, such losses are substantially dependent on the material's resistance, charge transfer reaction and diffusion rates of the materials. Therefore, due attention must be paid towards the choice of materials for meeting the required performance of the battery cell.

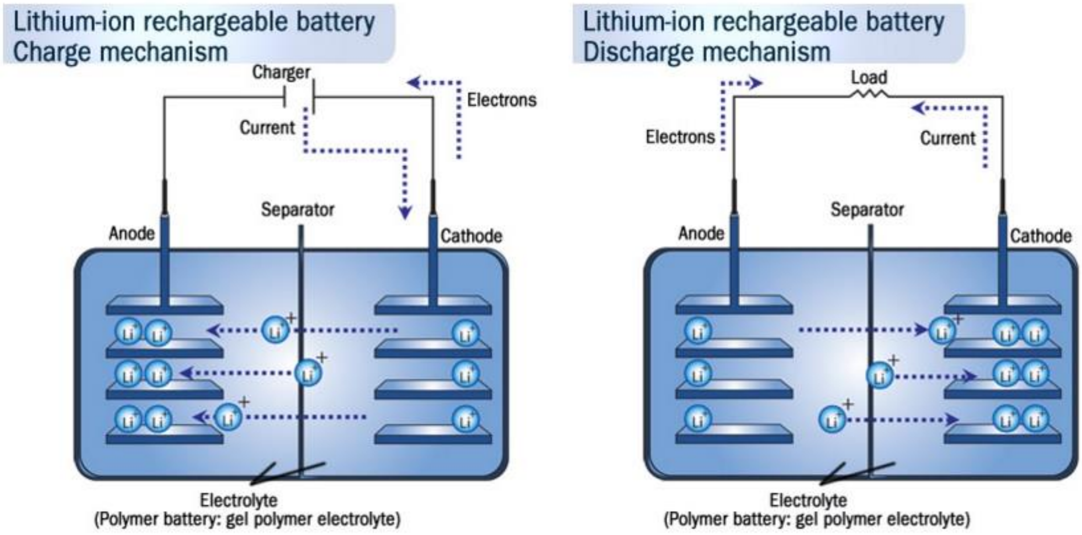

Figure 2.1: Schematic diagram representation of charge and discharge process in LIBs[60].

A brief of the LIB components and their properties are discussed below:

Positive Electrode (Cathode): Generally, the commercial LIB cathode materials are made from transition metal oxides or phosphates. The cathode has a high redox potential and is the primary source of lithium for lithiation and delithiation process.

Negative Electrode (Anode): Graphite has been the most commercially used anode material. During the lithiation process, anode materials either form an alloy with lithium (in silicon-based anodes) or lithium intercalates into the anode's layered structures (in graphitic anodes).

Current Collector: Current collectors are selected according to their respective corrosion resistance ability and conductivity in the electrochemical operating window[61]. Copper and aluminium are used as current collectors for anode and cathode, respectively[62,63]. During the redox reactions taking place at the electrode, the electrons are transferred from current collectors to the external circuit.

Electrolyte: The electrolyte acts as a medium where the lithium diffuses and provides an ionically conductive path between cathode and anode during operation. Commercially used liquid electrolytes generally contain an $LiPF_6$ conductive salt dissolved in a combination of organic solvents, such as ethylene carbonate (EC) or dimethyl carbonate (DMC) with special additives such as vinylene carbonate (VC).

Separator: The separators are thin, porous and highly wettable polymers which act as an electrically insulating layer while ionically conductive, separating the cathode and anode. The commercially available separators are generally single layer made of polypropylene (PP) or polyethene (PE), and tri-layer arranges as PP|PE|PP where PE acts as a shutter to stop lithium movement if the internal temperature of the battery rises above a specific level.

2.2 DOMINANT DEGRADATION MECHANISMS IN ANODES

During charge-discharge cycling, the capacity of the Li-ion batteries continually decreases over time or fades due to several mechanisms associated with side reactions and concurrent internal resistance build up. This capacity loss is mostly associated with overcharging (lithium deposition), current collector corrosion, self-discharge, electrolyte decomposition, passive layer formation, active material dissolution and phase changes within electrode material[64]. Quantifying some of these degradation mechanisms has enabled advances in material or electrode redesign. A considerable improvement is required in cell performance standards such as energy density and cycle life, without any compromise on safety, and cost. Energy density is an essential parameter for Li-ion batteries for electrified transport applications, especially where there are range thresholds. Storage capacity and durability remain a requirement in other applications such as grid storage and portable electronic devices. This need for improvement will require a deeper understanding of the material components within the battery and the underlying physicochemical processes that lead to resistance build-up and capacity loss.

With the array of different degradation mechanisms taking place inside the battery, this invariably modifies the electrode properties, affecting the longevity of the battery; capacity, impedance and voltage of the battery during storage or upon further cycling. Capacity loss or impedance rise can be measured and quantified, and related to the capacity fade and power fade using galvanostatic cycling with electrochemical impedance spectroscopy data. Charge-discharge cycling of the battery is influenced by the following parameters of the battery: (a) active anode material, (b) interface between the electrodes and electrolyte and (c) the composite electrode, *i.e.* active material matrix, conductive additives, porosity, binder, the current collector surface[65]. Microstructural evolution in the anode material has an influence on the degradation mechanisms and thereby to the battery performance[66–69].

The anode material's particle size, surface area and porosity have a significant influence on the battery's performance[50,68,70]. The lithium diffusion pathways are shorter for small particles which is beneficial for high power battery applications, but they also have a large surface area that indicates more opportunities for surface redox and side reactions[71,72]. Additionally, increase in porosity increases the effective surface area but reduces the lithium diffusion path lengths and the charge transfer resistance will be reduced. Large pores will accumulate more electrolyte and can generate more decomposition reactions at the interfaces.

A brief synopsis of various degradation mechanisms taking place at the anode is discussed below.

2.2.1 SOLID ELECTROLYTE INTERPHASE (SEI) LAYER

When silicon is cycled versus Li/Li$^+$, the electrolyte becomes reduced at the electrode surface at < 0.9 V[73]. This passivating layer formed as a result of electrolyte degradation protects both the electrolyte and electrode from further reaction. The decomposition product is electronically insulating but ionically conducting. Therefore, the SEI prevents the electrolyte from further reduction with the active particles from further corrosion. Various other reactions taking place at the SEI layer in the presence of an electrolyte is very detrimental to the battery's performance (see Figure 2.2) and is considered as the primary source of battery degradation[74].

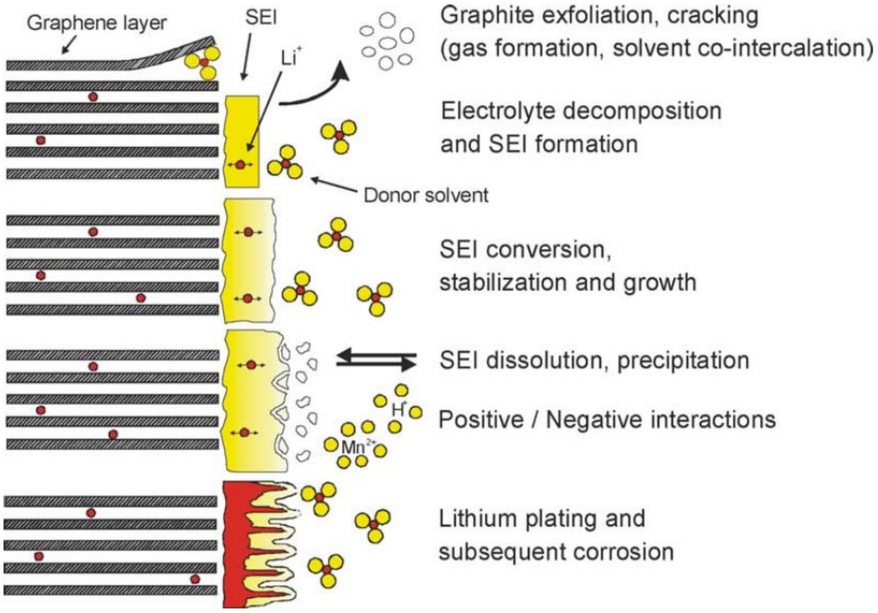

Figure 2.2: Various reactions taking place anode-electrolyte interphase. Reproduced with permission from [65]*. Copyright (2005), Elsevier Science.*

SEI has a direct influence on battery performance by passivating the anode's surface and hindering further electrolyte degradation[75]. Mostly the SEI layer is made of hydrocarbons, PEO-type oligomers, Li alkyl carbonates, LiF, LiOH[76–78]. The formation and stability of SEI are crucial for high coulombic efficiency and longevity of the battery. However, for the silicon electrode, the SEI is not stable because of the high volume change making it unstable. Therefore, there is a gradual increase in thickness of the SEI layer as during contraction (delithiation) the previously formed SEI breaks down, exposing fresh surface for reaction with electrolyte[65,79]. This exposed surface forms a fresh SEI layer, and this breakdown and formation of new SEI continue with cycling (see Figure 2.3). This affects capacity as there is a loss of additional Li^+ ions wherever the new SEI is formed and the thick SEI layer also affects the lithiation and delithiation kinetics for silicon[59]. With the gradual growth of the SEI layer, the porosity is affected resulting in impedance rise as the effective surface area decreases.

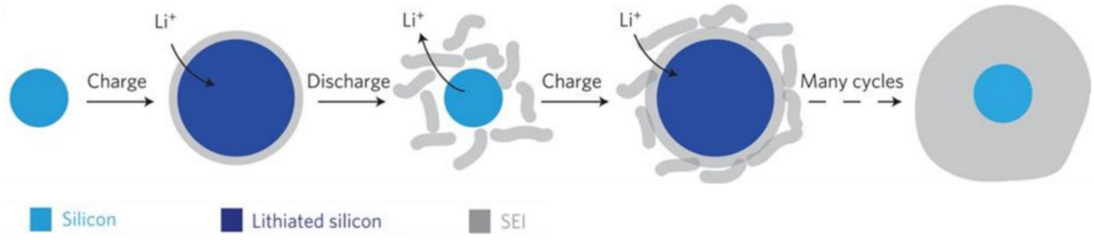

Figure 2.3: Schematic of continuum growth of SEI layer with cycling. Reproduced with permission from[80]. Copyright (2012), Springer Nature.

Generally, the formation of the SEI layer is followed by gas generation as a by-product from decomposition[81]. The irreversible capacity from the initial cycling is attributed to the formation of the SEI layer, which is also dependent on the anode particle's surface area and even the environmental condition (e.g. temperature, pressure) of the battery under operation[82]. Upon cycling for an extended period, the irreversible capacity can still be observed due to the diffusion of impurities and other anions from the electrolyte through the SEI layer.

The composition of the electrolyte has a major influence on the SEI composition as it is the decomposition product of electrolyte[83]. Therefore, appropriate additives for electrolytes are essential to form a stable SEI, which is beneficial in reducing further irreversible capacity loss, self-discharge and also reduction of additional reactions taking place at the SEI, as shown in Figure 2.2. The composition and morphology of the SEI layer changes with the rise in temperature and may even breakdown or succumb to dissolution. Even though the kinetics of lithium ion diffusion is improved at a higher temperature, and this change is very detrimental to the battery's performance[84]. The scenarios change a bit when operating at low temperature. The reversible potential of carbonaceous materials is close to lithium's reversible potential. Therefore, there is a high chance of plating lithium on the anode producing dendrite growth in conditions where lithium ion diffusion is reduced, e.g. because of growing

SEI layers[85]. Furthermore, the metallic lithium reacts with electrolyte and can promote battery degradation[86].

2.2.2 LOSS OF REVERSIBLE LITHIUM IONS

Lithium ions are lost irreversibly inside the batteries for three primary reasons: (a) SEI layer formation at the electrode surface during initial cycling from electrolyte decomposition, (b) side reactions with the electrolyte on further cycling of the battery, and (c) electrochemical isolation of active material due to volume expansion[87,88]. The majority of the lithium lost irreversibly is because of the SEI layer formation during initial cycling and subsequent growth upon further cycling[48]. The thick SEI layer reduces the lithium ion diffusion kinetics as these layers reduce the porosity volume of the electrode and thereby isolating the particles. The loss of reversible lithium ions is also related to the surface area of the active particles as a higher surface area and results in increased formation of the SEI layer[54]. However, higher surface areas are also considered a requirement for higher power density batteries. The extent of continued SEI-induced Li loss can be reduced by forming a stable SEI layer. This is possible by adding special electrolyte additives such as vinylene carbonate (VC)[45], fluoroethylene carbonate (FEC)[89]. These electrolyte additives undergo reductive deposition on electrode's surface at higher potentials thereby improving the cycling stability of electrode by forming a relatively low resistive and uniform SEI layer[90].

2.2.3 STRUCTURAL CHANGES

Within the electrode, the structure of the anode particles changes upon lithiation and delithiation. For example, graphite anodes undergo 10 % volume change upon lithiation and delithiation, whilst silicon materials undergo 280 % volume change at maximum lithiation capacity[9,91]. At the active particle's surface, many redox reactions and ion exchange reactions take place during cycling, but these might be adversely affecting battery's performance. For example, exfoliation of graphite, graphite particle cracking and SEI formation from electrolyte interaction at particle surfaces are all contributory factors responsible for cell failure[9].

During lithiation the structure of the anode particles can change, *i.e.* they undergo phase transformations (see Figure 2.4) or changes in the crystallographic structure. This results in stress build-up, which might lead to crack initiation and subsequent fracture of particles[92]. Lithiation of silicon generally occurs by a two-phase mechanism[10,90,93] (see Figure 2.5). Crystalline silicon reacts with lithium to form amorphous lithiated silicon (Li_xSi). The main reason behind these two phases is a large activation barrier for breaking the Si-Si bonds which is possible only if a high concentration of lithium ions is at close proximity[94]. The amorphous silicon formed is rich in lithium where $x = 3.4 \pm 0.2$ lithium atoms per silicon atom, the reported maximum value of x is 3.75[95]. The highly lithiated silicon formed is responsible for massive volume expansion of silicon particles building up the enormous strain on the particles.

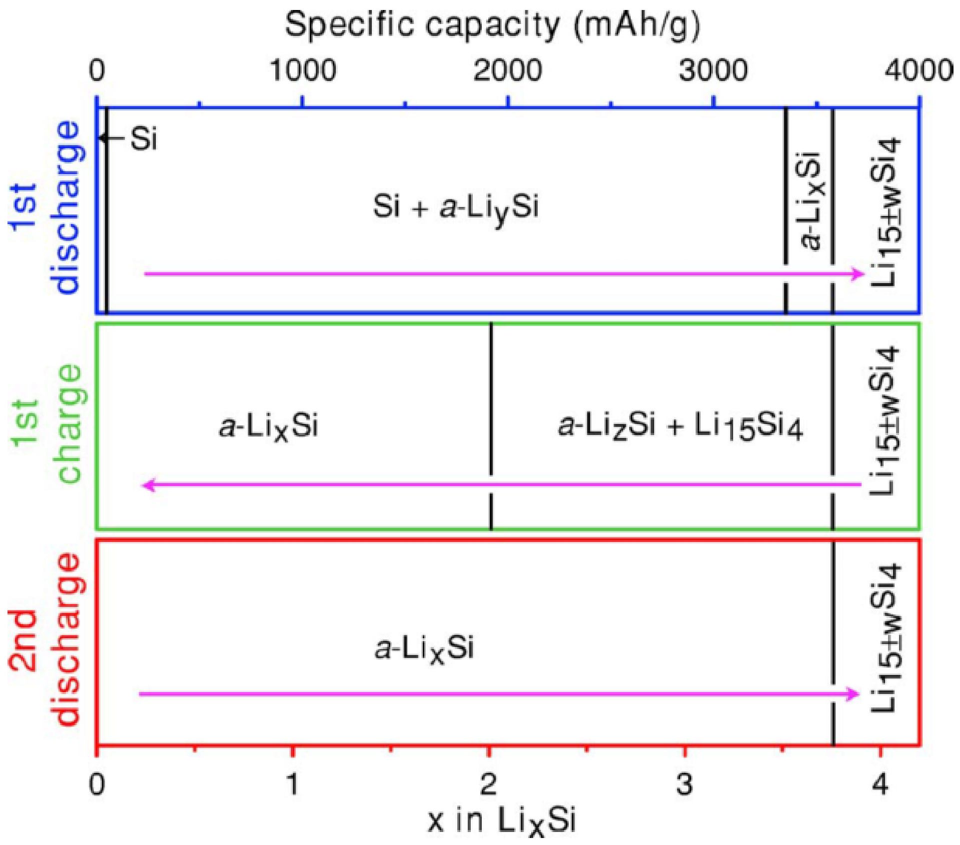

Figure 2.4: Phase diagram depicting different phases forming during cycling of a Li/Si electrochemical cell. Reproduced with permission from [96]. Copyright (2007), The Electrochemical Society.

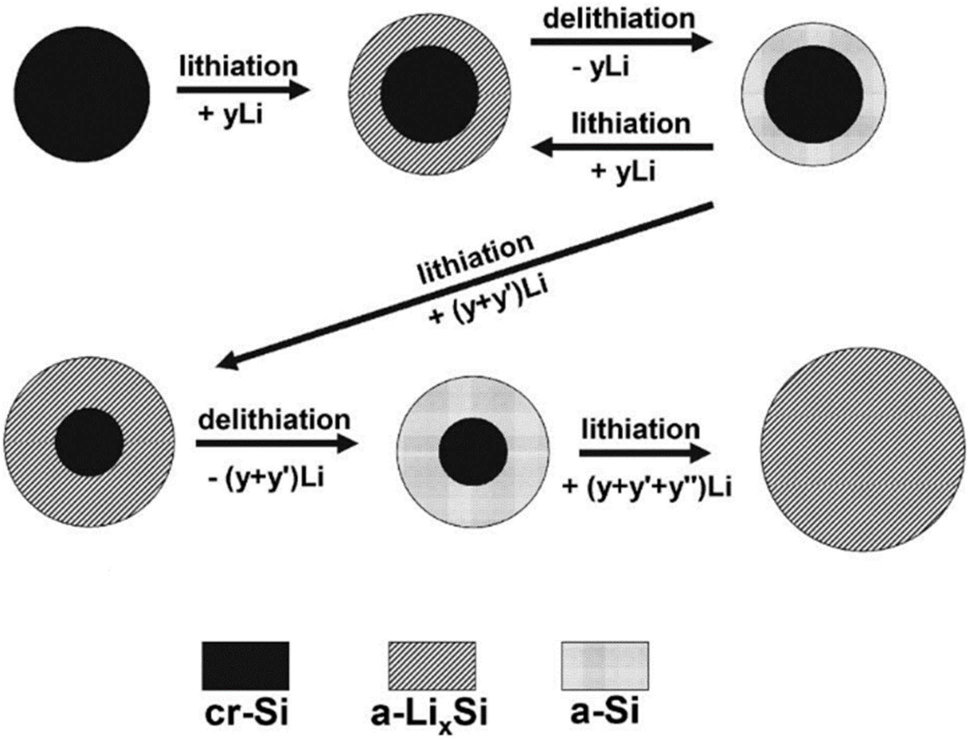

Figure 2.5: A schematic illustration of two-phase lithiation-delithiation mechanism in silicon particles during cycling. Reproduced with permission from [91]*. Copyright (2006), The Electrochemical Society.*

Wen *et al.* discovered the intermediate equilibrium phases that are formed in the Li-Si electrochemical system from coulometric titration experiment at 415°C[97]. At high temperature, the nominal compositions for these phases are $Li_{12}Si_7$, Li_7Si_3, $Li_{13}Si_4$, and $Li_{22}Si_5$, respectively[23,73,98–100]. The formation of these phases can be observed during the high-temperature electrochemical experiment as steps in galvanostatic voltage profile where each step corresponds to the stable phase(s). However, the galvanostatic voltage profile at room temperature reveals a relatively flat voltage plateau around 0.1 V suggesting a two-phase lithiation process. At room temperature inside the electrochemical system, solid-state transformations take place forming metastable amorphous lithiated silicon ($Li_{15}Si_4$) as the stable phase is kinetically hindered[101]. This transformation has been confirmed by various techniques, for example X-ray Diffraction (XRD)[96], scanning electron microscopy (SEM)[102], nuclear magnetic resonance spectroscopy (NMR)[23], and high-resolution transmission electron microscopy (HRTEM)[103].

2.2.4 CURRENT COLLECTOR CORROSION

Generally, copper (Cu) and aluminium (Al) are used as the current collector for anode and cathode electrodes, respectively. The main problems associated with these current collectors are adhesion with the electrode, localised corrosion (pitting), passive film formation and delocalised corrosion[64]. These problems increase the internal impedance during cycling and culminate in capacity loss and power fade. Al is very susceptible to pitting whilst Cu can be affected by environmentally-assisted cracking[104]. Braithwaite *et al.*[104] studied pitting of Al and environmental cracking of Cu under impedance spectroscopy, X-ray photoelectron spectroscopy and Auger electron spectroscopy. It was observed that upon cycling, Al became passive and the surface was covered with Li and phosphorus (P) from the electrolytes used. Environmentally assisted cracking of Cu occurs near lithium's reversible potential under appropriate conditions such as work hardened or large grain size.

To address the aforementioned problems, the commercial electrode foils are conditioned under acid-base etching, corrosion resistant coating, and conductive coating. These improve the resistance to corrosion and promoting adhesion between the electrode coating and the foil[64].

Corrosion at the current collectors is one of the causes of increase in internal resistance over cycling because of the formation of insulating corrosion products (such as Al_2O_3, AlF_3, Li_2O) at the surface[61,104]. The gradual corrosion of current collectors might lead to continued increase in the internal resistance of cells, which eventually contributes to capacity fade[61]. If the battery is overcharged, there is a possibility of copper dissolution due to its restricted stable electrochemical window to 0-3 V vs. Li/Li^+ for $LiPF_6$ salt based electrolytes[61]. Also, these reactions occur more rapidly because of the non-aqueous system of the battery. The copper ions formed as a result can re-deposit on the anode and grow dendritically. Such growth is diffusion limited, and runs the risk of puncturing the separator and causing catastrophic failure of the battery by way of an internal short circuit. Therefore, LIBs are specified to operate within a specific potential window.

2.2.5 LITHIUM PLATING

Pure lithium foil was once used as anode material for LIBs because of its light weight and high energy density, but its susceptibility towards dendrite formation made it unsuitable for LIBs. Graphite is the most successful and commercial anode material for LIBs; however, it is prone to lithium plating as its reversible potential is in close proximity to the reversible potential of lithium[85]. Metallic lithium deposition is reversible as it oxidises at a potential of 100 mV higher than the de-intercalation potential resulting in an overpotential during discharge[86].

Some of the factors that influence lithium plating on anode surfaces are namely, (i) capacity ratio between anode and cathode (represented as R) *i.e.* low R value will deposit metallic lithium as anode polarizes (ii) low temperature operation at high C-rate and (iii) composition of electrolyte, *i.e.* if ethyl carbonate (EC) is high in concentration promotes lithium deposition[85]. The kinetics of the battery anode is affected to a great extent from lithium plating[85].

The lithium plating is also influenced by the orientation of particles and non-homogeneous current distribution[105]. The latter results from this random orientation of particles in the initial cycling and promotes the formation of mossy to dendritic-like deposits[106]. These deposits grow between separator and anode, and the growth rate is directly proportional to temperature and current density. As mentioned previously, if the dendrite propagates, it can puncture the separator, resulting in a short circuit and thermal runaway. Lithium plating can be identified from the discharge curve’s voltage plateau and relates to the low coloumbic efficiency of the battery.

2.2.6 VOLUME CHANGES

Anode active particle fracture due to volume changes during lithiation and delithiation has a significant effect on the capacity fade in silicon electrodes[107]. For a better understanding of particle fracture, there is a need to understand these volume changes and the related stress and strain experienced by the particles. Rhodes *et al.*[108] used an acoustic emission technique to observe the effect of initial phase transformation taking place in silicon anodes. The study found more particle fractures during initial cycling in comparison with further cycling, suggesting that there is a difference in volume expansion occurring in the crystalline silicon lithiation compared with that occurring in amorphous silicon.

Some studies reveal that the volume expansion in crystalline silicon is anisotropic[107]. Lee *et al.*[107] studied the variation of geometric shape and crystallographic dependent volume changes upon lithiation and delithiation in silicon nano-pillars. These nano-pillars with axial orientations <100>, <110> and <111> synthesised from silicon wafer upon lithiation transformed into a cross, ellipse and hexagonal shapes, respectively (see Figure 2.6). It was observed that volume expansion is prominent at the <110> direction. Similarly, Goldman *et al.* observed anisotropic volume expansion under SEM, dominating at <110> direction[109]. The main reason behind this anisotropy is the differences in interfacial mobility of different directions during lithiation. Liu *et al.* observed that kinetics is favourable for lithium interaction along <110> direction compared to <111>[103].

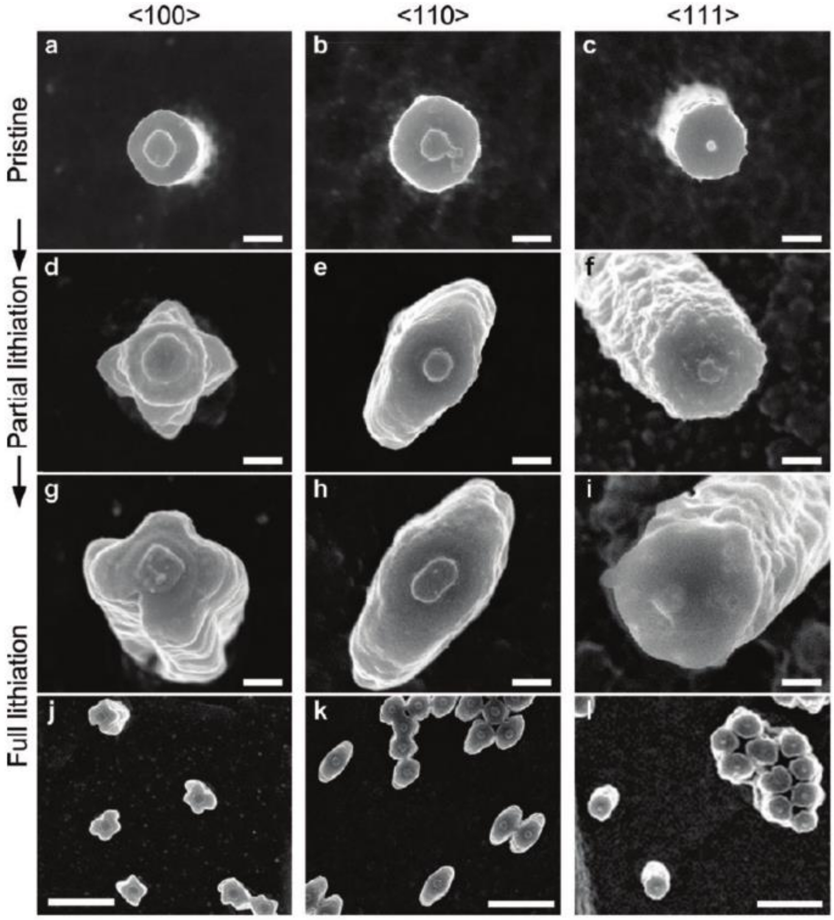

Figure 2.6: Anisotropic lateral expansion of crystalline Si nanopillars with three different axial orientations (<100>, <110> and <111>) upon lithiation. Reprinted with permission from [107]*. Copyright (2011), American Chemical Society.*

The volume expansion not only exerts effects at the particle level, but also affects the entire electrode architecture (see Figure 2.7). During lithiation, the particles expand and during delithiation particles partially contract. During these volume changes, the active particles lose contact from neighbouring particles and also from the current collector. These events result in an increase in internal resistance and an irreversible capacity loss to the battery. Furthermore, there is also a significant increase in the thickness of the electrode.

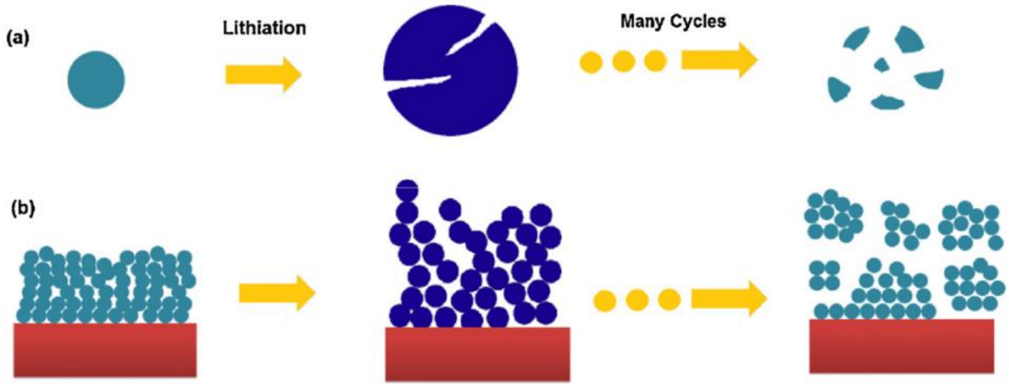

Figure 2.7: Schematic diagram representation of different failure mechanisms in silicon: (a) Si particle pulverization, (b) Si electrode's architectural disintegration. Reprinted with permission from [110]. Copyright (2012), Elsevier Ltd.

2.2.7 PARTICLE FRACTURE

With volume changes during lithiation, the particles are observed to fracture, and this is very dominant during the first charge-discharge cycle, contributing to the irreversible capacity loss in silicon anodes[108]. In crystalline particles, cracks initiate at the surface as a result of the lithiation stress experienced during the alloying process[103]. The cracks also creates a fresh surface for lithiation (and increased SEI), further adding to the structural expansion[111]. The crack evolution and propagation is different in a single-phase reaction compared with the two-phase reaction (in Li-Si system). The latter experiences tensile stress at the amorphous lithiated phase of silicon on the surface of the particle, which in turn enhances the probability for a crack generation (unlike in a single phase reaction)[112]. These surface cracks are found to be mostly dependent on the particle size and the rate of the lithiation process[112]. Anisotropic volume expansion influences the location where crack initiates, as <110> direction is a preferred site for the crack formation in the {110} plane[112]. Also, cracking and pulverisation results in loss of contact from the conductive network and thereby also leads to capacity fade.

Table 2.1 summarises various degradation mechanisms taking place at the anode and plausible ways to reduce such effects. The main contributors of capacity fade are continuous SEI layer formation and loss of contact among active particles while power fade is because of decreased accessibility to active particles from thick SEI layers.

Table 2.1: Various anode degradation mechanisms.

Cause	Effect	Leads to	Reduced by	Enhanced by
Electrolyte decomposition	➢ Lithium loss ➢ Rise in impedance	➢ Capacity loss ➢ Power loss	➢ Stable SEI by additives ➢ Rate decreases with time	➢ Higher temperature ➢ Higher SOC
Particle cracking, solvent co-intercalation and gas generation	➢ Active material loss ➢ Lithium loss	➢ Capacity loss	➢ Stable SEI by additives ➢ Electrode pre-treatment	➢ Overcharging
Reduced active surface area due to continual SEI growth	➢ Rise in impedance	➢ Power loss	➢ Stable SEI by additives	➢ Higher temperature ➢ Higher SOC
Decrease in Porosity	➢ Overpotential ➢ Rise in impedance	➢ Power loss ➢ Capacity loss	➢ Stable SEI by additives ➢ External pressure	➢ Higher current cycling ➢ Higher SOC
Electrode architecture disintegration	➢ Active material loss	➢ Capacity loss	➢ External pressure	➢ Higher current cycling ➢ Higher depth of discharge
Binder decomposition	➢ Lithium loss ➢ Reduced mechanical stability	➢ Capacity loss	➢ Good choice of binder	➢ Higher temperature ➢ Higher SOC
Current collector corrosion	➢ Inhomogeneous current distribution ➢ Rise in impedance	➢ Power loss	➢ Current collector pre-treatment	➢ Overdischarge ➢ Lower SOC
Lithium plating	➢ Lithium loss	➢ Capacity loss	➢ Narrow potential window	➢ Lower temperature ➢ Higher current cycling ➢ Poor electrode geometry misfit or capacity balance

2.3 SILICON ANODE DEVELOPMENT FOR LIBs

For the future application of LIBs such as electric vehicles and grid storage, there is a need for high capacity LIBs. Table 2.2 compares different materials that can host lithium and can be applied as LIB’s anode material.

Table 2.2: Comparison of various anode materials. Reprinted with permission from [44]. Copyright (2010), Elsevier B.V.

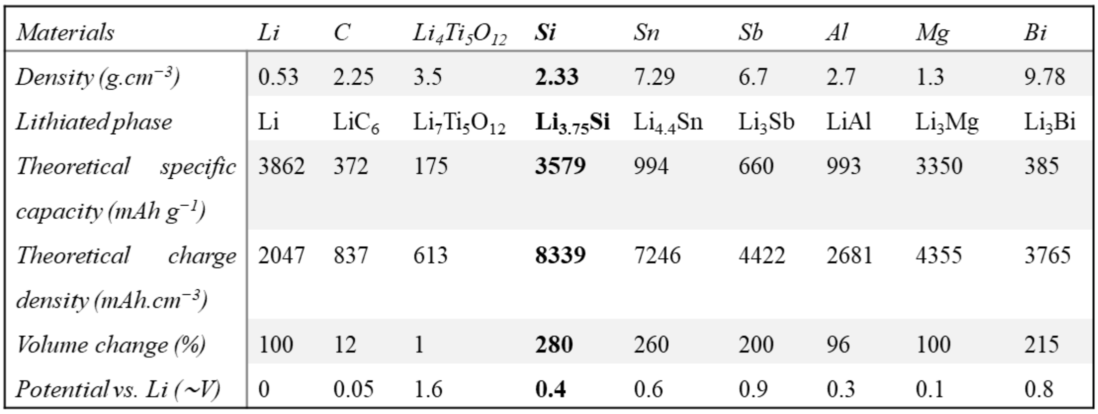

Materials	*Li*	*C*	*$Li_4Ti_5O_{12}$*	***Si***	*Sn*	*Sb*	*Al*	*Mg*	*Bi*
Density ($g.cm^{-3}$)	0.53	2.25	3.5	**2.33**	7.29	6.7	2.7	1.3	9.78
Lithiated phase	Li	LiC_6	$Li_7Ti_5O_{12}$	**$Li_{3.75}Si$**	$Li_{4.4}Sn$	Li_3Sb	LiAl	Li_3Mg	Li_3Bi
Theoretical specific capacity ($mAh\ g^{-1}$)	3862	372	175	**3579**	994	660	993	3350	385
Theoretical charge density ($mAh.cm^{-3}$)	2047	837	613	**8339**	7246	4422	2681	4355	3765
Volume change (%)	100	12	1	**280**	260	200	96	100	215
Potential vs. Li (~V)	0	0.05	1.6	**0.4**	0.6	0.9	0.3	0.1	0.8

Among the many anode candidates, Si is considered as the ultimate high capacity successor to the commercially mature anode graphite in LIB technology. This is due to its gravimetric capacity of 3579 mAh g^{-1} achieved by forming an alloy with Li, with the maximum capacity ratio being $Li_{3.75}Si$ with respect to lithium (see Figure 2.8a)[42,96]. From Figure 2.8b, it should be noted that often reported gravimetric capacity of 4200 mAh g^{-1} for Si is feasible only at high temperature (450 ºC) as observed during equilibrium coulometric titration experiment[110].

Additionally, Si has other advantages; namely, natural high abundance, low cost, and environmental benignity[90]. However, silicon's volume expansion and continual SEI growth culminate in conductivity loss and increase in internal resistance and finally into capacity fade[9]. The resulted capacity fade reduces the coulombic efficiency of the battery[113,114]. All of these operational issues have prevented Si's commercial uptake within Li-ion batteries, especially for more demanding applications such as transport and extended duration grid storage.

Both the mechanical and chemical degradation, alongside Si's lower intrinsic conductivity, leads to the inferior cycling performance and thereby hindering its commercialisation as a new-generation anode material for LIBs. Eventually, research advancement that needs to be achieved has to lead towards improving both the mechanical and chemical properties of the Si-based electrodes. The review below will summarise the significant approaches from the literature and augment the understanding gap in correlating the electrode's physicochemical considerations with electrochemical performance.

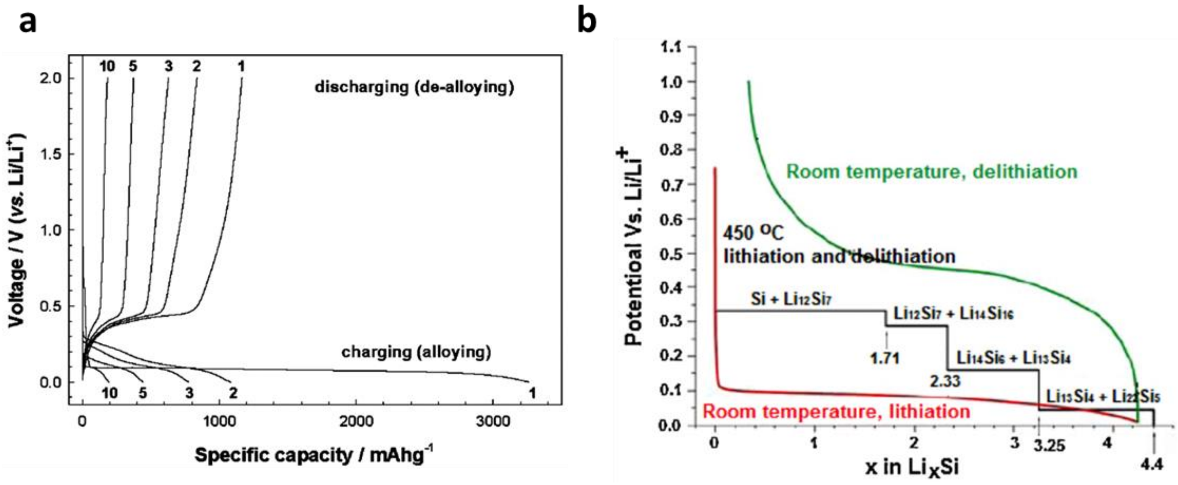

Figure 2.8: (a) Galvanostatic cycling plot for silicon anode[115]*, (b) Electrochemical cycling plot for silicon vs Li at room temperature and high temperature. Black line: theoretical voltage curve at 450°C. Red and green line: lithiation and delithiation of crystalline Si at room temperature, respectively. Reprinted with permission from* [96] *and* [110]*. Copyright (2004), The Electrochemical Society and Copyright (2012), Elsevier Ltd., respectively.*

2.3.1 STRATEGIES FOR IMPROVING ELECTROCHEMICAL PERFORMANCE

To address the aforementioned issues, much research has been carried out over the years to improve the performance of state-of-the-art silicon anodes in LIBs. In the last decade, considerable advancement in various techniques, such as modifying the silicon morphology, adding carbonaceous material, varying the binder systems[51,116,117]. This has helped to develop high-capacity silicon anode composites (with an appropriate polymer binder and carbon conductive material) with improved capacity retention capability. To date, the research carried out can be categorised into the following areas of development: nanostructures, modified porous silicon morphologies, conductive encapsulation, binders, artificial SEI formation, and composites. Silicon % loading, particle size and distribution and the ratio of other components play an essential role in determining the battery's performance regarding capacity retention and efficiency.

2.3.1.1 NANOSTRUCTURES

Nanostructuring has demonstrated the ability to dissipate the mechanical strain within the structure, and has produced a remarkable achievement in the longevity of capacity retention of silicon anodes.[50] A critical particle size to sustain the large volume strains without cracking was found in the first *in-situ* TEM study by Liu and Huang[50], with a particle diameter of ~150 nm. Additionally, Ryu *et al.*[118] demonstrated that SiNWs with diameters lower than ~300 nm is not susceptible to fracture during volume expansion. Thereby, multiple morphologies of Si nanostructures have been synthesised, namely, nanowires[119], core-shell nanofibers[120], nanopowders[52], nanotubes[80], nanofibers[121], nanorods[122], nanospheres[123], and other nanoporous[124] materials. These nanostructures can accommodate substantial volume change during lithiation and delithiation. Also, the nanostructures provide ample surface area higher rate performance[125]. However, the inherent large surface area also promotes large scope for side reactions and thereby increasing the impedance of the whole cell and resulting in capacity fade with aging[59].

Thin-films fabricated via various chemical and physical depositions are reported to be stable under high capacity cycling[126,127]. In thin-films there is the absence of a binder, conductive material and a low surface area to capacity ratio. However, the irreversible morphological degradation associated with thin films such as cracking, limits the thickness of the films. The critical thickness of amorphous Si thin films is estimated to be within 100 to 200 nm on a stainless steel substrate[128]. This extremely small thickness of the Si electrode significantly limits the battery capacity and thereby its application in a viable battery technology.

2.3.1.2 MODIFIED POROUS SILICON MORPHOLOGY

The principle behind a porous morphology is very similar to the nanostructures, *i.e.* to provide accommodating space for the volume expansion during lithiation of Si particles, but also to mitigate the mechanical strain. Additionally, these structures offer shorter diffusion pathways for alloying Li^+ ions. Macroporous silicon particles are synthesised via a chemical etching route (see Figure 2.9). These particles have porous structures throughout their volume to accommodate large volume changes but also serving to increase the surface area (for faster diffusion of Li^+ ions). This is a novel approach to improve capacity retention over cycling, and also efficiency. Bang *et al.*[51] synthesised three-dimensional (3D) porous silicon structures from 10 µm silicon particles via a two-step method. First, the Ag nanoparticles were deposited on bulk silicon powders via a galvanic reaction and then chemically etched to yield porous structures. Likewise, alternative synthesis routes also yielded a porous structure, namely, ball milling metallurgical grade silicon (with high impurities, e.g. Fe, Al) followed by stain etching[129]. It was observed that these structures exhibited improved first cycle capacity, coulombic efficiency and rate capability for initial cycling. However, high capacity fading, electrolyte decomposition and unstable SEI layer are hindering the applicability of these materials in LIBs[130]. Another downside is their lower volumetric capacity because of the porous nature of the particles.

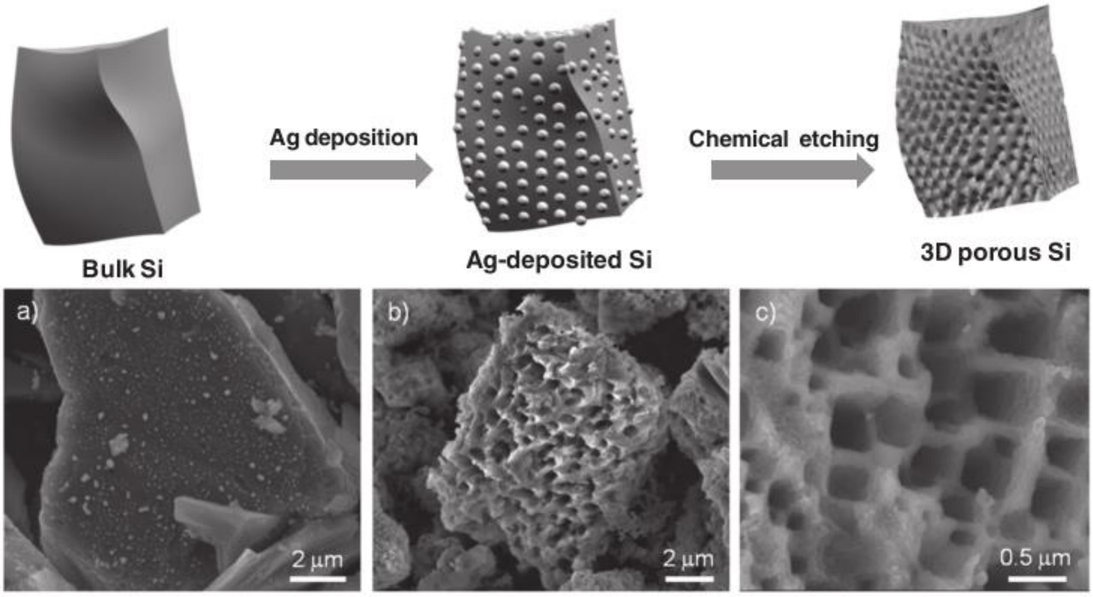

Figure 2.9: Schematic diagram representation of 3D macro porous silicon preparation from bulk silicon powders. Lower: a) SEM image of Ag- deposited Si, b) SEM image of chemically etched Si, c) magnified SEM image of samples seen in (b). Reprinted with permission from [51]*. Copyright (2012), WILEY-VCH Verlag GmbH & Co.*

2.3.1.3 CONDUCTIVE ENCAPSULATION

To address capacity fade in silicon, another approach have been applied *i.e.* by forming a conductive 3D network across the particles. Carbon-coated nanoparticles were synthesised to improve the electronic conductivity and also to mitigate the surface side reactions by forming a stable SEI. Liu *et al.*[116] synthesised a pomegranate-inspired silicon electrode (see Figure 2.10). Here, the silicon nanoparticles were coated with SiO_2 and then carbon encapsulated, with the SiO_2 coating subsequently etched away by HF solution. This leaves sufficient space between the silicon nano-particle and the carbon coating to accommodate the volume changes in the silicon. These encapsulated nano silicon particles were then further encapsulated by another thicker carbon coating, acting as a barrier to the electrolyte. Therefore, it was observed that the SEI formed was stable, resulting in higher longevity, volumetric capacity and improved coulombic efficiency. Analogous encapsulation framework was achieved with graphene sheets. Li *et al.*[131] and Zhu *et al.*[132] synthesised structures containing voids with graphene/carbon nanofibers showing enhanced cycling performance and rate capability. Zhu *et al.*[132] obtained an electrochemical performance of ~2000 mAh g^{-1} at a current density of 700 mAg^{-1} over 1050 cycles.

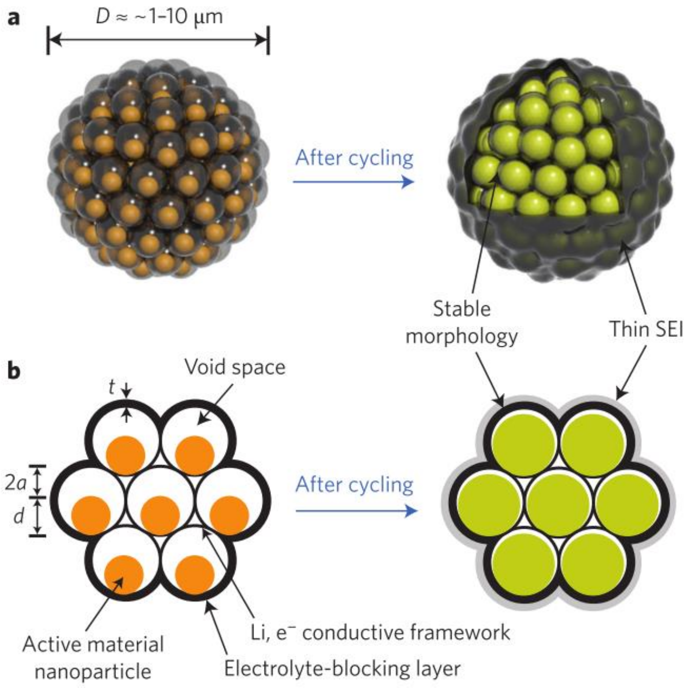

Figure 2.10: Schematic diagram of the pomegranate-inspired design. 3D view (a) and simplified two-dimensional cross-section view (b) of one pomegranate micro particle before and after electrochemical cycling (in the lithiated state). Reprinted with permission from [116]*. Copyright (2014), Springer Nature.*

However, the highly complex fabrication process along with huge manufacturing cost of these conductive encapsulated frameworks still poses practical questions for real applications.

2.3.1.4 INCORPORATION OF DIFFERENT BINDER CHEMISTRIES

Binders are an important component in composite anodes as they form cohesive networks and provide adhesion between the electrode matrix and current collector (see Figure 2.11). If the adhesion is weak, the electrode might lose contact from the current collector or the conductive network will breakdown with large volume changes, leading to increased cell resistance and capacity fade and subsequent failure of the cell. Any binder with enhanced mechanical properties will accommodate volume changes and enable a stable formation of SEI[133]. Therefore, key binder characteristics required for silicon anode include: (a) formation of a strong bond between the functional group and silicon particle; (b) maintenance of mechanical stability inside the electrochemical system during operation; (c) cohesive integrity in the composite electrode; (d) play a role as artificial SEI by forming thin conformal coating on as much of the silicon surface as possible and (e) reduce particle friction during volume expansion during lithiation[134].

Polyvinylidene fluoride (PVdF) has been the conventional binder for most LIBs, but it is not ideal for silicon anodes as it forms a weak Van der Waals force with silicon, resulting in contact loss upon volume changes[135]. Additionally, PVdF is a non-aqueous binder which needs to be dissolved in N-methyl-2-pyrrolidone (NMP), which is expensive and toxic. Poly acrylic acid (PAA) has been demonstrated to be a superior binder system for silicon anode compared with other polymers (such as PVdF, CMC) with high capacity retention[136,137]. PAA is a cheap and aqueous-based binder, therefore there is less demand for using hazardous organic solvents.

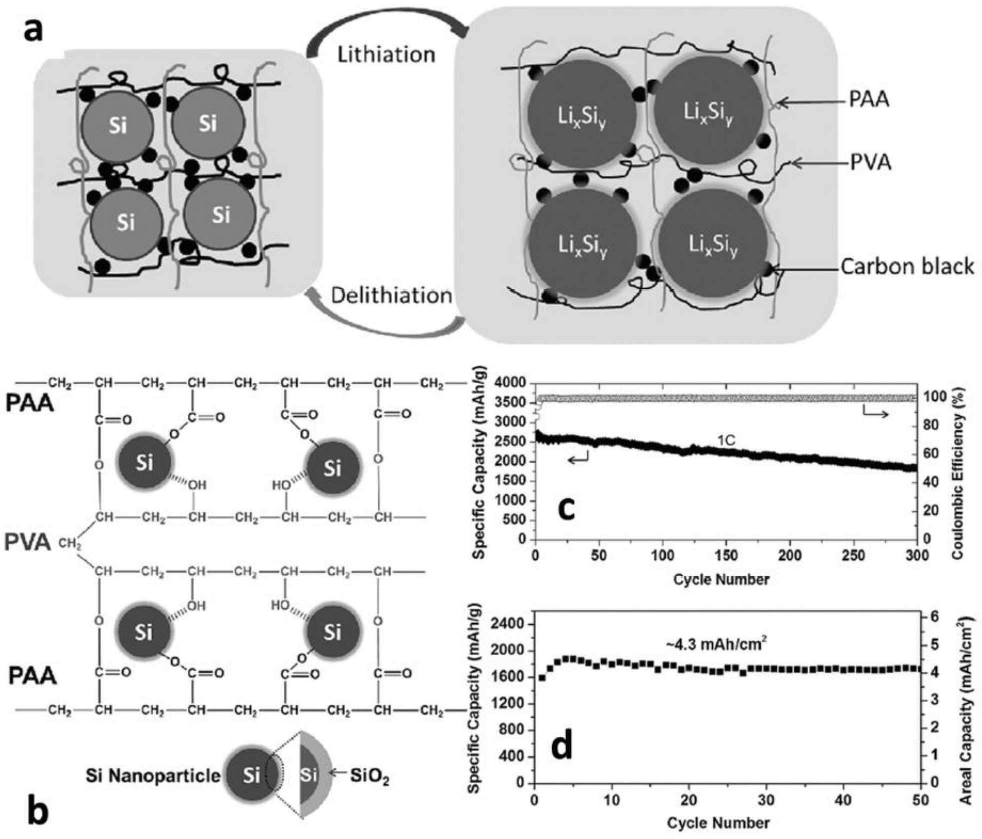

Figure 2.11: a) Schematic diagram representing lithiation and delithiation mechanism of the binder in Si-based anodes. b) Chemical structure and probable chemical bonding between binder's functional groups and partly oxidized Si surface. c) the electrochemical data with PAA-PVA binder at a current density of 4 A g^{-1}. d) areal capacity of Si anode with a higher Si mass loading of 2.4 mg cm^{-2}. Reprinted with permission from [117]. Copyright (2014), WILEY-VCH Verlag GmbH & Co.

2.3.1.5 ARTIFICIAL SEI FORMATION

Some coatings are artificially engineered onto the surface of active materials to reproduce the electrochemically formed SEI, thus minimising further electrolyte degradation (see Figure 2.12) and thus enhancing the electrochemical performance. From literature, the investigated SEI compositions which promoted cycling performance, researchers have tried to explore the use of similar compound coatings on particles. Compounds such as LiF, organic carbonates and LiF-Li$_2$CO$_3$ coatings were considered as artificial SEI[138–140]. Alternatively, carbon, metal oxides, and also doped Si were also investigated as coatings for producing stable SEI layers[141,142]. In addition, commonly used solid-state electrolytes were tested, namely, lithium phosphorus oxynitride (LiPON)[143]. However, in the presence of different combinations of solvents and co-solvents, electrolyte additives such as fluoroethylene carbonate (FEC), ethylene carbonate (EC), diethyl carbonate, propylene carbonate, vinylene carbonate (VC), dimethyl carbonate (DMC), and ethyl methyl carbonate, can drastically affect the composition of the SEI layer[144].

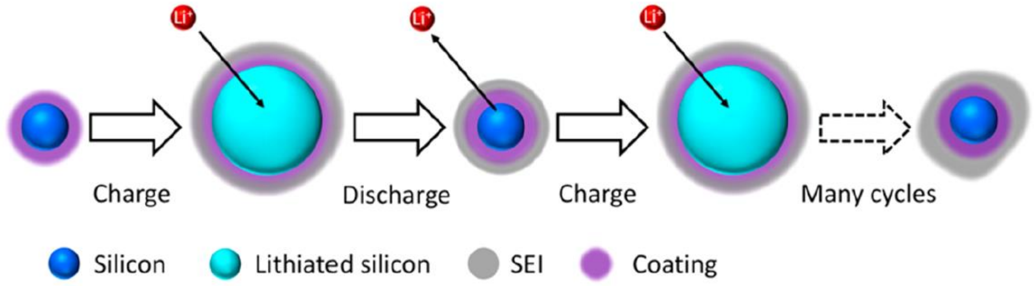

Figure 2.12: Schematic diagram of a stable SEI formation during electrochemical cycling on silicon particles with a synthetically engineered pre-SEI coating. Reprinted with permission from [144]*. Copyright (2017), American Chemical Society.*

Another approach to producing an artificial SEI layer is via pre-lithiation. Zhao *et al.*[138], incorporated 1-fluorodecane to the pre-lithiated silicon to produce artificial SEI. Commonly, pre-lithiation assumes the addition of either Li or a compound of Li to the electrode in the presence of an electrolyte to compensate for the irreversible loss of Li during the formation of SEI. These approaches also helps to pair higher capacity anodes with the lower capacity cathodes as otherwise, more cathode active material would be required to compensate for the loss of Li during natural SEI formation[145].

2.3.1.6 COMPOSITE SILICON ANODES

Aside from the quest for different morphologies of Si, conductive encapsulation and artificial SEI, composite Si anodes are another route towards practical realisation of high-performance Si-based anodes. Composite silicon anodes are a homogenous mixture of active material (nano-sized or micron size silicon powder), a conductive material (carbon black, graphite, graphene), binder (PVdF, CMC, SBR, PVA, PAA) and solvent (NMP, H_2O).

In addition to conventional composite materials formulation, various composite mixing methods have been considered. These include mixing Si with lithium-inactive materials[55], lithium-active materials[55], combining advanced nano-sized silicon particles[78], applying different binder systems[55,56,57] or by mixing silicon with carbonaceous materials[53]. Furthermore, the presence of metal in the composite is assumed to lower the resistance and also provide mechanical strengthening and enhance electrochemical performance[54]. These composites with higher electrical conductivity endure cycling stability even at higher current rates[146,147]. The incorporation of carbonaceous materials with silicon is also well-favoured, namely due to, flexibility, higher conductivity, and nominal volumetric change during lithiation[148]. Addressing the deeper understanding and comprehensive details of the aforementioned systems is beyond the scope of this review. Therefore, in this study, a commonly used method for formulating a composite or hybrid anode is based on combinations with another metals, carbonaceous materials, and use of other additives is considered.

MIXING SILICON WITH METAL, METAL OXIDES OR POROUS MATERIALS:

Recently, researchers have also investigated the benefits of Si-metal and Si-metal oxide composites as anodes for LIBs. Metals could not only enhance the conductivity of the Si-based anodes, but also can co-host Li^+ ions reversibly[149]. Metalloids, for example, germanium, a p-block element, in the same group of the periodic table as Si, exhibits a high lithiation capacity of 1624 mAh g^{-1}, but also undergoes volume change during lithiation and delithiation[150]. Abel *et al.*[151] investigated Si-Ge electrode and established that Ge content was directly proportional to the capacity retention. Despite the fact, Ge renders higher electrical conductivity and capacity retention, the lower abundance and high cost associated with Ge make it unfavourable to be considered for LIB anodes.

Tin (Sn), another p-block element, is an electrochemically lithium-active metal, exhibiting a maximum theoretical capacity about 994 mAh g^{-1} vs Li/Li^+ which is ca. 3 times the specific capacity of graphite 372 mAh g^{-1} [40,41]. Therefore, the inclusion of Sn doesn’t have a significant adverse effect on the energy density of the system. Also, Sn in turn enhances the electrode’s fatigue resistance during cyclic aging, which is helpful in achieving a longer cycle life of the battery[152]. Hybrid Si–Sn composite with diverse geometry have been studied in recent years to improve the cyclic performances of anodes for LIBs. Whiteley *et al.* introduced Si nano powders in Sn matrix for an application in the solid state batteries[153]. Ren *et al.* developed a 3D array of Si-coated SnO_2 nanowires (NWs) on carbon cloth substrate via chemical vapor deposition (CVD) method (for 3D SnO_2 NWs) and subsequently followed by plasma-enhanced CVD (PECVD) route (for thin Si coating on NWs)[154]. Lately, in an attempt to coat NWs with Sn, Kohandehghan *et al.*[146] have shown that the physical vapour deposited Sn onto Si NWs significantly improves the rate capability of the electrode. Also, Bogart *et al.*[147] have shown Sn incorporated Si NWs via supercritical fluid–liquid–solid growth mechanism enhances the rate capability of the NWs. With the similar idea of coating, Zhong *et al.*[155] prepared electrode with Sn by using tin dichloride as an additive for Si nanoparticles (SiNPs) with carbonaceous materials via annealing at 700°C and observed decrease in electrode resistance by half. These Sn-coated SiNPs anode showed > 75 % capacity retention after the first cycle and maintained 1100 mAh g^{-1} of capacity after 100 cycles. Subsequent attempts have been made towards binary Si-Sn NW electrodes where the NWs looked similar to mushroom with a Sn cap and Si stalk. Chockla *et al.*[156] synthesised Sn-seeded SiNWs via supercritical fluid−liquid−solid process and observed high reversible capacity. However, these highly complex fabrication approaches poses practical questions for real application.

Wu *et al.* prepared a homogeneous composite of Si-Sn powder (with 7:1 mass ratio) via high energy mechanical milling method[152]. Interpenetrating phase from milling resulted in higher electrical contact with mechanical integrity and thereby in electrochemical performance with reversible capacity of ~880 mAh g^{-1} after 29 cycles at the 0.5C rate. The ductile nature of Sn is assumed to act as a buffer for stress in the silicon composite during the huge volume changes during lithiation and delithiation process. Moreover, the redox potentials of Sn and Si are different during lithiation of Si, thereby Sn can act as an expansion buffer and vice versa. As Sn lithiates (lithiation onset voltage ~0.7V) before Si (lithiation onset voltage ~0.3V), an internal pressure builds up within the electrode, which is beneficial for hybrid electrode to achieve high reversible capacity. With the pressure build-up there is an improved contact at the interfaces and thereby decrease in impedance[157]. The same composite without Sn would undergo rapid degradation upon cycling. In a study conducted by Piper *et al.* [158] showed longer cycled life for silicon anodes with an application of pressure on silicon electrode and on a similar line Son *et al.*[159] and Yersak *et al.*[160] were successful in applying confined pressure on silicon particle by embedding them in $Li_xTi_4Ni_4Si_7$ matrix for improved reversibility. However, $Li_xTi_4Ni_4Si_7$ matrix is neither a conductor nor electrochemically very active[153].

Unlike Si-metals, Si-metal oxide composites typically form a core-shell structure[149]. Similar to the aforementioned ideas of Si particle encapsulation or surface coatings for stable SEIs, Lee *et al.*[161] obtained highly stable cycling retention by coating the Si nanoparticles with lithium silicate and lithium titanate (see Figure 2.13). The Si nanoparticles with multifunctional coating layers demonstrated increased rate capability due to the enhanced electrical and ionic conductivity from these multicomponent inclusions.

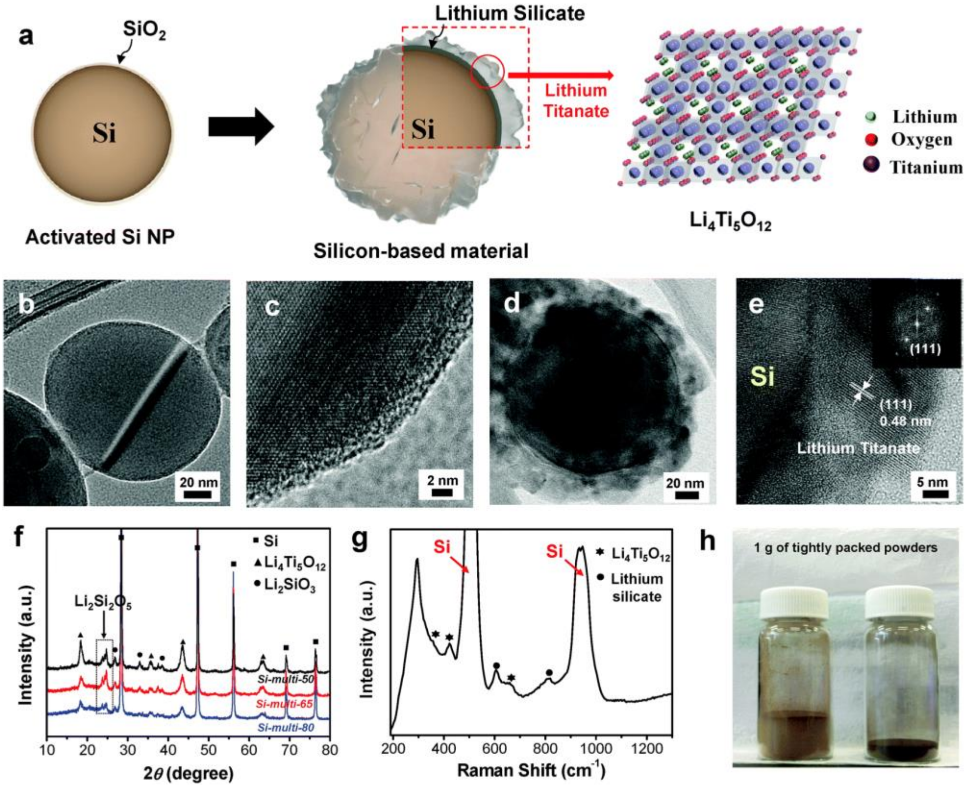

Figure 2.13: (a) Schematic diagram representation of multicomponent synthetic process. (b) A TEM image displaying native SiO_2 layer on the Si nanoparticles with (c) a magnified image showing 2 nm-thick SiO_2 layer on the Si nanoparticle's surface. (d) A TEM image displaying 20–30 nm-thick lithium titanate layer on the Si nanoparticles with (c) a magnified image showing its crystalline phase (Inset: the FFT pattern). (f) The XRD patterns and (g) Raman spectrum for different samples prepared with multifunctional coating layers. (h) Photographs of pristine Si nanoparticles (left) and Si nanoparticles with multifunctional coating layers containing 1 g of tightly packed powder[161].

Metal-organic frameworks (MOFs) are a group of crystalline porous materials and have a unique combination of physical properties, namely, high specific surface area, organic functional linkers and metal sites, with evidence of being an electrode material for electrochemical devices[162–164]. The inorganic unit consists of metal ions and metal oxide clusters, which in turn, can act as active sites during the electrochemical redox process (see Figure 2.14). These metal ions or oxides can be in the form of transition metals, alkaline earth metals or lanthanide groups, while the organic linkers are generally hydrocarbon molecules containing N- or O donor atoms (typically a compound with pyridyl, polyamine, and carboxylate structures)[165]. Along with conventional applications of MOFs in gas storage and capture[166], electronic sensors[167] as catalysts[168] and in drug delivery[169], use in electrochemical systems has been explored in recent years[164,165,170]. MOFs-dominant electrodes hold potential as an electrode material for next-generation electrochemical energy storage devices[171,172,173]. This is because of their tuneable pore structure and a wide possibility for a metal redox-active components. With suitable pore geometry, it is possible for the Li^+ ions to travel through the structure within the electrolyte solvents to reach the active sites during the electrochemical process.

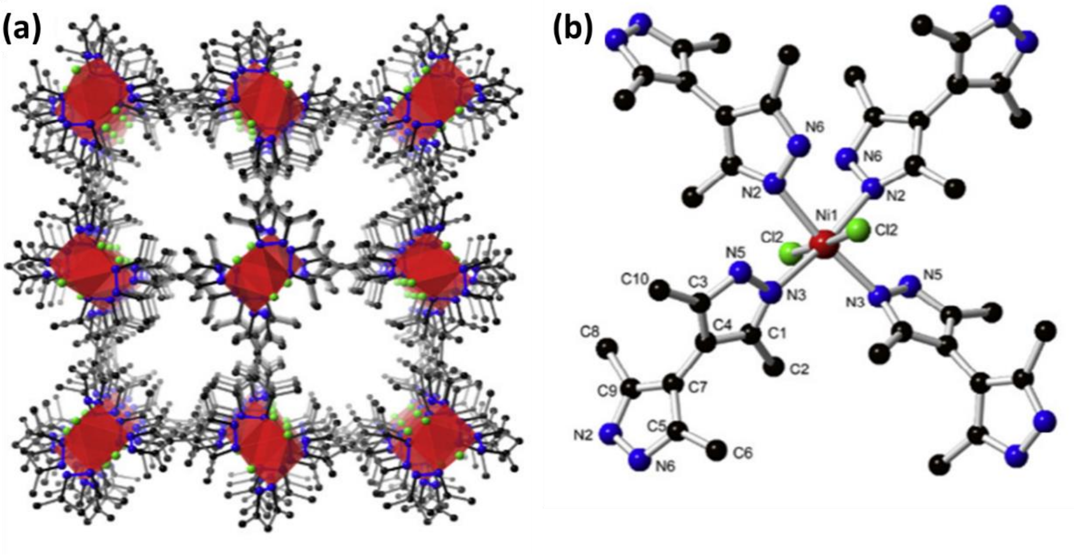

Figure 2.14: Schematic of MOF (Ni-Me$_4$bpz). (a) 1D channels along c-axis, (b) coordination mode. Reprinted with permission from [174]. Copyright (2015), Elsevier Inc.

Recently, research has been carried out to explore this possibility further to use MOFs as a cathode or anode material for LIBs and also as a host matrix for the active particles[175]. During the electrochemical process, metal components undergo oxidation and the organic linkers also participate in the redox process[176]. Charge obtained from these MOFs is dependent on the metal component's reduction and electrochemically reacting with Li^+ ions. Mostly, the MOFs chosen for anode or cathode materials consist of transition metal for their multiple redox states, for example, iron[177], nickel[174], vanadium[178], cobalt[179], manganese[180], and copper[181]. Unlike the other transition metals, a zinc-based MOF, Zn_4O (1,3,5-benzenetribenzoate) (MOF-177), demonstrated irreversible reaction with Li^+ upon cycling electrochemically[182]. However, another zinc-based MOF as an anode, $Zn_3(HCOO)_6$, cycled reversibly against lithium between the voltage range of 0.05 V – 3.0 V with a reversible capacity of 560 mAh g^{-1} after 60 cycles[183].

Despite the unique physical properties of redox active MOFs, their route to being used in a future practical LIB as the electrode's active material is, as yet, impractical in reality. There are a number of contributing reasons namely, the low density, limited Li^+ ion insertion capability, poor electronic conductivity, and irreversible structural modification over multiple cycles[164]. This irreversible structural degradation is a result of the change in oxidation state of the redox active metal component from changes in its coordination number[178]. The MOFs may also undergo pulverization upon Li^+ ion intercalation and deintercalation[174]. For these reasons as well as other functions, the rationale is to explore and understand redox active MOF for the LIBs, not as primary electrode materials but as flexibility enhancing additives. Herein, the UiO-66 and UiO-67 was selected as the additives to Si-based anodes with the dual purpose to improve and maintain the porous nature of the composite battery material but also to establish any active hosting sites for lithium. UiO-66 is made of $Zr_6O_4(OH)_4^{12+}$ metal nodes and linked to 1,4-benzenedicarboxylate organic linkers, forming a tetrahedral and octahedral frame with diameters 0.85 nm and 1.15nm, respectively[184]. UiO-67 has a similar structure except that it is linked to biphenyl-4,4'-dicarboxylate linkers forming tetrahedral and octahedral pores with diameters 1.15 nm and 2.15nm, respectively[184]. Zirconium-based MOFs are known for their high thermal and chemical stability[185].

COMBINING SILICON WITH CARBONACEOUS MATERIALS:

Various carbonaceous conductive additives have demonstrated enhancement in Si-based anode performance[186–189]. As silicon has relatively low electrical conductivity properties (*i.e.* is a semiconductor), conductive additive (such as graphite and carbon black or graphene) is required to improve the composite film electrical conductivity[47]. Nanostructured Si particles in the presence of carbon as conductive additives displayed improved performance due to enhanced electrical conductivity, stabilised SEI layer and also the ability to accommodate volume changes during cycling[190,191]. Carbon black and graphite are widely chosen as conductive additives because of the low cost and high electrical conductivity.

Structurally, graphene is a carbon allotrope and a carbon monolayer with 2D morphology. Recently, studies have been carried out using graphene as a conductive additive in silicon anodes to substantially ameliorate concerns related to Si-dominant as anode material for LIBs[187–189]. Graphene's remarkable electronic and mechanical properties have demonstrated enhanced electrode performance by improved reversible capacity retention and rate capability[192]. Researchers have investigated the application of graphene in Si-based anodes, fabricated via various synthetic routes[131,193–198].

Lee *et al.*[199] were the first among other researchers to study Si-graphene composite, where graphene was synthesised via graphite exfoliation. In the composite structure, the Si nanoparticles are anchored in between the graphene layers, thereby creating a 3D conductive network and promoting mechanical strength from the layered graphene sheets. Further, many Si-graphene composite studies have been made, with a various combination of Si and graphene, adopting different particle morphologies and synthesis routes. Graphene was synthesised via graphite oxidation and reduction, thermal exfoliation, and also via chemical vapour deposition (CVD) routes[200,201].

Carbon nanotubes (CNTs) are another conductive agent which also offers effective electrically conducting pathways such as those provided by graphene[202,203]. Generally, Si-CNT composites are prepared via physical mixing, chemically bonding and directional deposition[202]. Shu *et al.*[204] developed Si particles coiled inside CNTs that were grown via a CVD process. These cage-like Si-CNTs showed improved encasing compared to mechanically milled Si-CNTs composite. Additionally, it was also observed that long CNTs was more effective than the shorter CNTs in term of cycling stability due to a better conductive network from the wrapped CNTs on the Si surface[204]. Also, researchers have made efforts to develop unconventional Si-CNTs to exploit the extraordinary mechanical and structural strength of CNTs[149]. Wang *et al.*[125] reported 1D heterostructures encompassing Si droplets on vertically aligned CNTs (VACNTs) via CVD method (see Figure 2.15). The CVD process included a two-step liquid injection using xylene as the precursor and ferrocene as the catalyst. The VACNTs displayed outstanding electrical and mechanical robustness and thereby enhanced kinetics for both the electrons and participating Li^+ ions[125].

Another notable design proposed by Fan *et al.*[205] was based on Si as a shell with CNT as the core. A core-shell type structure was grown with Si on the outer wall of the CNTs, and the later were grown on a nickel or stainless steel substrate also acting as a current collector, via a plasma enhanced CVD (PECVD) process. With uniformly spaced CNTs, a conical structured Si shell was beneficial to accommodate the volume change from Si at the top. This hierarchical structure provided faster kinetics and resulted in lowered stress at the root-junction of the CNTs and the substrate.

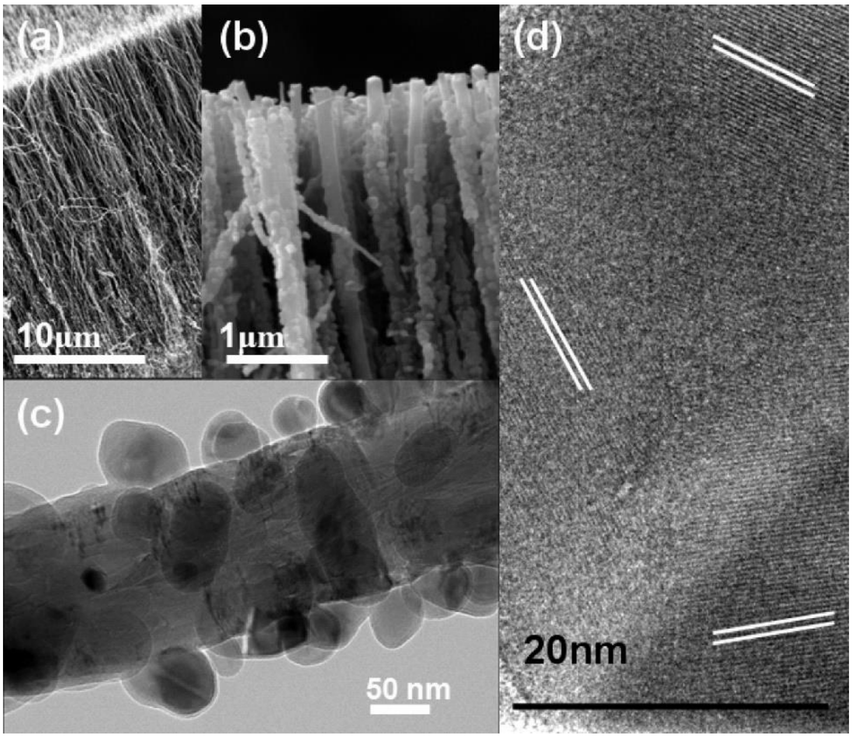

Figure 2.15: SEM image of (a) the aligned VACNTs only, (b) VACNTs with Si nanoclusters. (c) TEM image showing a single VACNT covered with multiple Si nanoclusters. (d) HR-TEM image showing multiple lattice fringe orientations within a Si nanoparticle (white lines indicate multiple lattice fringe orientations). Reprinted with permission from [125]*. Copyright (2010), American Chemical Society.*

In recent years graphene have been explored as good fit as a conductive additive for LIBs because of their excellent properties such as superior planar electrical conductivity, strength, specific surface area compared to other additives like carbon nanotubes[206]. Generally, the silicon composite is made by preparing a slurry of active silicon particles, conductive additive and binder solution. More detail on electrode ink preparation have been discussed in Chapter 4.

Furthermore, with the use of electrochemically inactive additives, porous morphologies, conductive additives, and binders – they all reduce the active mass percentage of the electrode, hence limit the energy density. The cycling stability and longevity are a trade-off for the balance between battery performance and energy density. Much research on composite silicon anodes has been carried out by varying the silicon content, different silicon morphologies, different composite anode systems, preparation techniques, and different battery cycling conditions[51,52,91,116,120,136,137,144,152]. A detailed review on the latter is beyond the scope of this study, and the reader is requested they refer to reviews by Obrovac *et al.*[9], McDowell *et al.*[10], Mingyuan Ge *et al.*[207] Rahman *et al.*[130] and Xin Su *et al.*[208]. However, it is difficult to draw a conclusive remark on which ratio of composite additives are best for LIBs as different binder systems with different ratio/mixture of conductive additives would vary the performance of the battery, and this has to be definitively demonstrated systematically and verified experimentally. In this study, physicochemical characterisations will be used as a tool to validate and analyse different types of failure mechanisms that are occurring in silicon anodes, which would give more insight into the material’s behavioural characteristics. More detail on the physicochemical characterisations is discussed in Chapter 4.

2.4 SUMMARY

Since LIB’s commercialisation in 1991, LIBs have transpired as a crucial commodity in daily life, embedded in a wide range of portable electronic gadgets, all the way to more recent sectors such as transport electrification. However, as the state-of-the-art battery materials for LIBs have neared their theoretical capacity limits, there remains no scope to push their energy density further by augmenting battery design based on conventional materials chemistry and manufacturing techniques. The requirement for high energy density and power battery packs for applications in EVs has stimulated the research towards advanced energy storage materials. In order to advance the capacity of their most advanced cylindrical cells, Tesla, Samsung, LG and Sony at present use a small fraction of silicon in graphite-dominant anodes to overcome issues around volume expansion and to extend operational life. However, to date no successful commercial product has reported containing silicon as the predominant lithium host material. The solutions offered so far in the literature involve complex chemical synthesis or intricate processing routes, and are not appealing as realistic solutions to produce feasible devices. This review has summarised the benefits of Si-based anodes, along with the key challenges that hinder their commercialisation.

A comprehensive analysis of different approaches aimed at tackling aforementioned issues has been discussed herein. Investigations to date have predominantly explored a porous or nanostructured active materials, complementing it with carbonaceous additives and robust binder. Unfortunately, to address the issues associated with Si-based anodes, they cannot be overcome with a single strategy – the approach needs to be holistic. An appropriate combination of the above approaches is required, with innovative means of characterising them. This will be key towards the viable commercialisation of Si-based LIBs.

In this study, an innovative approaches to stabilising silicon anodes via additives that can conveniently be synthesized, and are chemically compatible with the electrode components have been analysed. Evolution of the microstructure of Si anodes allows investigation of the benefits of composite Si anodes incorporating metals (tin), metal organic frameworks, and graphene as electrochemically active additives in preventing or mitigating the Si's microstructural breakdown. Furthermore, the influence of structure and porosity on impedance is investigated, providing knowledge on critical geometrical attributes towards superior understanding and correlation with electrochemical performance data.

CHAPTER 3. TOMOGRAPHY: BACKGROUND AND APPLICATION TO LITHIUM-ION BATTERIES

Despite the numerous studies and evolution of sophisticated characterisation techniques, relatively little is understood about the microstructural evolution and its impact and relation to the cell performance during operation and failure. Moreover, this lack of understanding of microstructure is made more complicated due to the dynamics of electrochemical reactions and the changes that take place as a result. The performance of a battery depends on the characteristics of the material it is composed of. In order to directly correlate the electrode microstructure to battery performance, a significant capability to understand the electrode microstructure needs further development. With a variety of tomography techniques available over multiple length scales, it is now possible to characterise and quantify a spectrum of microstructural occurrences. Notably, at the electrode level the particles present are of micron and sub-micron dimension; hence a better understanding of these characteristic features from micro-scale down to nano-scale is necessary.

3.1 CONSIDERATIONS AROUND THE IMPORTANCE OF ELECTRODE GEOMETRY AND TOMOGRAPHY CHARACTERISATION FOR LIBs

From Figure 3.1 it can be seen that the microstructure of the electrode is a 3D porous structure. It is crucial to have a procedure to quantitatively characterise the microstructure of the electrode in 3D. This is because, microstructure has a direct influence on the battery's properties and performance[209,210]. With reference to the electrochemical reactions in LIBs, the chemical diffusion of Li^+ ions in the bulk of the electrode's microstructure is a rate-determining step[211]. Porous networks within the structure act as transport pathways for the electrolyte, and facilitate the access of Li^+ ions for insertion into the host particles[212]. Therefore, a better understanding of the electrode's architecture and how it changes is essential for improved battery design. This is especially so when considering scalability within electrode manufacture.

Figure 3.1: Schematic diagram representation of a typical LIB during charging. Reprinted with permission from [209]*. Copyright (2014), Elsevier B.V.*

Numerous 2D and 3D characterisation techniques have been used to understand the correlation between battery performance and microstructure. With the development of tomographic imaging techniques, it is possible to observe and characterise a wide range of battery materials in 3D over multiple length scales. Figure 3.2 illustrates the variety of tomographic characterisation techniques with sample volume capability and achievable spatial resolution.

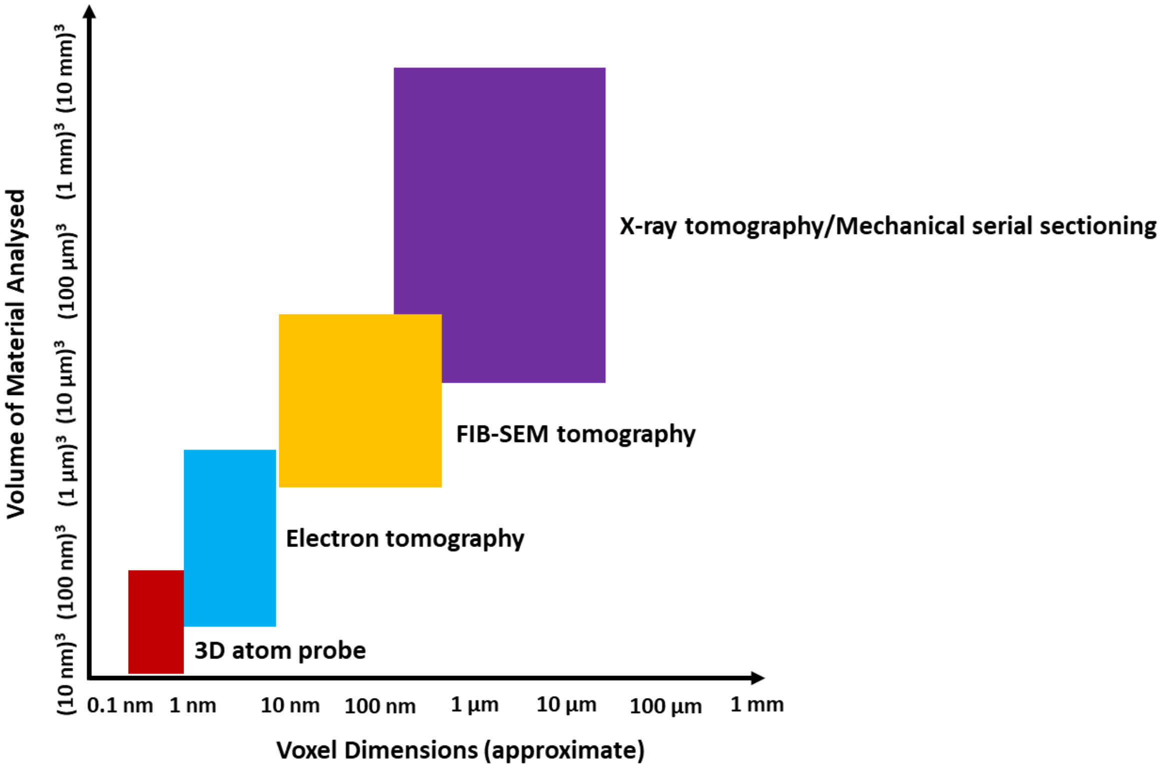

Figure 3.2: Graphical representation of the achievable spatial resolution and sample volume for different tomographic characterisation techniques. Adapted from Uchic et al [210]*.*

Selecting any of the above characterisation techniques represents a balance between the analysable sample volume and the corresponding resolution necessary for characterising the features of interest. Moreover, 3D microstructure analysis not only requires qualitative analysis but also needs quantification of the visual observations. In recent years, researchers have tried to visualise, segment and quantify the electrode's geometrical parameters, such as phase fractions, porosity, tortuosity, surface area, pore size distribution and particle size distribution[213]. The electrode's ageing and failure is associated with its microstructure dynamics, which can also be analysed using 3D datasets. The 3D electrode volume reconstruction from focused ion beam-scanning electron microscopy (FIB-SEM) tomography, followed by further image processing and analysis, has been proven to be an highly effective tool for quantifying geometrical parameters of LIB electrodes[68]. Additionally, X-ray computed tomography (CT) is a non-invasive, non-destructive technique which opens up the possibility for *in-situ* and *operando* experiments, thereby allowing 3D imaging studies in real time[63]. It must be noted that various imaging techniques come with their limitations[32] as outlined in section 3.4. The majority of the imaging data obtained have resolution limitations, for example, porosity or particle in the nanometre scale length[214].

3.2 FIB-SEM TOMOGRAPHY

FIB instrumentation has emerged as an essential technique for a wide range of material characterisation, ranging from circuit editing[215], TEM sample preparation[216] to microstructural analysis[67]. Most FIB milling instruments, in conjunction with SEM, is a versatile platform for imaging[217]. This section will specifically review their use in 'slice and view' tomography.

FIB-SEM tomography is a conventional imaging approach to study the 3D microstructure of battery materials and is used as a tool in this study[66–69]. This approach combines an SEM for obtaining high-resolution cross-sectional images of the electrode, with FIB milling to remove thin slices of the sample sequentially. FIB-SEM tomography provides high resolution, down to tens of nanometers, which is otherwise below the capability limits of conventional laboratory-source X-ray computed tomography (CT)[218]. 3D reconstructed volumes of the microstructure from precise milling and imaging is used to analyse various microstructural details, such as true features and sizes with the spatial distribution of such features over relevant areas and volumes[210]. Most importantly, the length-scales over which FIB-SEM tomography can operate makes it an effective tool for analysing battery electrodes[210]. The resolution attainable is sufficient to enable a detailed study of the finer pore sizes and the different phases involved. Thus, this shall provide insights into clarifying structure-property-performance relationships.

A schematic of 3D imaging using FIB-SEM tomography is presented in Figure 3.3. This example showcases the importance of 3D imaging to visualise and quantify electrode microstructural evolution in terms of the porosity and its connectivity throughout the bulk electrode. Additionally, the porosity network and pore size distribution are also estimated from the data, which affects the transport properties and tortuosity within the electrode. Thus, 3D images of the electrode microstructure of LIBs could aid further understanding of physical failure mechanisms.

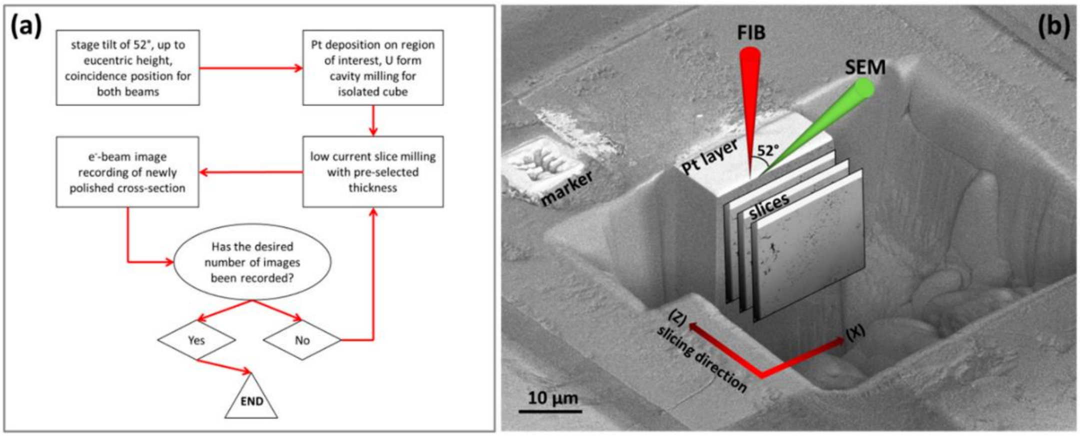

Figure 3.3: (a) A flow chart demonstrating the sequential sectioning procedure of FIB-SEM tomography; (b) a schematic diagram representation of a typical FIB-SEM setup and milling geometry indicating prepared region of interest for tomography technique in a FIB-SEM[219].

3.2.1 FIB-SEM TOMOGRAPHY THEORY

FIB-SEM tomography also referred to as “slice-and-view” creates a 3D microstructure from a series of 2D images as in surface-SEM, taken at incremental depths created by focusing highly energetic ions at the sample’s region of interest under vacuum[26]. These ions are generated via liquid metal ion sources (LMIS), which was developed in the 1980s[217]. There are a variety of LMIS sources, among them the most extensively used source is a Ga-based blunt needle. The rationale for wide adoption of a Ga source was its low melting temperature (30°C), low volatility and low vapour pressure[217]. The Ga^+ ions are generated using an electric field across a Ga-wetted tungsten needle. Accelerated Ga^+ ions collide with the sample, and there is a transfer of kinetic energy to the atoms in the sample. These physical collisions remove material (also referred to as ‘milling’) from the sample’s surface. Moreover, it should be noted that the Ga^+ ions may get implanted in the sample, affecting atomic translational alteration or deposition on the sample’s surface. Prior to milling, a layer of platinum is deposited onto the interested area of the sample’s surface, thereby enabling charge conduction and impeding undesirable ‘curtaining’. These artefacts generated due to local charges or phase differences in the sample may diminish the precision of the final 3D reconstructions. A detailed review of the theory, recent developments and application of FIB-SEM tomography has been investigated by Zaefferer *et al.*[31].

Figure 3.4 illustrates the process of ion-beam milling with EBSD analysis positions. Generally, the ion source is at an angle of 52° with respect to the electron source. While milling with the ion source the electron beam can be used for imaging, simultaneously. The arrangement of the two beams columns is instrumented with precision to provide the two beams in congruent onto the specimen. For ‘slice and view’, the milling via Ga^+ ions is done by tilting the sample, so that the sample’s top surface (x-z plane) is normal to the Ga^+ ion beam (y-direction). The progressive milling way of the sample (z-direction) can be done with simultaneously imaging (x-y plane) without and reorientation of the sample[31]. Typically FIB-SEM tomography instruments can go down to tens of nanometer scale of achievable resolution[26].

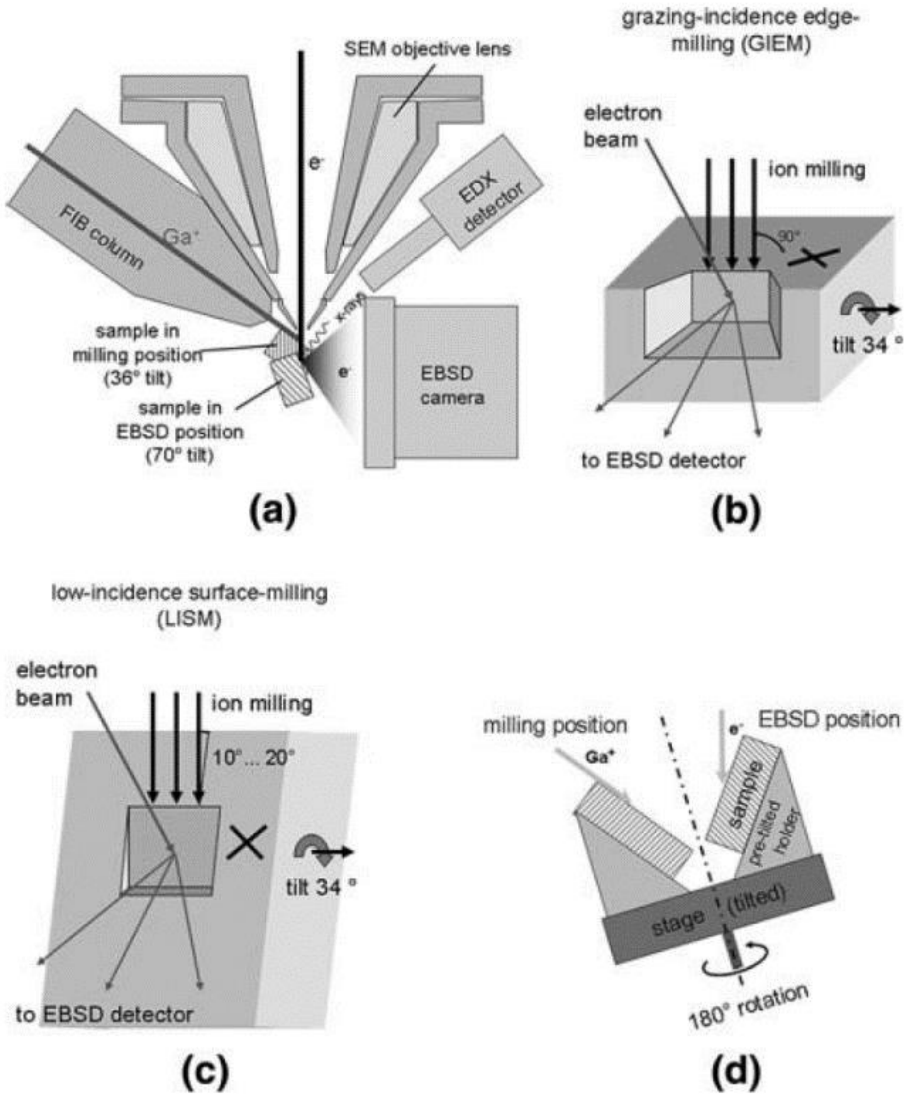

Figure 3.4: A typical FIB-SEM setup and milling geometry. (a) Cross-section of the instrument chamber, showing the sample's milling positions and sample's EBSD analysis position (b) grazing-incidence edge milling (GIEM) method (c) the low-incidence surface-milling (LISM) method (d) The 180° rotation geometry, showing the EBSD and milling positions together[31].

3.2.1.1 ELECTRON-SPECIMEN INTERACTIONS

This section will give a concise review of SEM column instrumentation and SEM imaging to construct a basis for understanding the greyscale intensity maps in those generated images. A detailed review on this is beyond the scope of this study, the interested reader is directed to Amelinckx *et al.*[220] and Goldstein *et al.*[221].

The SEM primarily consists of two components (as shown in Figure 3.5):

Electron column: The electron column is composed of an electron gun, which acts as a source of accelerating electrons (typically in the energy range of 0.5 - 30 keV). Field emission guns have gained popularity as the electron source, compared with the conventional tungsten filament. They deliver benefits at low accelerating voltages, whereby the field emission gun source typically delivers a three orders of magnitude increase in brightness compared with a thermoionic source[220].

Electron detectors: When the electron beam impacts on the sample's surface, a large number of electromagnetic radiation phenomena occur. Various detectors are employed for simultaneous detection of these radiation signals in a raster pattern, thereby generating an image/map with associated signal intensity.

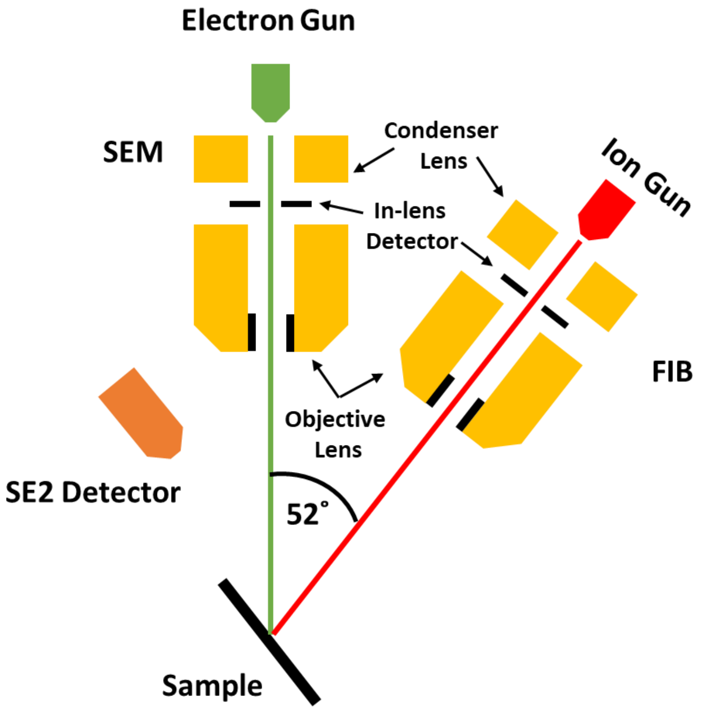

Figure 3.5: A schematic diagram of a typical FIB-SEM setup with components. Adapted from Jørgensen et al.[222].

The primary electrons from source interacts with the sample's atomic electron shells.The detectable secondary electrons (SE) can be categorised as following (see Figure 3.6):

SE$_1$ are generated as the primary electrons enters the sample. They carry a large amount of information since they are generated from the point where the primary electrons hits the sample.

SE2 are generated as the backscattered electrons (BSE) exits the sample. Due to the extensive volume interaction of BSE (depending on the accelerating voltage), the SE_2 carries relatively minimal location-specific information.

SE3 are generated as those BSE exits the sample and have hit the pole piece of the microscope. This interaction generates SE proportional to the BSE produced.

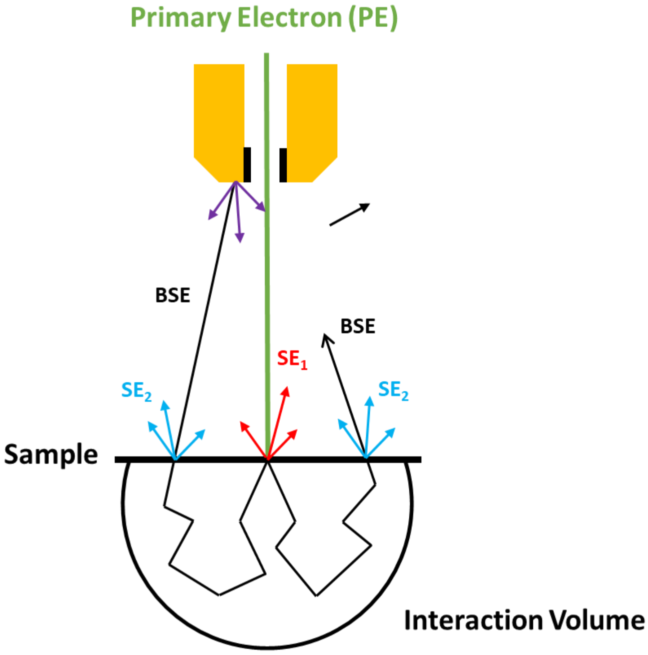

Figure 3.6: The interaction of the primary electrons (PE) from source with the sample. Adapted from Jørgensen et al.[222].

3.2.1.2 ION-SPECIMEN INTERACTIONS

Similar to the electron-specimen interactions, ion-specimen interactions also result in numerous events. Three more additional kinds of interactions which are essential for FIB-SEM tomography are discussed below:

Milling of atoms from the sample may take place due to the transfer of kinetic energy from incident ions to the atoms on the sample's surface. If this conveyed kinetic energy is larger than the sample's surface binding energy, then an atom from the sample's surface is ejected. The milling yield can be defined as the number of atoms removed from the sample per incident ion. The milling yield is dependent on the composition of the sample, along with the incident angle and generally ranges between 10^{-1} to 10^{2}. This milling of atoms away from the sample is the primary purpose of the FIB system in FIB-SEM tomography.

Re-deposition of milled atoms may occur during the FIB milling of a deep and/or narrow trench section of the sample. The milled atoms exit the sample with a certain kinetic energy, and if it collides with the sample again during its ejecting trajectory, it may get re-deposited on the sample. The re-deposition rate depends on a number of factors, namely, the kinetic energy of milled atoms, the milling yield, and the geometry of the milling trench and the property of the material under investigation.

Gas deposition can be used for controlling deposition of metals or insulators on top of the sample surface. A precursor gas of regulated amount is injected into the sample chamber in close proximity to the incident spot of the FIB. Thereafter, upon interaction with the ion beam, the precursor gas will get decomposed into volatile and nonvolatile constituents. The non-volatile element of the gas is deposited on the surface as a layer. Generally, the materials used for deposition are metals such as tungsten or platinum. The prime purpose of this deposited layer is to form a protective layer for the investigated sample during FIB-SEM tomography. This gas deposited surface layer also serves as an appropriate surface for placing fiducial markers (see section 4.3.7).

It is possible to utilise the imaging results from the ion-specimen interactions similar to the SEM images. However, this study has not employed any ion imaging and thus will not be covered in the review.

3.2.1.3 IMAGE CONTRAST

There is a correlation between image contrast and sample property (atomic number) and the tilt angle, forming two different contrasts, namely, compositional contrast and topographic contrast. The obtained image contrast is primarily dependent on the detection of electron yield from a spot size and its conversion into an intensity map. The detection of the electron yield can be achieved using a range of detectors having a divergent capacity. Different microscopes come with different detectors capabilities;

the below detector descriptions is from FEI Scios Dual-Beam instrument that has been used in this study for all tomography work.

The Everhart Thornley detector (ETD) is located inside the sample chamber's wall and is capable of detecting a mixture of BSE and SEs (SE_1, SE_2 and also SE_3). The detector operates by accelerating the electrons via a huge positive potential gradient tunnel kept in between 10 - 12 kV, which then strikes a scintillator material. The positive potential gradient enables low energy BSE and SE to the scintillator and produces light. The generated photons are guided outside the microscopic chamber, via a sealed vacuum tunnel, where it is converted into a recordable electrical signal. A Faraday shield encircles the detector to prevent any influence on the electron beam due to the enormous potential in the detector. For further efficient SE detection, a separate bias potential can be applied to the Faraday shield. Depending on the bias potential applied, positive or negative, can either result in increased or reduced SE detection. With the application of a significantly large positive bias, the detection efficiency of SE emitted from the sample increases, also including those emitted in the same direction that otherwise would not have hit the detector (see Figure 3.6). Only the BSE emitted at small solid angles contributes directly towards the signal intensity. However, the ETD detector signal intensity may contain significant contribution from the SE_3, produced as the BSE hit the chamber walls. The ETD detector is effective for imaging non-planar samples due to the topological contrast created from its placement in the chamber. The observed images obtained from the ETD detector can be perceived as similar to illuminated objects in reality.

The In-lens detector is located in the beam path prior to the terminal lens. This detector operates by applying an electrostatic field in the pole, to decelerate the electron beam towards the ending accelerating voltage. The incoming electrons hits the scintillator of the In-lenses detector similar to the ETD detector as the applied electrostatic field absorbs and accelerates the incoming electrons.

The In-lens detector primarily detects BSE, SE_1, and SE_2 with negligible signals from SE_3 due to its location. Therefore, the obtained signal carries more surface information in comparison to the ETD detector since both the SE_1 and SE_2 are produced near the sample's surface. Also, due to its location, the topographic contrast obtained here is lower than that obtained with ETD detector. Therefore, the obtained image seems to be flatter, which is a great advantage during the quantitative analysis of the tomography data. The FEI Scios dual-Beam instrument has lower in-lens BSE detector (T1), an upper in-lens SE detector (T2) and an optional in-column detector (T3).

Ion Conversion and Electron (ICE) detector is a charged particle detector for secondary ions (SIs) and electrons (SEs) located at the end of the ion column. Its novel design is optimized for imaging with the ion column in both ion and electron collection mode. Additionally, ICE has a high current and low current mode, increasing the useful beam current dynamic range. The ICE detector can be used in combination with the charge neutralizer, enabling secondary ion imaging while the specimen is flooded with electrons to neutralize charge.

For quantitative analysis of the obtained greyscale images from the above detectors signals, the contrast of the image is very critical. The image contrast may vary with sample composition and feature dimensions under the electron beam. There are three major components of image contrast, which are discussed below.

Compositional contrast is generated due to the difference in atomic number within the sample. The BSE detector detects strong signals when the beams strike part of the sample with a high atomic number, in comparison to those with a lower atomic number. Therefore, the resulting difference in intensity also has an influence from SE_3 detection. The contrast yields of other SE_1 and SE_2 from the atomic number is minimal.

Topographic contrast arises due to the differences in the angle of incidence between the sample and the electron beam. Also, the angle of incidences between the sample surface and the detector determines the yield of both BSE and SE. Therefore, both the angle of incidences influences image intensity. As a result, there occurs a shadowing effect, as seen in most of the images obtained via the ETD detector. A surface oriented away from the ETD detector will have fewer electrons hitting the detector, and vice versa. A large positive bias potential applied on the ETD detector will increase SE detection, which would otherwise have a trajectory away from the detector and thus reduce the shadowing effect.

Channeling contrast also referred to as crystallographic contrast, is produced due to differing crystallographic orientations with respect to the incident electron beam. The

PE's penetration depth is determined by the crystallographic orientation and thereby affects the yield and thus the image contrast.

The utilisation and interpretation of these image contrasts for segmentation of the tomography data are further discussed in chapter 4.3.3.

3.2.2 APPLICATION OF FIB-SEM TOMOGRAPHY TO LIBs

In the past decade, FIB-SEM tomography has been widely adopted 3D characterisation technique for energy materials. The 3D microstructural reconstruction of the anode of the solid-oxide fuel cell using FIB-SEM was first demonstrated by Wilson *et al.*[30]. Since then numerous microstructural analyses on electrodes of lithium-ion batteries have been performed and has been reported by several groups[25,29,67,214,223,224]. For example, Wilson *et al.*[29] used FIB-SEM-tomography to elucidate 3D microstructural information such as cracks inside $LiCoO_2$ (LCO) phase in a fresh, positive electrode of a commercial LIB and the impact of these cracks on the electrochemical performance was evaluated.

As observed in Figure 3.7, FIB-SEM tomography enables visualisation of constituent phases in the battery electrode. Additionally, it also enables quantitative evaluation of the complex geometrical parameters, for example, phase volume fractions, phase surface areas, electrode thickness, particle size distribution, porosity and tortuosity[25,29,39,214,223–226].

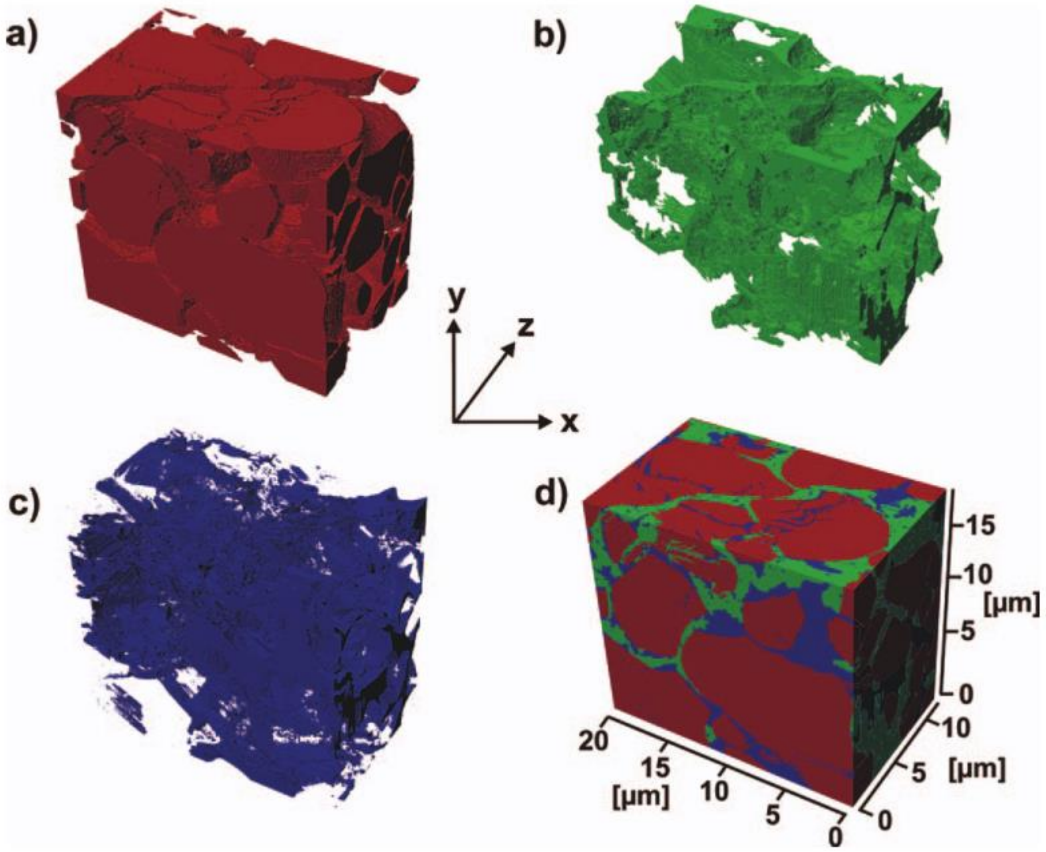

Figure 3.7: Visualisation of reconstructed 3D microstructure of LCO-based cathode material into its constituent phases of (a) LCO, (b) binder, (c) pore network and (d) combination of three phases. Reproduced with permission from [227]*. Copyright (2011), The Electrochemical Society.*

Hutzenlaub *et al.*[227] reconstructed 3D microstructure of LCO-based cathode material into its constituent phases (see Figure 3.7). Three phases *i.e.* LCO, binder and pore space were segmented to identify and emphasise the anisotropic behaviour of effective electrical conductivity, tortuosity and porosity. Hutzenlaub *et al.*[228] also presented a method to quantify porous LCO-based electrode, including all the resolvable pores during image reconstruction into pore spacing, resulting in very high tortuosity values. For a realistic picture of ionic transportation, pores in the carbon-binder phase should be considered, which are bigger than the resolution limit of the instrument. Otherwise counting the carbon-binder phase as pore space during reconstruction is least comparable to the original morphology. Similar to the backfilling of material, this approach best emulates the situation where tortuosity outcome is in agreement to the well-established Bruggeman coefficient of $\alpha \approx 1.5$. Chen-Wiegart *et al.*[224] also characterised LCO material and calculated the tortuosity distribution of the electrode to overcome the limitations using single value of tortuosity.

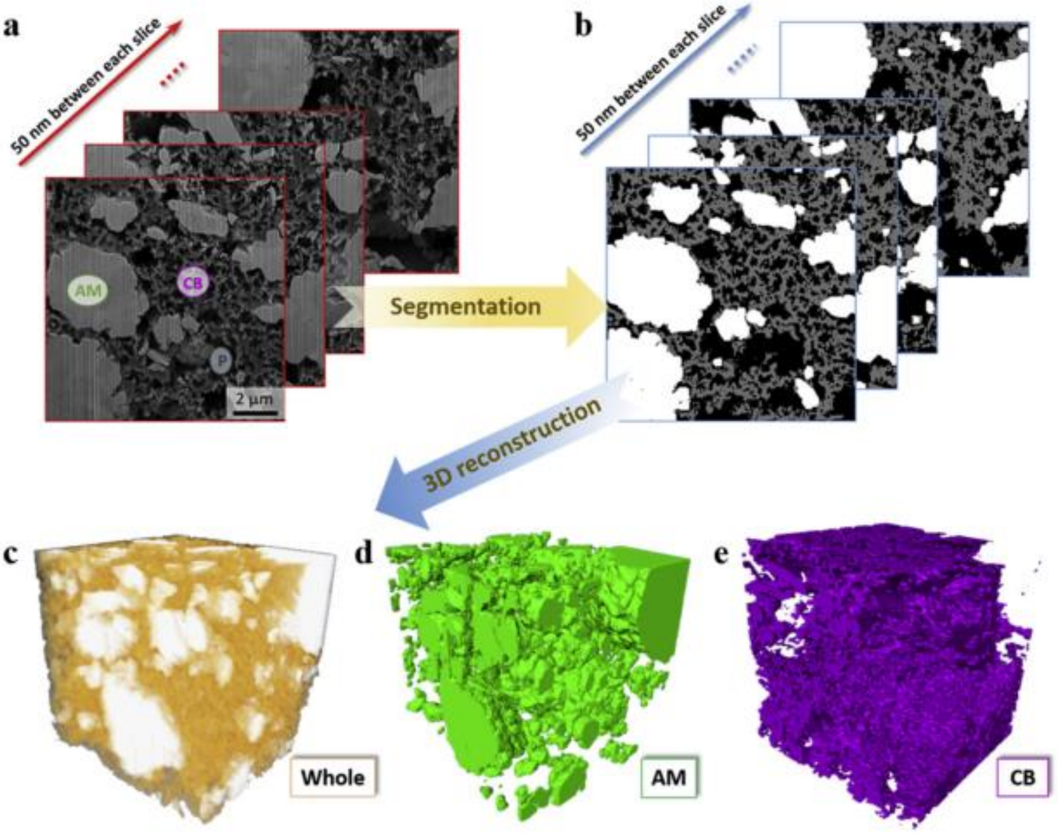

Figure 3.8:.Illustration of 3D reconstruction after (a) sequential SEM imaging after FIB milling, (b) corresponding cross-sectional images after segmentation; (c) volume reconstruction of combined $LiNi_{1/3}Mn_{1/3}Co_{1/3}O_2$ *(NMC) cathode electrode and into constituent (d) active material (AM) – NMC and carbon black (CB). Reproduced with permission from* [69]*. Copyright (2015), Elsevier B.V.*

Other battery cathode chemistries were also analysed using FIB-SEM-tomography technique. Ender *et al.*[25] used the 3D microstructure data of $LiFePO_4$ (LFP) to critically quantify volume fraction, volume-specific surface areas and tortuosity of carbon black (electronic conductor), LFP (active material) and pore volume. Liu *et al.*[229] also studied tortuosity in the pore network of conventional and carbon template LFP-based electrodes for electron and Li^+ ion transport. It was concluded that the hierarchical hydrogen carbonate-based template showed high rate performance due to retained pore network and conductive network during charge-discharge cycling.

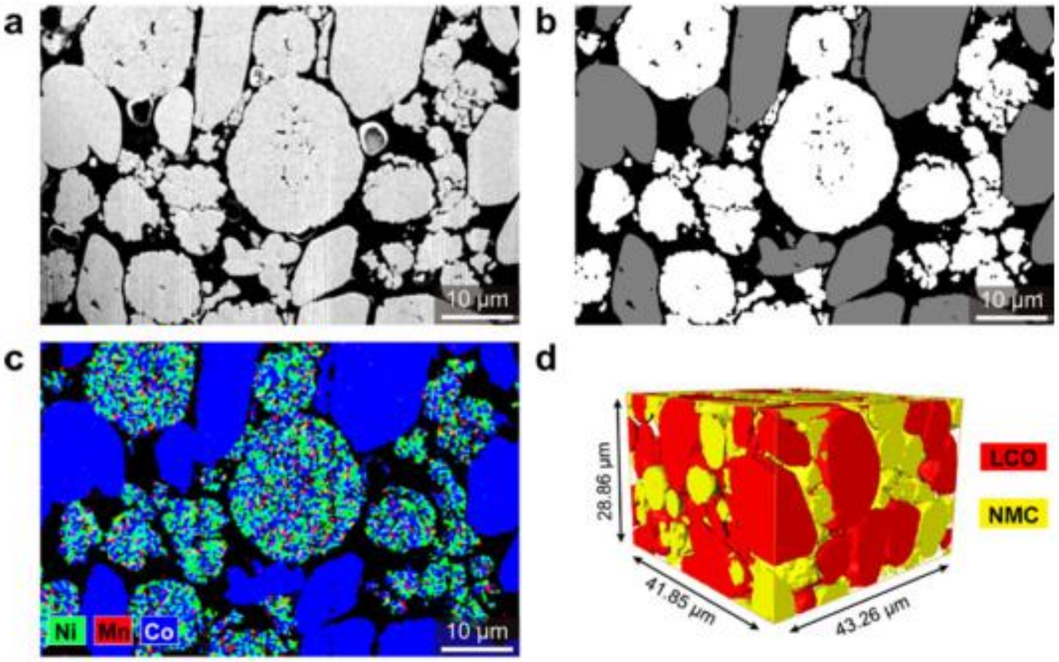

Figure 3.9: (a) Cross-sectional SEM image of blended LCO-NMC electrode. Corresponding image (b) after image processing, where NMC is represented in white, LCO in grey and epoxy filled porosity in black; (c) with EDS mapping. (d) Visualisation of reconstructed 3D microstructure. Reproduced with permission from [223]*. Copyright (2012), Elsevier B.V.*

Furthermore, analysis on blended cathode materials was carried out by Etiemble *et al.*[230]. Tomography on different cathode materials namely, $LiNi_{1/3}Mn_{1/3}Co_{1/3}O_2$ (NMC), LFP and also on blended NMC-LFP electrodes was carried out to quantify geometrical parameters. This included phase volume fractions, surface areas, and particle size distributions and their influence on rheological properties. Similarly, Liu *et al.*[223] studied LCO and blended LCO-NMC electrodes (see Figure 3.9) using FIB-SEM tomography for multiple 3D image volumes from different positions of geometrical parameters. The results indicated that structural inhomogeneity limits the ability to detect statistically distinguishable structural changes. Also, Liu *et al.*[69] reconstructed NMC based cathode materials with different cyclic aging, revealing loss of conductive networks around the active particles with an increased number of cycles.

For improved segmentation, Biton *et al.*[67] developed a contrast enhancing sample preparation route (using epoxy impregnation) for carbon-based LIB cathode material. This approach delivered accurate phase distribution and volume fraction estimation (see Figure 3.10). Vierrath *et al.*[231] used ZnO as contrast enhancer to distinguish pores inside the carbon-binder domain in the LCO electrode. It was found in the cycled electrodes that the inhomogeneous clustering of the carbon-binder domain impedes electronic conductivity, by increasing tortuosity. Reducing the carbon content by 30 % resulted in similar electronic conductivity. Furthermore, reducing the carbon content would also allow higher active material content and increase the energy density of the cell. Additionally, the tomography analysis also suggested replacing PVDF with binder materials that swell less with electrolyte solvents, for example, cross-linked polymers[232].

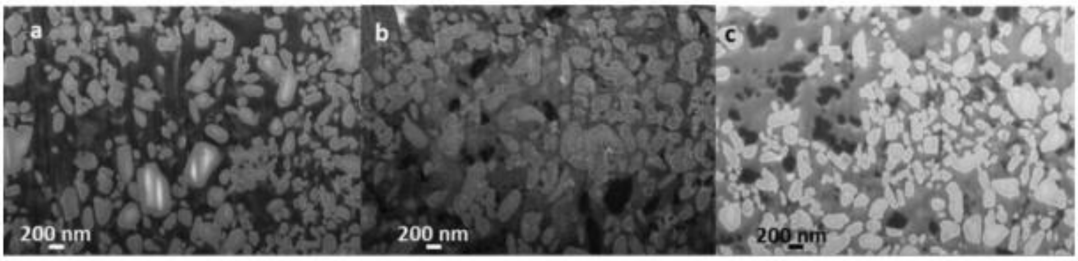

Figure 3.10: Cross-sectional SEM image of LFP-based electrode impregnated with epoxies containing (a) carbon, (b) silicon, and (c) bromine. Reproduced with permission from [67]*. Copyright (2016), The Electrochemical Society.*

To enhance the understanding of the electrode structure, the tomography data was used as an input for electrochemical modelling. Wiedemann *et al.*[28] developed a finite-volume model for LCO cathode material from reconstructed microstructural geometry obtained through FIB-SEM tomography (see Figure 3.11). The computational model depicts localised variations in the Li^+ ion's transport property and electrostatic potential within the solid-phase as a function of discharge rate. The existence of spatial variations within real microstructure in 3D was compared with the idealised microstructure from spherical particles. Further, Stephenson *et al.*[225] also modelled porous 3D microstructures of LCO electrodes to understand their relationship with ionic transportation resistance. The study used a dynamic particle packing model and stochastic grid (SG) models to quantify tortuosity within the electrodes with different porosity values. The results indicate that carbon additives create highly tortuous domains impeding overall ionic transportation in the electrodes.

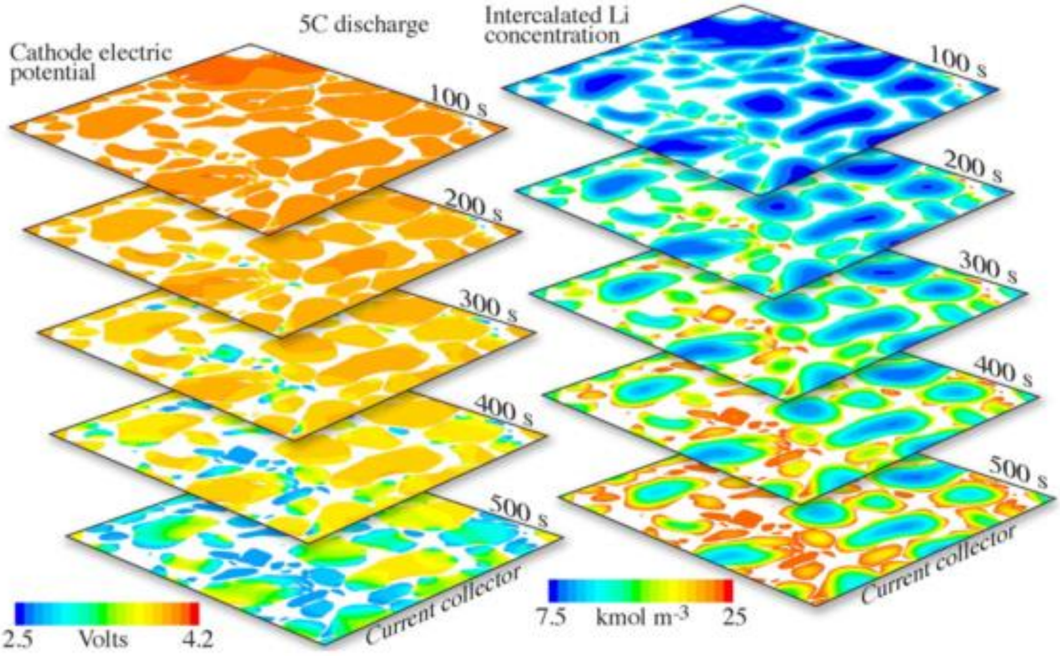

Figure 3.11: Localised variations in the Li$^+$ ion transport property and electrostatic potential within the cathode material as a function of time with 100 s intervals during a 5C discharge. Reproduced with permission from [28]. Copyright (2012), Elsevier B.V.

Further simulation modelling work had been carried out by Gully *et al.*[226], to study effective transport properties by integrating FIB-SEM tomography approach with mathematical homogenization theory and image processing. The effective transport coefficients are most likely to vary if the phases are not segmented into all its constituent phases. It was also found that with partial microstructural information (such as carbon-binder domain merging into the pore space), even the well-established Bruggeman's formula deviates in certain regimes. This study also quantifies the uncertainty in the effective transport coefficients due to partial microstructural information about the constituent phases. Zielke *et al.*[39] applied a hierarchical imaging approach to obtain multi-length scale reconstruction of the LCO-based electrode for understanding characteristic transport parameters at different length scales (see Figure 3.12). As an outcome, it was observed that the nanoporosity in the carbon-binder domain accounted for an additional 42 % accessible surface area for ion exchange between the electrolyte and the active particles. As a consequence, from incorporating the structures into the stochastic model, it was found that the ionic conduction increased by a factor of 3.6. Therefore, the spatial resolution from FIB-SEM tomography to resolve the nanoporosity inside the carbon-binder domain helps in understanding its impact on the ionic conduction and accessible contact area.

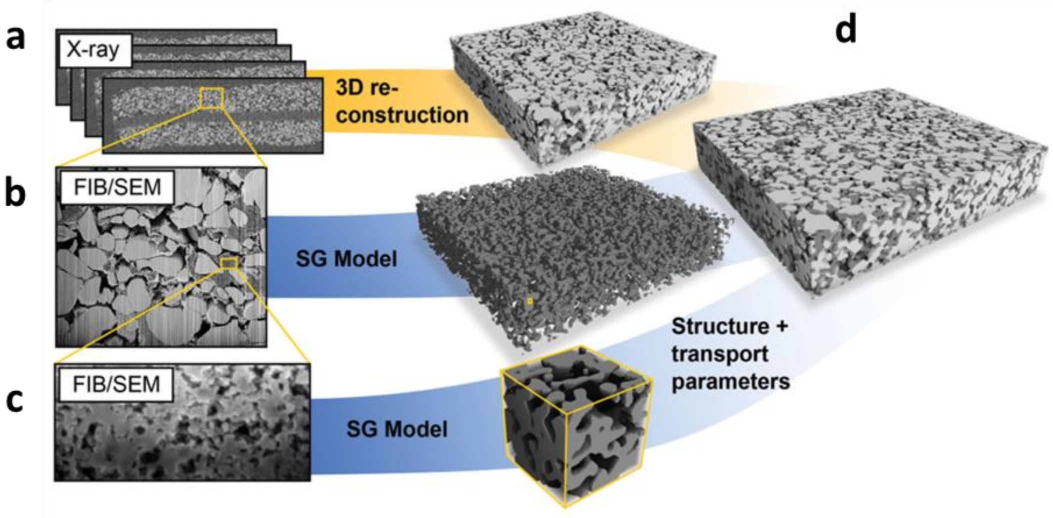

Figure 3.12: Hierarchical imaging approach to obtain multi-length scale reconstruction of the LCO-based electrode via (a) X-ray CT, (b) FIB-SEM tomography and (c) high-resolution FIB-SEM tomography, for understanding characteristic transport parameters at (d) the complete model to predict the electrochemical performance. Reproduced with permission from [39]*. Copyright (2014), WILEY-VCH Verlag GmbH & Co.*

FIB-SEM tomography studies have been predominantly used to study cathode materials. Recently, Etiemble *et al.*[68] studied Si-based anode electrodes to understand their microstructural evolution with electrochemical cycling. To understand the cause for capacity decay, Si and pore phases were segmented for electrodes with incremental cycle numbers (as shown in Figure 3.13). It was deduced that electrode cracking and SEI growth both resulted in the reduction in pore volume fraction, size and connectivity, thereby contributing to capacity fade.

Additionally, there are limitations to the application of FIB-SEM tomography techniques mainly because of the FIB sectioning capability. The rate at which the sample can be milled is related to the stopping distance of the Ga^+ ions in the sample material. For example, graphite milling is very slow due to the strong covalent bonding of the carbon atoms. Moreover, it is a destructive technique, as the focused-ion-beam physically removes material from the region of interest. However, FIB-SEM tomography operates in the critical resolution range between 10 nm to 10 µm[67,233]. The high SEM image quality in FIB-SEM tomography provides high-quality 3D datasets and by increasing the FIB milling current, the sample sizes can be enhanced with minimal resolution compensation.

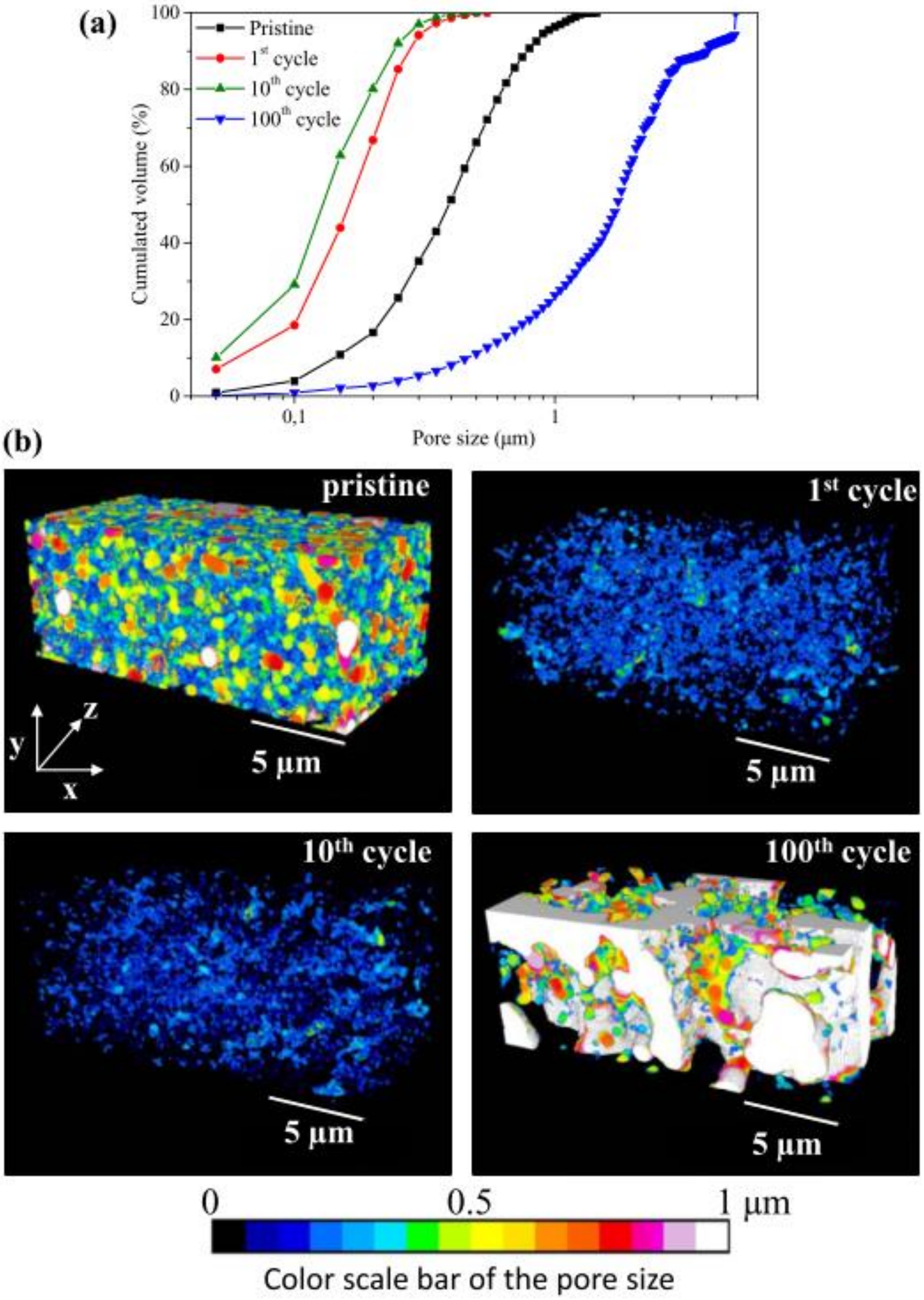

Figure 3.13: (a) Cumulative pore size distribution graph and (b) 3D reconstruction of pore network for electrode cycled at different cycle numbers. Reproduced with permission from [68]. Copyright (2016), The Electrochemical Society.

The use of FIB-SEM tomography demonstrates its importance to the understanding of degradation and failure mechanisms in battery electrodes. Although there are numerous structural studies of various battery electrodes, the relationship between 3D microstructural evolution and electrochemical cyclic performance remains relatively un-investigated for anode materials. In this study, an *ex-situ* FIB-SEM characterisation for 3D microstructural reconstruction and is employed to study the structural changes in silicon-based anodes for LIBs during electrochemical cycling. This is to attain a detailed insight into the anode degradation mechanisms as reviewed in section 2.2.

3.2.3 EXPERIMENTALLY INDUCED DATA ANALYSIS CHALLENGES

Considerable time is required for FIB-SEM tomography and can result in undesirable artefacts in the raw image dataset. There is a need to address these artefacts before any of the 3D analysis is performed on the raw data for a meaningful interpretation.

Anisotropic pixel size: The finite angle difference between the electron beam and the sample surface would mean a rectangular image from rectangular pixels instead of a square image if no corrections are performed. However, this geometrical artefact can be addressed either directly at the microscope software level or during image processing before any analysis. Once the tilt correction has been applied to the images, it looks as if the images were acquired by positioning the detector perpendicular to the imaged plane. In this study, the tilt correction was made as the first step of the image processing.

Systematic image drift: Similar to the anisotropic pixel size, this geometric artefact occurs in sequential images as a drifting of the imaging plane (in the z-direction). If the stack of raw images from tomography were looked into, it would appear as if the protective layer coating is moving downwards. This drift of the sample position in the image stack is also a result of the finite angle difference between the electron beam and the sample surface. The amount of the systematic drift is directly dependent on the thickness of layers removed by FIB milling during tomography characterisation.

Random drift: This artefact is primarily a result of the steady sample movement with respect to the ion column and electron column. However, there could be many factors contributing to this random drift, namely, (i) mechanical motion of sample stage, (ii) any thermal alteration in the microscopic chamber and sample chamber, (iii) external vibrations, (iv) electromagnetic alteration, (v) charge build-up on the sample, and (vi) instability of the sample. Among the above factors thermal drift of the sample, electrical instability, and sample instability might dominate during FIB-SEM tomography. All of the above phenomena limits the 3D tomography of large electrode volumes.

Non-uniform voxel size: Since individual SEM image resolving a 3D volume has a finite thickness (referred as voxel) and represents a small volume element. Drifting could result in SEM image stack with varying slice thickness that might cause difficulty in 3D reconstruction, whilst defining the z-directional voxel size. Automated drift correction procedure has been performed after every milling step with the help of two fudicial markers as reference point, one in the imaging plane and the other in the milling plane. Therefore, in this study it is assumed that there is uniform slicing during every FIB milling step.

Non-uniform illumination: The U-shaped trench milled around the interested sample volume often causes a shadowing effect in acquired images at the bottom or sides. This artefact is predominantly caused by the narrow trenches that limit the yield of electrons reaching the detectors. As a consequence, there is non-uniformity in illumination in the acquired images where the top area looks brighter than the bottom. Visually even if there is a subtle difference in illumination, it creates a massive barrier during data analysis automation.

A detailed method to address all the above artefacts will be discussed in the section 4.3.7.2.

3.3 OTHER TOMOGRAPHY TECHNIQUES

There are alternative tomography approaches that exist for visualisation and quantification of 3D volumes of battery materials. With different approaches, there are differences in image resolution, volume of interest for reconstruction and time required for the process.

3.3.1 X-RAY COMPUTED TOMOGRAPHY (CT) TECHNIQUE

X-ray CT is a non-destructive and non-invasive imaging technique that provides internal information for a whole host of materials from energy materials to shale rock to biological samples. It supports multi-scale length research from sub-micron to nano-scale resolution and allows 3D microstructural analysis, enabling visualisation and quantification of the internal structure of samples without destroying or affecting them in any way. X-ray CT can be used with a variety of X-ray sources[234].

Selecting any of the X-ray sources represents a balance between the analysable sample volume and the corresponding resolution to be necessary for resolving the features of interest. Moreover, a few other important factors that have to be considered during selection are namely, the material property, *i.e.* materials X-ray attenuation coefficient.

X-ray CT allows 3D reconstruction of the internal structure of a sample from a series of 2D X-ray projection images called radiographs. These radiographs are imaged as the sample is rotated about a single axis in a complete 360° rotation or 180° rotation[235] (see Figure 3.14). In a laboratory-based X-ray CT setup, X-rays are generated inside a tube source. An electric field is applied between the cathode and anode or target to accelerate or decelerate electrons generated from the cathode. After acceleration, the electrons are decelerated very sharply upon collision with the target producing Bremsstrahlung radiation (generally the target is a heavy metal, for example, Cu, Mo or W). X-ray radiation is generated from decelerating electron, and most of the energy is lost as heat. In laboratory-based CT, the X-ray source's focal spot size, system geometry and detector's pixel size determines the achievable spatial resolution[236]. Reducing the X-ray focal spot size helps in reducing penumbral blurring and thereby improves the image resolution, for this reason, most of the commercially available CT instruments have micro-focus X-ray sources[237] to achieve focal spot sizes near few micrometres or even smaller.

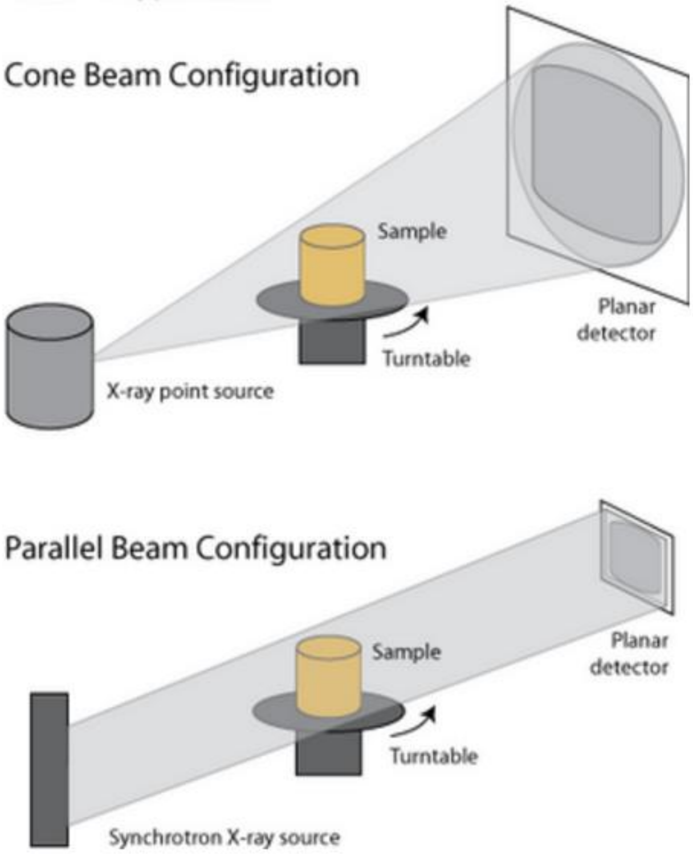

Figure 3.14: Schematic diagram representation of computed tomography process (synchrotron tomography using a parallel beam and laboratory based tomography using a cone beam)[235].

3.3.2 SERIAL SECTIONING TECHNIQUE

Serial sectioning techniques[238–240] is based on sequential polishing of the sample and imaging by light microscope to acquire a 3D microstructural reconstruction. The layer separation between sequential polishing may vary between 0.2 µm to 20 µm[239,240]. Despite this technique is applied to steel samples, this technique can be used for battery electrodes under SEM for high-resolution imaging. However, polishing after every SEM imaging needs the sample to be removed out from the SEM chamber and thus making the process very laborious and time-consuming.

3.3.3 TRANSMISSION ELECTRON MICROSCOPY TECHNIQUE

Transmission Electron Microscopy (TEM) nanotomography[241] enables high spatial resolution of about nanometer scale. However, with constrained thin samples (generally much less than 1 µm) makes it limited to gathering volumetric information of the microstructure.

3.4 SUMMARY

With conventional metallographic techniques, researchers often make presupposition about the morphology, spatial distribution, and connectivity network in 3D about constituents from the bulk. Recent studies have proved that these presuppositions can be inaccurate. Various approaches towards 3D analysis of LIB electrode's microstructure is demonstrated herein the review.

In LIB electrodes, one major disadvantage of the X-ray CT technique is the incomprehensive distinguishability of the carbon-binder domain from the pore space due to smaller particle size and the lower X-ray attenuation of the carbon and binder materials[218,242]. Recently, Zielke *et al.*[218] performed X-ray CT imaging of LCO-based cathode and with the statistical modelling they incorporation carbon-binder domain, as it remains a significant difficulty with X-ray CT imaging to obtain a high spatial resolution 3D structure of all the three phases. Further to resolve the three phases inside the 3D hierarchical structure, FIB-SEM tomography was performed[39].

In recent years, there has been a swift advancement in the 3D reconstruction methodology. X-ray CT imaging has been primarily chosen for 3D studies because of its non-invasive characterisation with the capability of real-time (4D) characterisation[70,243,244]. For X-ray CT a number of X-ray transmitted projections are collected and used for 3D reconstruction of the sample. However, the obtained voxel resolution usually ranges between sub-micrometer to tens of micrometer, which is mostly incapable of distinguishing features on the nanometer scale. Even though the TEM nanotomography addresses the spatial resolution limit of X-ray CT, this technique can only reconstruct smaller volumes. A possible substitute for X-ray CT and TEM nanotomography is serial sectioning[238–240]. The serial sectioning procedure primarily consists of two steps, which are then sequentially looped until the requested sectioning depth is met. The foremost step is sample sectioning, usually attained via cutting, polishing, or milling, where a constant depth and thickness of individual sectioning is essential for accurate reconstruction. Sectioning is followed by image collection where the 2D images are obtained from individual slices. Depending on the method, the image collection could also be done simultaneously whilst sample sectioning. While comparing all serial sectioning techniques, FIB-SEM tomography approach is highly potent for 3D reconstructions. FIB operates by generating a highly focused bearing a smaller spot size and energised ion beam onto the sample. With the interaction between the ion beam and the sample, the material under focus gets removed subsequently. Earlier, FIB-SEM dual-beams were more prominently employed for site-specific analysis and specially designed nanofabrication rather than 3D serial sectioning[215,216]. However, this technique is highly beneficial for automatic serial sectioning. The exceptional high-resolution image with a pixel size of tens of nanometer from FIB-SEM tomography method enables a better understanding of the microstructural evolution at multiple length scales.

In the past few years, FIB-SEM tomography[66–69] and X-ray CT[27,33,34,245,246] have been an effective tool for analysing 3D morphologies of LIB electrodes. X-ray CT is a non-destructive technique, but the conventional laboratory X-ray source systems are limited with spatial resolution up to micrometer. However, the synchrotron X-ray source systems provide high spatial resolution up to tens of nanometers, but the experimental setup is not trivial. Conversely, FIB-SEM tomography is a destructive technique but is capable of performing high spatial resolution 3D imaging (generally, few tens of nanometers) which otherwise is beyond the limits of laboratory-based X-ray CT instruments[247].

So far, the application of FIB-SEM tomography in LIBs has majorly been applied for the *ex-situ* characterisation of cathodes[25,29,39,214,223–226]. Recently, structural changes (particle cracking and porosity evolution) in silicon-based anodes under cycling aging have been studied[68] but the microstructural changes after prolonged cycling under different capacity limits have not been analysed at the electrode level. This study aims to apply tomography and other physicochemical characterisation for a better insight into the microstructural evolution and dynamics that occur inside the LIBs during operational ageing. Therefore, it can be concluded that the use of imaging techniques, such as FIB-SEM tomography, alongside other conventional physical characterisations to advance towards a more in-depth understanding of electrode's microstructural evolution at the different operating condition and a possible root causes of failure. In this thesis, the application of *ex-situ* FIB-SEM 3D imaging is implemented to interpret the comprehensive Si-based anode degradations and failure.

CHAPTER 4. RESEARCH METHODOLOGY

This chapter will focus on the fabrication of silicon-based electrodes and various techniques to characterise the resulting electrodes. Characterisation analysis includes electrochemical to physicochemical approaches that are largely important for growing the understanding of how to correlate the microstructure with performance.

4.1 MATERIAL PREPARATION

4.1.1 SYNTHESIS OF METAL-ORGANIC FRAMEWORKS (MOFs)

4.1.1.1 SYNTHESIS OF UiO-66

1,4-Benzenedicarboxylic acid, 1.19 g, and zirconium(IV) chloride, 0.823 g, (2:1 molar ratio) were weighed and dissolved in *N*,*N*-dimethylformamide (50 ml). To this solution, 10 ml of hydrochloric acid (35%) was added and the resulting mixture was stirred at room temperature for 30 minutes. The reaction vessel was sealed inside a 200 ml Teflon-lined stainless-steel autoclave and heated under hydrothermal conditions, at 120 °C for 12 hours. The product was obtained as a white solid by filtration and subsequent washing with methanol and then dried in air at 70 ^{o}C. All chemicals were used as supplied by Sigma-Aldrich.

4.1.1.2 SYNTHESIS OF UiO-67

4,4'-Biphenyldicarboxylic acid, 1.082 g, and zirconium(IV) chloride, 0.805 g, in a 1.3: 1 molar ratio, were dissolved in *N*,*N*-dimethylformamide (60 ml). To this solution, 6 ml hydrochloric acid (35%) was added and the resulting mixture was stirred for 30 minutes at room temperature. Then, the reaction was heated at 80 °C under hydrothermal conditions in a 200 ml Teflon-lined stainless-steel autoclave for 24 hours. The product was obtained through filtration as a colourless solid, which was then stirred in *N*,*N*-dimethylformamide at 50 °C for 12 hours to remove unreacted biphenyl-4,4'-dicarboxylic acid, then filtered and washed with methanol, before drying at 70 °C overnight. All chemicals were used as supplied by Sigma-Aldrich.

4.1.2 SYNTHESIS OF GRAPHENE AND SILICON-GRAPHENE POWDERS

4.1.2.1 SYNTHESIS OF GRAPHENE POWDER (FLG_{WJM})

Graphene was prepared from natural graphite (+100 mesh, Sigma Aldrich) following the method developed by Del Rio-Castillo *et al.*[248](see Figure 4.1). Graphite is dispersed in N-methyl-2-pyrrolidinone (NMP) solvent (> 97 %, Sigma Aldrich) in order to obtain a dispersion of 100 g of powder in 10 L of solvent. The dispersion was then subjected to a wet-jet milling procedure[248] to allow the exfoliation of graphite in few-layer graphene flakes. In this process, the exfoliation of graphite is promoted by the shearing forces due to the turbulent flow of the solvent forced to pass through the nozzles.

4.1.2.2 SYNTHESIS OF SILICON-GRAPHENE (Si- FLG_{WJM}) POWDER

Si-FLG_{WJM} composite powder was prepared following a modified wet-jet milling procedure. In this case, a mixture of graphite particles (+100 mesh, Sigma Aldrich) and silicon powder (<100 nm, Sigma Aldrich) in equal amount were dispersed in N-methyl-2-pyrrolidinone (NMP) solvent (> 97 %, Sigma Aldrich) in order to obtain a dispersion of 100 g of powder in 10 L of solvent and the obtained mixture was placed in a container and mixed with a mechanical stirrer, to homogenize the dispersed flakes/powders.

The mixture was subsequently passed through the wet-jet mill apparatus in the following manner:

- the mixture is inserted in the apparatus by high pressure pump system;

- a particle liquid phase jet stream was then generated and forced to flow through a nozzle;

- the pressurised jet stream creates a turbulent flow that promote the collision of the particles;

- the previous steps are repeated with 4 different nozzles of decreasing diameter.

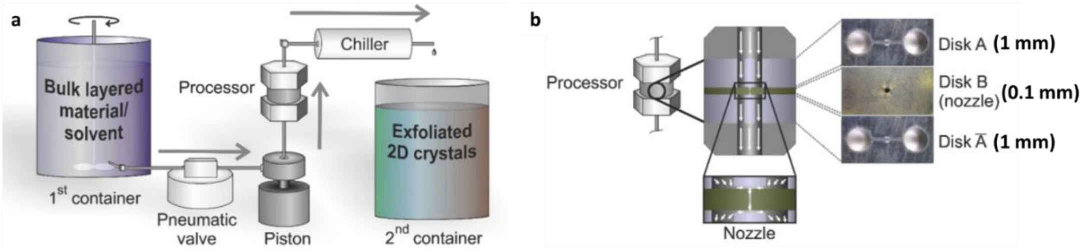

Figure 4.1: (a) Schematic diagram representation of the wet-jet mill system, and a (b) zoomed in vied of the processor depicting the configuration of channels and disks. The arrows indicating the solvent flow inside the WJM. In (b) the top right image shows the top view image of disks with hole diameters. Reprinted with permission from [248]. *Copyright (2018), The Royal Society of Chemistry.*

The wet-jet mill apparatus allows for the simultaneous exfoliation of graphite and disaggregation and distribution of silicon particles onto the graphene flakes, by creating a turbulent flow when the solvent is forced to pass through the nozzle. Using of the wet-jet milling technique, disaggregation of silicon particle is promoted by the collision of the particles in the high pressurized stream of liquid dispersion, whilst the exfoliation of graphite is promoted by the shearing forces due to the turbulent flow of the solvent. To obtain the final as-synthesized powder, the solvent was evaporated by rotavapor and the resulting powder was dried overnight under vacuum at 70 °C.

The FLG_{WJM} and Si- FLG_{WJM} powders used in this study were prepared at the Graphene Laboratories, IIT Central Research Labs, Genoa, Italy.

4.1.3 SYNTHESIS OF Sn-Si HETEROSTRUCTURES VIA PLASMA ENHANCED CHEMICAL VAPOUR DEPOSITION AND VAPOUR-LIQUIDUS-SOLIDUS SiNW GROWTH

Consistent with the Hume-Rothery limits of binary solubility, Sn and Si have atomic radii differences significantly > 15 % and as a result have limited solubility in each other. This is despite their other favourable common properties in this respect, namely crystal structure, valence and electronegativity[249]. It is this limited solubility with Si that makes Sn a good catalyst in this instance as it tends to generate atomically sharp heterostructures[250]. This part of the study essentially integrates a Sn granular thin film with nano-crystalline and amorphous phase Si nanowires (SiNWs), to generate a degradation-resistant, high capacity anode system. In order to synthesise the Si nanowires, a radio-frequency plasma enhanced chemical vapour deposition (RF-PECVD) technique was used. This growth of nanowire by way of the vapour-liquid-solid (VLS) method, which is described as a “bottom-up” method[251]. In this process, the substrate coated with Sn as a catalyst is heated in the presence of a silane precursor gas, which becomes preferentially absorbed and precipitated out of the Sn catalyst. Upon dissolution into the droplet, Si atoms form a liquid eutectic alloy with the underlying Sn catalyst. Eventually – with continuous flow of SiH_4 - the alloy becomes supersaturated whereby the nucleation barrier is surpassed and Si precipitates at the liquid-solid interface, minimising the free energy of the system[252]. Because the mechanism consists of adsorption, dissolution, diffusion and precipitation in the liquid phase – these are thermodynamic processes that work towards equilibrium - one can use the SnSi equilibrium phase diagram in Figure 4.2 to predict how the catalyst will work. As illustrated in the schematic diagram in Figure 4.3 the kinetics of the VLS mechanism consist of 4 steps:

(1) Mass transport in the gas phase.
(2) Chemical reactions at the vapour-liquid interface.
(3) Diffusion in the liquid phase.
(4) Incorporation of atoms in a crystal lattice[253].

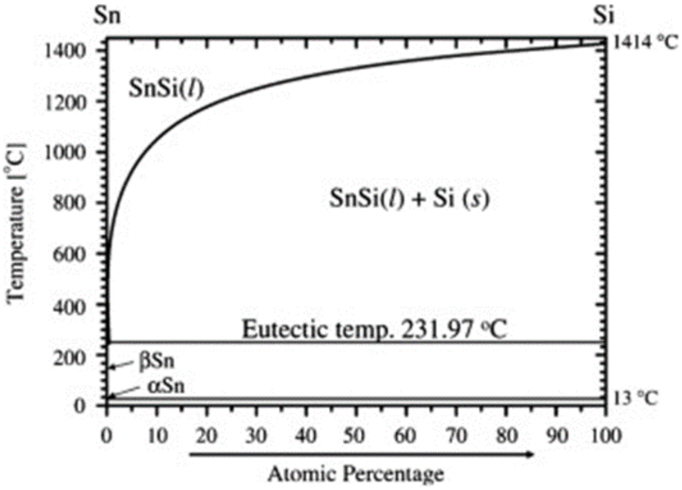

Figure 4.2: The Si Sn Equilibrium Phase Diagram[254].

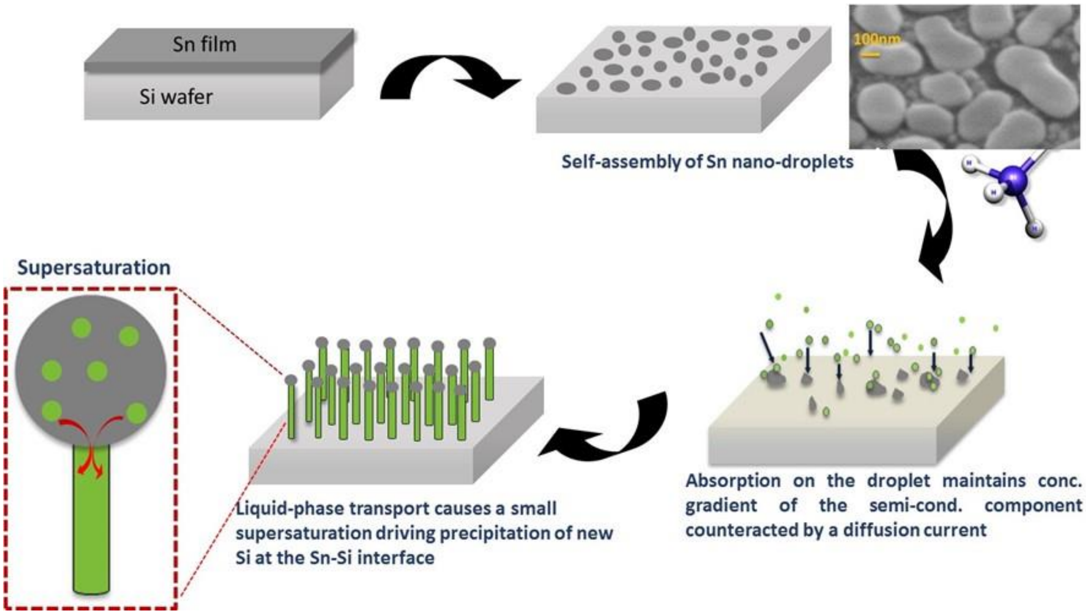

Figure 4.3: Schematic diagram illustration of the growth of SiNWs via vapour–liquid–solid mechanism. Sn film coated substrate is exposed to H-plasma to obtain self-assembled Sn spherical nanoparticles. Si atoms are adsorbed and precipitated from Sn nanoparticles to obtain nanowires that are directly grown from the substrate (i.e. nanowires are electrically welded to the bottom conductive Cu sheet as chosen substrate).

Copper (Cu) foil and mesh sheets were obtained from Dexmet Corporation and cut into 30 × 30 mm (length and width). Corning glass (Alkali Free Borosilicate - 7059) and p-Silicon wafer (500 μm thickness, 1-20 Ω cm, 100 orientation) were cleaned using an RCA process and the native oxide on Si wafers was removed by immersing wafers in a buffered hydrofluoric (HF) acid solution for 10 seconds. Residual HF was removed by rinsing thoroughly in deionised water. The Cu foil, mesh, glass, and Si wafer were loaded in a thermal evaporator (Edwards AUTO 306) to deposit 100nm thin film of tin (99.999 % purity) at 10 Å s^{-1} at 8 e^{-7} mbar base pressure. Real-time thickness was monitored using a quartz microbalance. All substrates coated with tin on one side was loaded into a capacitively-coupled RF-PECVD (radio frequency - plasma enhanced chemical vapor deposition) chamber (Oxford plasmalab) and pumped down to 5 mTorr base pressure. The temperature was raised to 400 °C and held for 5 min, followed by hydrogen plasma pre-treatment (hydrogen gas flow at 1.67×10^{-6} m^3 s^{-1}, 500 mTorr chamber pressure and, 33 mW cm^{-2} RF power density) for 5 min. Whilst still under vacuum, 3.34×10^{-7} m^3 s^{-1} of SiH_4 gas was introduced to existing H-plasma to initiate the growth process of silicon nanowires (SiNWs). This was continued for 15 min, samples were then removed from the PECVD chamber and cooled to below 50 °C. Real-time thickness was monitored using a quartz microbalance during the evaporation.

This Sn-Si heterostructure film used in this study was prepared at Emerging Technologies Research Centre (EMTERC), De Montfort University, Leicester, United Kingdom.

4.1.4 SILICON-BASED ELECTRODE FORMULATION

Electrode manufacturing process includes two main steps, namely, (i) electrode material slurry preparation, and (ii) electrode coating process.

4.1.4.1 ELECTRODE MATERIAL SLURRY PREPARATION

In this research work hybrid anode materials was studied, namely, silicon-MOFs, silicon-graphene, and silicon-tin powders via conventional mixing route.

In the first study, the first use of metal-organic frameworks (MOFs) as an additive, namely UiO-66 and UiO-67, to enhance the electrochemical performance of high-capacity silicon anodes in Li-ion batteries is reported. The electrode slurry was prepared from silicon powder with average particle size of 2.2 µm (Elkem Silgrain e-Si), carbon black (Super C65, TIMCAL C-NERGY), graphite (SFG-6, TIMCAL C-NERGY), carbon nanotubes (Tuball Inc.) and few-layer graphene (GNPs) (thickness of 6 - 8 nm, XG Sciences). A carbon mixture was formulated from 88 % carbon nanotubes, 6 % carbon black and 6 % GNPs in deionised water with a solids content of 64 %. The heterogeneous carbon mixture was added to enhance both the long-range (planar) and the short-range (depth) conductivity of coating with a possible mechanical strengthening from graphene[58]. The formulation ratio of electrode slurry used was Si: polymer binder: carbon-mixture: additive: 70:7:11:12 (wt.%) as shown in Figure 4.4. The additives were dispersed in a mixture of deionised water and isopropanol (1:5 wt%) and sonicated for 30 min to break any agglomerates.

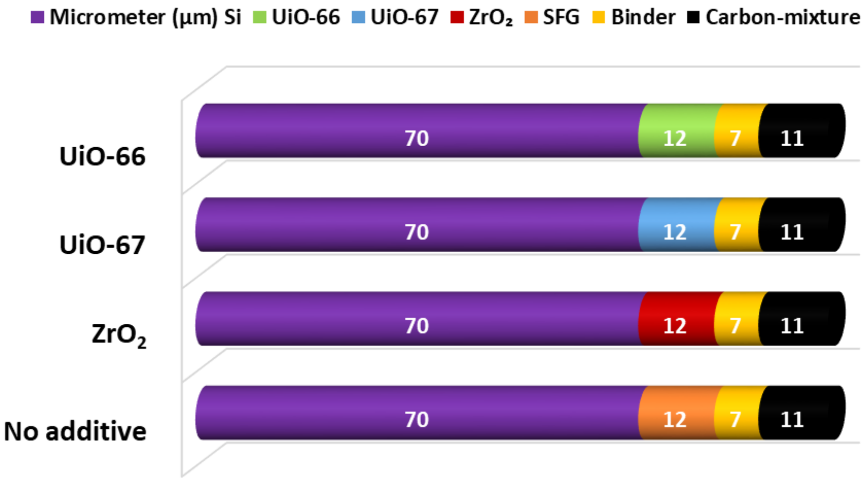

Figure 4.4: Formulation matrix for MOFs in Si-based anodes study.

In the second study, to study the influence of graphene in Si-based anodes six different formulations were compared (see Figure 4.5). To obtain the electrode slurries starting from silicon-graphene composite powder via wet-jet milling procedure (Si-FLG$_{WJM}$), µm sized silicon powder with average particle size of 2.2 µm (Elkem Silgrain e-Si), nm Si powder with average particle size of 200 nm (Sigma-Aldrich), as-synthesised graphene powder and few-layer graphene (GNPs) (thickness of 6 - 8 nm, XG Sciences). As conductive carbon, carbon black (Super C65, TIMCAL C-NERGY) were added.

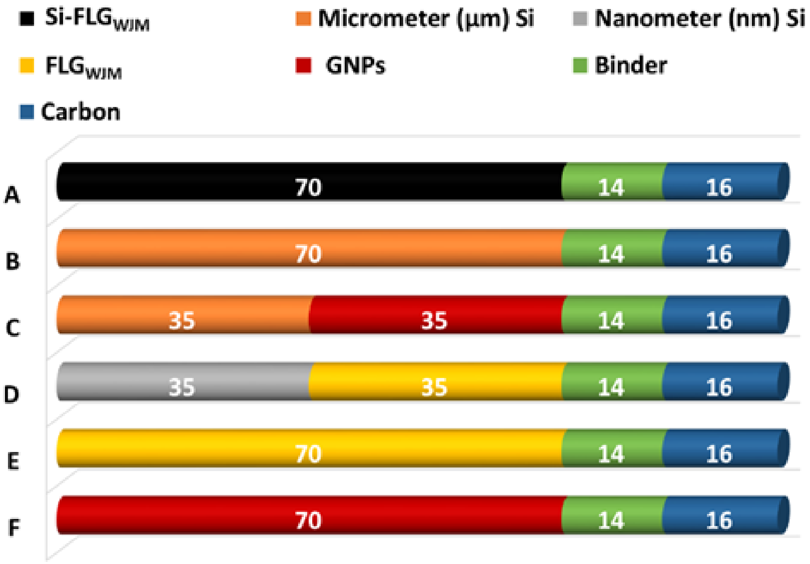

Figure 4.5: Formulation matrix for graphene in Si-based anodes study.

In the third study, to investigate the influence of tin in Si-based anodes, three different formulations were compared (see Figure 4.6). The electrode slurries were made from µm sized silicon powder with an average particle size of 2.2 µm (Elkem Silgrain e-Si) and µm sized tin powder with an average particle size of 3 µm (Sigma-Aldrich). As the conductive additive, carbon black (Super C65, TIMCAL C-NERGY) was used.

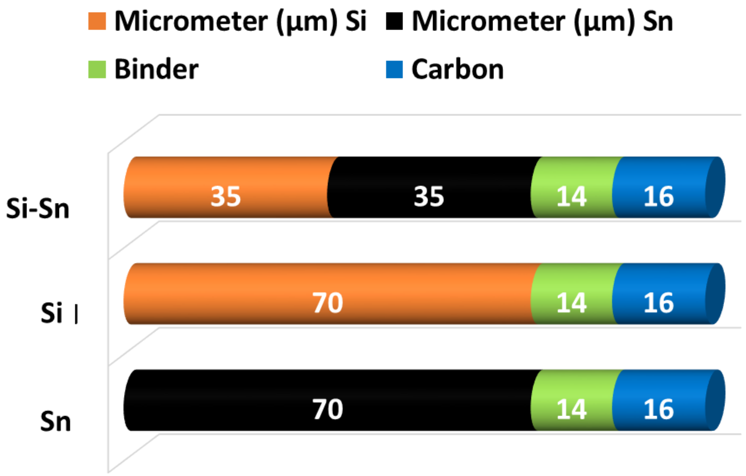

Figure 4.6: Formulation matrix for Sn in Si-based anodes study.

The electrode was prepared from a slurry of silicon powder, carbon mixture, additives and water as the polymer binder solvent (for every 10 g of silicon 20 g of deionised water was added). The formulations were processed using a high-speed Homodisperer (Model 2.5, PRIMIX) for 30 min at 1000 rpm. The resulting mixture was ultrasonically processed (UP400S, SciMED) for two periods at 60 % amplitude for 7.5 min each. The ultra-sonication step is aimed to break up any carbon agglomerates for homogeneous particle distribution. Following this, the Na-PAA binder solution was added to the solution prior to high-speed dispersion for 30 min at 1000 rpm. Finally, the slurry was transferred to a Filmix disperser (Model 40-40, PRIMIX, Japan) for homogenisation and breakdown of any secondary agglomerations. This was a two-step process, first at 10 ms^{-1} for 30 secs and then at 25 ms^{-1} for 30 s.

The aqueous binder was made from PAA power (average Mwt ~450,000, Sigma-Aldrich, UK) dissolved in deionised water with 13 % concentration and mixed in Turbula (T2F, Glen Mill, US) for 48h. The resulting solution was left to stand for 24h to eliminate any air bubbles generated from mixing. Sodium hydroxide was added to the solution for partial neutralization to a degree of 70 % as proposed by Huang *et al.*[58] and was stirred with spatula for 5 min and left overnight to complete the neutralization reaction. The neutralisation step is to extend the chain configuration of the PAA as it might incite the electrolytic dissociation and also suppress the agglomeration of carboxyl groups in PAA from hydrogen bonding. The polymer chains in Na-PAA are stretched due to electrostatic repulsion and it also exhibits higher viscosity[255] improving adhesion and cohesion of the electrode materials.

4.1.4.2 ELECTRODE COATING PROCESS

The coating process deposits and spreads the prepared slurry onto a current collector of copper foil (10 µm, Oak Mitsui, electrodeposited) using a draw-down coater with a micrometer-controlled blade (K control coater Model 101, RK Print, UK). The gap between the blade and the copper foil can be adjusted between the ranges of 0 – 100 mm, and for this study, a blade gap of 100 µm was used. After coating the slurry onto the copper foil, the coating was dried on a preheated hot plate, set at a temperature of 50 °C to eliminate any solvent. The coating was subsequently dried in a vacuum oven set at 50 °C overnight to ensure maximum moisture removal.

4.1.5 FABRICATION OF COIN CELLS

Typically, a coin cell consists of bottom base, top cap, gasket, spring, spacer(s), electrodes and a separator arranged in a sequence and crimped to ensure a hermetic sealing (see Figure 4.7). Generally, coin cells can be categorized as full cells or half cells. Full cells consist of a cathode (generally transition metal oxides or phosphates) and anode material (generally graphite or silicon) where as in half cells, the negative electrode is pure lithium. In cathode half-cells lithium act as cathode while in anode half-cell lithium act as anode because of the reversible potential of these materials. Prior to coin cell assembly electrodes and separators are cut into sizes using an appropriate cutter or punch.

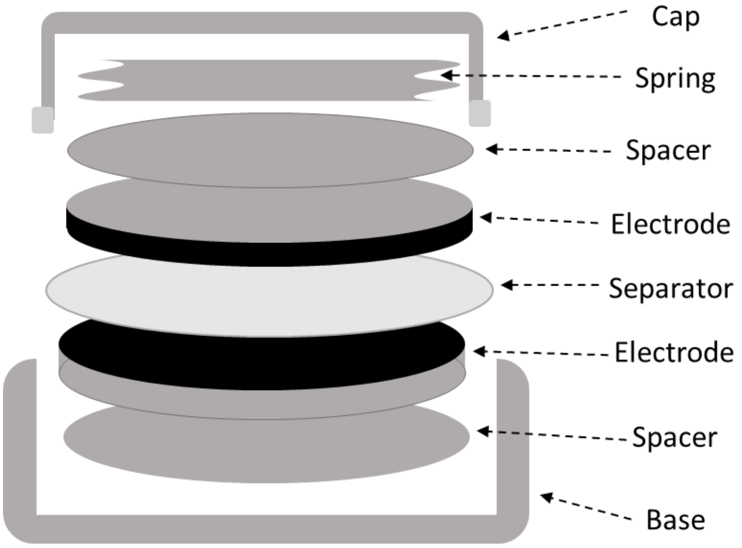

Figure 4.7: Schematic diagram representation of a coin cell.

Electrodes were cut from vacuum dried electrodes in a dry room (with a dew point of -45° C) to ensure there was no exposure to moisture during the cell assembly process, which is detrimental for the battery performance. In this study, anode half cells were prepared. During cell making silicon electrodes were placed on the bottom cap against lithium (diameter = 15.6 mm, PI-KEM) on top and a PP|PE|PP microporous trilayer membrane (Celgard 2325) as separator in between. The electrolyte used in this study was RD265 (1.2 M $LiPF_6$ in ethyl carbonate/ethyl methyl carbonate (1/3 v/v), 15 % fluoroethylene carbonate and 3 % vinylene carbonate) (PuriEL, SoulBrain). After assembling the cell as shown in Figure 4.7, the cell was crimped using MSK-110 crimper. For statistically reproducible results three half-cells corresponding to each formulation were made. Following cell fabrication, the open circuit voltage (OCV) was measured to make sure there was no internal short-circuit before the cell was electrochemically characterised.

4.2 MATERIAL CHARACTERISATIONS

Electrochemical characterisation techniques are used to analyse the performance of a battery, which will greatly depend on the properties of the materials inside the battery. This determines electrochemical parameters (for example, capacity, impedance), and provide feedback to enable improving present systems and evaluate new and emerging chemistries. In a typical electrochemical cell, current is supplied to the counter electrode and the working electrode while the potential is controlled between a reference electrode and the working electrode. A detailed description of every type of electrochemical characterisation technique is beyond the scope of this thesis. The reader is referred to the book from Linden[256] and Bard and Faulkner[257]. A few of these technique (electrochemical cycling, differential capacity and AC impedance) will be discussed briefly in the following sections and these would be used within this study.

4.2.1 ELECTROCHEMICAL CYCLING

Galvanostatic cycling, *i.e.* a cell is charged and discharged galvanostatically *i.e.* under constant current, measuring voltage and operating under upper and lower voltage limits is a widely used technique for LIB research. The cycling result provides charging and discharging profiles for Li-ion battery under simulated practical application situations. The limiting voltages are estimated from the Gibbs free energy of the material undergoing lithiation and delithiation. The lower cut-off voltage for most of the anodic alloying material for Li-ion battery is 10 - 50 mV while the upper cut-off voltage is in between 3.4 - 4.3 V. Often the current applied is expressed as ‘C-rate’ where ‘C’ represents battery capacity.

A battery subjected to C-rate charge/discharge means the rate at which a battery is charged/discharged to get maximum achievable capacity. For example, a 1C discharge rate means that the battery would be discharge within 1 hour. Therefore, a 10 Ah battery discharged at 1C rate would mean that the battery would deliver a current of 10 A for 1 hour, whereas a 5C rate would mean that the same battery would deliver a current of 50 A for one-fifth of an hour and a 0.5 C discharge rate would be 5 A for 2 hours.

There are two main charging methods for Li-ion batteries, namely, constant current (CC) charging and constant current-constant voltage (CC-CV) charging whilst other different charging methods include trickle charging, float charging, taper charging and pulsed charging. The CC-CV charging method (see Figure 4.8) includes two step charging method. The first charging step is by CC until the battery meets its upper potential limit, then the charging is by CV mode until the current drops to a specified limit (generally 3 - 5 % of the initial charge current). During this CV mode the battery attains its full capacity, which is generally not met by only CC charging.

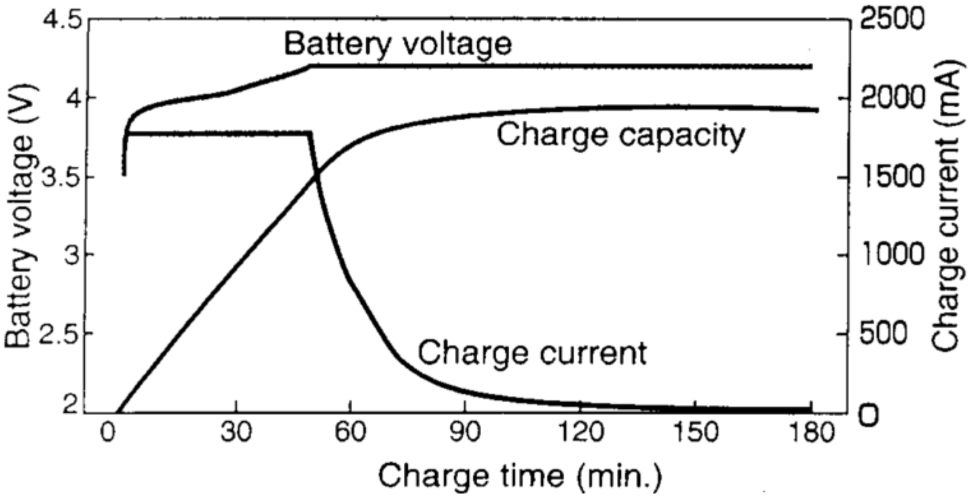

Figure 4.8: A typical CC-CV charging of 18650 cylindrical lithium ion battery at 20°C [256].

The results obtained from galvanostatic cycling reveal a lot of information regarding phase transformations in materials operating under different kinetics, rate performance, cycling efficiency, structural change (crystalline to amorphous or vice-versa), operating potential window and cycle life prediction. The sub-section below discusses briefly the differential potential-capacity profile, which represents another approach to presenting galvanostatic cycling data.

The electrochemical cycling was characterised using a multi-channel potentiostat, VMP3 (Bio-Logic) at room temperature. The cells were charged and discharged using a constant current mode. For the first cycle, a C-rate of 0.05 C was used to initiate SEI formation and from the second cycle, a rate of 0.2 C was applied where C denotes capacity of the cell. A cut-off voltage of 50 mV was applied to avoid re-crystallizing $Li_{15}Si_4$ from highly lithiated amorphous silicon[42]. Electrodes from all of the formulations were cycled at three different silicon capacity: 1200 mAh g^{-1}

(corresponding to a current density of 238 mA g^{-1} at 0.2 C), 1800 mAh g^{-1} (corresponding to a current density of 358 mA g^{-1} at 0.2 C), and 3579 mAh g^{-1} (corresponding to a current density of 716 mA g^{-1} at 0.2 C). Cells were cycled at the full capacity of silicon to compare the effects of these additives towards capacity retention and cycle life under more extreme operational parameters, and also at 1800 mAh g^{-1} and 1200 mAh g^{-1} capacity limits to minimise any pulverization from large volume expansion upon lithiation[42]. The upper cut-off voltage applied was 1 V to avoid any overcharging.

4.2.2 DIFFERENTIAL CAPACITY CYCLING

This approach plots differential capacity (*dQ*) and differential voltage (*dV*) against voltage (*V*) where the peaks represents redox reactions (see Figure 4.9) of the electrochemical system. *dQ/dV* analysis gives insight into different phase transformation of the electrode during lithiation and delithiation. Each peak can be considered as a "performance fingerprint" and reveals significant information such as peak shift, peak intensity, upon successive cycling of the battery. Information from cycling data can be used to plot either *dQ / dV* or *dV / dQ*, against voltage. In the *dQ / dV* plots, the peaks depicts phase equilibria, whilst in *dV / dQ* plots, the peaks depict phase transitions[258].

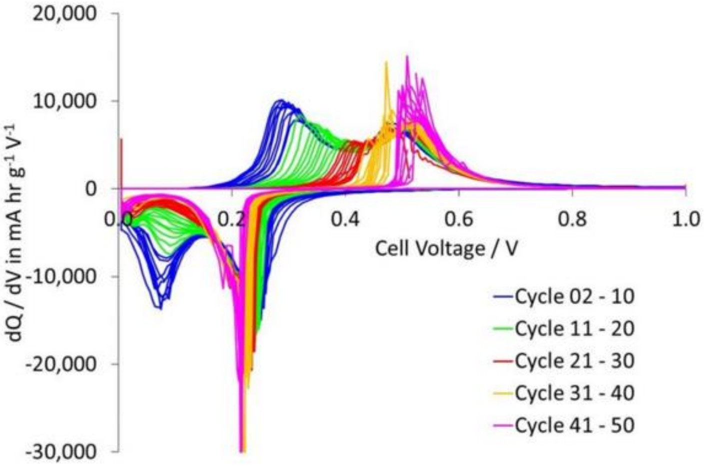

Figure 4.9: Differential capacity plot for a composite silicon anode. Reprinted with permission from [258]. Copyright (2015), The Electrochemical Society.

4.2.3 ELECTROCHEMICAL IMPEDENCE SPECTROSCOPY

Electrochemical Impedance Spectroscopy (EIS) is also referred to as AC impedance spectroscopy. For more detailed understanding of the fundamentals and principal behind EIS measurements the reader should refer to texts by Barsoukov and Macdonald[259] and Orazem and Tribollet[260]. The EIS data are often represented using electrical equivalent circuits (EECs) (see Figure 4.10).

EIS has been extensively applied for analysing lithium battery systems to draw insights into battery characteristics relating to performance limiting factors such as conductivity[261,262], charge-transfer properties[263–265], SEI layer[259], and temperature. Capacity loss during storage has been a big concern for many application and has been studied with EIS along with extended cycling capacity loss[266,267].

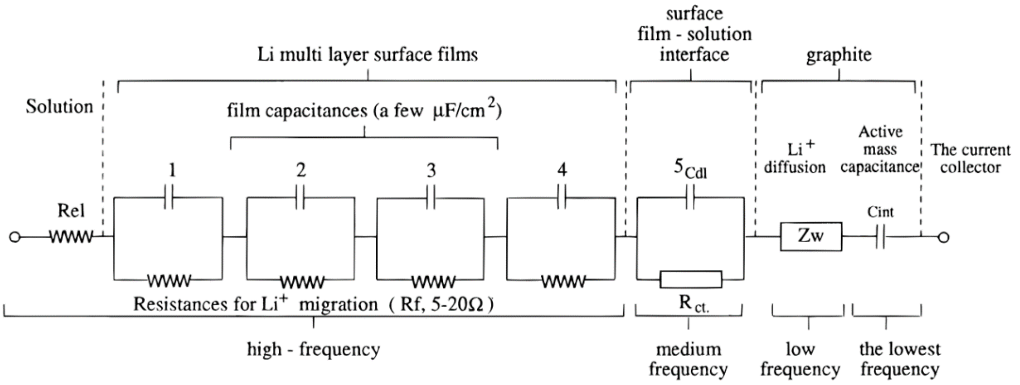

Figure 4.10: Schematic diagram representation of lithiation-delithiation in lithium-graphite system in the form of EECs. Reprinted with permission from [268]. Copyright (1997), American Chemical Society.

The electrode material's composition dynamically changes under charge-discharge cycling and these changes takes place because of the different ionic transport processes involved, such as lithium ion transport mechanisms, electron transport processes and the series resistance from the separator and electrodes[269]. EIS is an important tool to analyse these different processes separately (as they each have different time constants -see Figure 4.11), such as resistance from the SEI layer and charge transfer resistance. EIS is an effective tool in analysing various degradation effects and so can allow one to reverse engineer electrodes to improve efficiency, cycle life and rate capability.

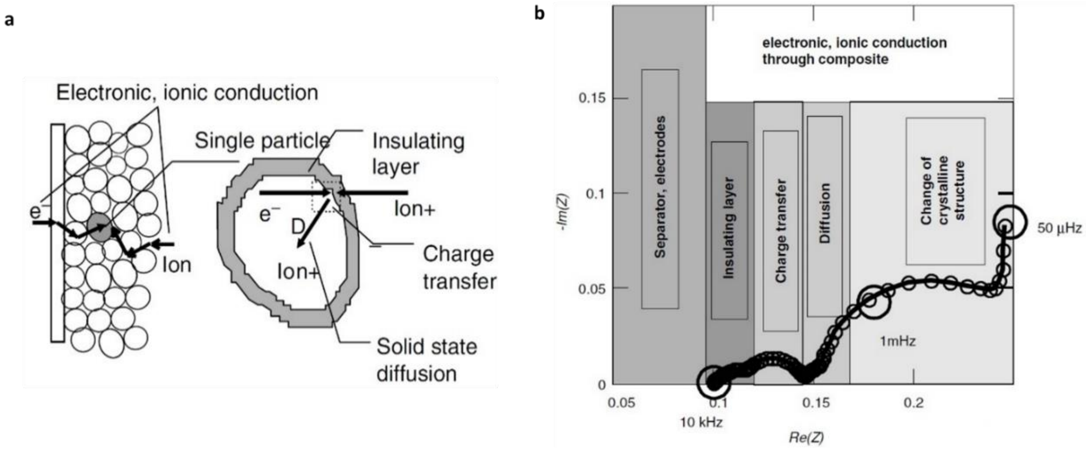

Figure 4.11: (a) typical kinetic steps inside battery electrode, (b) relating impedance spectra with characteristic properties of intercalation material. Reprinted with permission from [259]*. Copyright (1969), John Wiley and Sons.*

Impedance measurements were carried out after the first cycle and for every 10 cycles. A potentiostatic EIS measurement technique was applied together with galvanostatic cycling at 50 % state of charge (during lithiation step by limiting lithiation to 2.5 hrs). The frequency range applied for this analysis was from 100 KHz down to 10 mHz (with 10 frequencies scanned per decade) with a sinus amplitude of 10 mV. Information regarding the specific capacities over cycling, real-time voltage data and columbic efficiency was all recorded for analysis.

4.3 PHYSICOCHEMICAL CHARATERISATION

4.3.1 SCANNING ELECTRON MICROSCOPY (SEM)

SEM characterisation was performed with field-emission SEM (FE-SEM) microscope (Sigma, Carl Zeiss, Germany) equipped with an Energy Dispersive Spectrometer (EDS) (Xmax 50, Oxford Instruments). In this study SEM imaging was used for sample’s topographic visualization, distribution of different components in composite electrodes and also to characterise the morphological evolution after cycling. After completion of cycling the cell was disassembled in a glove box under an argon atmosphere. A part of the electrode was cut and attached to an SEM stub for imaging using secondary lens and In-lens detection at higher magnifications. To obtain the SEM image an accelerating voltage of 5 kV was applied with a current value of 100 pA using in-lens detection. The working distance was around 2.5 mm. EDS analysis was conducted using the same FE-SEM with an accelerated voltage of 20 kV and an SE detector. The working distance was adjusted to 8.5 mm for the EDS analysis.

4.3.2 INDENTATION TEST

The indention test was conducted using a Berkovich indenter (NanoTest Extreme, Micro Materials Ltd, UK) with a diameter of 25 µm. A load was applied to the electrode until it reached 20 mN, it was then held for 300 s to make sure the creep exponent has been removed during unloading. A thermal drift correction was followed for the 60 s after removing the load. For each electrode, 20 indentations were performed to produce statistically valid results. Reduced hardness and Young's modulus were analysed from the test data set by calculating the slope from the unloading curve. Indentation test was performed for Si-MOF electrodes and Si-graphene electrodes.

4.3.3 THERMOGRAVIMETRIC ANALYSIS (TGA)

For Si-MOF electrodes thermogravimetric analysis (TGA) – differential scanning calorimetry (DSC) was performed using a Mettler Toledo TGA/DSC1 instrument under a nitrogen atmosphere, with a heating rate of 10 °C·min^{-1} from 25 °C to 1000 °C.

For Si-graphene electrodes, the experiment was conducted in a TGA (Q500, TA Instrument) and the temperature scan comprised a run to 800 °C at 5 °C min^{-1} followed by an isothermal step of 2 hours at 800 °C.

4.3.4 X-RAY POWDER DIFFRACTION (XRD)

Powder X-ray diffraction patterns of as-synthesised MOFs and pristine and cycled electrodes with MOFs were measured for sample identification. The XRD instrument

(Panalytical X’Pert Pro MPD), is equipped with monochromatic Cu $K_{\alpha 1}$ radiation (λ = 1.54056 Å) and a PIXcel solid state detector.

4.3.5 RAMAN SPECTROSCOPY ANALYSIS

To compare the quality of two kinds of graphene, Raman spectra of FLG_{WJM} and GNPs, were obtained. Raman spectroscopy was performed using a Renishaw Invia micro-Raman spectrometer, with a diode-pumped solid-state laser (RL523C50) at an excitation wavelength of 532 nm. Spectra were obtained at 10 % power with an integration time of 10 seconds.

4.3.6 TRANSMISSION ELECTRON MICROSCOPY (TEM) ANALYSIS

TEM imaging and selected area electron diffraction imaging of SiNW in Sn-Si heterostructure film were performed with Talos F200X microscope (FEI), operated at accelerating voltage of 200 kV.

4.3.7 FIB-SEM TOMOGRAPHY

Two-dimensional (2D) analysis is insufficient to fully characterise the complex evolution in the pore shape characteristics of the electrodes[25,29,30,68]. To overcome the limitations of 2D analysis, 3D characterisation using FIB-SEM tomography was employed. The FEI Scios Dual-Beam instrument has been used in this study for all tomography work. In this study, the influence of electrochemical cycling on Si-based anodes’ microstructure will be analysed from 3D perspective. The microstructure of both pristine and cycled Si-based anodes were reconstructed as illustrated in Figure 4.14. The electrochemical cycling-induced microstructural evolution of different anode systems were quantitatively evaluated in order to analysed the influence of additives (MOFs, graphene and tin) on electrochemical cycling. The experimental methodology used in this study for acquiring and quantitatively evaluating 3D dataset is described below.

4.3.7.1 SAMPLE PREPARATION

The sample preparation for tomography is similar to SEM imaging sample preparation. The disassembly of the cycled cells was performed inside a glove box under an argon atmosphere. A small section of the electrode was mounted on to the SEM stubs and transferred to the FIB-SEM's sample chamber. The ETD detector was used to identify the region of interest. The same ETD detector was used for the eucentric height adjustment at 52° angle for both the ion and electron column, before further proceeding towards milling.

4.3.7.2 INSTRUMENT SETUP TO LIMIT ARTEFACTS DURING SAMPLE ANALYSIS

The creation of a relatively sizeable U-shaped trench around the region of interest (ROI) is effective in reducing the shadowing effects. It is more profound in the acquired images from ETD, mainly due to BSEs as they provide enhanced compositional contrast between the solid composite and the pores. The shadowing artefact occurs mostly in the lower region of ROI, and is caused by the walls of the U-shaped trench that isolate the sample volume. This wall acts as obstacles in the ejected electron's trajectories from the lower section of ROI. Therefore, a relatively large trench around the sample volume of interest will reduce the shadowing effect on the imaging plane. The cut was reasonably large in order to enhance the quality of the SEM images and also to maximize the field of view. Figure 4.12 shows the dimension of the trench milled in this study to eliminate the same artefact by providing enough free space for the electron to travel to the detectors. Additionally, the large trenches are to remove adjacent material that could affect the number of electrons entering the detector. However, it is time consuming to mill away a relatively large section of the material especially when the material is hard, thick and poorly conductive. Thus, in this study across all samples trench sizes varied from 80 × 60 μm^2 to 100 × 100 μm^2 and were made depending on the thickness of the cycled Si electrodes.

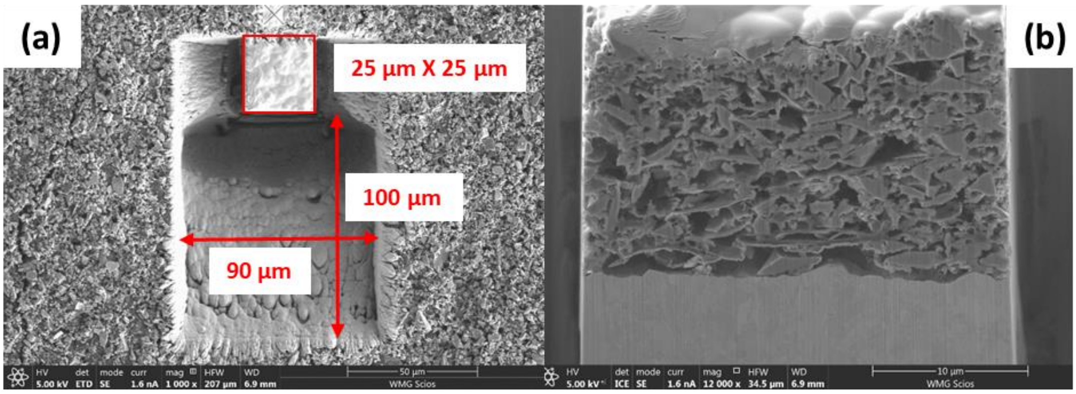

Figure 4.12: (a) The dimension of the trench milled used in this study and (b) cross-sectional SEM image without any illumination effect.

Additionally, the edge charging effect is more prominent in highly porous materials such as battery electrodes. The issue was addressed by limiting the incident electron's intensity through lower accelerating voltage and beam current for every electron imaging after sequential milling. Thus in this study across all the samples acceleration voltage of 3 kV and a probe current of 1.6 nA were used with 25 µs dwell time for electron imaging.

During FIB milling with the application of high ion beam current can cause implantation of the Ga^+ ions into the sample, which in turn may lead to surface defects and topography alteration. Identical effects can occur through FIB imaging and gas deposition. To minimise these potential effects, the surface of the interested volume is protected by coating a layer of platinum up to 1 µm. This is assumed to be adequate for any electron charging and also any further potential damage. The interaction volume between the Ga^+ ions and the sample is small in comparison to electrons. The Ga^+ ions accelerated at 30 kV voltage can penetrate up to tens of nanometers into the sample's surface in comparison to micrometers from electrons under the same accelerating voltage[270,271]. Therefore, the platinum coating of 1 µm in thickness protects the ROI from any damage induced by the ion beam. Additionally, a lower ion beam current of 1nA was used during FIB milling for tomography to minimise the ion dose[272]. During tomography even though the freshly formed cross-section is still under the protection of platinum coating, there is minimal contamination of the cross-sectional surface due to the smaller contact angle.

The U-shaped cut around the platinum layer was initially made with a 30 nA ion beam current. But the ion beam current was sequentially reduced to 7 nA, 3nA and then 1 nA to polish the sides on the selected volume of interest.

4.3.7.3 SECTIONING AND IMAGING AUTOMATION

In this study the 3D data sets were collected automatically using ‘slice and view’ software (FEI) where images were recorded using multiple detectors after each slice milled by the FIB (see Figure 4.13). An ion beam voltage of 30 kV and an electron beam voltage of 1 kV was used throughout. For generating the 3D volume of data, an ion beam current of 1 nA was used to cut 50 nm thick slices contained in a typical data stack. SEM images were captured after every slice with 25 µs dwell time and using multiple detectors. The detectors used for this study was the Everhart-Thornley Detector (ETD) and the Ion Conversion and Electron (ICE) detector for secondary electrons. For the Si-MOF anode electrodes, 200 consecutive cross-section images were obtained for a reconstructed volume of 3000 µm^3 and 300 cross-section images were obtained from the Si-FLG electrodes corresponding to a reconstructed volume of 3000 µm^3. For the Si-Sn anode electrodes, 300 consecutive cross-section images were obtained for a reconstructed volume of 1500 µm^3. The total 3D reconstructed volume is analysed to measure the volume fractions of the solid and pore phase. The pore phase is further analysed as discussed in section 4.3.7.3.

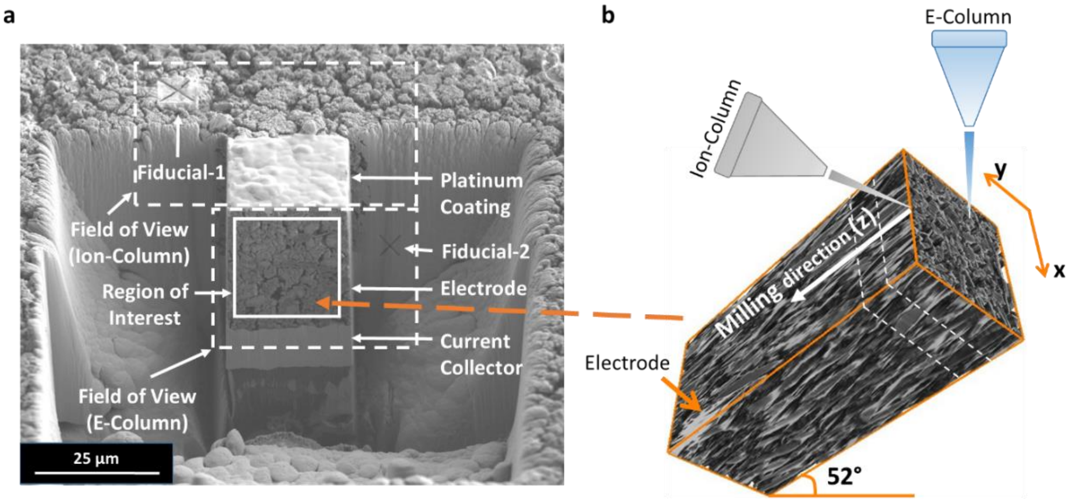

Figure 4.13: a) SEM image of the electrode after the final polishing step with two fiducial markers, (b) schematic diagram representation of FIB-SEM imaging process.

4.3.7.4 IMAGE PROCESSING

The reconstructed 3D volume has a lateral (x-y spatial resolution) resolution between 16 nm to 35 nm along with the longitudinal (z spatial resolution) resolution of 50 nm. The spatial distributions of pore phase and solid phase (including the active material, carbonaceous additives, and binder) were then reconstructed. Two fiducial markers were placed inside the field of view to reset any drift that occurs during data collection. Fiducial-1 marker, on the surface of the electrode, was for aligning the ion beam during milling whilst the Fiducial-2 marker in the cross-section was for electron beam alignment. This reduces the amount of misalignment between images, and in this case negated the requirement for a data alignment process. The stack of SEM images were converted into a 3D volume and used to reconstruct both the pore volume and bulk material following the steps described in Figure 4.14. This sequential imaging processing on tomographic dataset can be summarized into four tasks: (i) image correction for correcting experimentally induced artefacts, (ii) segmentation, (iii) visualization, and (iv) quantification.

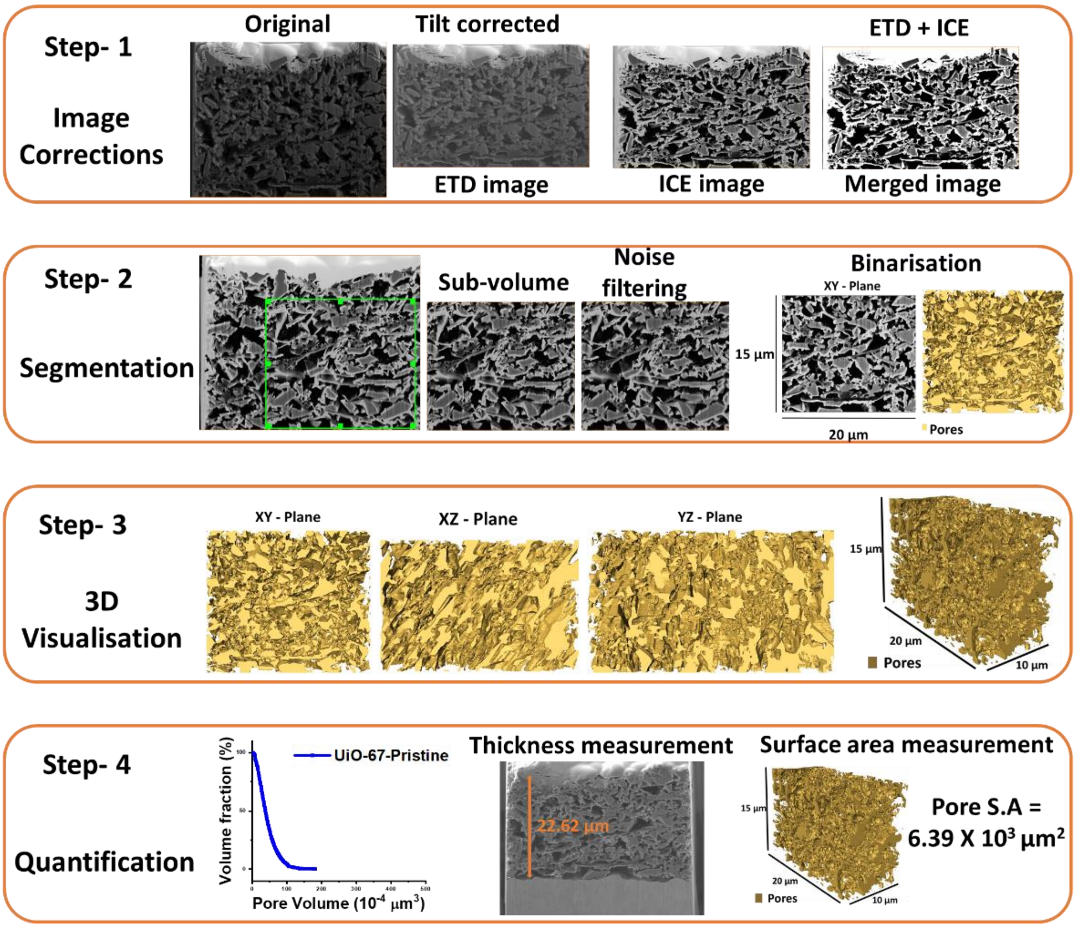

Figure 4.14: Schematic diagram representation of sequential imaging processing on tomographic dataset for UiO-67 pristine electrode.

IMAGE CORRECTION:

Each image following FIB milling is made of voxels (3D pixels), representing the smallest unit volume from the sample. As discussed in section 3.2.3, each of these voxels are anisotropic. The acquired SEM images (in the XY imaging plane) are rectangular instead of square. As discussed in section 3.2.1, the sample stage is inclined at 52º to the electron column with the ion column being perpendicular to the surface (see Figure 4.13b). Thus the acquired images are deviated by an angular factor of cos(38º) from the normal vertical projections. This affects the pixel dimension in the y-direction. To rectify this dimensional issue the acquired y-dimension is to be divided by cos(38º). This rectification can be done in the following two methods: (i) by enabling "Dynamic Focus" function in the microscope controller which takes into consideration the varying focal point of the electron beam on the tilted XY plane[219], and (ii) numerically processing the images using open software such as ImageJ[273], Fiji[274] or in FEI Avizo[219]. In contrast, each thickness slices (in the z-direction) from FIB milling is assumed to be constant. Thus, typically in voxel size the z-directional dimension is greater than the pixel size in the XY imaging plane.

SEGMENTATION:

For faster data analysis, cuboidal sub-volume was extracted from the complete tomographic volume (referred to as region of interest). After extracting sub-volume from the region of interest image filters were applied for making the image smooth and also reducing the background noise in the image. The SEM images from FIB-SEM were initially processed by merging the ETD images and ICE images. They were further processed by histogram equalisation and then by median noise filtering. The processed image sequences were binarised by threshold segmentation process, where greyscale of the images was utilized to separate the solid phase from the porous phases (see Figure 4.15). The image segmentation is generally performed on the basis of different contrast from the constituent phases or elements within the sample. In this study, the image generated after filtering was a smooth image with sharp edges that was subsequently converted to a binary image (white and brown) by applying threshold segmentation in Avizo (FEI). The brown represents pores and white the solid phase, *i.e.* silicon, carbonaceous materials, binder, and additive. There is no manual segmentation involved, a process which in addition to being labour intensive could add a bias to the data analysis.

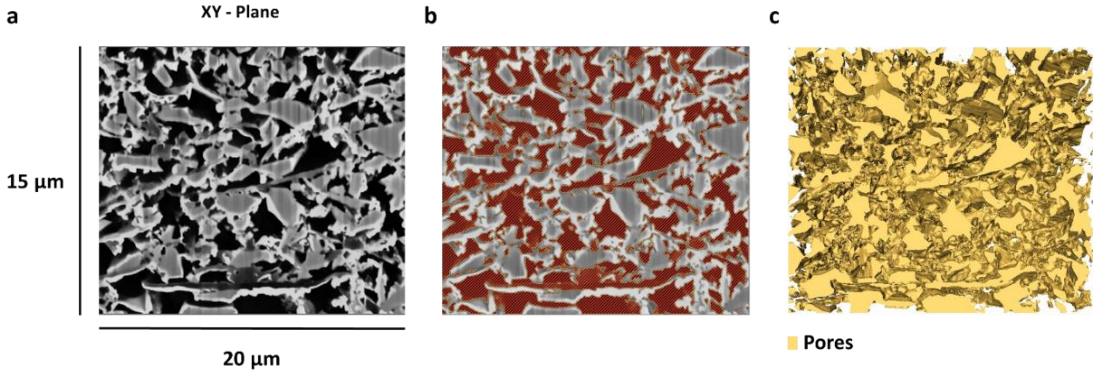

Figure 4.15: (a) XY-plane image slice for UiO-67 pristine electrode, (b) pore phase is highlighted as red, (c) result after the segmentation.

VISUALISATION:

After the segmentation process to visualize in 2D (Figure 4.16a-c), ortho-slices mode was selected in using FEI Avizo software. Similarly, to visualize the segmented object in 3D (Figure 4.16d) volume rendering mode was selected.

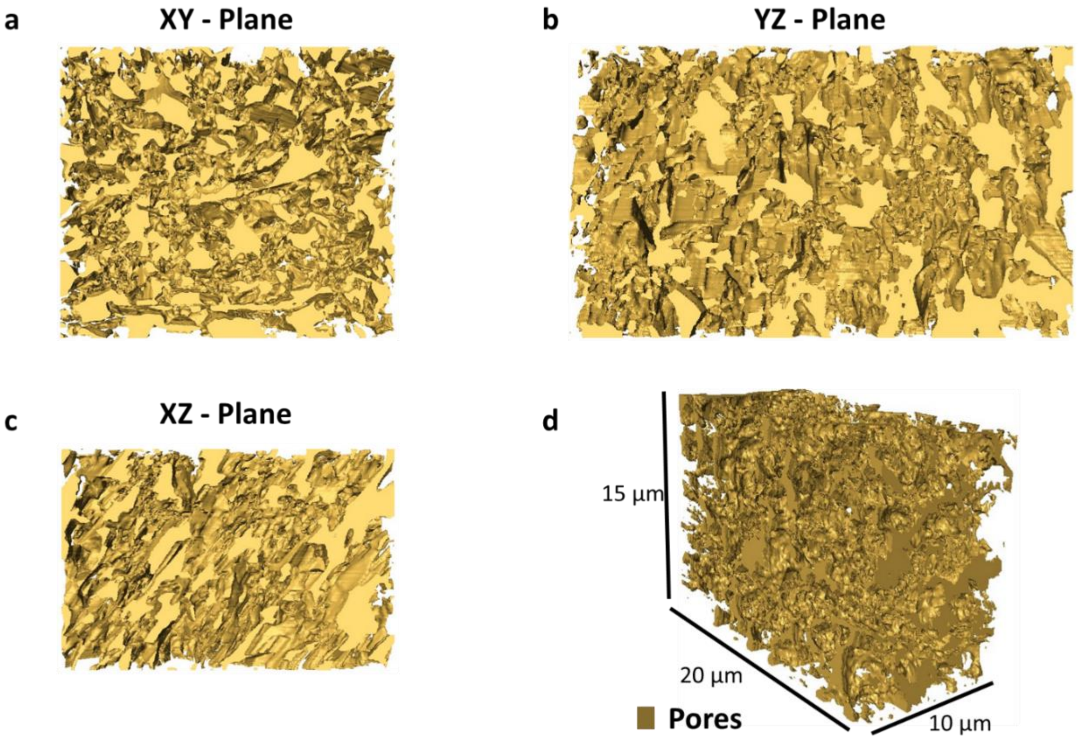

Figure 4.16: 3D volume rendering of pore phase volume of 20 × 15 × 10 µm^3 for UiO-67 pristine electrode.

QUANTIFICATION:

From the reconstructed 3D volume, analysis on phase volume, electrode thickness and surface area were made using Avizo (FEI) whereas tortuosity was calculated by open source *TauFactor*. *TauFactor* was employed within MATLAB for simulation of τ, where the binary segmented 3D reconstructed volume was the input[275].

4.3.7.5 REPRESENTATIVE VOLUME ELEMENT (RVE) ANALYSIS

For reconstructing a statistically significant volume to compute geometrical parameters (such as porosity, pore surface area, and tortuosity), the largest possible cuboid volume was chosen as a region of interest across all the tomographic dataset.

However, to ensure that the selected region of interest is a representative of the whole electrode, representative volume element (RVE) analysis was carried out for porosity as a geometrical parameter of interest. The electrode constituent's morphology and physical properties determine the size of the RVE. In this study, this RVE was estimated by systematically analysing the influence of volume size on porosity as a parameter of interest (see Figures 4.17a and 4.17b). Additionally, consistency of area selection was considered in performing tomography on the material at the centre for all the electrodes in the whole study.

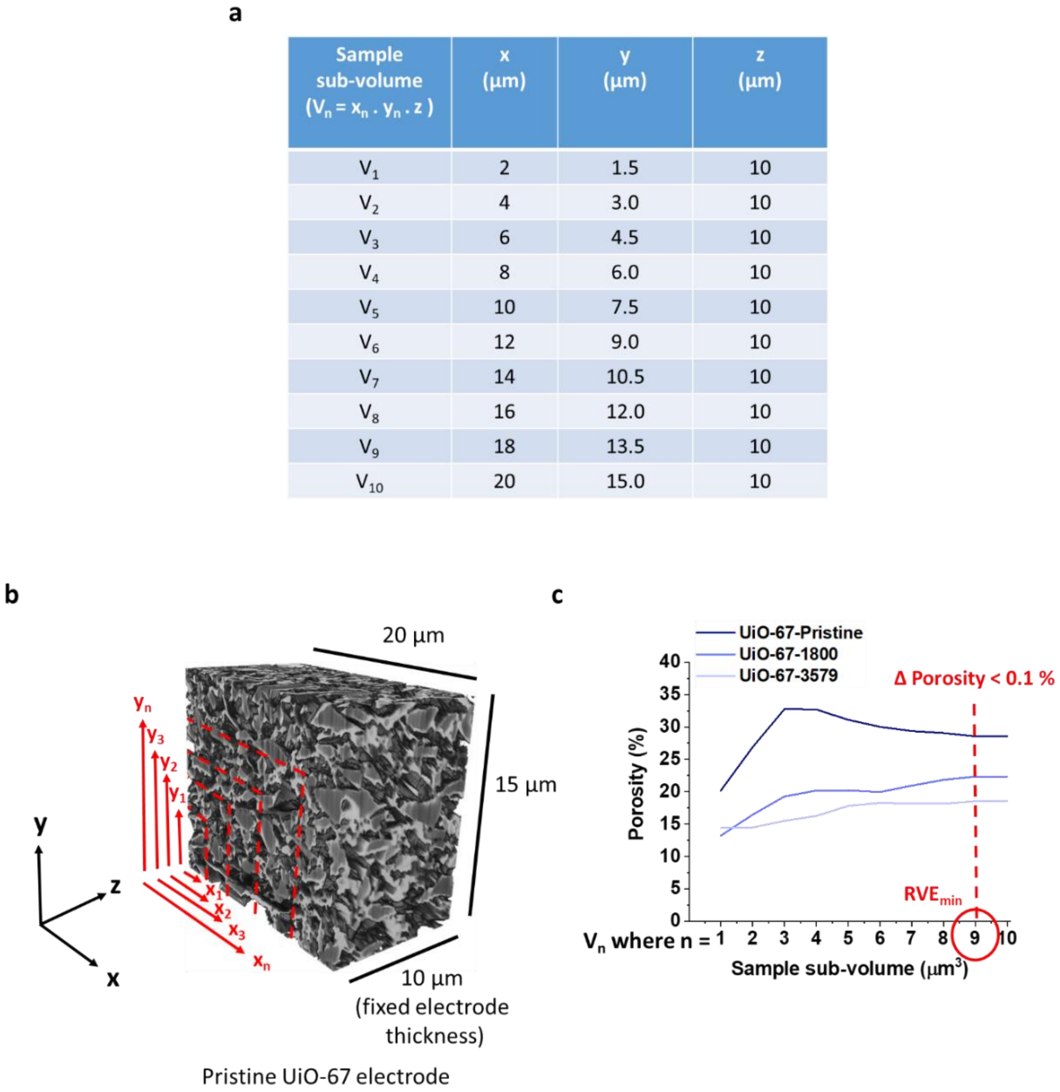

a

Sample sub-volume ($V_n = x_n \cdot y_n \cdot z$)	x (µm)	y (µm)	z (µm)
V_1	2	1.5	10
V_2	4	3.0	10
V_3	6	4.5	10
V_4	8	6.0	10
V_5	10	7.5	10
V_6	12	9.0	10
V_7	14	10.5	10
V_8	16	12.0	10
V_9	18	13.5	10
V_{10}	20	15.0	10

Pristine UiO-67 electrode

Figure 4.17: (a) The dimensions of sub-volumes of UiO-67 electrodes analysed for representing the minimum RVE (RVE_{min}), (b) Schematic diagram representation of RVE analysis by increasing the electrode sub-volumes in x and y-direction and keeping the thickness fixed (z-direction), (c) Relationship between porosity and volume size and estimation of RVE_{min}.

As seen from Figure 4.17c, the minimum RVE is 18 × 13.5 × 10 μm^3 Si-MOF electrodes, as after this point the volume size has insignificantly influenced porosity and is seen as a distinctive flat distinct plateau. The change in porosity after this point was less than 0.1 %. However, for better representation of the bulk electrode, the whole volume of 20 × 15 × 10 μm^3 was analysed.

Similarly, for Si-graphene formulations, the calculated minimum RVE is 18 × 9 × 15 μm^3, as after this point change in porosity is minimal with increasing volume size (see Figure 4.18). The change in porosity after RVE$_{min}$ was less than 0.5 % and a distinctive flat distinct plateau is visible. However, for better representation of the bulk electrode, the whole volume of 20 × 10 × 15 μm^3 was analysed.

a

Sample sub-volume ($V_n = x_n \cdot y_n \cdot z$)	x (μm)	y (μm)	z (μm)
V_1	2	1	15
V_2	4	2	15
V_3	6	3	15
V_4	8	4	15
V_5	10	5	15
V_6	12	6	15
V_7	14	7	15
V_8	16	8	15
V_9	18	9	15
V_{10}	20	10	15

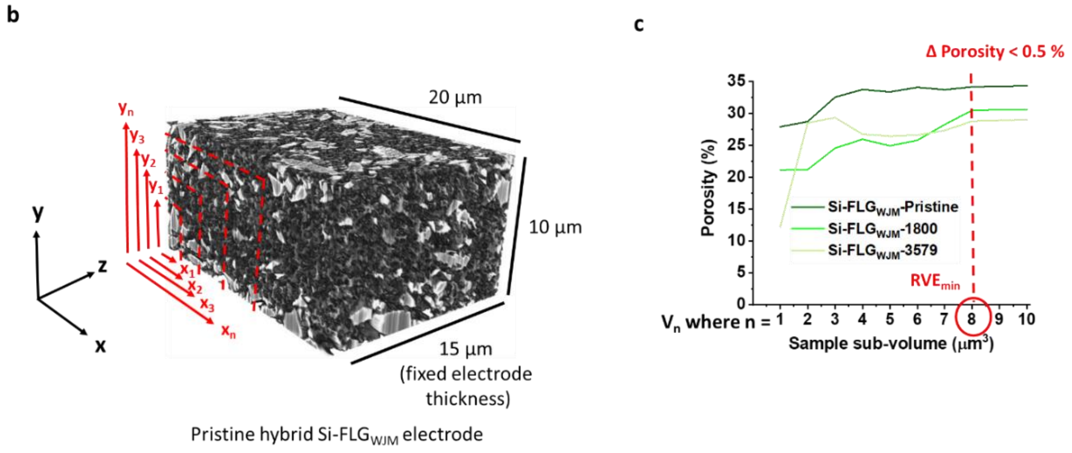

Figure 4.18: (a) The dimensions of sub-volumes of hybrid Si-FLG$_{WJM}$ electrodes analysed for representing the RVE$_{min}$, (b) Schematic diagram representation of RVE analysis by increasing the electrode sub-volumes in x and y-direction and keeping the thickness fixed (z-direction), (b) Relationship between porosity and volume size and estimation of RVE$_{min}$.

Furthermore, for Si-Sn formulations, the calculated minimum RVE is 18 × 4 × 15 μm^3, as after this point change in porosity is minimal with increasing volume size (see Figure 4.19). The change in porosity after RVE$_{min}$ was less than 0.5 % and a distinctive flat distinct plateau is visible. However, for better representation of the bulk electrode, the whole volume of 20 × 5 × 15 μm^3 was analysed.

a

Sample sub-volume ($V_n = x_n \cdot y_n \cdot z$)	x (μm)	y (μm)	z (μm)
V_1	2	0.5	15
V_2	4	1.0	15
V_3	6	1.5	15
V_4	8	2.0	15
V_5	10	2.5	15
V_6	12	3.0	15
V_7	14	3.5	15
V_8	16	4.0	15
V_9	18	4.5	15
V_{10}	20	5.0	15

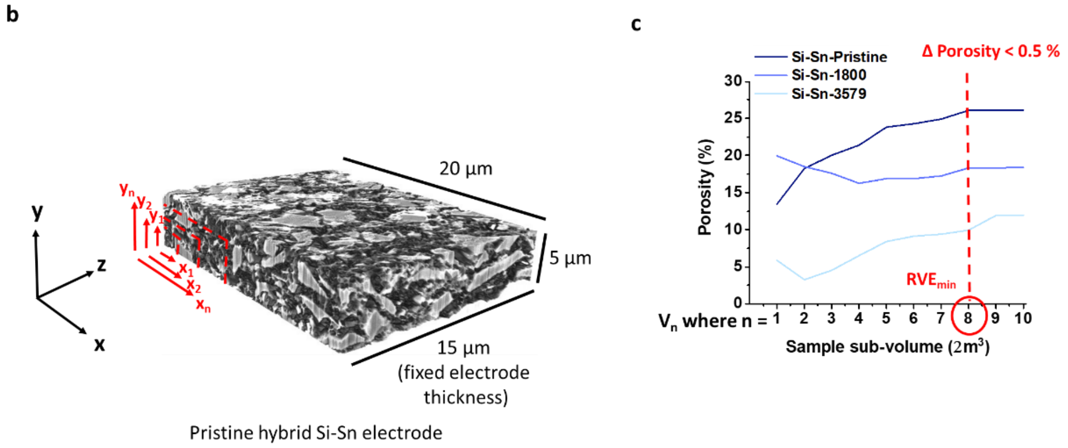

Figure 4.19: (a) The dimensions of sub-volumes of hybrid Si-Sn electrodes analysed for representing the RVE$_{min}$, (b) Schematic diagram representation of RVE analysis by increasing the electrode sub-volumes in x and y-direction and keeping the thickness fixed (z-direction), (b) Relationship between porosity and volume size and estimation of RVE$_{min}$.

CHAPTER 5. POROUS METAL-ORGANIC FRAMEWORKS FOR ENHANCED PERFORMANCE SILICON ANODES IN LITHIUM-ION BATTERIES

Maintaining the physical integrity of electrode microstructures in Li-ion batteries is critical to significantly extend their cycle life. This is especially important for high capacity anode materials such as silicon, whose operational volume expansion exerts huge internal stress within the anode, resulting in electrode destruction and capacity fade. This study demonstrate that by incorporating metal-organic frameworks (MOFs) with carboxylate organic linkers into Si-based anodes, a stable and flexible pore network is generated to maximize and maintain Li^+ ion flux throughout the electrode's architecture. This study shows that the zirconium carboxylate MOF UiO-67 is a versatile co-material to boost performance and mitigate the rate of anode degradation that presently limits the lifetime of Si anodes. The cage-like pores in UiO-67 and flexural properties of the 4, 4'-biphenyldicarboxylate organic linker are proposed to create robust "ionophores" in the anode film to enhance longer-term durability and performance.

5.1 MOTIVATION TO INCORPORATE MOFs AS AN ADDITIVE

Attempts to circumnavigate the problems associated with silicon (as discussed in section 2.2) have broadly used two distinct approaches. The first involves the modification of the silicon morphology, including amorphous thin films[126,127], nanowires, macro-porosity, nano-sized silicon particles[78] and surface coatings[116]. The second approach focuses on the development of hybrid silicon anodes and includes composite development with variation in the silicon content, morphology, composite composition, preparation techniques, and dispersion methods. Additives include lithium-inactive materials[55], lithium-active materials[55], and various binder systems[55, 56, 57] as well as combining silicon with carbon materials[53]. However, the highly complex synthesis methods along with excessive manufacturing cost of these materials still poses practical questions for real applications.

In this chapter, an investigation into how the electronic and ionic conductivity of silicon anodes may be optimised by incorporating metal-organic frameworks (MOFs) alongside carbon hierarchies. This study reveals the beneficial effect of adding the structurally flexible MOF component to the composite, demonstrating improved mechanical properties via modification of the porosity. MOFs are a class of crystalline porous materials and have a unique combination of physical properties, namely high specific surface area, organic functional linkers and metal sites[276], and with evidence pointing towards their application as electrode materials for electrochemical devices[162, 163, 164]. The tuneable pore structures and functional redox-active components of MOFs may conceivably make it possible for Li^+ ions to travel more homogenously through the anode[277].

The practical use of redox-active MOFs in lithium-ion batteries (LIBs) as the primary Li host material is unrealistic for several reasons, namely, the low density, limited Li^+ ion insertion capability, poor electronic conductivity, and irreversible structural modification over multiple cycles[164]. The rationale is to explore and understand MOFs for LIBs, as flexibility and porosity enhancing additives. The robust zirconium carboxylate MOFs, UiO-66 and UiO-67 were selected with the dual purpose of improving and maintaining the porous networks of the anode whilst enhancing the cohesion of the components. Both MOFs contain carboxylate organic linkers, chosen for the possible esterification reaction between the surface carboxyl groups in both the MOFs and in the polyacrylic acid (PAA binder) with silanol groups on the surface of Si in the electrode system[117]. Certain MOF materials, particularly UiO-66, have emerged as being stable with respect to conditions of temperature, water or other chemical environments. UiO-66 has also been shown to intercalate Li by way of interaction with the aromatic components of the constituent ligands[276].

Pore distribution plays a key role in cell performance through the electrochemical reaction kinetics, as well as the electrode’s transport properties[278]. Impedance spectroscopy and physical characterisation are used to capture and quantify the evolution of internal morphology and the build-up of resistance.

5.2 RESULTS AND DISCUSSION

To understand the benefits of MOFs a systematic study was carried out by comparing MOF-modified anodes with control formulations (ZrO_2 and without any additive). ZrO_2 was chosen as an electrochemically inert ceramic additive, containing the same chemical elements as the two MOFs (UiO-66 and UiO-67), whilst a conventional conductive additive, synthetic flake graphite (SFG-6, TIMCAL C-NERGY) in place of MOF additives. The formulation ratio of electrode slurry used was Si: binder: carbon-mixture: additive: 70:7:11:12 (wt.%). The reader is requested to refer to section 4.1.4.1 (Figure 4.4) for formulation details.

5.2.1 MATERIALS CHARACTERISATION

5.2.1.1 THERMOGRAVIMETRIC ANALYSIS (TGA)

Figure 5.1 shows the thermograms obtained for the all the formulations. Data were recorded in nitrogen atmosphere to eliminate any oxidation of the copper in the electrodes, which otherwise results in a large mass loss above 500 °C in air. The additional mass loss in the electrodes that contain the MOFs correlates with the TGA signature of the pure MOFs.

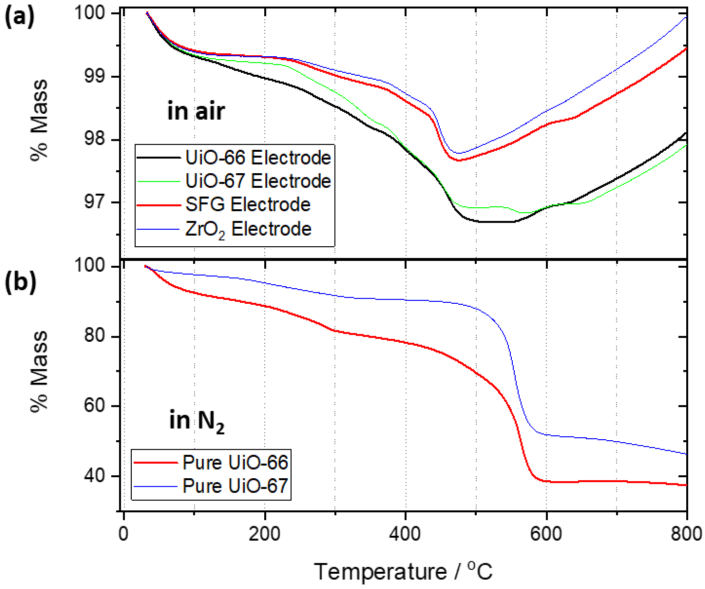

Figure 5.1: Thermogravimetric analysis data of all electrodes with data from UiO-66 and UiO-67 plotted for comparison. TGA carried out in (a) air for all electrodes and (b) N_2 atmosphere for MOF powders.

5.2.1.2 X-RAY POWDER DIFFRACTION (XRD)

As observed in Figure 5.2 the XRD peaks confirms the as-synthesised UiO-66 and UiO-67 MOF powders from the literature.

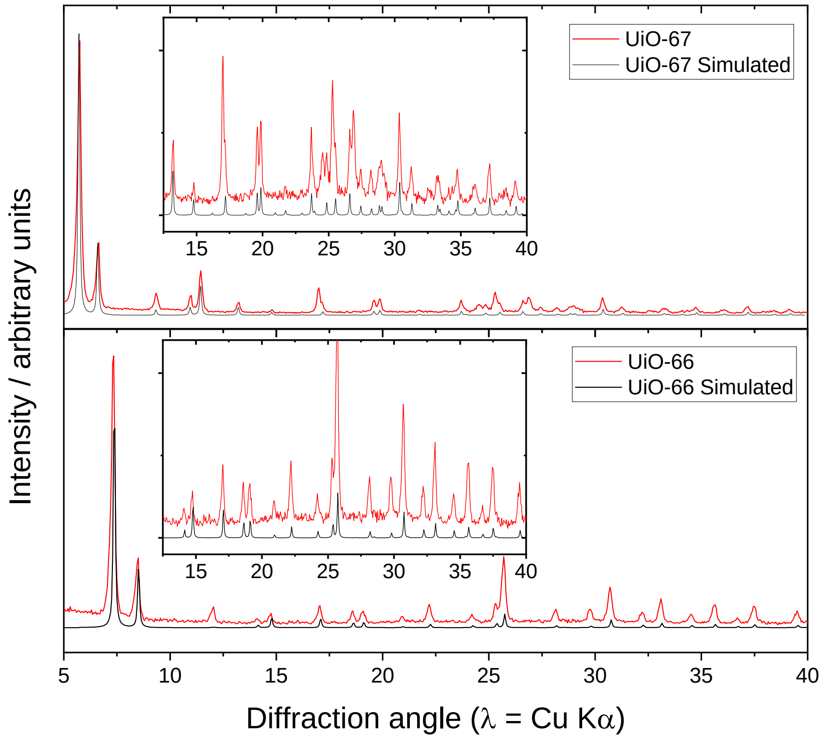

Figure 5.2: Powder XRD of as-synthesised UiO-66 and UiO-67 compared to simulated patterns from the literature.[279]

From Figure 5.3, the MOF electrodes post electrochemical cycling were compared to the pristine electrodes to understand their behaviour upon electrochemical cycling. As observed, the intensity peaks corresponding to MOFs have decreased after cycling indicating MOFs as electrochemically active species in the electrode. Further electrochemical analysis of MOFs is discussed in section 5.2.3.

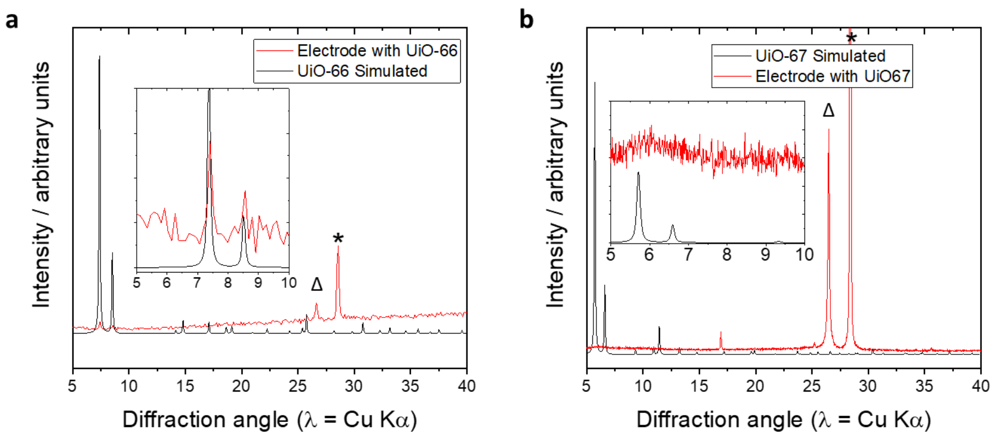

*Figure 5.3: Powder XRD of (a) cycled UiO-66 electrode compared with simulated pattern of UiO-66 and (b) cycled UiO-67 electrode compared with simulated pattern of UiO-67. Red line denotes cycled electrode. (Δ denote carbon and * denote silicon).*

5.2.1.3 STRUCTURE AND ELECTRODE FLEXIBILITY TEST

UiO-66 consists of $[Zr_6O_4(OH)_4]^{12+}$ metal nodes connected by 1,4-benzenedicarboxylate organic linkers, forming an open-framework containing two distinct cages, tetrahedral and octahedral, with pore diameters of 0.85 nm and 1.15 nm, respectively[184,185] (see Figure 5.4a). UiO-67 has an isoreticular structure except that it is connected by the more extended biphenyl-4, 4'-dicarboxylate linkers forming tetrahedral and octahedral pores with diameters 1.15 nm and 2.15 nm, respectively[184] (see Figure 5.4b). Figure 5.4c shows a plot of depth *vs* load from nano-indentation tests. Hardness and Young's modulus are calculated using data taken from the slope of the tangent to the unloading curve, summarised as Table 5.1. Young's modulus is an intrinsic property of the material and it can be observed from Table 1 that the formulation with UiO-67 shows diminished reduced Young's modulus in comparison to other additives. Therefore, it can be postulated that the UiO-67 provides an effective inclusion to accommodate volume expansion stresses from silicon upon cycling. In comparison to UiO-66[280], there is enhanced performance from maintaining the structural integrity of the electrode with UiO-67, as observed in electrochemical cycling data (see Figure 5.7).

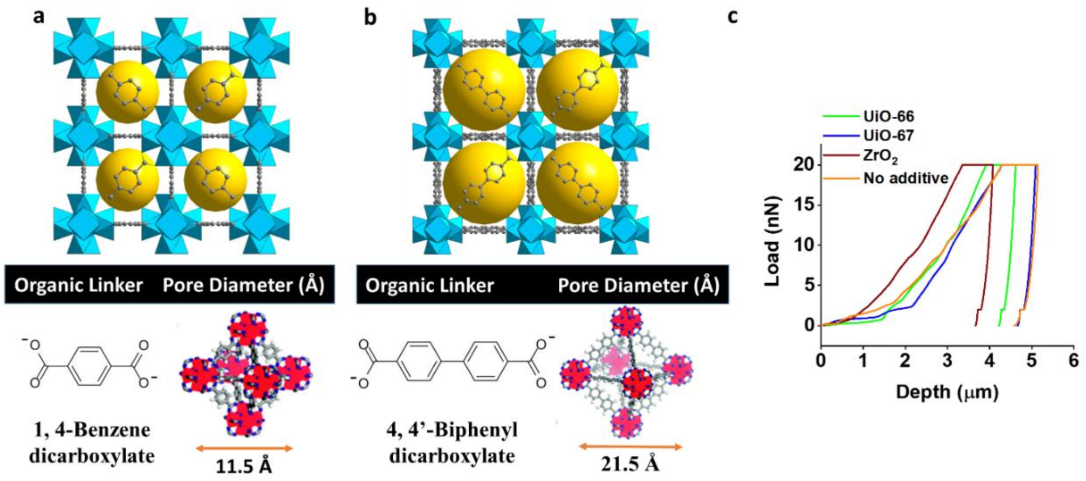

Figure 5.4: MOF structures and tensile property of all 4 formulations. Crystal structures of the MOFs (a) UiO-66 and (b) UiO-67; (c) tensile curves from nano-indentation test. In (a) and (b) the blue polyhedral represent Zr-centred oxy coordination polyhedra, and the yellow spheres represent the maximum free pore space.

Table 5.1: Maximum contact depth, hardness and Young's modulus achieved from nano-indentation tests.

Additive	**Maximum Depth (μm)**	**Hardness (GPa)**	**Reduced Young's Modulus (GPa)**
UiO-66	4.62±0.20	0.041±0.003	4.00±0.25
UiO-67	5.04±0.50	0.035±0.007	3.92±0.80
ZrO_2	4.08±0.20	0.053±0.005	5.09±0.39
No additive	5.11±0.19	0.033±0.002	3.55±0.38

5.2.2 MORPHOLOGY

Figure 5.5 shows the distribution of silicon, MOFs and carbonaceous particles in the electrode slurry prepared after drying as seen by scanning electron microscopy (SEM). The SEM images reveal the morphology and size of the electrode particles and the homogeneous distribution of silicon particles, MOFs in carbon network. The average size of silicon particles is 3 µm along with MOF particles sizes ca. 200 nm. SEM images shows that the MOFs in the electrodes have formed a hierarchical network between the Si, GNPs, graphite, carbon nanotubes and carbon black. The carbon mixture with GNPs is for long-range planar conductivity, graphite for bulk conductivity while carbon black serves for short-range conductive pathways between particles[58]. As observed in Figure 5.6, the EDS mapping confirms presence of Zr-based MOFs in the electrode slurry.

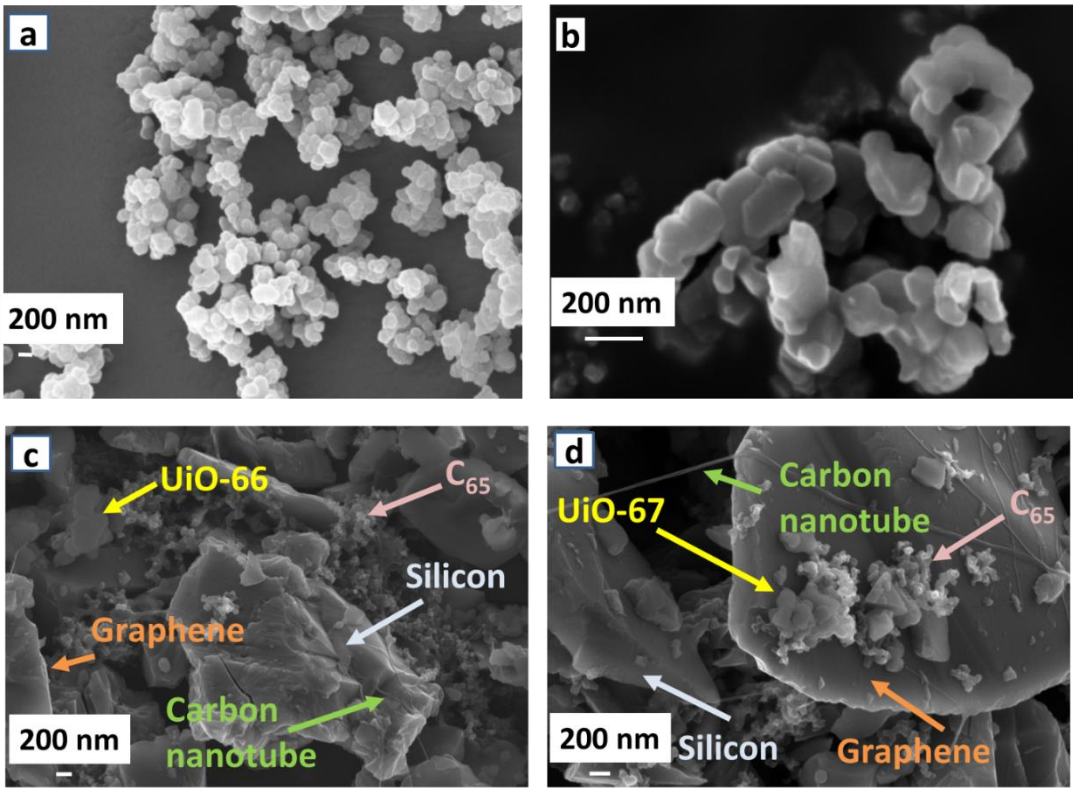

Figure 5.5: SEM images of (a) only UiO-66 MOF powder; (b) only UiO-67 MOF; (c) UiO-66 in Si electrode; and (d) UiO-67 in Si electrode.

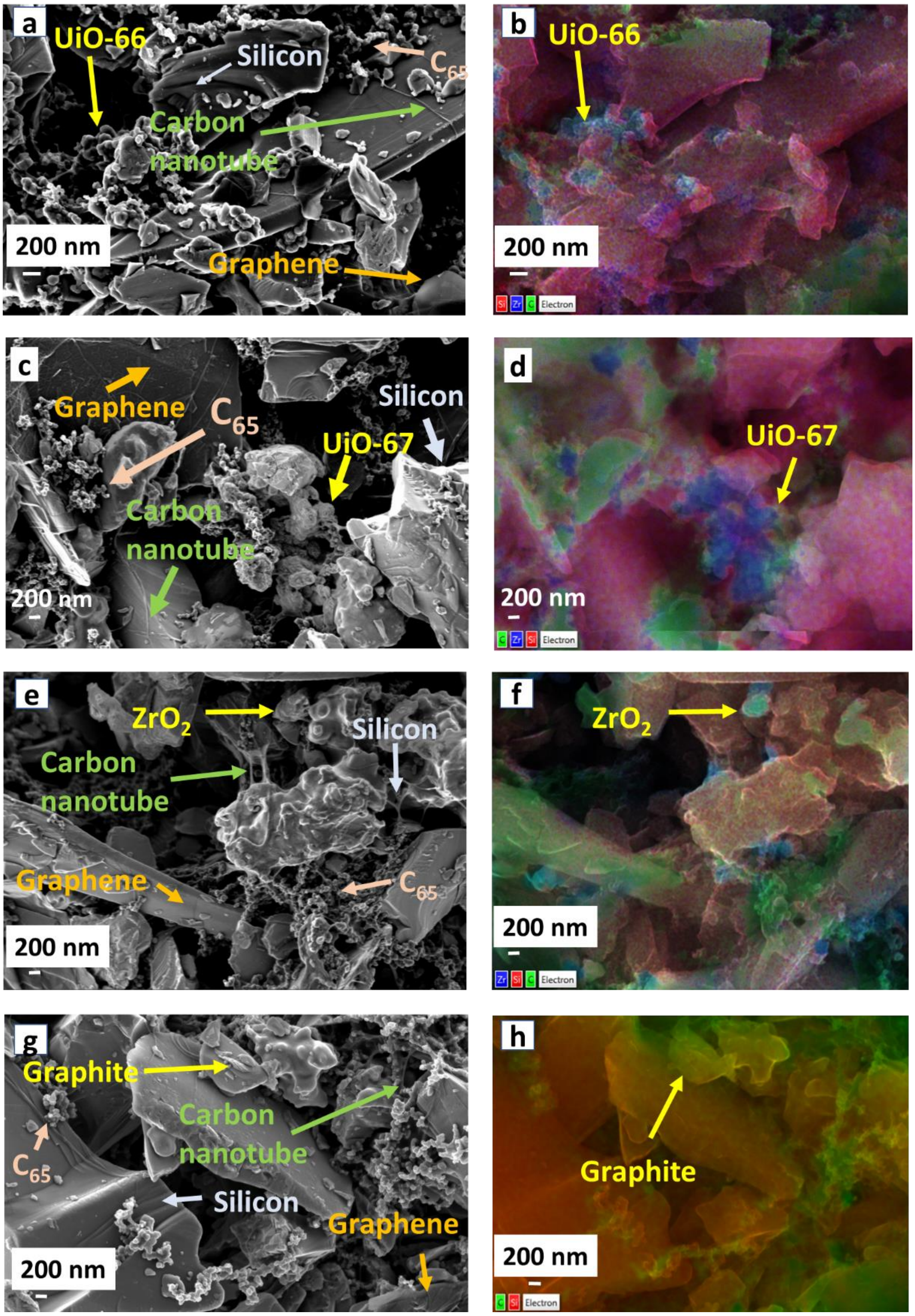

Figure 5.6: SEM images of (a,b) UiO-66 in Si electrode; (c,d) UiO-67 in Si electrode; (e,f) ZrO_2 in Si electrode; and (g,h) Si electrode with no additive. Energy dispersive spectra (EDS) derived chemical distribution maps showing the presence of Zr-based MOFs (UiO-66 and UiO-67) in the electrode slurry as shown in (b and d, respectively).

5.2.3 ELECTROCHEMICAL CYCLING PERFORMANCE

Galvanostatic cycling results are plotted in Figure 5.7. Cells were cycled at the full capacity of silicon and also at lower capacity limits to compare the effects of these additives towards capacity retention and cycle life. From Figure 5.7a and 5.7b it can be observed that the capacity of the cell decreases over longer cycling, as expected for such devices. The cells cycling at the full experimental capacity of silicon show obvious capacity fade effects after 70 cycles (Figure 5.7a) whilst for the cells cycling at the half experimental capacity of silicon it is prolonged to more than 90 cycles (Figure 5.7b). The main reason for this effect can be attributed to breaking down and continual growth of SEI, which in turn results in pore clogging and an increased resistance for Li^+ ion movement.[65,281] From the cycling profiles, it is evident that incorporation of the MOFs in the Si anode has a significant positive effect on stabilising the electrode. Furthermore, the capacity fade is delayed as the capacity limit is reduced from 3579 mAh g^{-1} to 1800 mAh g^{-1} and then further to 1200 mAh g^{-1}. The fact that UiO-67 shows superior additive properties in comparison to UiO-66 could be attributed to an increased innate structural flexibility (owing to the nature of the more extended organic linker: see below for a description of the structure) and larger pore size (see Figure 5.4a and 5.4b). This could allow freer movement of Li^+ ions throughout the bulk of the electrode material by a small reduction in tortuosity. In this sense these pores also help to maintain sufficient void structure around the active particles, providing “porous network” to the electrode architecture. This is evident from the cell with UiO-67 cycling at the half capacity limit of silicon.

In Figure 5.7b, it can be shown how the anode with UiO-66 also outperformed the non-modified anode before starting to degrade after 40 cycles. This could be related to the smaller pore sizes (compared to UiO-67) and relatively rigid framework resulting in higher tortuosity for Li^+ ion transport and thus increasing cell resistance. From Figure 5.7c it is seen that all the formulations cycled reversibly up to 100 cycles with 1200 mAh g^{-1} capacity limit. However, the UiO-67 additive has better longevity compared to UiO-66. In order to understand lithium interaction with the MOFs used within the same cut-off voltages, MOF-dominant electrodes were prepared from 80 % MOF, 10 % binder and 10 % carbon black. It can be observed from Figure 5.7d that UiO-66 can contribute about 271.67 mAh g^{-1} while UiO-67 contributes to 387.34 mAh g^{-1} with a large first cycle loss of 242.92 mAh g^{-1} and 354.58 mAh g^{-1}, respectively. The reversible capacity obtained from the MOF- dominant electrodes was lower than reported in a previous study[276] and this is due to the different operating voltage cut-offs. Tang *et al.*[276] cycled UiO-66 cells between 0.01 V to 3 V *vs* Li/Li$^+$ whereas in this study the cells were cycled between 0.05 V to 1 V *vs* Li/Li$^+$.

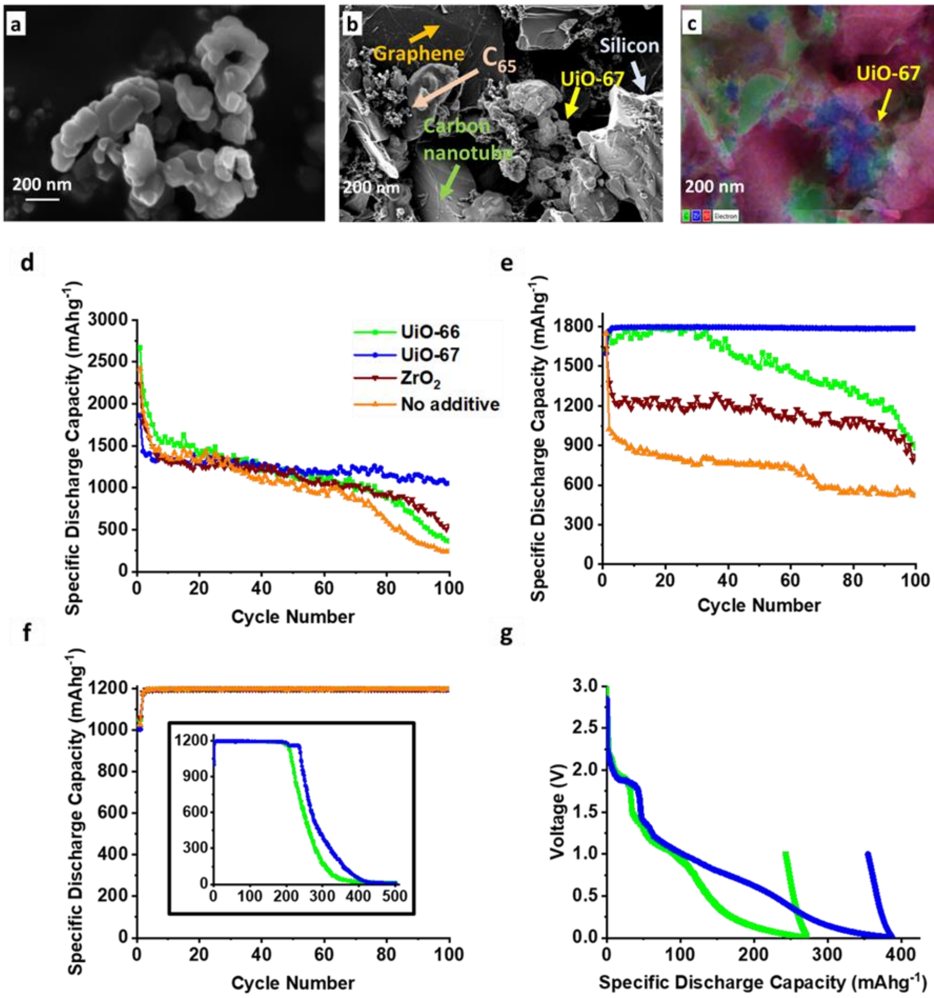

Figure 5.7: SEM images and specific discharge capacity (based on active mass of silicon) profiles at the different capacity limits. SEM image of (a) only UiO-67 MOF; (b,c) UiO-67 in Si electrode with energy dispersive spectra (EDS) derived chemical distribution maps showing the presence of Zr-based MOF (UiO-67) in the electrode slurry as shown in (c); specific discharge capacity (based on active mass of silicon) profiles at the different capacity limits. Specific discharge capacity at (d) full capacity of silicon (3579 mAh g^{-1}) (e) half capacity of silicon (1800 mAh g^{-1}) (f) one-third capacity of silicon (1200 mAh g^{-1}) (longer cycling of Si-MOFs are shown as the inset) (g) first lithiation-delithiation voltage profiles for MOFs. The legends for (d) also applies to (e-g).

Further electrochemical analysis of MOF-dominant electrodes is presented in Figures 5.8 and 5.9. In this study the MOF-dominant electrodes were electrochemically cycled to observe their stability and their electrochemical response under the battery operating conditions. From Figure 5.8, it was noted that the UiO-66 and UiO-67 reversibly contribute to about 28.95 mAh g^{-1} and 31.5 mAh g^{-1}, respectively (which is < 1 % of lithiation capacity of silicon). This study further compared the dQ/dV plot of the Si-MOF electrodes and the electrode without any additive. There was no distinguishable electrochemical response from the MOFs under the operating potentials. Therefore, it can be confirmed that the improved cycling performance of the Si-MOF electrodes is from the physical presence of MOFs. However, they can also act as lithium hosts (see Figure 5.7g) at a current density of 10 mA g^{-1}.

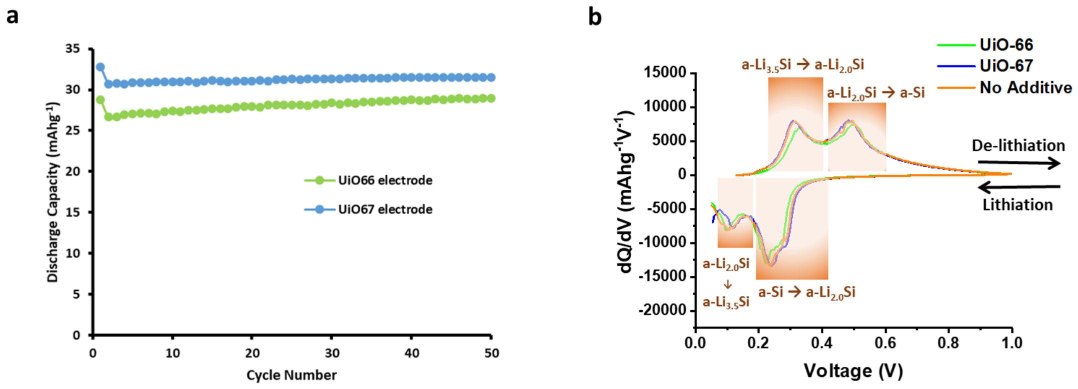

Figure 5.8: (a) Reversible discharge specific capacity for MOFs dominant electrode (80 % MOF, 10 % binder and 10 % carbon black) under a current density of 39 mA g^{-1}. (b) dQ/dV plot for 2nd cycle of UiO-66, UiO-67 and No additive electrode. Presented data are for the cells cycled at full capacity of silicon corresponding to a current density of 716 mA g^{-1}.

From Figure 5.9 it is also observed that with increasing cycle number there is a decrease in peak intensity and also shift in the voltage of the peaks. The above can be attributed to the increase overpotential within the electrode, *i.e.* impedance due to continuum SEI growth and architectural breakdown. After 100 cycles the area beneath the lithiation peaks have decreased by a vast amount for the electrode without any additive. In conclusion, the differential capacity plot of the Si-MOF electrode indicates that flexible MOF frameworks provides stability electrochemically and enhance performance.

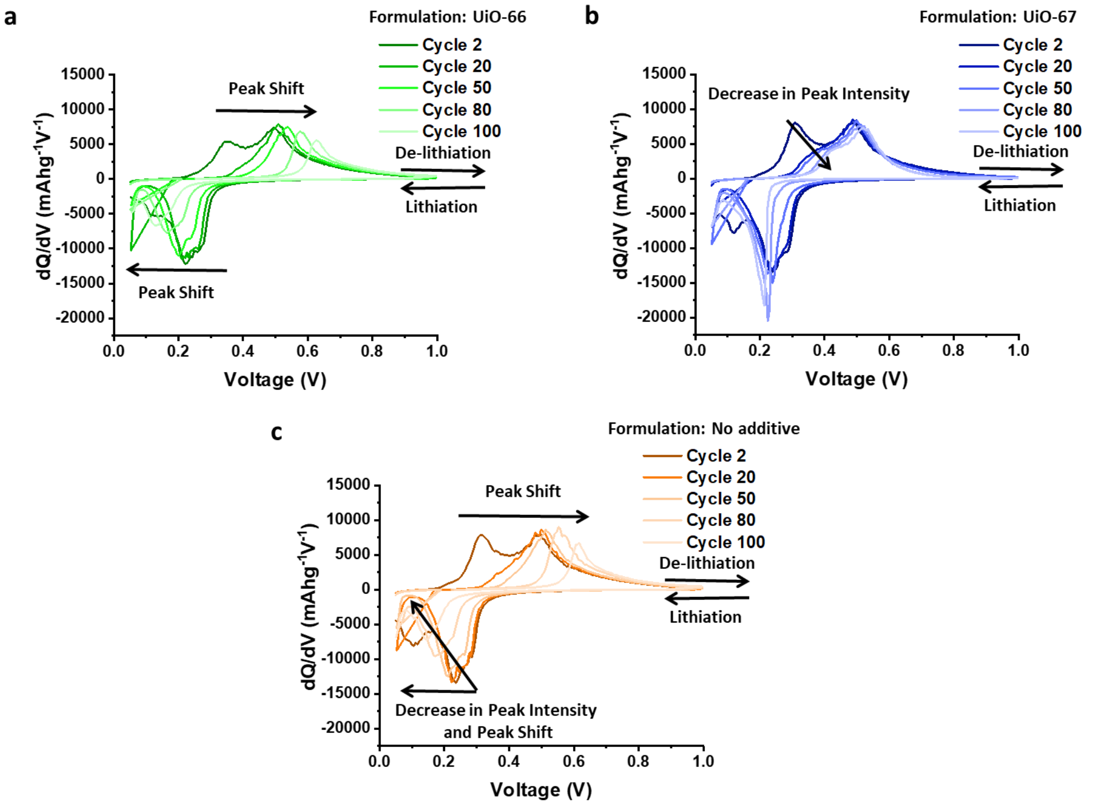

Figure 5.9: dQ/dV plot with incremental cycle numbers for (a) UiO-66, (b) UiO-67, and (c) No additive formulations. Presented data are for the cells cycled at full capacity of silicon corresponding to a current density of 716 mA g^{-1}.

5.2.4 MICROSTRUCTURAL EVOLUTION

Focused ion beam-scanning electron microscopy (FIB-SEM) tomography allows three-dimensional (3D) visualisation and quantification of geometrical parameters such as thickness, pore surface area, phase volume fraction and tortuosity for a better understanding of the cell performance and its microstructural evolution[25]. Tomography was performed on the pristine and aged electrodes (after 100 cycles). The region of interest for samples ranged between 25 × 20 μm^2 to 25 × 46 μm^2; since the cycled electrodes had a variable change in thickness of the electrode. From there a 3D reconstructed volume of 20 × 15 × 10 μm^3 for all the samples were obtained (Figure 5.10 and 5.11). The flexibility from the MOFs, plays favourable towards the electrode's stability and porosity retention during lithiation/de-lithiation.

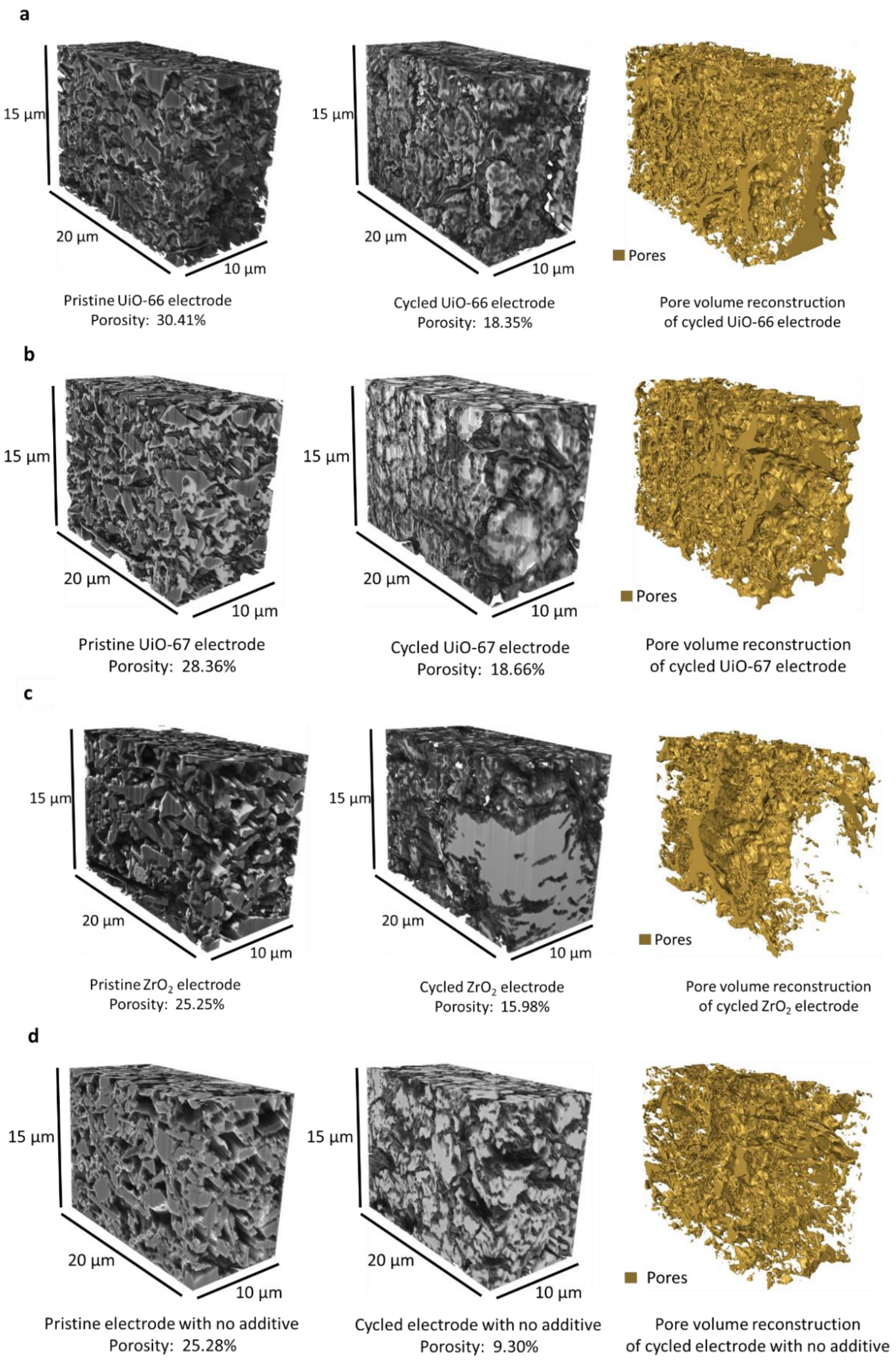

Pristine UiO-66 electrode
Porosity: 30.41%

Cycled UiO-66 electrode
Porosity: 18.35%

Pore volume reconstruction
of cycled UiO-66 electrode

Pristine UiO-67 electrode
Porosity: 28.36%

Cycled UiO-67 electrode
Porosity: 18.66%

Pore volume reconstruction
of cycled UiO-67 electrode

Pristine ZrO_2 electrode
Porosity: 25.25%

Cycled ZrO_2 electrode
Porosity: 15.98%

Pore volume reconstruction
of cycled ZrO_2 electrode

Pristine electrode with no additive
Porosity: 25.28%

Cycled electrode with no additive
Porosity: 9.30%

Pore volume reconstruction
of cycled electrode with no additive

Figure 5.10: 3D FIB-SEM tomography reconstruction of all formulation at full capacity. The greyscale 3D reconstructed volume of the electrode with (a) UiO-66, (b) UiO-67, (c) ZrO2, and (d) no additive, before and after cycling for 100 cycles.

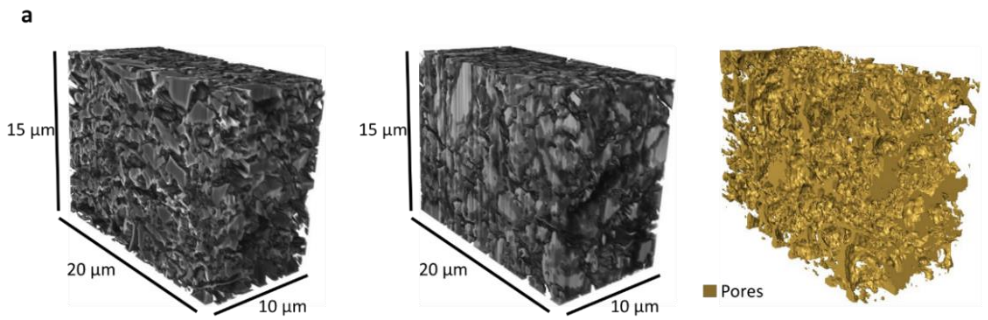

Pristine UiO-66 electrode
Porosity: 30.41%

Cycled UiO-66 electrode
Porosity: 20.94%

Pore volume reconstruction
of cycled UiO-66 electrode

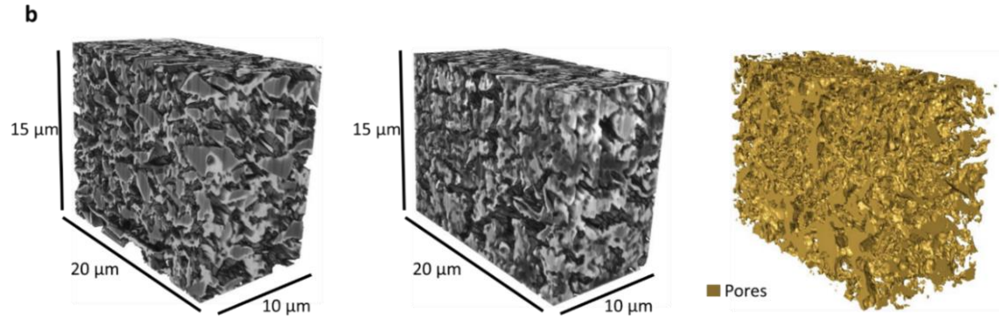

Pristine UiO-67 electrode
Porosity: 28.36%

Cycled UiO-67 electrode
Porosity: 22.25%

Pore volume reconstruction
of cycled UiO-67 electrode

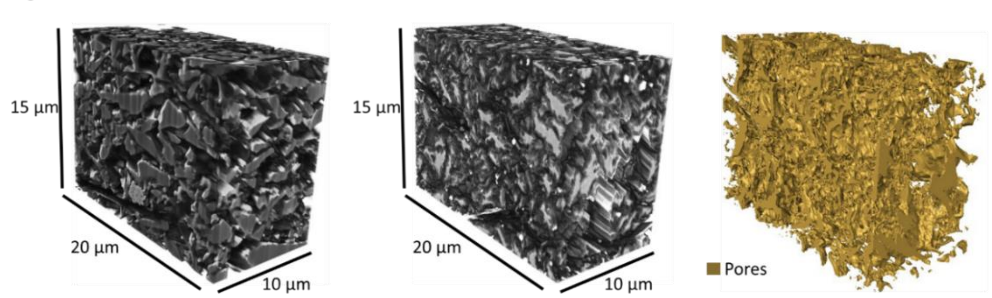

Pristine ZrO_2 electrode
Porosity: 25.25%

Cycled ZrO_2 electrode
Porosity: 18.73%

Pore volume reconstruction
of cycled ZrO_2 electrode

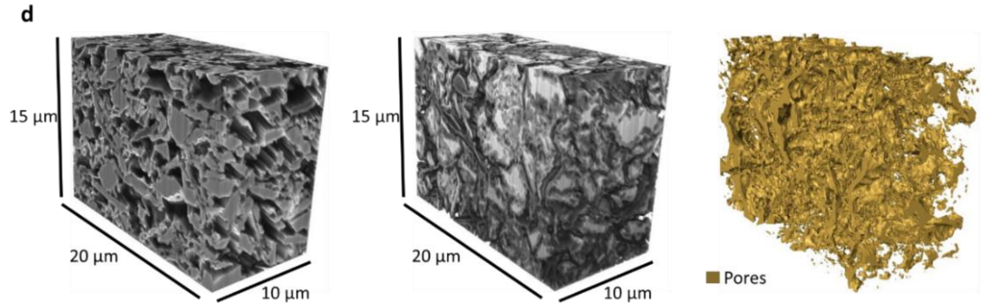

Pristine electrode with no additive
Porosity: 25.28%

Cycled electrode with no additive
Porosity: 13.54%

Pore volume reconstruction
of cycled electrode with no additive

Figure 5.11: 3D FIB-SEM tomography reconstruction of all formulation at half capacity. The greyscale 3D reconstructed volume of the electrode with (a) UiO-66, (b) UiO-67, (c) ZrO2, and (d) no additive, before and after cycling for 100 cycles.

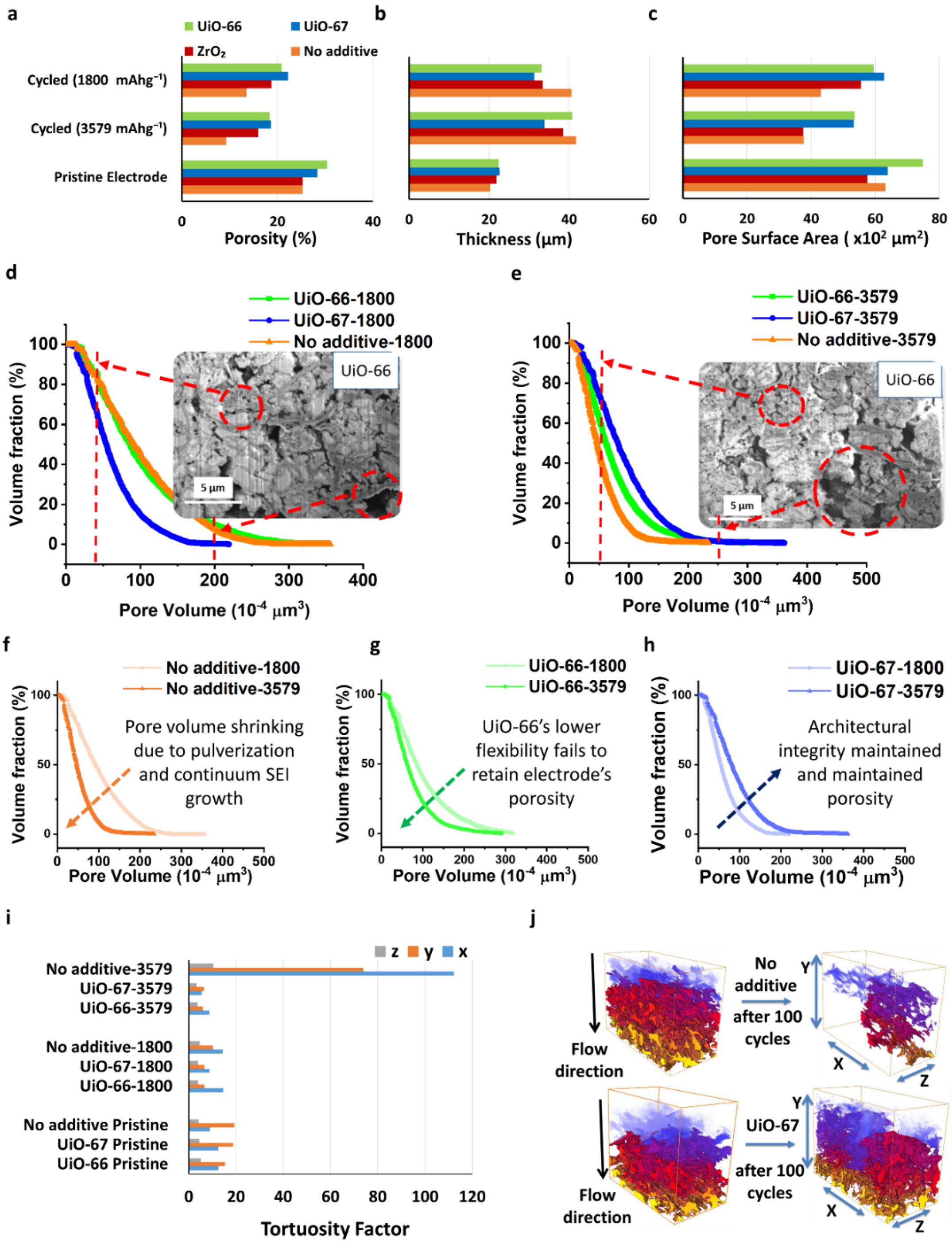

Figure 5.12: Geometrical property comparison at silicon's half and full capacity cycling. Electrode's (a) porosity, (b) thickness and (c) pore surface area comparison; cumulative pore volume distribution comparison of all cycled electrodes with (d) half capacity of silicon, (e) full capacity of silicon and individually for (f) no additive, (g) UiO-66, (h) UiO-67 electrodes. The legends for (a) also applies to (c,d).

The porosity retention is higher in the MOF electrodes in comparison to the control electrodes. It can be seen that the porosity of the cycled electrodes at half capacity has decreased by only 31 % and 22 % for the UiO-66 and UiO-67, respectively (see Figure 5.12a) with respect to their pristine electrode. Reduced porosity or increased tortuosity may adversely affect the lithium permeability and diffusion into the active material, resulting in capacity decay or loss. The observation of cracks on the electrode surface is consistent with previously reported studies[79,282,283]. This observation can also be supported by the impedance study (see Figure 14) and tortuosity factor (see Figure 5.13) for the electrodes.

The initial thickness of the pristine electrode was recorded as well as the post-cycling thickness. There is an incremental change in the thickness of the electrode cycled at half capacity by >50 % in the control samples compared with 48 % and 38 % for the UiO-66 and UiO-67, respectively (see Figure 5.12b). Another observation that can be made is that electrodes cycled at half capacity have a lower increment in the electrode thickness with respect to electrodes cycled at full capacity of silicon. Comparing the pore surface areas in contact with the electrolyte for a pristine electrode and a cycled electrode, it can be seen that there is a large decrease in specific surface area, around 50 % in the control samples compared to *ca* 29 % for MOF electrodes at full capacity (see Figure 5.12c). This suggests that the surface of the particles has undergone redox reaction, *i.e.* there is continuum formation and growth of SEI.[284] The UiO-67, however, has undergone the least change in pore surface area at half capacity demonstrating a significant advantage of having this MOF in the electrode.

From Figure 5.12d and 5.12e it can be observed that there is a segregation of pore-volume distribution upon cyclic aging. Coalescence among the particles in the cycled electrodes can also be seen, which is likely from the huge volume expansion and electrochemical fusion of silicon particles - similar to observations made in the previous studies.[79] It has been reported elsewhere that silicon has a tendency to fuse together upon electrochemical cycling.[285] The observed changes in porosity are likely to impact the permeability towards the electrolyte solvents and be responsible for the eventual decay in performance of the anode.

There is a significant change in the pore volume and distribution after 100 cycles for each of the electrode formulations. Upon aging, there is a shift towards the lower end of the pore volume which may be an indication that the macropores are becoming filled with detached SEI products upon cycling (see Figure 5.12f and 5.12g). However, on careful observation in Figure 5.12d and 5.12e it can be seen that there are many pores with large volume (*i.e.* towards the right-hand side of the distribution) which can be explained by the large volume expansion that active silicon particles undergo. This correlates with the decrease in charge transfer impedance upon full capacity cycling (see later in Figure 5.14j). From Figure 5.12e it can be seen that electrodes with UiO-66 and no additive have a higher volume percent of lower pores compared to UiO-67 electrode attributing to the Si-fusion and subsequent pulverisation from large volume expansion resulting in microstructure fragility. Therefore, it can be concluded that the UiO-67 acts as a flexible pore channel for the active silicon particle undergoing volume changes upon lithiation/de-lithiation and maintaining “porous networks” for the electrolytes. From Figure 5.12 there is direct evidence of UiO-67 as the superior additive. This may be ascribed to it having larger pore diameter, and a longer organic linker than UiO-66 to provide a more flexible structure to absorb the continuous strain from silicon particle upon cycling.

5.2.5 TORTUOSITY FACTOR CALCULATION

Tortuosity factor (τ) is an important parameter that provides information on resistance to ionic transport property of ions through pores. τ was calculated by simulating the steady-state diffusion flow through the 3D pore network[286]. From Figure 5.13, it can be seen that τ values for each of the electrodes have decreased upon cycling at half capacity, except for the formulation with no additive. The explanation for this is that in the absence of any cushioning additive effect which can help to sustain the volume changes, the mesopores are filled by fragmented SEI layers. For electrodes with MOF additives, τ decreases, as the volume changes from silicon particles have resulted in macro-voids and it can be proposed that these cracks act as carrier path for the electrolyte. The architectural degradation is minimal in the MOF-containing anodes as inferred from impedance measurement and also reflected in the τ values (see Figure 5.14). Therefore, the gradual decrease in pore volume from broken SEI would thereby impede the flow of Li^+ ions through the porous network. Formulations with UiO-66 and UiO-67 when cycled at full capacity have lower τ when compared to the cells cycled at half capacity since the former has undergone macro cracking with large volume changes with silicon's expansion. This observation is also supported by impedance measurements (see Figure 5.14j).

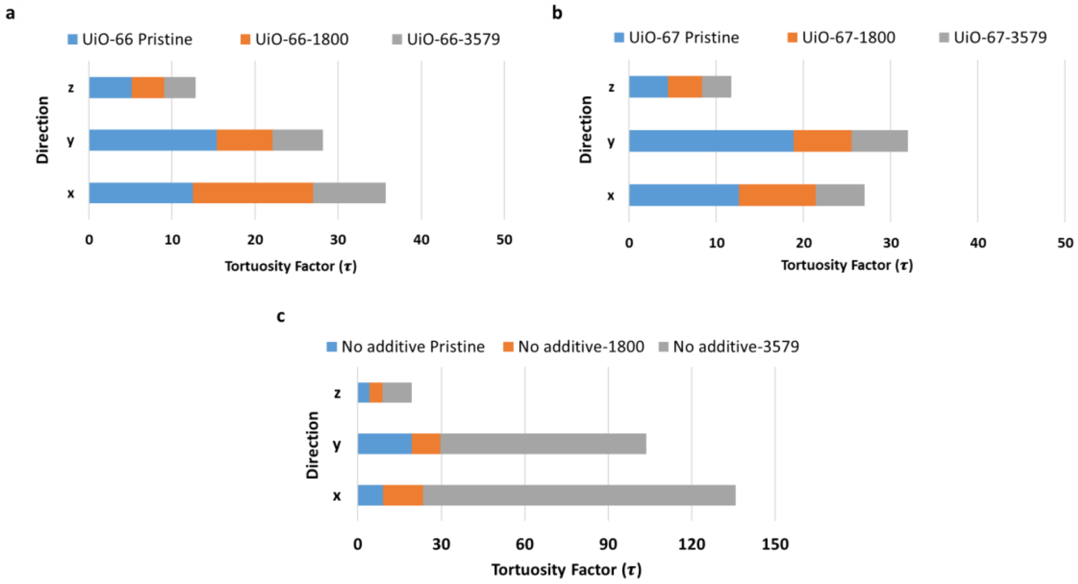

Figure 5.13: Tortuosity factor comparison between pristine electrodes and cycled electrodes after 100 cycles at Si's half and full capacity cycling for Formulations: (a) UiO-66; (b) UiO-67 and (c) No additive.

5.2.6 ELECTROCHEMICAL IMPEDANCE INVESTIGATIONS

Nyquist plots obtained from potentiostatic electrochemical impedance spectroscopy (PEIS) provide information on the kinetics of the reaction and diffusion processes corresponding to certain frequency ranges.[287–289] The two features occurring in the high-frequency range correspond to interfacial phenomena, the first can be attributed to an insulating SEI layer, while the second to charge transfer resistance.[289] R_{SEI} gradually increases with the cycle number, which indicates that the SEI layer is continuously growing because of the large volume changes. Thus, one hypothesis can be made is that fragments of the SEI layer break from the surface and migrate to the pores in the electrode and continue to accumulate as a function of aging.[65,79] This phenomenon has a strong influence on the impedance of the electrode and is very evident from Figure 5.14i and 5.14l. During this aging period, where the thick SEI layer breaks off, there is re-formation of a new SEI layer and therefore, an increased series resistance from pore clogging. This formation of new SEI results in consumption of Li^+ ions which should result in capacity loss; however, in the present study, an excess of Li^+ ions from the Li foil used in a half cell. Upon cycling, the consumption of Li^+ ions in the SEI layer reduces its concentration in the electrolyte and it is reflected in the slight increase in ionic resistivity, *i.e.* R_{series}.

The segregated pores and heterogeneous distribution of the pores from FIB-SEM results (see Figure 5.12d and 5.12e) hinder the passage of intercalating Li^+ ions resulting in an increased resistance. The equivalent circuit used for this calculation is shown in Figure 5.14g where the capacitance of the SEI layer and the capacitance of the double layer are denoted by constant phase elements CPE_1 and CPE_2, respectively.

Figure 5.14h-m shows the resistance values for all the different formulation and it can be observed the Si-MOF electrodes showed less resistance in comparison to the control electrode. For the control electrodes with no additive, cycled at half capacity of silicon the impedance gradually increased until 70 cycles and after which there was huge resistance increase: this is likely to be due to the continuum growth of an insulating (SEI) layer and high charge transfer resistance, which is entirely consistent with the cyclic data (see Figure 5.7). The R_{CT} for cells cycled at full capacity of silicon tends to decrease after 50 cycles for all of the formulations (Figure 5.14j) and can be explained as a result of large cracks that have resulted in the electrode's structure due to huge periodic volume changes from silicon particles. The charge transfer process involves two steps, namely, de-solvation of the solvated Li^+ ions in the electrolyte and transportation of these Li^+ ions through the SEI layer until it accepts an electron at the electrode's surface[290]. The large voids allow comparatively easy transportation of electrolyte within the electrode and thereby facilitate the availability of Li^+ ions to diffuse through the active particles. The large cracks also result in a fresh surface for further side reactions, increasing the R_{SEI} which also increases the R_{series} as they reduce the electrical conductivity of the electrode as a whole.

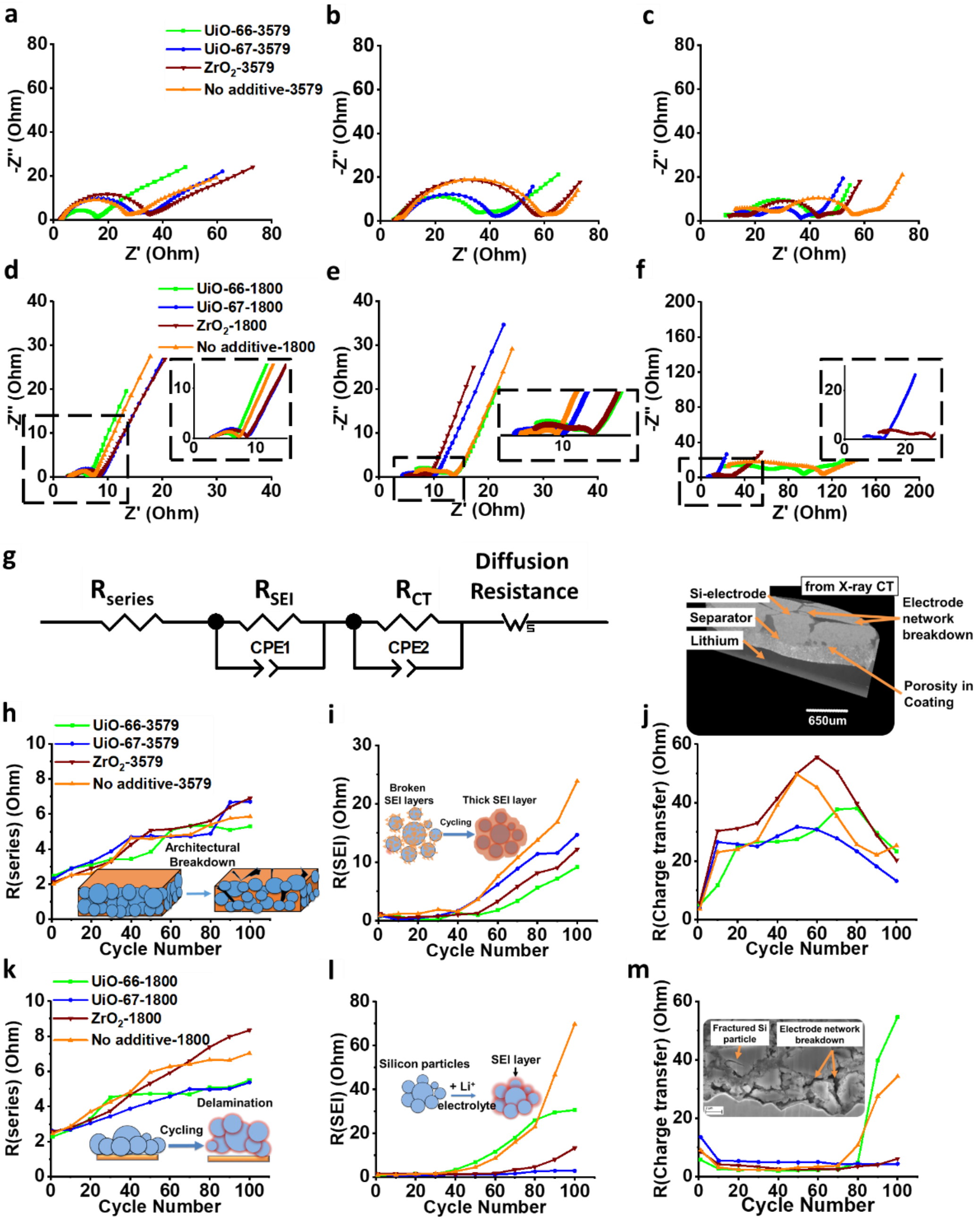

Figure 5.14: Nyquist plots and impedance fitting results. Nyquist plots during the charging process for all formulations cycled with full capacity of silicon (3579 mAh g^{-1}) after (a) 10 cycles, (b) 50 cycles and (c) 100 cycles; with half capacity of silicon (1800 mAh g^{-1}) after (d) 10 cycles, (e) 50 cycles and (f) 100 cycles (zoom-in plot shown as the inset); (g) the electrochemical equivalent circuit used for fitting the Nyquist plots; and the impedance fitting result comparison between (h-j) 3579 mAh g^{-1} and (k-m) 1800 mAh g^{-1} against (h,k) Series resistance (i,l) SEI resistance (j,m) interphase contact and charge transfer resistance (a reconstruction of the degradation methods during cycling are illustrated with schematics as the insets). The legends for (a) also applies to (b-c, h-j) whilst the legend for (d) further applies to (e-f, k-m).

5.3 SUMMARY

The porous zirconium carboxylate MOFs UiO-66 and UiO-67 as additives in Si-based anodes have the dual purpose of improving and maintaining the porous nature of composite battery materials. It has proven possible to improve the performance of a silicon electrode by the homogeneous inclusion of MOFs with large pore size facilitating “porous networks” via their flexible structures. The highly reversible electrochemical performance of the silicon electrodes that incorporate MOFs as additives significantly improve cell performance, especially with UiO-67. The MOFs can act as lithium hosts, contributing up to 387 mAh g^{-1} of capacity when cycled *vs* Li/Li^+, but more importantly, the flexible frameworks of MOFs are able to maintain a high degree of porosity upon battery cycling, overcoming pore blockage and increased tortuosity that usually takes place in silicon anodes due to large volume changes on alloying/de-alloying. This study proposes that these findings provide a novel perspective towards robust Si anodes for use in LIB materials, especially in the field of space, marine or defence application where performance is the priority despite the cost/weight penalties. Furthermore, hierarchical modification of the porosity of MOFs could be combined with a judicious choice of the functionalised ligands to provide improved compatibility with the anode components.

CHAPTER 6. THE LAYERED SILICON-GRAPHENE HETEROSTRUCTURES FOR HIGH CAPACITY SILICON ANODES IN LITHIUM-ION BATTERIES

Hybrid anode material for lithium-ion batteries, encompassing silicon nanoparticles embedded onto graphene, was synthesized via a scalable wet-jet milling method. This synthesized composite, reinforced by a network of conductive carbon black, demonstrated high Li^+ ion storage capacity, longer cycling stability and superior high-rate capability. The anode exhibited high reversible discharge capacity. This significantly supersedes the performance of a Si-dominant electrode structures. This superior electrochemical performance is ascribed to the highly layered, silicon-graphene porous structure as investigated via FIB-SEM tomography. Moreover, this morphology can not only accommodate the large volume strains from active silicon particles, but also maintains robust electrical connectivity, for faster transportation of electrons and ions with significant permeation of electrolyte within the electrode. Physicochemical characterisations were performed to further correlate the electrochemical performance with the microstructural dynamics.

6.1 MOTIVATION TO INCORPORATE GRAPHENE AS AN ADDITIVE AND CO-HOST

As discussed in section 2.2, the electrochemical and mechanical instability of Si-based electrodes is currently precluding their commercial viability but remains a compelling research challenge[72]. To address these issues, researchers have found that one effective way to achieve prolonged cycling is to fabricate uniform distributions of active silicon nano-particles onto a flexible and conductive matrix, to not only accommodate the volume changes in Si, but also to enhance electrical conductivity[194]. Recently, studies have been carried out using graphene-based materials as a conductive additive in silicon anodes to substantially ameliorate concerns relating to Si as the dominant anode mass in LIBs[187–189]. Pristine graphene exhibits excellent electrical conductivity, mechanical strength and, has a large surface area providing substantial sites for Li^+

ion interaction, making it a preferential choice among other additives for silicon-based anodes[187,291–294]. Furthermore, graphene's unique hierarchical structure and turbostratic distribution in a coating, generates porous layers which enable the unrestricted flow of electrolyte throughout the electrode's architecture and operational lifetime[295].

The incorporation of graphene has been postulated to restrict electrochemical silicon fusion during volume expansion, whilst enhancing and maintaining the electrical contact between Si particles[73]. It maintains the electrode architecture against the huge volume changes from silicon and also it improves the kinetics of electrochemical reactions[58,73]. An homogeneous distribution of active silicon particles within the matrix is crucial to achieve high performance LIBs, as Si nanoparticles (SiNPs) tend to agglomerate, which adversely affects electrochemical performance. Previous attempts to manufacture hybrid Si-graphene anode materials have been carried out via chemical vapour deposition[296,297], atomic layer deposition[87], electrospinning[298], vacuum filtration[299–301], dip coating[302] and electrostatic spray deposition[303,304]. However, these processes are complex, expensive and difficult to scale up. In contrast to the aforementioned synthesis routes, this study demonstrates a high-pressure wet-jet milling (WJM) method, developed to efficiently exfoliate graphite and produce few-layers pristine graphene sheets (FLG_{WJM})[248] in the presence of Si particles leading to a Si-FLG_{WJM} composite. This method is cost-effective and easily scalable, providing a facile and versatile approach to synthesize defect-free and high-quality multifaceted dispersion materials.

This novel strategy uses a liquid-phase mechanochemical approach in a continuous liquid flow, yielding a layer-by-layer structure. It was found that the SiNPs are sandwiched in between the graphene sheets and interconnected in multiple directions with branch-like carbon black "chains". This interconnected porous framework is suggested to buffer the volume expansion strains from SiNPs to facilitate and maintain transportation of electron and ions, in a more stabilised microstructure. The evidence for this is based on studies of electrochemical impedance spectroscopy (EIS) combined with sophisticated physical characterisation techniques able to capture and quantify, at the nanoscale, the evolution of internal morphology and the build-up of resistance. The resulting anodes display superior performances and a limited capacity fading of only 0.11 % after 200 cycles. This study methodically explore and compare a conventionally fabricated Si-graphene composite anode, thus establishing the influence of different microstructure geometries from both fabrication approaches on LIB performance.

6.2 RESULTS AND DISCUSSION

Figure 4.5 (refer to section 4.1.4.1) summarizes the sample formulations reported and tested in this study. In addition to the silicon–graphene (Si-FLG_{WJM}) composite obtained by wet jet milling (labelled as Formulation A), a further five formulations have been prepared and used as systematic comparison. These were based on µm and nm Si materials incorporating a comparison of the graphene type into the formulation. The rationale for this was to compare the influence of Si particle dimension, graphene type and hybridisation approach. All the Si-FLG hybrid used in this study was prepared with a Si:FLG weight ratio of 1:1 and they were mixed with a conductive carbon (Super C65) and polyacrylic acid (PAA) as binder using the formulation ratio described in section 4.1.4.1.

6.2.1 MATERIAL CHARACTERISATION

6.2.1.1 THERMOGRAVIMETRIC ANALYSIS (TGA)

TGA was performed to determine the content of silicon within the Formulation A composite (see Figure 6.1). The same program was used for a pristine silicon sample as a control comparison, with all the measurements carried out in air. Figure 6.1 shows the thermograms obtained for the two samples. In the case of Si-FLG_{WJM} composite powder, mass loss starts above 600 °C and at the end of the scan approximately 55.4 wt. % is lost. While, in the case of the only Si powder, the weight starts to rise above 300 °C due to the formation of SiO_x species, acquiring the 10 % of weight at the end of the scan. From the analysis of the two curves, the weight ratio between Si and FLG_{WJM} was calculated in the composites and is 54.6 and 45.4 respectively. The rough mass ratio (1:1) of Si to graphene in Formulation A can be estimated herein.

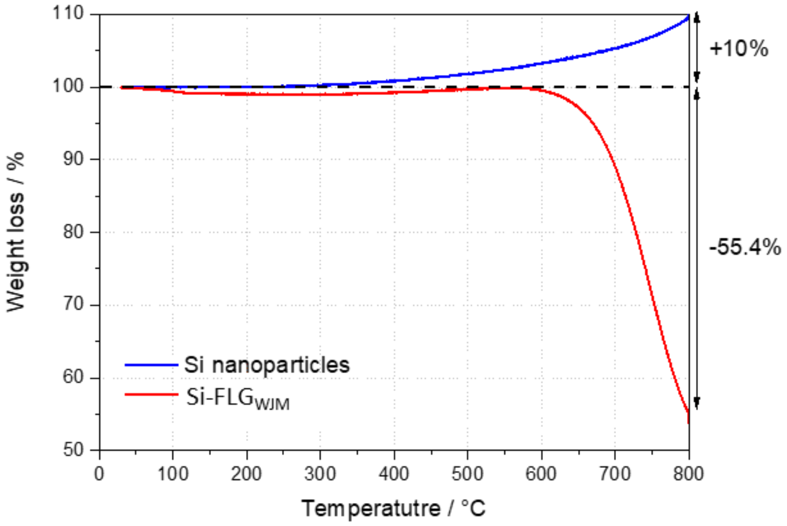

Figure 6.1: Thermogravimetric analysis of Formulation A composite and SiNPs heated at 800 °C in air-flow at 5 °C min^{-1}.

6.2.1.2 RAMAN SPECTROSCOPY ANALYSIS

As shown in Figure 6.2, three characteristic peaks can be seen. The intensity peaks at 1350 cm^{-1} (D band) is attributed to the edge defects on graphene layers and defects in its honeycomb structure whilst at 1580 cm^{-1} (G band) is attributed to the bond stretching from carbon atoms in the in-plane sp^2. The intensity peak at 2720 cm^{-1} (2D band) can be attributed to the phonon branch splitting or electronic branch splitting[305]. Using the ratio of peak intensities $I_{D/G}$, the defect density of graphene can be estimated. The lower ratio of FLG$_{WJM}$ (0.18), compared to that of GNPs (0.38), indicates a higher graphene quality from wet-jet milling procedure. For an ideal monolayer graphene powder $I_D = 0$[306].

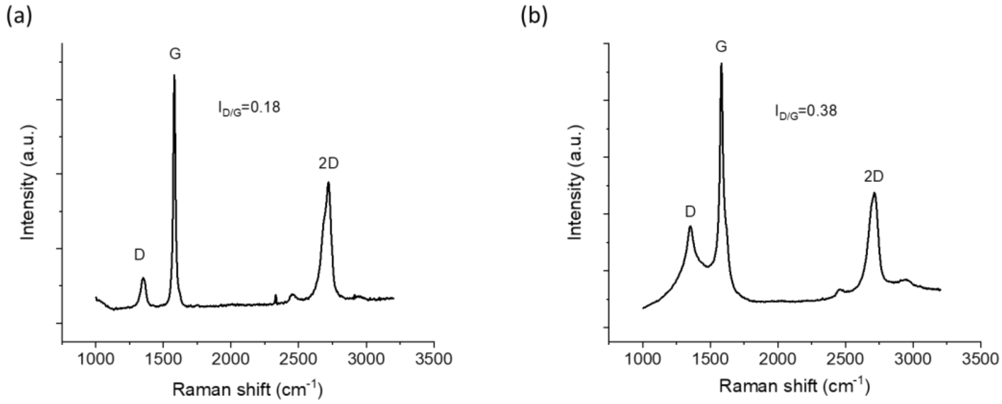

Figure 6.2: Raman spectrum of (a) FLG$_{WJM}$ and (b) GNPs.

6.2.1.3 INDENTATION TEST

It is believed that the highly conductive and flexible graphene sheets are suitable to form a buffer matrix to sustain Si particles' volume strain during lithiation/de-lithiation process[307]. To elucidate the above claim in this study nano-indentation testing was performed on the prepared electrodes. The grid indentation procedure is a quick and reliable method to measure and compare composite electrodes for their mechanical properties[58,308]. Figure 6.3a demonstrates the load-depth curve for all the samples including graphene dominant electrodes (Formulation E and F). The reduced elastic modulus is calculated using data taken from the slope of the tangent to the unloading curve. The results of the maximum depth and reduced modulus from unloading segment are shown in Figure 6.3b. It can be observed from Figure 6.3b that for graphene dominant electrodes, the tensile curves display a larger indentation depth and lower reduced modulus, indicating a more elastic property compared with the Si-FLG$_{WJM}$ composite. This is possible due to the larger GNPs flakes in comparison FLG$_{WJM}$, which also result to a larger pore size within the electrode. As a result, the µm sized Si-GNPs composite demonstrates larger contact depth and lower reduced modulus. Comparing Formulation A and D, the latter is a physically blended nm Si particles and as-synthesised graphene, it can be noted that the Formulation D shows similar contact depth but much lower reduced modulus. This might be due to more porosity introduced between nm Si and FLG$_{WJM}$ during the physical mixing and drying process, whilst in the Formulation A composite electrode, the SiNPs are firmly attached to graphene flakes. Therefore, it can be postulated that the graphene provides an effective mechanical flexibility to accommodate volume expansion stresses from silicon upon cycling. In comparison to Formulation D, there is enhanced performance from maintaining the structural integrity of the electrode with Formulation A, as observed in electrochemical cycling data (further discussed in section 6.2.3).

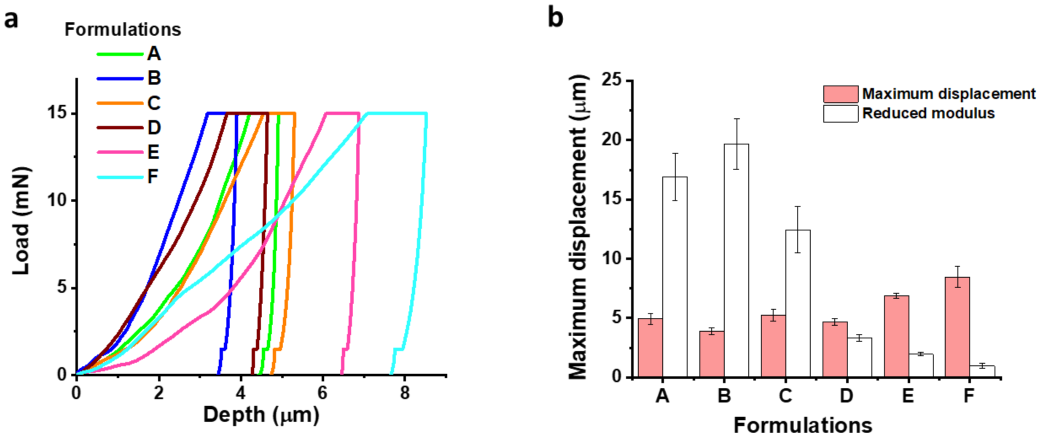

Figure 6.3: (a) Tensile curves and (b) maximum displacement, reduced Young's modulus deduced from nano-indentation tests.

6.2.2 STRUCTURE AND MORPHOLOGY

Ample sharp folds or defects on the graphene sheets may act as anchoring region for SiNPs. Figure 6.4 shows the SEM images of the pristine powders (on the top) and the electrodes cross-section (below). The graphene powder synthesized via mechanochemical wet-jet milling (FLG_{WJM}) exhibits a parallel planar morphology of large graphene sheets (Figure 6.4a). In the Si-FLG_{WJM} composite (Figure 6.4b and 6.4c) is can be observed that SiNPs, having a dimension of *c.a.* 100 nm in diameter, are homogeneously distributed on the surface of graphene flakes and anchored on and between the graphene sheet stacks.

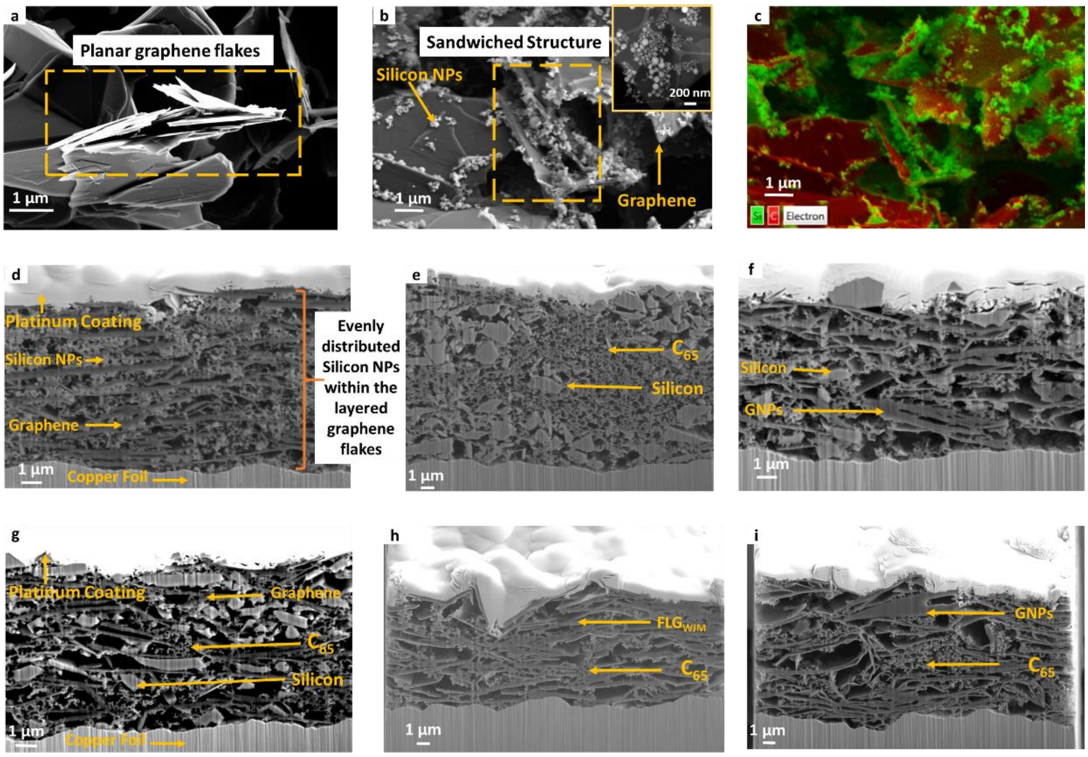

*Figure 6.4***:** *SEM images of (a) FLG_{WJM} powder, (b) as-synthesised Si-FLG_{WJM} (zoomed Si-FLG_{WJM} powder as inset) with energy dispersive spectra (EDS) derived chemical distribution maps showing the presence of Si in the planar flakes of FLG_{WJM} as shown in (c); cross-sectional images of electrode with (d) Formulation A - Si-FLG_{WJM} composite, (e) Formulation B - Si-dominant, and (f) Formulation C - composite µm Si with GNPs powders, (g) Formulation D - composite nm Si with FLG_{WJM} powders, (h) Formulation E - FLG_{WJM} dominant, and (i) Formulation F - GNPs dominant powders.*

Looking at the electrode cross-section (Figure 6.4d), in the electrode with Formulation A (Si-FLG_{WJM}), it is interesting to note that FLG_{WJM} encompasses the SiNPs forming a sandwich-like 3D structure. Such structural arrangement is not visible in the other two formulations, in which the two component were simply co-dispersed and not processed by wet jet milling (Figure 6.4e, Figure 6.4f and Figure 6.4g). Furthermore, it is evident that the retention of SiNPs onto graphene's surface is maintained, despite undergoing high shear mixing during electrode ink preparation. This demonstrates a good degree of structural integrity and robustness. It can be seen in the cross-sectional image of Figure 6.4d that the graphene sheets form a continuous conductive network throughout the Si particles, and to the current collector, resulting in a mechanically robust sandwich-like architecture. This inter-connected layered arrangement may promote a higher rate performance and prolonged cycle life[302], further supported later in this report by an impedance study and supported by previous literature[148,197,199,293,294]. From the above microstructural analysis, it can be concluded that the Si-FLG$_{WJM}$ composite (Figure 6.4d) via wet-jet milling approach containing SiNPs is well distributed throughout the graphene matrix. The homogenous spread of porosity is visible in the layered composite. It can be concluded that the exploited synthesis route is economical and scalable compared to majority of the chemical methods.

6.2.3 ELECTROCHEMICAL CHARACTERISATION

All the electrodes were tested under galvanostatic cycling at a voltage range of 0.05-1.0 V at 0.2 C. To understand the relationship between cycling stability and electrode structural changes, the cells were cycled at both moderate and extreme capacities. A limited discharge capacity (de-lithiation) of Si, *i.e.* 1800 mAh g^{-1} would minimize the volume expansion and thus avoid the likelihood of pulverization[42]. When cycling at the full capacity of Si (corresponding to a current density of 716 mA g^{-1} at 0.2 C) this study expects to verify the contribution of graphene on the structural integrity and capacity retention, given its favourable tensile properties.

Figure 6.5a and 6.5b show the cycling behaviour of the Formulations A-D under galvanostatic conditions. When cycled without any limitation on capacity as in Figure 6.5a, it can be observed that a continuous capacity decrease upon cycling. In particular, Formulation B, consisting of µm Si without graphene, after 100 cycles exchange only the half of the initial capacity. The addition of GNPs graphene (Formulation C) is able to improve the performance of this type of silicon. Nevertheless, performances are lower compared to the samples prepared with nm Si (Formulation A and D). In this case, despite the initial capacity drop during the first 30 cycles, capacity values become more stable for prolonged cycling. In particular, Formulation A, the composite prepared by wet jet milling, shows higher discharged capacity values compared with all the formulations.

The electrochemical behaviour observed for Formulation B and C could be related to the larger Si-particle dimensions, leading to a relatively rigid framework resulting in pulverisation and higher tortuosity for Li^+ ion transport. This could increase the cell resistance, which is alleviated by the addition of nm Si particles in Formulation A.

Further improvements in the electrochemical performance can be obtained by cycling the cell at limited capacities (50 % of capacity, *i.e.* 1800 mAh g^{-1}) – as shown in Figure 6.5b. It should be noted that all the graphene-containing formulations cycled up to 200 cycles under a current density of 358 mA g^{-1}. Formulation A showed prolonged cycle life with nearly no capacity degradation even after 400 cycles (Figure 6.5b), compared with other formulations comprising graphene (Formulation C and D). The main reason for capacity loss in Formulation C and D could be attributed to the collapse of the electrode's architecture (microstructure) and continuous growth of SEI. These further results in the pore clogging and increased resistance for Li^+ ion movement[65,281], as discussed in the following sections (where the tomography and impedance studies are presented). From the cycling profiles, it is evident that the incorporation of graphene in the Si-electrode has a significant and positive effect on the cyclic stability, and that the mechanochemical method via continuous liquid exfoliation provides the superior performing materials.

The electrochemical behaviours of commercial GNPs and FLG_{WJM} are similar to that of microcrystalline graphite[73]. However, studies have shown that with decreasing flake thickness additional strain is exerted upon the graphene flakes during ion insertion[309]. The voltage profiles (voltage vs capacity) for the 1st cycle of the hybrid Formulation A composite and Formulation B electrode is shown in Figure 6.5c. The distinctive slope between the 0.8 V to 0.2 V can be attributed to the electrochemically active graphene in the composite[187]. During the first lithiation step, below 0.1 V, the long flat plateau is a characteristic of silicon anodes (vs Li) corresponding to the formation of amorphous metastable lithium silicide phase (a-Li_xSi) via solid-state amorphisation[100,310]. However, with the incorporation of FLG into the system, the lithiation capacity below the characteristic 0.1 V had decreased by 27 % in comparison to the Si-dominant electrode. This can be attributed to the electrochemically activity FLG_{WJM} which participates in the lithiation process between 0.9 - 0.1 V, but to a much lower lithiation capacity.

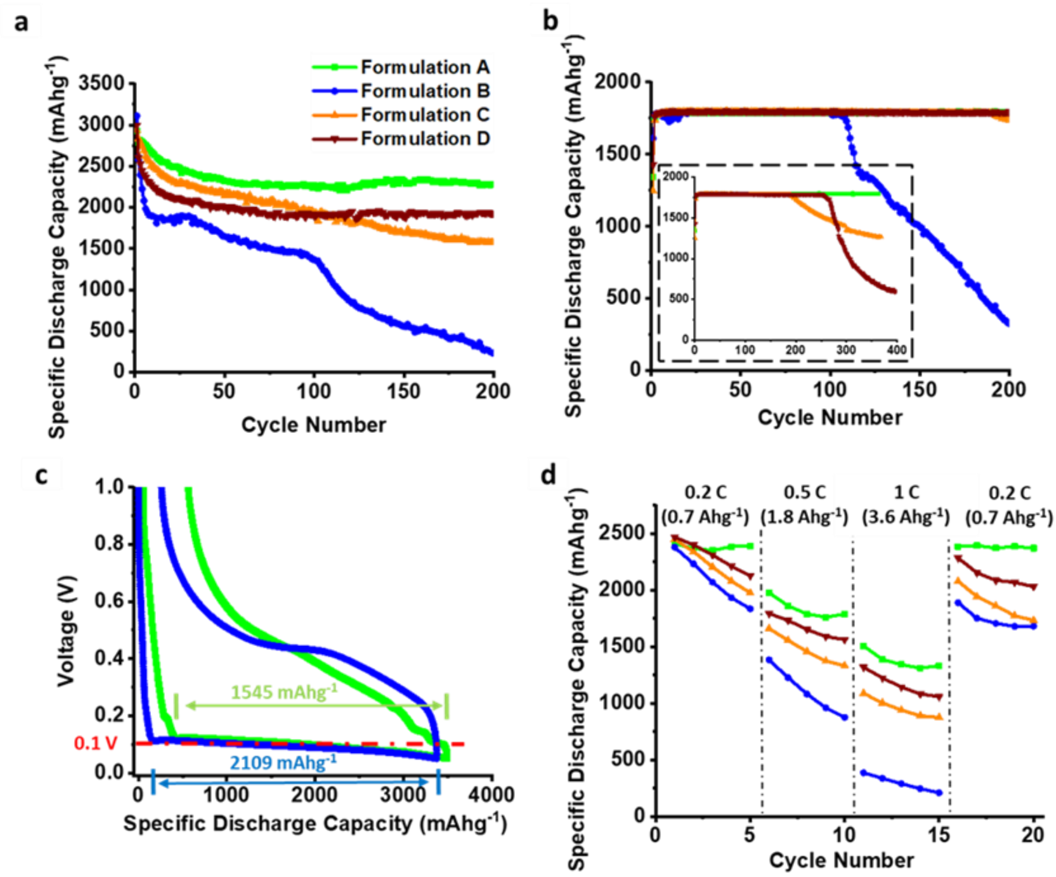

Figure 6.5: Specific discharge capacity or de-lithiation (based on the silicon's active mass) profiles of formulations cycled at (a) full capacity of silicon (3579 mAh g^{-1}), (b) half capacity of silicon (longer cycling of all Si-FLG hybrid electrodes are shown as the inset), (c) first lithiation-delithiation voltage profiles for Formulation A and B, and (d) rate capability test for all the formulations. The legends for (a) also applies to (a-d).

Herein the rate performance of all the formulations were further explored at different current densities including, 0.2 C, 0.5 C, and 1 C (Figure 6.5d). As summarized in Figure 6.6, the Si-FLG$_{WJM}$ composite electrode possesses 81.77 % of its initial capacity at 0.2 C. By increasing the current density, the reversible capacity drops to 1789.08 mAh g^{-1} at 0.5 C (61.13 % retention) and subsequently to 1333.09 mAh g^{-1} at 1 C (45.55 % retention). Upon lowering the current density to 0.2 C, the reversible capacity of Formulation A composite increases to 2371.27 mAh g^{-1} at 0.2 C (81.03 % retention). Thus, Si-FLG$_{WJM}$ composite electrode, presumed to undergo a minimal degradation under higher current density due to the conductive network and buffering of the volumetric changes from SiNPs.

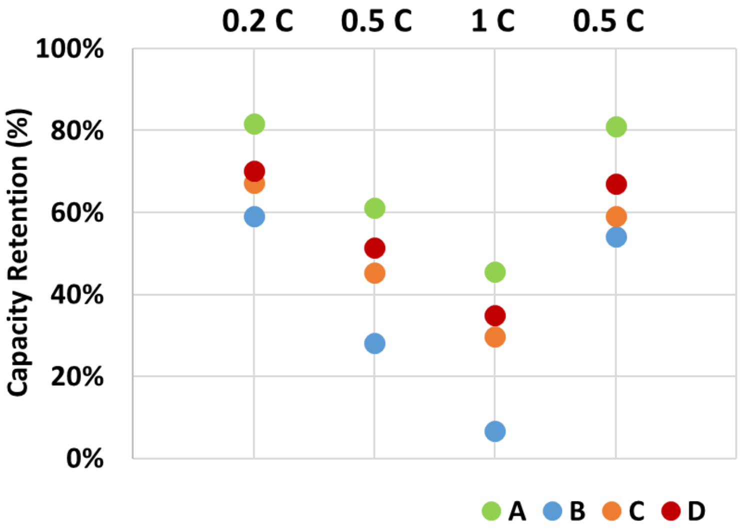

Figure 6.6: Specific discharge (de-lithiation) capacity retention after cycling for 5 cycles at different current densities.

In order to augment the understanding of the hybrid composites, the redox reactions and the transformation steps of Formulation A composite vs Li/Li$^+$ during lithiation/de-lithiation processes need to be analysed. The differential capacity plot (dQ/dV vs. V) in Figure 6.7a shows more details on the electrochemical reactions taking place during lithiation and de-lithiation vs. Li/Li$^+$. There are five redox peaks during lithiation/de-lithiation of the Formulation A composite electrode in contrast to only two redox peaks for Si-dominant electrode. Herein, during lithiation, the fourth cathodic peak encompasses two reactions corresponding to the formation of LiC_{12} and simultaneously the amorphous $Li_{3.5}Si$[23,73,98–100]. Furthermore, the cathodic peak at 0.06 V is attributed to the formation of LiC_6[100]. Similar to the lithiation process, there are five stages of de-alloying during the de-lithiation process, corresponding to the reformation of a-Si and LiC_{72}. The first anodic peak at 0.13 V corresponds to the formation of LiC_{12} from LiC_6 while further at 0.17 V the LiC_{12} is further converted to LiC_{18}[100]. The third anodic peak at 0.28 V encompasses two processes *i.e.* formation of $Li_{2.0}Si$ and also LiC_{36}[73,100]. The fourth anodic peak at 0.45 V corresponds to the de-alloying of a-$Li_{2.0}Si$ to form amorphous Si with the onset potential of ~ 0.41 V[73]. Further, above 0.5 V can be attributed to the formulation of LiC_{72}[99].

It can also be seen with increasing cycle number there is a decrease in peak intensity and also shift in the peaks' occurring voltage (see Figure 6.7b and Figure 6.7c). The above can be attributed to the increase overpotential within the electrode *i.e.* impedance due to continuum SEI growth and architectural breakdown. In particular, after 200 cycles the area beneath the lithiation peaks have decreased by a vast amount for the Si-dominant electrode compared to Formulation A composite electrode. In conclusion, the differential capacity plot of the Formulation A composite indicates that both Si and FLG$_{WJM}$ are electrochemically active within the operating potential range.

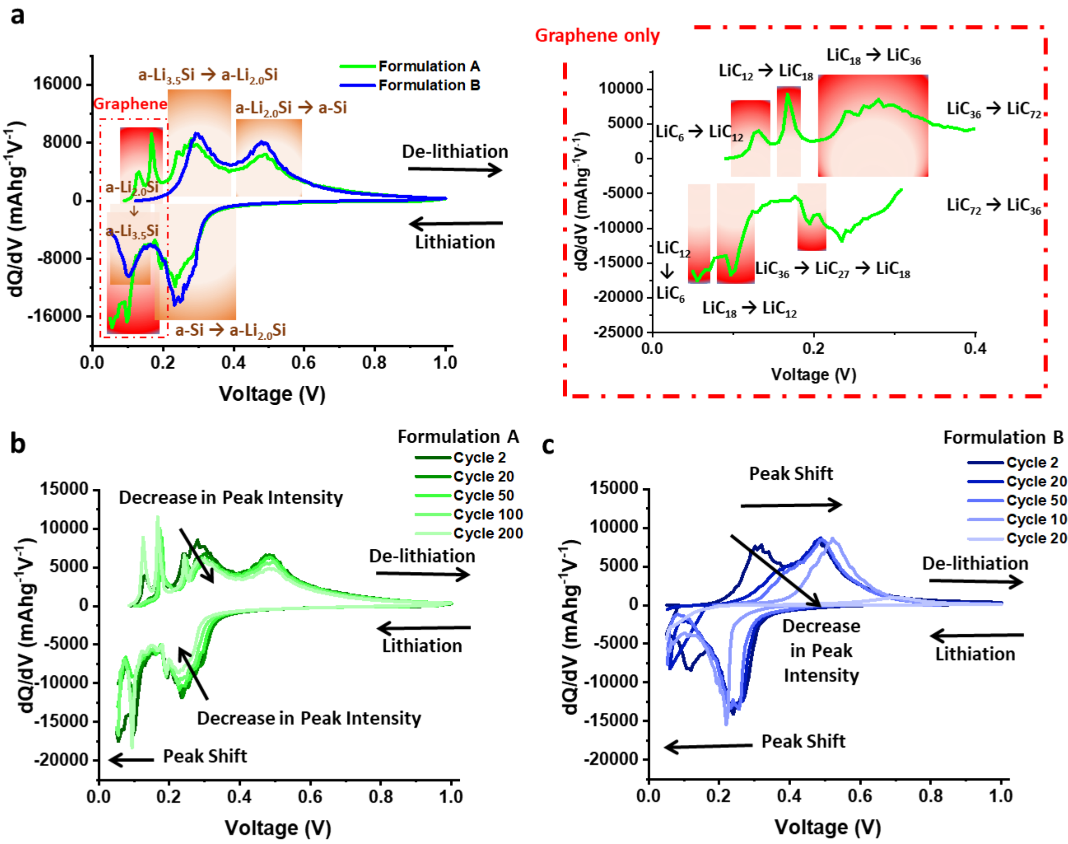

Figure 6.7: (a) dQ/dV plot for 2nd cycle of Si-FLG$_{WJM}$ composite electrode (Formulation A) and Si-dominant electrode (Formulation B) relatively (dQ/dV profile for FLG$_{WJM}$ graphene (Formulation F) between 0.0-0.4 V is shown as the inset); dQ/dV plot with incremental cycle numbers for (b) Formulation A and (c) Formulation B. Presented data are for the cells cycled at full capacity of silicon.

In order to estimate the capacity contribution from the FLG$_{\mathrm{WJM}}$ and GNPsS in the composite electrodes within the same cut-off voltages, this study also reports the electrochemical performance obtained by the use of graphene dominant electrodes (Formulation E and F). It can be observed from Figure 6.8a, that the FLG$_{\mathrm{WJM}}$ can contribute about 143.27 mAh g^{-1} while GNPs contributes to 127.40 mAh g^{-1} reversibly after 200 cycles, with a large first cycle loss of 80.21 mAh g^{-1} and 251.77 mAh g^{-1}, respectively (see Figure 6.8b). The reversible capacity obtained from the graphene-dominant electrodes was lower than reported in a previous study[58] and this is due to the higher applied current density (*i.e.* 715.8 mA g^{-1} in comparison to the literature's 357.9 mA g^{-1}) in this study. It is important to note that the FLG$_{\mathrm{WJM}}$ and GNPs had a much lower contribution towards the composite's reversible capacity (< 6 % in comparison to Si's reversible capacity) due to its relatively lower activity for Li storage under the applied current and voltage cut-offs. Therefore, the graphene's contribution to the effective capacity is comparatively insignificant.

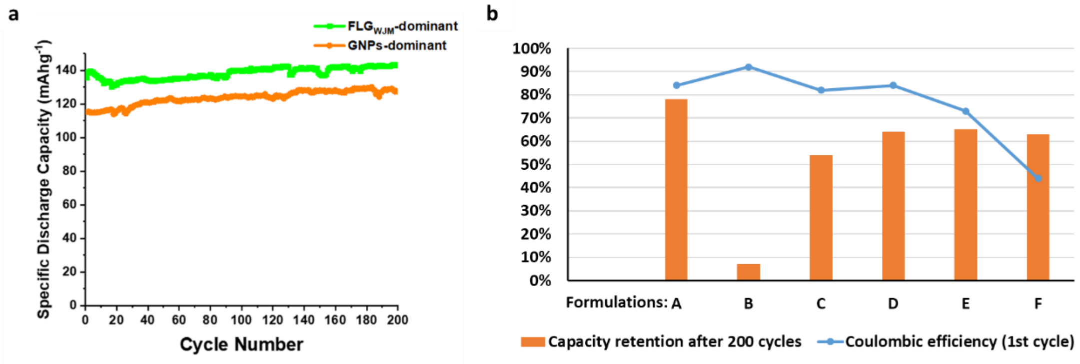

Figure 6.8: (a)Specific discharge capacity (based on the FLG's active mass) plot for graphene dominant electrodes and (b) Discharge-charge capacities, coulombic efficiency for the 1st cycle at 179 mA g^{-1} and capacity retention after 200 cycles at 715.8 mA g^{-1}.

Figure 6.8b displays comprehensive data on the first cycle and after 200 cycles. For Formulation A (Si-FLG$_{\mathrm{WJM}}$ composite), the first cycle coulomb efficiency is 84 % slightly lower than for the Formulation B (Si-dominant system). The higher capacity loss in the composite (Formulation A) can be accredited to a greater electrolyte decomposition on the large surface area of FLG$_{\mathrm{WJM}}$ and SiNPs. Nevertheless, from Figure 6.8b it is worth noting that all the Si-graphene based hybrid formulations are very promising anodes for their highly stable reversible capacity cycling in comparison to the Si-dominant electrode. The Formulation A (Si-FLG$_{\mathrm{WJM}}$) electrode offers a reversible discharge capacity of 2280.71 mAh g^{-1} with capacity retention of 77.81 % after 200 cycles with a capacity loss of only 0.11 % per cycle, a value that is superior to previously reported Si-FLG hybrid anodes in the literature[131,193–197]. The beneficial effect of GNPs for the electrochemical performance of silicon can be noticed also in Formulation C composite that exhibit enhanced the cycling performance compared to Formulation B (Si-dominant formulation), which lost 87 % less specific capacity. However, when compared to the other formulations (Formulation B, C and D), the Formulation A composite by wet jet milling displays improved capacity retention.

The proposed method here yields the best capacity retention of any reported anodic materials proposed to date with such a large Si wt % content. To support this statement, Table 6.1 outlines a range of other studies, which used a variety of methods to generate silicon-carbon composite materials. Some of these approaches used a considerably lower Si content than this study (50 – 70 %) and this is an important consideration when comparing electrochemical performance.

Table 6.1: Summary of cyclability performance of Si-carbon electrode through different approaches.

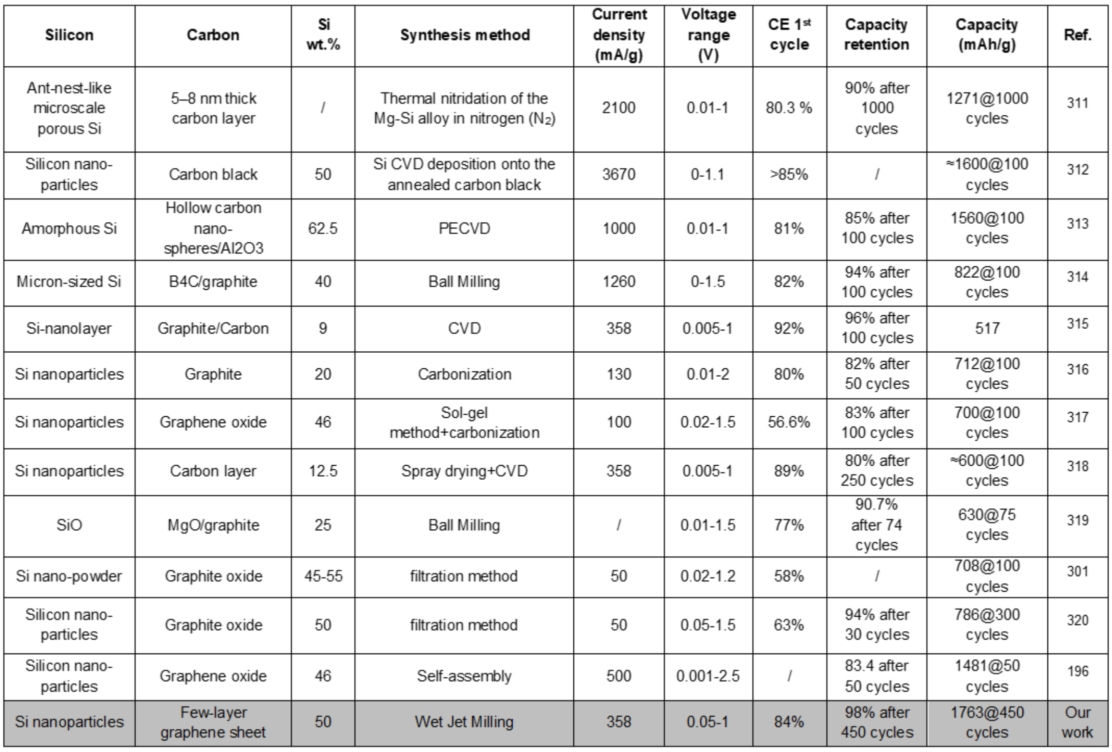

Silicon	**Carbon**	**Si wt.%**	**Synthesis method**	**Current density (mA/g)**	**Voltage range (V)**	**CE 1st cycle**	**Capacity retention**	**Capacity (mAh/g)**	**Ref.**
Ant-nest-like microscale porous Si	5–8 nm thick carbon layer	/	Thermal nitridation of the Mg-Si alloy in nitrogen (N_2)	2100	0.01-1	80.3 %	90% after 1000 cycles	1271@1000 cycles	311
Silicon nano-particles	Carbon black	50	Si CVD deposition onto the annealed carbon black	3670	0-1.1	>85%	/	≈1600@100 cycles	312
Amorphous Si	Hollow carbon nano-spheres/Al2O3	62.5	PECVD	1000	0.01-1	81%	85% after 100 cycles	1560@100 cycles	313
Micron-sized Si	B4C/graphite	40	Ball Milling	1260	0-1.5	82%	94% after 100 cycles	822@100 cycles	314
Si-nanolayer	Graphite/Carbon	9	CVD	358	0.005-1	92%	96% after 100 cycles	517	315
Si nanoparticles	Graphite	20	Carbonization	130	0.01-2	80%	82% after 50 cycles	712@100 cycles	316
Si nanoparticles	Graphene oxide	46	Sol-gel method+carbonization	100	0.02-1.5	56.6%	83% after 100 cycles	700@100 cycles	317
Si nanoparticles	Carbon layer	12.5	Spray drying+CVD	358	0.005-1	89%	80% after 250 cycles	≈600@100 cycles	318
SiO	MgO/graphite	25	Ball Milling	/	0.01-1.5	77%	90.7% after 74 cycles	630@75 cycles	319
Si nano-powder	Graphite oxide	45-55	filtration method	50	0.02-1.2	58%	/	708@100 cycles	301
Silicon nano-particles	Graphite oxide	50	filtration method	50	0.05-1.5	63%	94% after 30 cycles	786@300 cycles	320
Silicon nano-particles	Graphene oxide	46	Self-assembly	500	0.001-2.5	/	83.4 after 50 cycles	1481@50 cycles	196
Si nanoparticles	Few-layer graphene sheet	50	Wet Jet Milling	358	0.05-1	84%	98% after 450 cycles	1763@450 cycles	Our work

In summary, the reversible capacity retention of Si-FLG hybrid systems are invariably higher than the Si-dominant electrode for all the different current densities tested. Both the cycling stability and rate capability reaffirm that Formulation A is more resilient to capacity fade from volume expansion strain in comparison to other graphene incorporated Si anodes. Alongside the unique morphology of Formulation A, the 3D porous layered structure of the electrode attributes to the superior cyclability. Herein, the poor capacity retention in Si-dominant electrodes is attributed to the higher resistance from continuous growth and breakdown of SEI along with a diminishing pore network. Therefore, the Formulation A composite electrode displayed superior cyclic performance, which could be ascribed to the unique porous multi-layered morphology of the electrode. The graphene flakes provide structural rigidity and hinders Si particles from detaching due to pulverization, from the graphene matrix. Finally, it is conceivable that the stability of Formulation C underwent structural degradation under higher current due to larger Si particle size in comparison to Formulation A.

The performance of a battery depends on the characteristics of the material it is composed of. In order to directly correlate the electrode microstructure to the battery performance, focused ion beam in conjunction with scanning electron microscopy (FIB-SEM) tomography was exploited to study 3D microstructure of battery materials[66–69].

6.2.4 MORPHOLOGY EVOLUTION

Porosity plays a key role in cell performance through the electrochemical reaction kinetics, as well as the Li^+ ion’s transport properties including tortuosity[278]. The morphological evolution of the Formulation A and Formulation B for pristine electrodes and cycled electrodes (200 cycles) were analysed using focused ion beam in conjunction with scanning electron microscopy (FIB-SEM), which allows for the visualization and quantification at the three-dimensional (3D) scale[25,29,30,68,231]. These studies are precious to offer more evidence of the benefits on the electrode structural changes brought by the incorporation of graphene in silicon-based anodes. Results are given in Figure 6.9 and Figure 6.10 that reports the comparison among all the formulations at full and half capacity before and after cycling. Despite the coalescence of SiNPs after cycling, cycled electrodes were found to retain their porous 3D morphology. The 3D conductive network from graphene, along with the flexibility from the nano-sheets, plays favourable towards the electrode's stability during lithiation/de-lithiation. This accommodates the huge volume changes of SiNPs while maintaining electrical connectivity of all throughout the electrode.

Tomography was performed on the pristine and aged electrodes (after 200 cycles) for all four of the formulations studied. The subsequent SEM images were reconstructed to obtain a 3D volume of the bulk material, which gives an indicative porosity and phase fraction change as a function of capacity limit. Figure 6.9 and Figure 6.10 shows processed images that graphically represent the porosity of the materials for all the formulations. The region of interest for all the samples ranged between 25 × 10 μm^2 to 25 × 33 μm^2, since the cycled electrodes had a variable change in thickness of the electrode. From this a 3D reconstructed volume of 20 × 10 × 15 μm^3 across all the samples was obtained. The porosity can be calculated from the processed images, and in Figure 6.9 and Figure 6.10 it can be observed that there is a segregation of pore groups upon cyclic aging. In Formulation B, merging among the particles in the cycled electrodes can also be seen (see Figure 6.9b and Figure 6.10b). This is most likely to result from volume expansion and electrochemical fusion of particles - similar to observations made in previous studies[79,285].

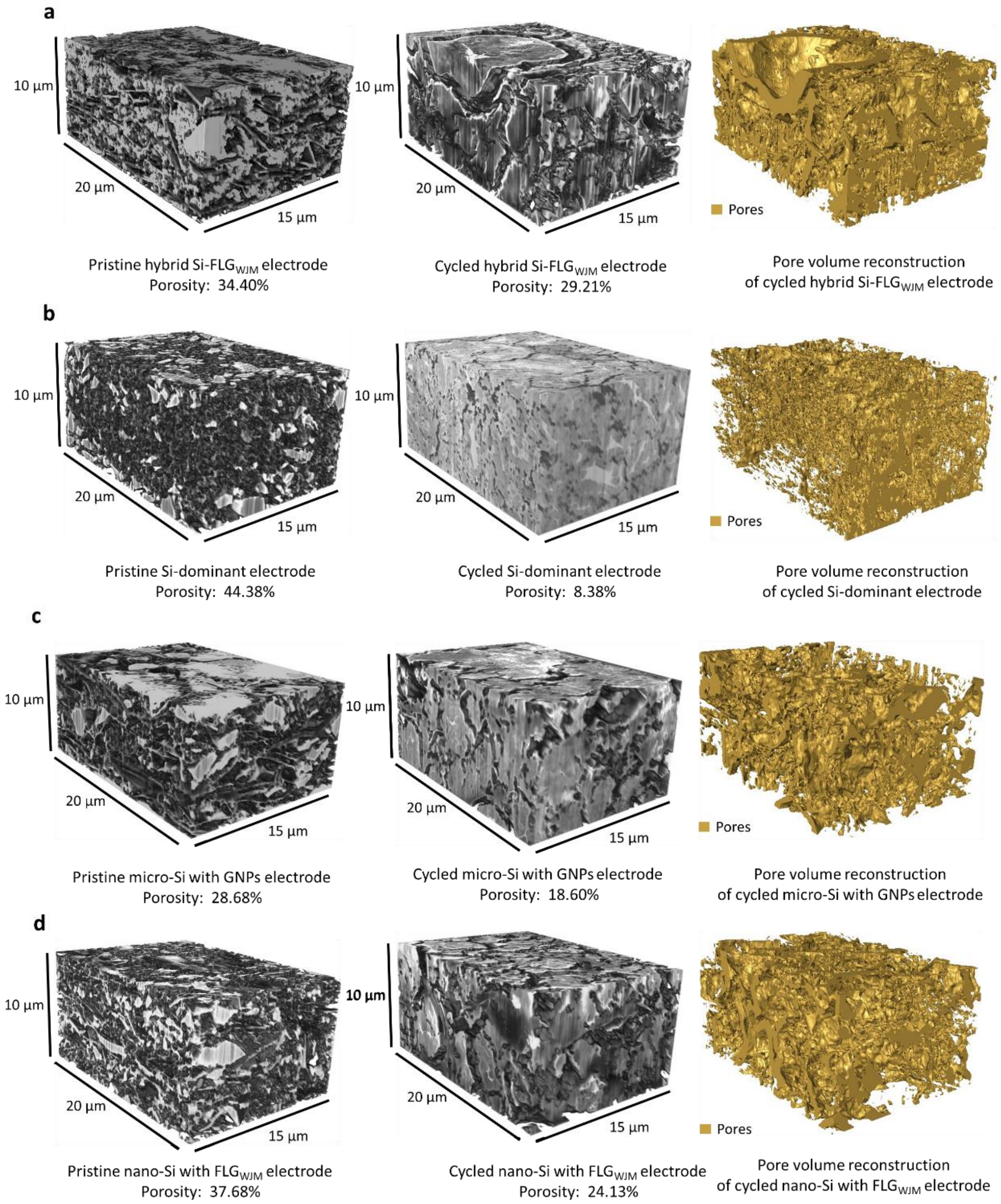

Figure 6.9: The greyscale 3D reconstructed volume of the electrode with (a) Formulation A - Si-FLG$_{WJM}$ composite, (b) Formulation B - Si-dominant, (c) Formulation C - composite µm Si with GNPs powders, (d) Formulation D - composite nm Si with FLG$_{WJM}$ powders, before and after cycling at full capacity for 200 cycles.

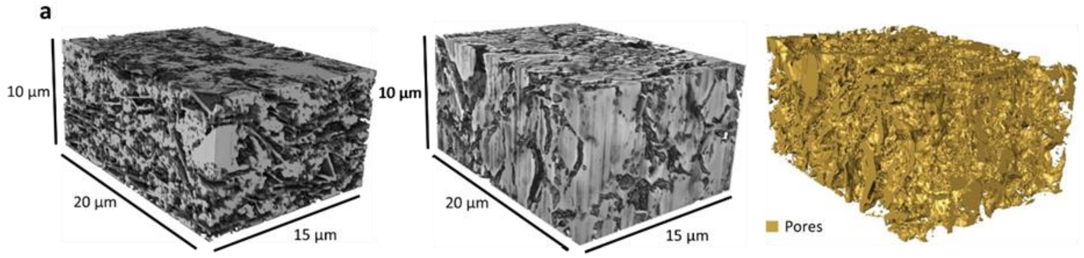

Pristine hybrid Si-FLG$_{WJM}$ electrode
Porosity: 34.40%

Cycled hybrid Si-FLG$_{WJM}$ electrode
Porosity: 30.59%

Pore volume reconstruction
of cycled hybrid Si-FLG$_{WJM}$ electrode

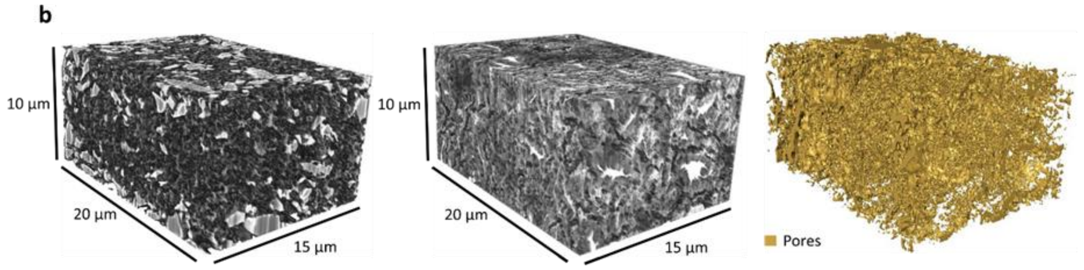

Pristine Si dominant electrode
Porosity: 44.38%

Cycled Si dominant electrode
Porosity: 15.62%

Pore volume reconstruction
of cycled Si dominant electrode

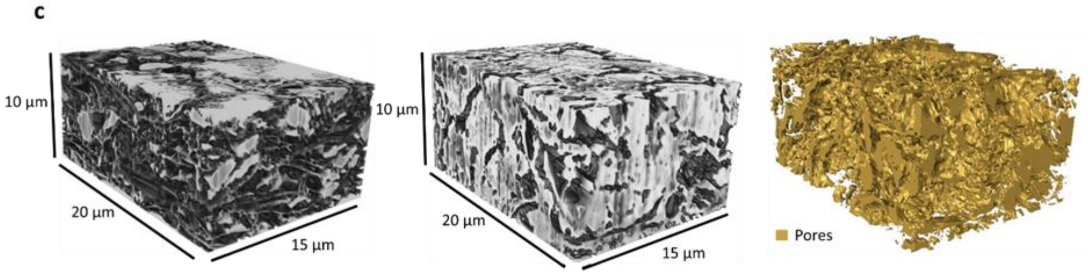

Pristine micro-Si with GNPs electrode
Porosity: 28.68%

Cycled micro-Si with GNPs electrode
Porosity: 19.82%

Pore volume reconstruction
of cycled micro-Si with GNPs electrode

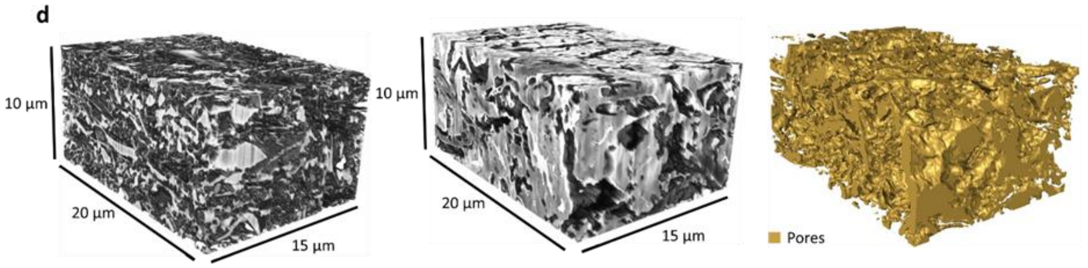

Pristine nano-Si with FLG$_{WJM}$ electrode
Porosity: 37.68%

Cycled nano-Si with FLG$_{WJM}$ electrode
Porosity: 25.97%

Pore volume reconstruction
of cycled nano-Si with FLG$_{WJM}$ electrode

Figure 6.10: The greyscale 3D reconstructed volume of the electrode with (a) Formulation A - Si-FLG$_{WJM}$ composite, (b) Formulation B - Si-dominant, (c) Formulation C - composite µm Si with GNPs powders, (d) Formulation D - composite nm Si with FLG$_{WJM}$ powders, before and after cycling at half capacity for 200 cycles.

The fact that Si-FLG hybrid electrodes shows superior additive properties in comparison to Formulation B electrode could be attributed to an increased innate structural flexibility of the coating[87]. As showed in Figure 6.11a, the porosity retention (after 200 cycles) is higher in all Si-graphene based hybrid anodes (Formulation A, C and D) in comparison to the Formulation B. When SiNPs are used, it can be seen that the porosity of the cycled electrodes at full capacity decreases by only 15 % and 36 % for the Formulation A and D, respectively (see Figure 6.11a). In particular, with cells cycled at half capacity, it can be seen that the Formulation A shows little change in porosity of about 11 % with respect to the pristine electrode. In this sense, these pores also help to maintain sufficient void structure around the active particles proving "porous networks" to the electrode architecture. Reduced porosity or increased tortuosity may adversely affect the lithium permeability and diffusion into the active material, resulting in capacity loss. The observation of cracks on the electrode surface is consistent with previously reported studies[79,282,283]. This observation can also be supported by the tortuosity factor (see Figure 6.13) and impedance study (see Figure 6.14) for the electrodes.

The presence of graphene in the electrode is believed to buffer the stresses in the structure during lithiation of Si, and this influence is very much evident in the electrode's thickness post-cycling. The initial thicknesses of the pristine electrodes were recorded as well as the post-cycling thicknesses and they are showed in Figure 6.11b. In the case of electrode with µm silicon particles (Formulation B) there is an increase in the thickness of electrodes after cycling at full capacity by > 204 %. Whilst the thickness value post-cycling decreases to 160 %, 176 % and 187 % in the Si-FLG_{WJM} composite (Formulation A), nm Si with FLG_{WJM} (Formulation D) and µm Si with the commercial GNPs (Formulation C), respectively (see Figure 6.11b). Another observation is that electrodes containing graphene, that have been cycled at half capacity, have a lower increment in the electrode thickness with respect to Si-dominant electrodes cycled at full capacity of silicon. Comparing the surface areas in contact with the electrolyte for a pristine electrode and a cycled electrode, as reported in Figure 6.11c, it can be seen that there is a huge decrease in the specific surface area for all the formulation. Specifically, in the Formulation B the surface area is reduce of > 61 %. This value slightly decrease when GNPs graphene is added (Formulation C). Contrarily, for the Formulation A and nm Si with FLG_{WJM} (Formulation D) is around

43 % and 49 %, at full capacity respectively (see Figure 6.11c). All the Si-FLG hybrid anodes have undergone least changes in pore surface at full capacity and this shows the advantage of having graphene in the electrode.

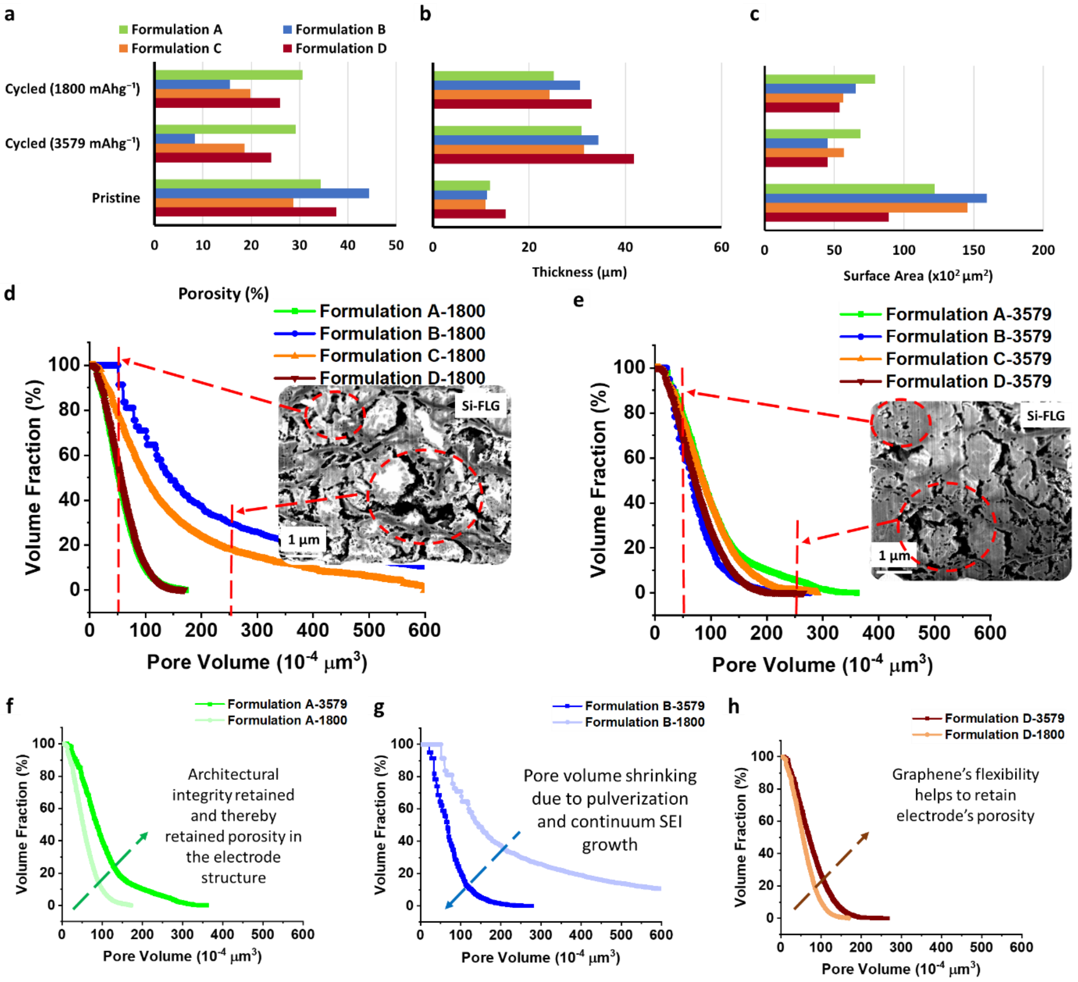

Figure 6.11: Geometrical property comparison after cycling at silicon's half and full capacity. Electrode's (a) porosity, (b) thickness and (c) pore surface area comparison; cumulative pore volume distribution comparison of all cycled electrodes with (d) half capacity of silicon, (e) full capacity of silicon (the inset cross-sectional SEM images for Formulation A after 200 cycles under half and full capacity, respectively) and individually for (f) Formulation A, (g) Formulation B, (h) Formulation D. The legends for (a) also applies to (b,c).

In this study the porous volumes of the electrodes was also calculated after cycling. As observed in Figure 6.11, there is a significant change in the pore volume after 200 cycles for each of the electrode formulations. Upon aging, there is a shift towards the lower end of the pore volume spectrum, which may be an indication that the pores are becoming filled with detached SEI products upon cycling (see Figure 6.11g) unlike Si-graphene based hybrid electrodes (Figure 6.11f and Figure 6.11h). However, upon careful observation in Figure 6.11d and 6.11e it can be seen that there are many pores with large volume, which can be explained by the large volume expansion and pulverisation that active silicon particles undergo. This correlates with the decrease in charge transfer impedance upon full capacity cycling (see later in Figure 6.11g). The FLG_{WJM} component in Formulation A electrodes facilitates a flexible-porous network for the active silicon particle undergoing volume changes upon lithiation and de-lithiation and maintaining "porous networks" for the electrolyte. From Figure 6.11 there is direct evidence of Si-FLG_{WJM} composite as the superior structure bestowing larger pore channels, longer and flexible conductive network, to absorb the continuous volumetric stains from silicon particle upon cycling. Therefore, it can be concluded that by accommodating volume expansion, the electrode structure is more structurally robust and the pulverization dominates the capacity fade of the cell under the limitation of half capacity. While for cells cycled under full capacity the electrochemical particle fusion through SEI is more significant and both SEI growing and particle pulverization contribute to the cell degradation.

Further, the porosity, thickness and surface area change for graphene dominant formulations were studied and presented in Figure 6.12, Table 6.1 and Table 6.2. In particular, these cells were cycled under the same current as formulation under full capacity. It can be seen from Figure 6.12 that the FLG_{WJM}-dominant electrode (Formulation E) showed higher porosity retention in comparison to the GNPs-dominant electrode (Formulation F). In this sense, the FLG_{WJM} graphene provides improved structural stability to maintain pores that provide "porous networks" for electrolyte movement. Similarly, the FLG_{WJM}-dominant electrode (Formulation E) shows lower change in the surface area of the electrode (see Table 6.1) and also the total thickness of the electrode after 200 cycles (see Table 6.2). Therefore, the graphene-dominant electrode's analysis shows that the FLG_{WJM} is much more electrochemically stable and robust compared to GNPs.

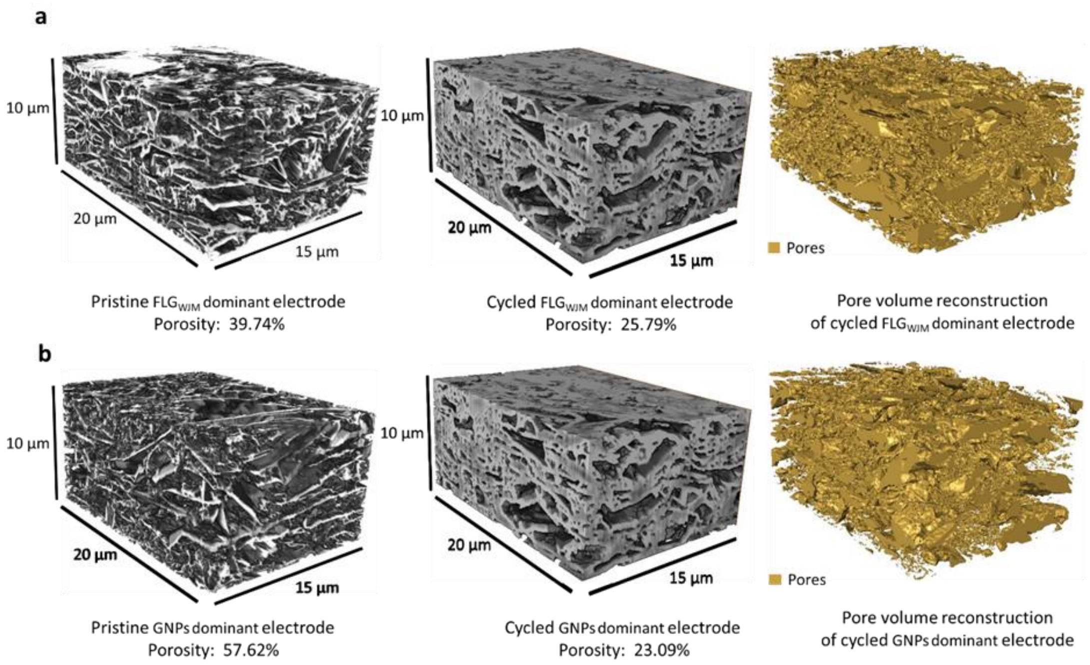

Figure 6.12: The greyscale 3D reconstructed volume of the electrode with (a) Formulation E - FLG$_{WJM}$ dominant, (b) Formulation F - GNPs dominant, before and after cycling for 200 cycles at the same current as applied to Formulation A - Si-FLG$_{WJM}$ composite.

Table 6.2: Surface Area (SA) comparison for graphene dominant electrodes before after cycling at the same current as applied to Formulation A - Si-FLG$_{WJM}$ composite.

Samples	SA – μm^2		SA – μm^2 (% change)
	Pristine	Cycled	Cycled
Formulation E	1.01755e+10	7.8323e+09	23.03%
Formulation F	1.28485e+10	6.43731e+09	49.90%

Table 6.3: Electrode thickness (SA) comparison for graphene dominant electrodes before after cycling at the same current as applied to Formulation A - Si-FLG$_{WJM}$ composite.

Samples	Thickness – µm		Thickness – µm (% change)
	Pristine	Cycled	Cycled
Formulation E	10.57	10.94	-3.50%
Formulation F	11.49	12.64	-10.01%

6.2.5 TORTUOSITY FACTOR CALCULATION

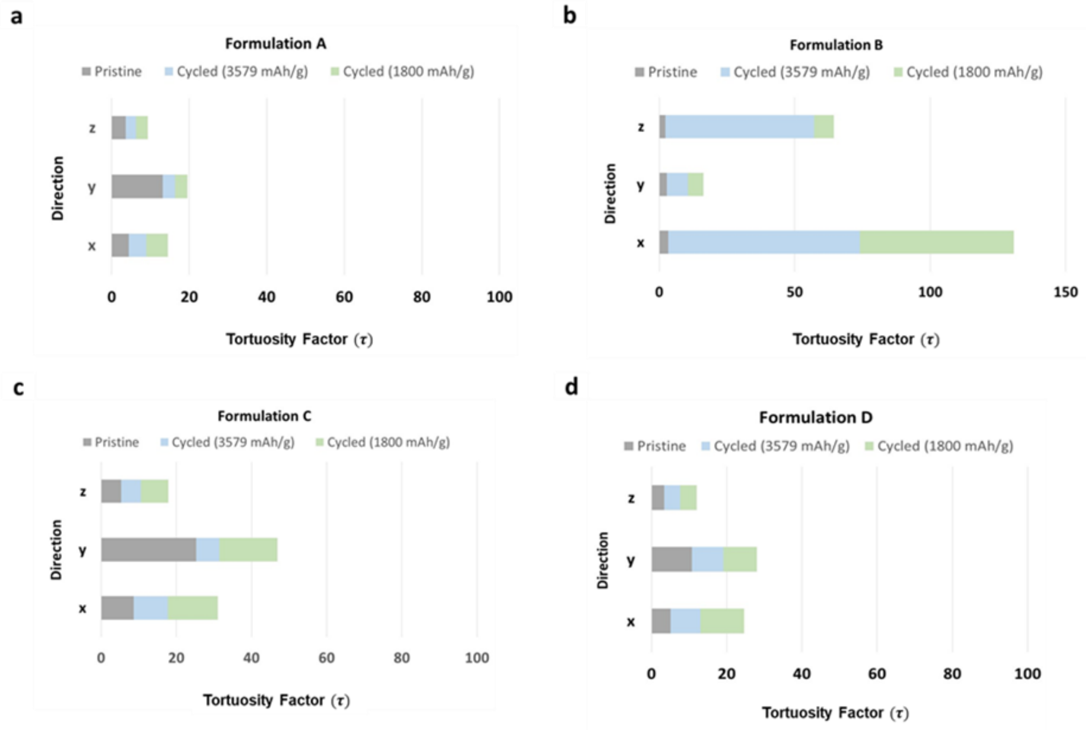

Figure 6.13: Tortuosity factor comparison between pristine electrodes and cycled electrodes after 200 cycles at Si's half and full capacity cycling for Formulations: (a) A; (b) B; (c) C and (d) D.

The tortuosity factor ($\boldsymbol{\tau}$) is an important parameter which is directly proportional to the ionic transport property of ions through pores[230]. $\boldsymbol{\tau}$ is calculated by simulating the steady-state diffusion flow through the 3D pore network[321]. In this work, tortuosity is calculated using the reconstituted structures from FIB-SEM characterisation, and

Figure 6.13 presents a series of measurements comparing pristine electrodes with those of cycled electrodes at full and half capacities. Formulations A to D were analysed in three directions x,y,z in the electrode areas sampled.

Formulation A (Figure 6.13a) has clearly retained the lowest $\boldsymbol{\tau}$ values in all directions in both the pristine and post 200 cycled samples. This is in alignment with the resulting superior electrochemical performance of the Formulation A electrodes in terms of a retained higher level of cycling efficiency and longevity. Formulation D (Figure 6.13d) also maintains a comparable level of x-y-z tortuosity after 200 cycles; these were based on a composite electrode of nano Si powder and $\mathrm{FLG_{WJM}}$. Formulation B (Figure 6.13b) demonstrated the highest level of tortuosity (especially in the x direction). These electrodes, based on predominantly micron-Si, experience the highest degree of volume expansion and particle fusion. This will dominate the structural transformation and it is consistent with the porosity reductions outlined in Figure 6.11. Tortuosity values calculated for Formulation C (Figure 6.13c) were between those of A and D and of B; these electrodes were based on a composite of $\mathrm{FLG_{WJM}}$ and micron-Si. The $\mathrm{FLG_{WJM}}$ enables porosity retention, mechanical resilience and also reduces the degree of electrochemical fusion of micron-Si particles. Long-range electrical conductivity also improves charge transfer levels – this is discussed in more depth in the next section on impedance characterisation. From Figure 6.13 generally, it can be seen that $\boldsymbol{\tau}$ values for each of the electrodes decrease upon cycling at full capacity, except for the formulation Formulation B. The explanation for this is that the Formulation B does not have any flexibility effect, which can help to sustain the volume changes, thereby the mesopores are continually filled by fragmented SEI layers.

For electrodes with graphene additives, $\boldsymbol{\tau}$ decreases, as the volume changes from silicon particles have resulted in macro-voids and these cracks act as carrier path for the electrolyte. The gradual decline of pore volume with broken SEI impedes the flow of Li^+ ions through the porous network. The architectural fragmentation is minimal in the Si-graphene hybrid anodes as inferred from impedance measurements reported in the following section and also reflected in $\boldsymbol{\tau}$. Formulations with Si-$\mathrm{FLG_{WJM}}$ (Formulations A and D), when cycled at full capacity, have a lower $\boldsymbol{\tau}$ when compared with cells cycled at half capacity. At full capacity, the electrode undergoes macro cracking with large volume changes exerted from the silicon fraction. It is assumed that Si's electrochemical fusion has been prevented by incorporation of graphene.

6.2.6 ELECTROCHEMICAL IMPEDANCE INVESTIGATIONS

The significance of incorporating graphene to improve the electrodes structural stability is further demonstrated by the sizeable improvement in the impedance relative to that of the Si-dominant anode. The Nyquist plots obtained from potentiostatic electrochemical impedance spectroscopy (PEIS) and the equivalent circuit used for the calculations are shown in Figure 6.14.

In Nyquist plots showed in Figure 6.14b-d and Figure 6.14h-j, the intersection point of the x-axis at 100 kHz refers to the series resistance (R_{series}). The first semicircle due to the SEI (R_{SEI}) can be identified between the frequency range of 100 kHz to 10 kHz, while the second semicircle of the charge transfer (R_{CT}) can be identified between the frequency range of 10 kHz to 10 Hz. The impedance response at lower frequencies between 10 Hz to 10 mHz seen as an angular line is generally attributed to diffusion processes[157]. Furthermore, the CPE_1 and CPE_2 reflect the double layer capacitance of the surface of SEI and active particles.

Figure 6.14b-d shows the Nyquist plots for full capacity cycling (3579 mAh g^{-1}) after 20, 50 and 100 cycles respectively, while Figure 6.14h-j are the Nyquist plots for half capacity cycling (1800 mAh g^{-1}) at the same cycle numbers. It is clear that in both cycling conditions, the high frequency and medium-high frequency (100 kHz – 10 kHz) responses of Formulation B increase the most significantly, being much larger than other formulations after 100 cycles. In accordance with cycling performance in Figure 6.5a and 6.5b, this indicates that the main failure mechanisms of the Si-dominant electrodes are caused by significant increases in both series resistance and SEI resistance.

With reference to Figure 6.14e-g and Figure 6.14k-m, the fitted impedance data of longer term cycling at full and half capacity respectively, there is a clear alignment with features of the corresponding Nyquist plots in Figure 6.14b-d and h-j. Generally, the series resistance (R_{series}) gradually increases upon cycling (as shown in Figure

6.14e and 6.14k), which can be caused by structural degradation within electrodes, during the volume changes as a function of cycle number. It can also be observed that for electrodes containing mainly Si (Formulation B) cycled at full capacity (Figure 6.14f), there is significant growth in series resistance after 30 cycles. This is likely to be caused by severe electrode pulverisation, which consumes a large quantity of Li^+ ions when forming new SEI. This is a continual process which reduces the Li^+ ion concentration in the electrolyte, thus decreasing the ionic conductivity. Similar behaviour has also been noticed for the Si-dominant electrode (Formulation B) cycled under half capacity (Figure 6.14k).

As observed in Figure 6.14f and 9l, the R_{SEI} generally increases with the cycle number, which indicates that the SEI layer is continuously growing caused by electrode pulverisation under large volume changes. The Si dominant electrodes (Formulation B) exhibit a steep rise in the R_{SEI} after 50 cycles at full capacity cycles (Figure 6.14f) due to the onset of severe electrode pulverisation, whereas the same situation is delayed up to 160 cycles for half capacity cycling (Figure 6.14l). Comparing with that, Si-graphene electrodes and particularly the Formulation A demonstrate much more stable R_{SEI} over cycling. It is possibly because the FLG_{WJM} flakes assist to maintain a stable structure under the large volume changes of Si nanoparticles and postpone the significant electrode pulverisation, thereby, reduce the opportunity to form new SEI on the freshly exposed Si surface.

It can be observed from Figure 6.14m that for all electrodes cycled under half capacity, the R_{CT} is mostly maintained at a relatively stable level. The initial decrease for the first 10 cycles can be explained as a result of denser packing of active particles with conductive graphene networks, under internal pressure from Si's large volume expansion[157]. While cycled under full capacity (Figure 6.14g), for electrodes with Formulation B, C and D, the R_{CT} increased after a few cycles and exponentially declines thereafter. To explain the R_{CT} result, it is better to firstly understand that the charge transfer process normally involves two steps, namely, de-solvation of the solvated Li^+ ions in the electrolyte and transportation of these Li^+ ions through the particle surface until it accepts an electron at the electrode's surface[290]. Therefore, it is possible that when the internal pores being clogged up with SEI species[65,79], there are less available Li^+ ions to be de-solvated and transported to the particle surface, which in turn increases the R_{CT}. This situation will be changed when there are large cracks appearing within electrode.

The large voids allow comparatively easy transportation of electrolytes within the electrode and thereby facilitate the availability of Li^+ ions to be transferred onto the surface of active particles, thus reduced the R_{CT}. However, for electrodes with Formulation A, it can be noticed that the R_{CT} remains at a stable level even cycled under the full capacity. It indicates that there is neither significant electrochemical agglomeration nor severe electrode pulverisation occurs during first 200 cycles. This is agreement with the tortuosity findings in Figure 6.14, which also supports the hypothesis that the synergistic effect of Si and FLG in the electrode composite enhances the cycling longevity, as FLG_{WJM} flakes impart long-range charge transfer networks and mechanical rigidity. Additionally, any pulverized Si particles could precipitate onto FLG_{WJM} flake surfaces and thereby still be electrically connected to contribute to capacity.

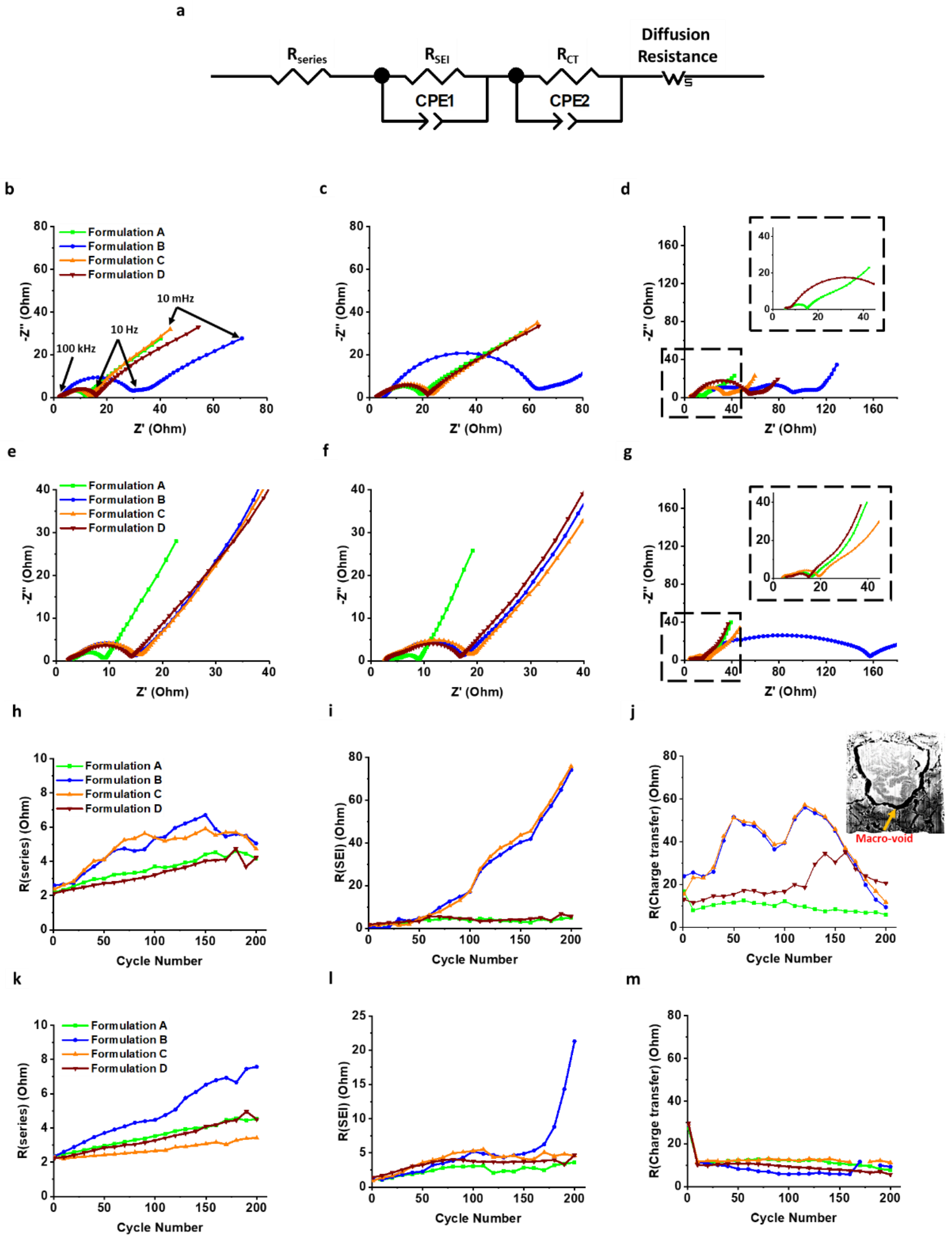

Figure 6.14: (a) The electrochemical equivalent circuit used for fitting the Nyquist plots; Nyquist plots during the charging process for all formulations cycled with full capacity of silicon (3579 mAh g^{-1}) after (b) 10 cycles, (c) 50 cycles and (d) 200 cycles (zoom-in plot shown as the inset); with half capacity of silicon (1800 mAh g^{-1}) after (e) 10 cycles, (f) 50 cycles and (g) 200 cycles (zoom-in plot shown as the inset); and the impedance fitting result comparison between (h-j) 3579 mAh g^{-1} and (k-m) 1800 mAh g^{-1} against (h,k) Series resistance (i,l) SEI resistance (j,m) interphase contact and charge transfer resistance. The legends for (b) also applies to (c-m).

6.3 SUMMARY

This study demonstrates that a facile one-step wet-jet milling applied to a dispersion of silicon and graphite, leads to a Formulation A (Si-FLG$_{WJM}$) composite that constitutes a high-performance anode, exhibiting enhanced capacity retention and the ability to function at a higher current density of 716 mA g^{-1}. In this composite, the silicon nanoparticles remain sandwiched between few-layer graphene flakes, the latter obtained by the direct liquid-phase exfoliation of graphite. Silicon and FLG$_{WJM}$ form a layered porous conductive network. The uniform distribution of silicon nanoparticles on the FLG$_{WJM}$ flakes surface forms an optimised "porous network" structure, allowing the effective transport of electrons and Li$^+$ ion with unconstrained electrolyte movement. This Si-FLG$_{WJM}$ composite powder when used as anodic material yields highly reversible electrochemical performance (reversible discharge capacity > 2280 mAh g^{-1} after 200 cycles) with exceptional capacity retention and higher rate-capacity compared to the Si-dominant electrode or to electrodes obtained by simply mixing Si and FLG$_{WJM}$ or commercial graphene nano-platelets. The superior stable cycling and rate performance of the Si-FLG$_{WJM}$ composite electrode can be attributed to several factors: (i) the high surface area of FLG$_{WJM}$ flakes, with enhanced electrical conductivity (providing increased electron transport pathways between the silicon particles); (ii) the highly porous network of Formulation A composite allowing facile pathways for electrons and lithium ions, enhancing the electrical conductivity and lithium diffusion rate; (iii) the voids surrounding the silicon nanoparticles can accommodate the volume changes from silicon particles (essential for superior performance), and (iv) the FLG$_{WJM}$ flakes restricts the silicon particle from electrochemical fusion (coalescence) resulting in more stable electrochemical performance, (v) the planar FLG$_{WJM}$ flakes-like structure imparts a degree of flexibility to the electrodes and thereby endure the volume strains during silicon lithiation. Due to the 3D carbonaceous framework, the Formulation A composite electrode demonstrates excellent cycling stability even under silicon's full capacity cycling. This excellent performance with further optimisation of the electrode formulation is propounded to improve high-capacity cycling stability and also scalability of the product makes it a prospectus anode material for LIBs.

CHAPTER 7. HYBRID SILICON-TIN ELECTRODE AS HIGH CAPACITY ANODE IN LITHIUM-ION BATTERIES

Carbonaceous materials are a common conductive additive for improving the performance of high capacity anode materials such as silicon. With an increased weight fraction of these conductive additives in the composite, there results a decreases in the battery's gravimetric and volumetric capacity. In this study, the performance synergy between silicon and tin was investigated and was compared with the individual contribution of each material separately. The hybrid composite exhibits a stable specific discharge capacity, suggesting a promising high capacity anode material. The enhanced performance of this hybrid anode can be accredited to tin because of its metallic, ductile property and the complemented charge transfer. Physicochemical analysis has indicated that the Si-Sn hybrid composite electrode is a prospective anode material for lithium-ion batteries. Furthermore, the Si-Sn heterostructure using Sn-seed catalysts for the SiNW growth with combined nano-crystalline and amorphous Si phases via a radio-frequency PECVD technique was also studied.

7.1 MOTIVATION TO INCORPORATE TIN AS AN ADDITIVE AND CO-HOST MATERIAL

The inactive carbonaceous components within the composite affects the gravimetric and volumetric capacity[129,322,323]. This motivates us to incorporate a component in the electrode composite that acts with a dual purpose, as a lithium host and also as a conductive agent. Intense and widespread research efforts into new materials for LIBs have focused a lot of interest on the group IV elements (Si and Sn primarily)[324,325]. Si and Sn are the two most studied materials both individually and as alloy negative electrode materials and both have made some progress towards entering the commercial arena[326,327].

More recently there have been attempts at hybridising Si and Sn within the same electrode, e.g. an investigation using Sn nanoparticles as an effective, conductive additive for Si-based anodes in Li-ion half-cells[155,328,329]. The first study claimed that the presence of the Sn (as low as 2 %) dramatically improves the electrode's performance in terms of both charge capacity and cycling stability[328]. It proposed to have achieved this by being uniformly dispersed in the Si network but also reducing the electrical resistance of the electrode structure as a whole. As such, Mangolini *et al.* the synergistic effects between the materials lead to batteries that exceed the performance of each of the two components alone[328]. This is attributed to the high electrical conductivity and good reversible energy storage capacity of Sn. Other researchers have looked at silicon-tin hybrid anode systems for solid-state Li-ion batteries achieving reversible capacities up to 700 mAh g^{-1} [330]. Combining hybridised "yin-yang" silicon-tin porous nanocomposites with graphene has also been used as an approach for generating low-cost and low energy consumption materials with promising electrochemical performance[328]. The benefits from Sn in the Si-based electrode largely depends on the microstructure of the composite. In this study, the performance synergy between silicon and Sn was demonstrated that outperforms the individual contribution of each material alone.

In this study the following two approaches to generate hybrid Si-Sn electrode was applied:

Approach one: Conventional electrode mixing;

Approach two: Si-Sn heterostructure film synthesis via plasma-enhanced chemical vapour deposition.

In the conventional electrode mixing approach, 50 % of the active Si was substituted by Sn, *i.e.* 1:1 active mass ratio. Herein the first approach towards optimising the Si-Sn hybrid system as an advanced anode material for LIBs is presented. A hybrid composite containing silicon and Sn was prepared by high-energy, high-shear mixing. This process results in a very homogeneous distribution of Sn particles in the silicon matrix. Addition of Sn to the silicon-based anode enhances the electrochemical performance of the composites[152,153]. This study investigates the performance synergy between silicon and Sn compared with the individual contribution of each material alone. Although no research has been carried out on understanding microstructural evolution for the hybrid Si-Sn composite electrodes, advanced characterisation is needed to better understand the degradation modes of this hybrid system.

In the second approach, silicon and Sn were co-deposited using an advanced manufacturing technique (plasma-enhanced chemical vapour deposition), shown to be a scalable process that can facilitate film growth on 3D substrates. Uniform and hybrid crystalline-amorphous Si nanowire (SiNW) growth is achieved via a vapour-liquid-solid mechanism using a Sn metal catalyst. SiNWs of less than 300 nm diameter are known to be less susceptible to fracture and when grown this way have direct electrical conductivity to the current collector, with sufficient room for expansion[118]. Electrochemical characterisation along with morphological analysis using SEM and TEM were carried out in this feasibility study. The findings are thought to have an impact on the development of flexible batteries and wearable energy storage.

7.2 HYBRID ANODE VIA CONVENTIONAL MIXING

Figure 4.6 summarises the sample formulations reported and tested in this study. In addition to the silicon-tin (Si-Sn) hybrid composite obtained by conventional mixing, two other formulations have been prepared and used as a systematic comparison. These were based on Si-dominant and Sn-dominant as control formulations. The rationale for this was to compare the influence of Sn incorporation. The Si-Sn hybrid used in this study was prepared with Si:Sn weight ratio of 1:1 and they were mixed with a conductive carbon (Super C65) and polyacrylic acid (PAA) as the binder. The formulation ratio of electrode slurry used was active mass: binder: carbon: 70:14:16 (wt.%). The reader is requested to refer to section 4.1.4.1 (Figure 4.6) for formulation details.

7.2.1 RESULTS AND DISCUSSION

7.2.1.1 ELECTROCHEMICAL CHARACTERISATION

All the electrodes were tested under galvanostatic cycling at a voltage range of 0.05-1.0 V at 0.2 C. To understand the relationship between cycling stability and electrode structural changes, the cells were cycled at both moderate and extreme capacities of silicon. A limited discharge capacity (de-lithiation) of Si, *i.e.* 1800 mAh g^{-1} would minimise the volume expansion and thus avoid the likelihood of pulverisation[42]. For Si-Sn hybrid electrodes, the capacity contribution from Sn is assumed to be 994 mAh g^{-1} [40,41]. When cycling the Si-Sn hybrid at full capacity *i.e.* at 2286 mAh g^{-1}

$\left(\frac{1}{2}\,(3579, from\ Si) + \frac{1}{2}\,(994, from\ Sn) = 2286.5\right)$ corresponding to a current density of 228.6 mA g^{-1} at 0.2 C. Whereas the half capacity for the Si-Sn hybrid is 1447 mAh g^{-1} $\left(\frac{1}{2}\,(1800, from\ Si) + \frac{1}{2}\,(994, from\ Sn) = 1447\right)$ corresponding to a current density of 144.7 mA g^{-1} at 0.2 C. Electrodes were cycled at maximum experimental capacity and also at restricted capacity to understand the influences from Sn in the hybrid electrode.

Figures 7.1a and 7.1b show the cycling behaviour of the Si-Sn hybrid and Si-dominant electrodes under galvanostatic conditions. When cycled without any limitation on capacity as in Figure 7.1a, it can be observed that a continuous capacity decrease upon cycling. In particular, the Si-dominant electrode, consisting of µm Si without Sn, after 100 cycles delivers less than half of the initial capacity. The addition of Sn (in Si-Sn hybrid) can improve the performance of this type of silicon. In the hybrid electrode, despite the initial capacity drop during the first 10 cycles, capacity values become more stable for prolonged cycling.

The behaviour observed for Si-dominant electrode could be related to the larger Si-particle dimensions, leading to a relatively rigid framework resulting in pulverisation and higher tortuosity for Li^+ ion transport. This increases cell resistance, which is alleviated by the addition of µm Sn particles in Si-Sn hybrid formulation as discussed further in electrochemical impedance section 7.2.1.3.

Further improvements in the electrochemical performance can be obtained by cycling the cell at a limited capacity of silicon (50 % of Si’s capacity, *i.e.* 1800 mAh g^{-1}) - see Figure 7.1b. It should be noted that the Si-Sn hybrid electrode formulation cycled up to 200 cycles under a current density of 289 mA g^{-1}. The Si-Sn hybrid showed prolonged cycle life with no significant capacity degradation until 125 cycles (Figure 7.1b), compared with Si-dominant formulations. The main reason for capacity loss in Si-Sn hybrid formulation after 125 cycles could be attributed to the collapse of the electrode’s architecture (microstructure) and continuous growth of SEI in µm Si and Sn particles. These further results in the pore clogging and increased resistance for Li^+ ion diffusion[65,281], as discussed in the following sections (where the tomography and impedance studies are presented). From the cycling profiles, it is evident that the incorporation of Sn in the Si-electrode has a significant and positive effect on cyclic stability.

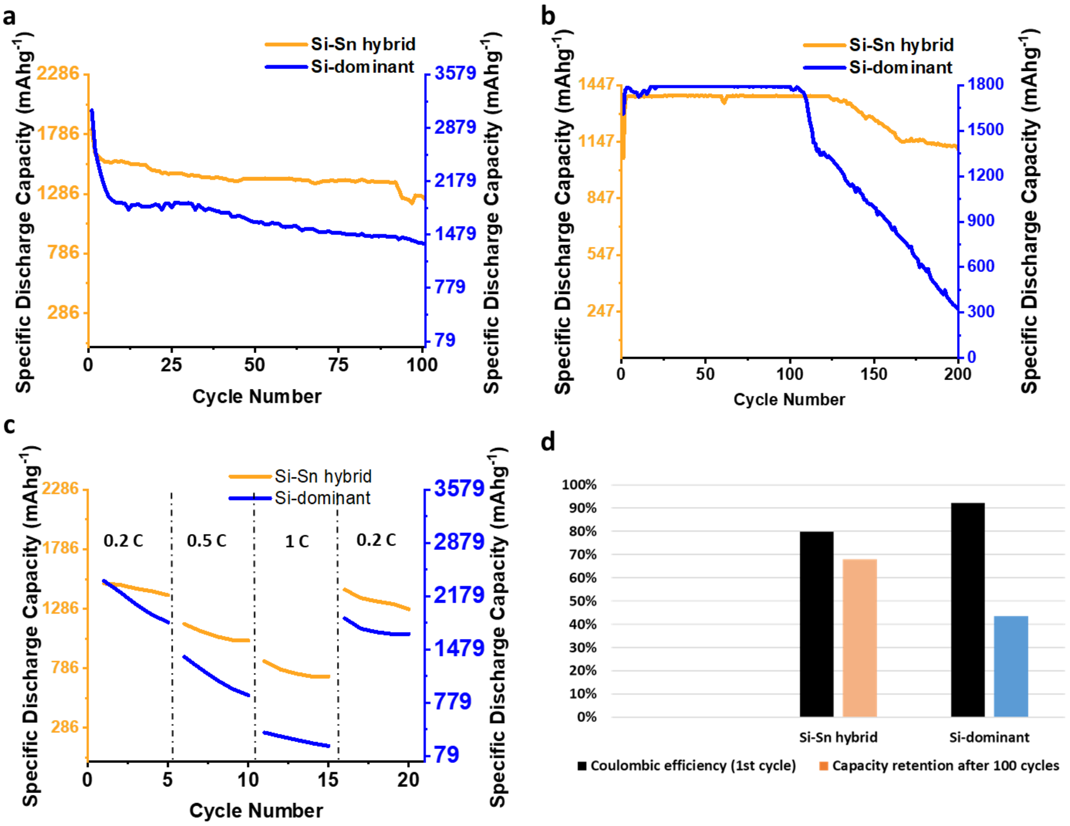

Figure 7.1: Specific discharge capacity or de-lithiation (based on the active mass) profiles of formulations cycled at (a) full capacity (2286 mAh g^{-1} for Si-Sn hybrid and 3579 mAh g^{-1} for Si-dominant), (b) half capacity (1447 mAh g^{-1} for Si-Sn hybrid and 1800 mAh g^{-1} for Si-dominant), (c) rate capability test for both the formulations, and (d) coulombic efficiency for the 1st cycle at 114 mA g^{-1} and 179 mA g^{-1}, respectively for Si-Sn hybrid and Si-dominant electrode; capacity retention after 100 cycles at 456 mA g^{-1} and 716 mA g^{-1}, respectively for Si-Sn hybrid and Si-dominant electrode.

The lithium interaction behaviours of Sn and silicon are similar, *i.e.* alloying compared with intercalation, as occurs within graphitic anodes[73,153]. This study further explores the rate performance of all the formulations at different current densities including, 0.2 C, 0.5 C, and 1 C (Figure 7.1c). As observed in Figure 7.1c, the Si-Sn hybrid electrode possesses 63.22 % of its initial capacity at 0.2 C after 5 cycles. By increasing the current density, the reversible capacity drops to 1018.48 mAh g^{-1} at 0.5 C (45.98 % retention) and subsequently to 719.02 mAh g^{-1} at 1 C (32.45 % retention). Upon lowering the current density to 0.2 C, the reversible capacity of Si-Si hybrid increases to 1282.63 mAh g^{-1} at 0.2 C (57.90 % retention). Thus, Si-Sn hybrid electrode presumed to undergo a minimal degradation in comparison to Si-dominant electrodes at higher current density. This could be attributed to the metallic and ductile nature of Sn, which could buffer of the volumetric changes from Si particles and also maintain a conductive network.

Figure 7.1d displays comprehensive data on the first cycle and after 100 cycles at full capacity. For a Si-Sn hybrid composite, the first cycle coulombic efficiency is 80 %, which is slightly lower than for the Si-dominant system. The higher capacity loss in the 1st cycle for Si-Sn hybrid composites can be accredited to a greater electrolyte decomposition on the surfaces of Si and Sn. Nevertheless, from Figure 7.2d it is worth noting that the Si-Sn hybrid formulation is promising for the stable reversible capacity cycling in comparison to the Si-dominant electrode. The Si-Sn hybrid electrode offers a reversible discharge capacity of 1243 mAh g^{-1} with a capacity retention of 68.08 % after 100 cycles with a capacity loss of 3.2 % per cycle, a value that is superior to Si-dominant electrodes.

In order to augment the understanding of the hybrid composites, the redox reactions and the transformation steps of Si-Sn hybrid vs Li/Li^+ during lithiation/de-lithiation processes need to be analysed. The differential capacity plot (dQ/dV vs. V) in Figure 7.2a shows more details on the electrochemical reactions taking place during lithiation and de-lithiation vs. Li/Li^+. There are only three redox peaks during lithiation/de-lithiation of the Si-Sn hybrid electrode and also in the Sn-dominant electrode. However, the redox peaks above 0.6 V are not distinctively visible in the Si-Sn hybrid which corresponds to the formation and conversion of Li_2Sn_5 phase[331]. In Si-Sn hybrid, during lithiation, the third cathodic peak corresponds to the formation of $Li_{22}Sn_5$ and simultaneously the amorphous $Li_{3.5}Si$[23,73,98–100]. Similar to the lithiation process, there are three stages of de-alloying during the de-lithiation process, corresponding to the reformation of a-Si and $Li_{22}Sn_5$[73,331]. The first anodic peak at 0.28 V corresponds to the formation of $Li_{2.0}Si$[73]. The second anodic peak at 0.45 V corresponds to the de-alloying of a-$Li_{2.0}Si$ to form amorphous Si with the onset potential of ~ 0.41 V[73]. Further, above 0.5 V can be attributed to the formulation of β-LiSn and further to delithiated Sn[331,332].

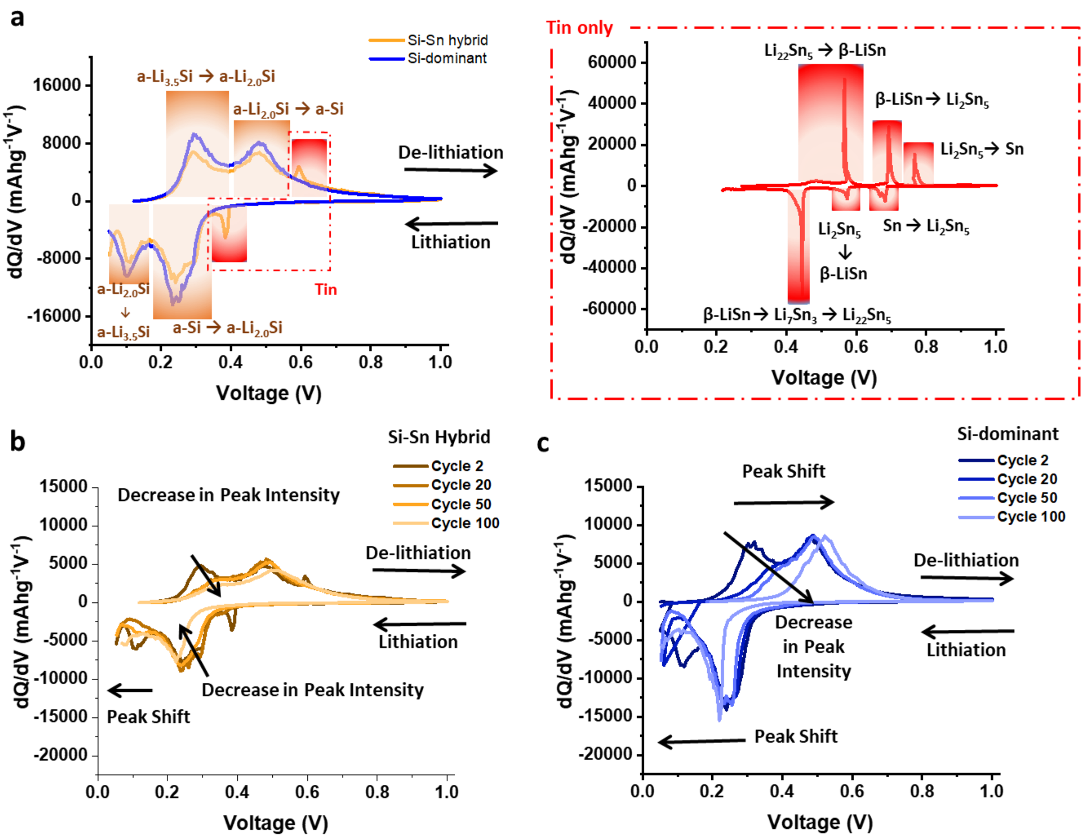

Figure 7.2: (a) dQ/dV plot for 2nd cycle of Si-Sn hybrid electrode and Si-dominant electrode (dQ/dV profile for Sn-dominant electrode between 0.05-1.0 V is shown as the inset); dQ/dV plot with incremental cycle numbers for (b) Si-Sn hybrid electrode and (c) Si-dominant electrode. Presented data are for the cells cycled at full capacity of electrodes.

It is also observed that with increasing cycle number there is a decrease in peak intensity and also shift in the peaks' occurring voltage (see Figures 7.2b and 7.2c). The above can be attributed to the increase overpotential within the electrode, *i.e.* impedance due to continual SEI growth and architectural breakdown. After 100 cycles the area beneath the lithiation peaks has decreased by a vast amount for the Si-dominant electrode compared with the Si-Sn hybrid electrode. In conclusion, the differential capacity plot of the Si-Sn hybrid composite indicates that both Si and Sn are electrochemically active within the operating potential range.

In order to estimate the capacity contribution from Sn in the composite electrodes within the same cut-off voltages, the electrochemical performance obtained by the use of Sn-dominant electrode is presented. It can be observed from Figure 7.3, that the Sn can contribute about 233.85 mAh g^{-1} reversibly up to 15 cycles, after which the electrode undergoes huge capacity fade. After 100 cycles the Sn-dominant electrode contributes to only 40.47 mAh g^{-1} (see Figure 7.3). It is important to note that Si and Sn provides a synergistic performance in comparison to individual dominant electrodes. Therefore, the contribution of Sn to the effective capacity is distinctively significant.

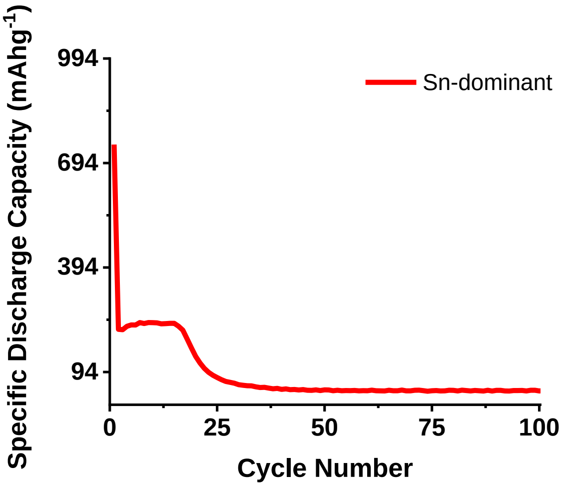

Figure 7.3: (a) Specific discharge capacity plot for Sn-dominant electrode.

In summary, the reversible capacity retention of Si-Sn hybrid system is invariably higher than the Si-dominant electrode for all the different current densities tested. Both the cycling stability and rate capability reaffirm that Si-Sn hybrid is more resilient to capacity fade from volume expansion strain in comparison to Si-dominant or Sn-dominant electrode. Herein, the reduced capacity retention in Si-dominant electrodes is attributed to the higher resistance from continuous growth and breakdown of SEI along with a diminishing pore network. The superior cyclic performance of Si-Sn hybrid composite electrode could be attributed to the retained morphology of the electrode as discussed further in section 7.2.1.2. The Sn provides structural rigidity and hinders Si particles from detaching due to pulverisation, from the conductive network of Sn.

7.2.1.2 MORPHOLOGY EVOLUTION

The morphological evolution of the Si-Sn hybrid composite, Si-dominant and Sn-dominant for pristine electrodes and cycled electrodes (200 cycles) were analysed using FIB-SEM, which allows for the visualisation and quantification at the three-dimensional (3D) scale[25,29,30,68,231]. These studies are valuable in offering more evidence of the benefits on the electrode structural changes brought about by the incorporation of Sn in silicon-based anodes. Results are given in Figures 7.4 and 7.5 that reports the comparison of Si-Sn hybrid composite electrode with Si-dominant and Sn-dominant, before and after cycling. Despite the µm Si and Sn particles in the Si-Sn hybrid electrode, after cycling the electrodes were found to retain their porous 3D morphology. The metallic and ductile nature from the Sn plays favourably towards the Si-Sn hybrid electrode's stability during lithiation/de-lithiation. This accommodates the huge volume changes of silicon particles while maintaining electrical connectivity throughout the electrode and thereby improves the electrode's fatigue property during cycling aging.

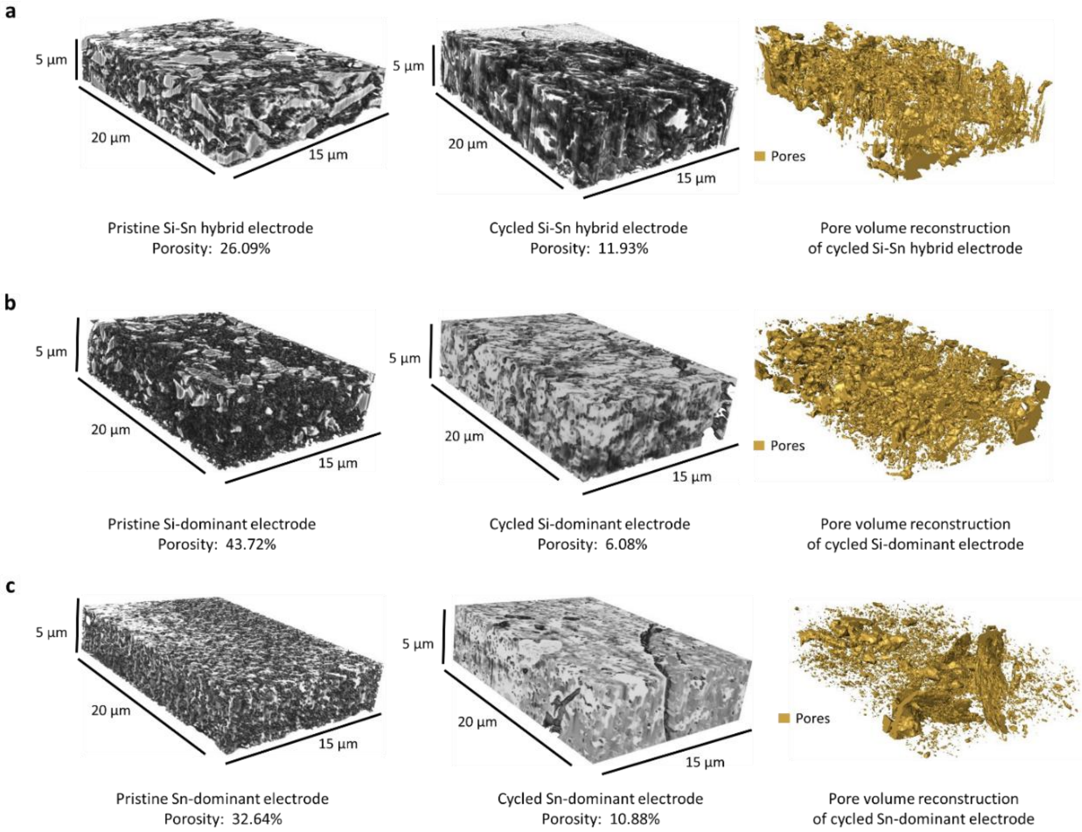

Figure 7.4: 3D FIB-SEM tomography reconstruction of all formulation at full capacity. The greyscale 3D reconstructed volume of the electrode with (a) Si-Sn hybrid, (b) Si-dominant, and (c) Sn-dominant, before and after cycling for 100 cycles.

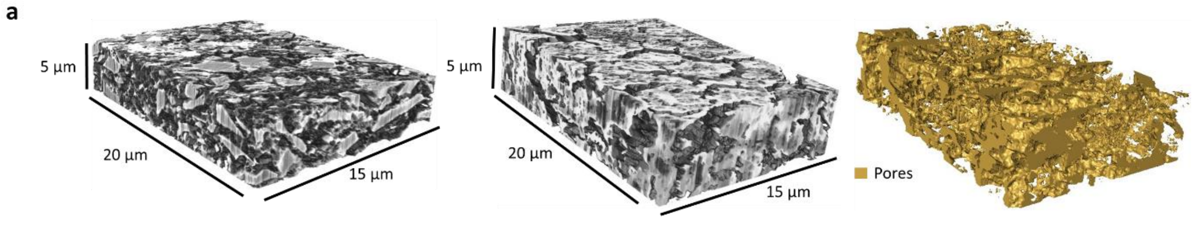

Pristine Si-Sn hybrid electrode
Porosity: 26.09%

Cycled Si-Sn hybrid electrode
Porosity: 18.42%

Pore volume reconstruction
of cycled Si-Sn hybrid electrode

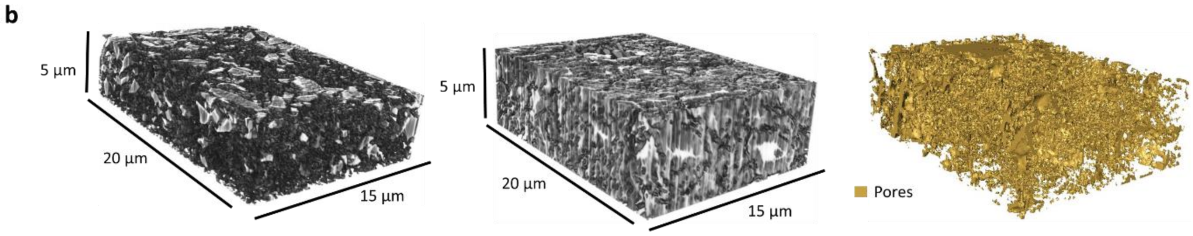

Pristine Si-dominant electrode
Porosity: 43.72%

Cycled Si-dominant electrode
Porosity: 15.18%

Pore volume reconstruction
of cycled Si-dominant electrode

Figure 7.5: 3D FIB-SEM tomography reconstruction of all formulation at half capacity. The greyscale 3D reconstructed volume of the electrode with (a) Si-Sn hybrid and (b) Si-dominant, before and after cycling for 100 cycles.

Tomography was performed on the pristine and aged electrodes (after 100 cycles) for all three formulations studied. The subsequent SEM images were reconstructed to obtain a 3D volume of the bulk material, which gives an indicative porosity and phase fraction change as a function of capacity limit. Figures 7.4 and 7.5 show processed images that graphically represent the porosity of the materials for all the formulations. The region of interest for the samples ranged between 25 × 12 μm^2 to 25 × 35 μm^2 since the cycled electrodes had a variable change in thickness of the electrode. From this, a 3D reconstructed volume of 20 × 5 × 15 μm^3 across all the samples was obtained. The porosity can be calculated from the processed images, and in Figures 7.4 and 7.5 it can be observed that there is a segregation of pore groups upon cyclic aging. In Si-dominant electrodes, merging among the particles in the cycled electrodes can also be seen. This is most likely to result from the huge volume expansion and electrochemical fusion of particles - similar to observations made in previous studies[79,285].

The fact that Si-Sn hybrid electrodes show superior synergy properties in comparison to the Si-dominant and the Sn-dominant electrodes could be attributed to ductile nature of Sn which act as a mechanical buffer for stress in the silicon composite during the huge volume changes during lithiation and delithiation processes[333]. As showed in Figure 7.6a, the porosity retention is higher in the Si-Sn hybrid anodes in comparison to Si-dominant and Sn-dominant electrodes. When Sn is introduced into the formulation, it can be seen that the porosity of the cycled electrodes at full capacity decreases by only 54 % for the Si-Sn hybrid in comparison to 86 % for the Si-dominant hybrid (see Figure 7.6a). In particular, the Si-Sn hybrid electrode when cycled at half capacity, shows less change in porosity of about 29 % with respect to the pristine electrode. In this sense, these pores also help to maintain sufficient void structure around the active particles providing “porous networks” to the electrode architecture. Reduced porosity or increased tortuosity may adversely affect the lithium permeability and diffusion into the active material, resulting in capacity loss. The observation of cracks on the electrode surface is consistent with previously reported studies[79,282,283]. This observation can also be supported by the impendence study, which is discussed below.

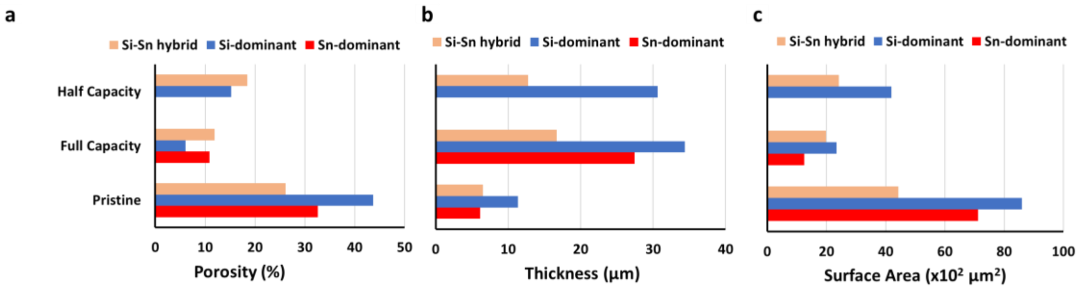

Figure 7.6: Geometrical property comparison after cycling at half and full capacity. Electrode’s (a) porosity, (b) thickness and (c) pore surface area comparison.

The presence of Sn in the electrode is believed to buffer the stresses in the structure during lithiation of Si, and this influence is very much evident in the electrode’s thickness post-cycling[152,153]. The initial thicknesses of the pristine electrodes were recorded as well as the post-cycling thicknesses, and these are shown in Figure 7.6b. In the case of Si-Sn hybrid electrode, there is a relatively smaller increase in the thickness of the electrodes after cycling at full capacity by > 157 %. Whilst the thickness value post-cycling increase to 204 % and 346 % in the Si-dominant electrode and Sn-dominant electrode, respectively (see Figure 7.6b). Another observation is that electrodes containing Sn, which have been cycled at a half capacity, have a lower increment in electrode thickness with respect to Si-dominant electrodes cycled at half capacity. Comparing the surface areas in contact with the electrolyte for the pristine electrodes and the cycled electrodes, as reported in Figure 7.6c, it can be seen that there is a huge decrease in the specific surface area for all the formulation. Specifically, in the Si-dominant electrode, the surface area is reduced by > 73 %. These values slightly decrease to 55 % when Sn is added (Si-Sn hybrid). The Si-Sn hybrid anodes have undergone the least changes in pore surface area at full capacity, and half capacity and this shows the advantage of having Sn in the electrode.

The Sn in Si-Sn hybrid formulation maintains a porous network for the active silicon particle undergoing volume changes upon lithiation and de-lithiation and maintaining “porous networks” for the electrolyte. From Figure 7.6 there is direct evidence of Si-Sn hybrid composite as the superior structure bestowing larger pore channels with longer and more flexible conductive networks, to absorb the continuous volumetric stains from silicon particles upon cycling. Therefore, it can be concluded that by accommodating volume expansion, the electrode structure is more structurally robust and that pulverisation dominates the capacity fade of the cell under the limitation of half capacity. While for cells cycled under full capacity the electrochemical particle fusion through SEI is more significant and both SEI growing and particle pulverisation contribute to the ultimate cell degradation.

7.2.1.3 ELECTROCHEMICAL IMPEDANCE

The significance of incorporating Sn to improve the electrodes structural stability was demonstrated by the sizeable improvement in the impedance relative to that of the Si-dominant anode. The Nyquist plots obtained from potentiostatic electrochemical impedance spectroscopy (PEIS) and the equivalent circuit used for this calculation are shown in Figure 7.7.

The first semicircle due to the SEI (R_{SEI}) can be identified between the mid frequency range of 100 kHz to 10 kHz, while the second semicircle of the charge transfer (R_{CT}) can be identified between the frequency range of 10 kHz to 10 Hz. The impedance response at lower frequencies between 10 Hz to 10 mHz seen as an angular line is generally attributed to diffusion processes[157]. Furthermore, the CPE_1 and CPE_2 reflect the double layer capacitance of the surface of SEI and active particles.

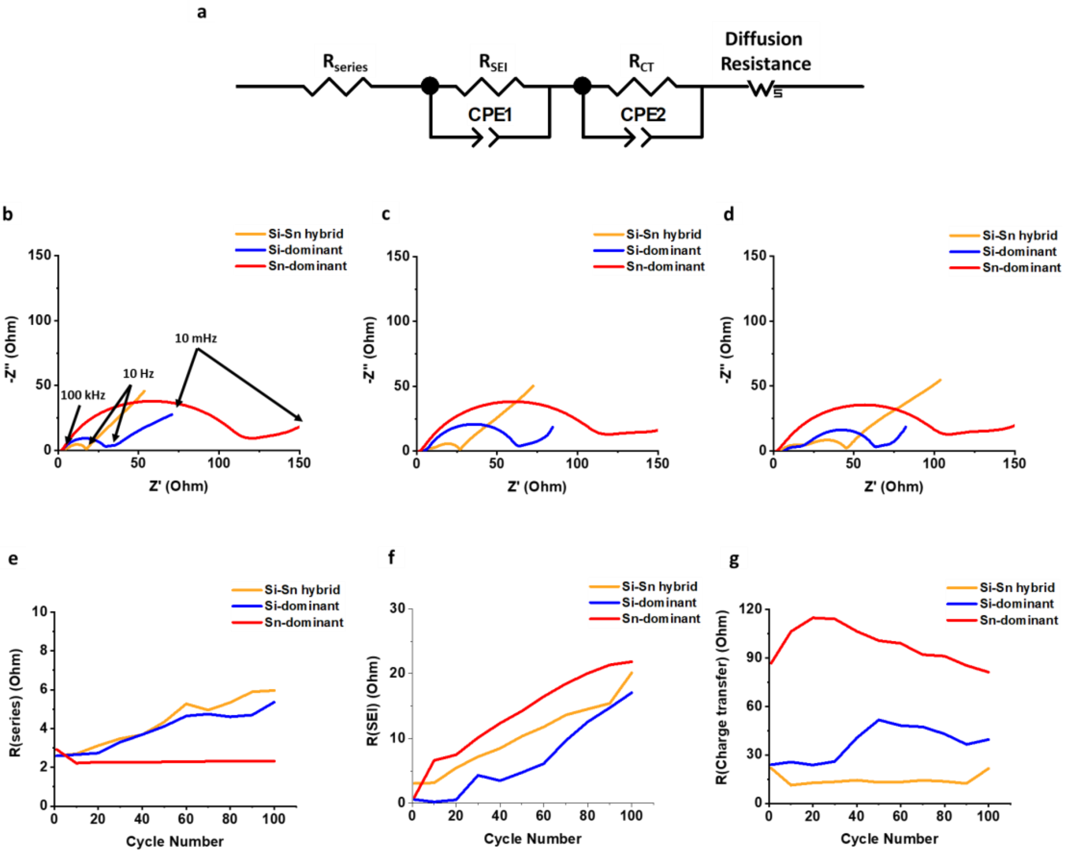

Figure 7.7: (a) The electrochemical equivalent circuit used for fitting the Nyquist plots; Nyquist plots during the charging process for all formulations cycled with full capacity after (b) 10 cycles, (c) 50 cycles and (d) 200 cycles; and the impedance fitting result comparison against (e) Series resistance (f) SEI resistance (g) interphase contact and charge transfer resistance.

According to the Nyquist curves in Figures 7.7b-c, upon cyclic aging, the Si-Sn hybrid electrodes display substantially low impedance compared to Si-dominant electrodes due to lower charge transfer resistance. Figures 7.7e-g shows the fitted impedance values of all the different formulation, which are in correspondence with Nyquist plots.

Generally, the series resistance (R_{series}) gradually increases upon cycling (as shown in Figure 7.7e), which is possibly caused by the micro-cracks generated within electrodes during the large volume change over cycles. However, the lower R_{series} displayed by Sn-dominant electrode could be attributed to the metallic property of Sn.

As observed in Figure 7.7f, the increasing trend in the R_{SEI} could be attributed to the continuum growth of the SEI layer, mainly due to the pulverisation of the active particles due to large volume changes.

It can be observed from Figure 7.7g that the R_{CT} increased after a few cycles and exponentially declines thereafter. To explain this observation it is important to understand the charge transfer process. It typically involves two steps, namely, de-solvation of the solvated Li^+ ions in the electrolyte and transportation of these Li^+ ions through the particle surface until it accepts an electron at the electrode's surface[290]. Therefore, as the micropores are being clogged up with broken SEI species[65,79], there is reduced availability of Li^+ ions to be de-solvated and transported to the particle surface, thereby increasing the R_{CT}. This situation is reversed with the appearance of large cracks. The large voids allow comparatively easy transportation of electrolytes within the electrode and facilitates the availability of Li^+ ions, thus reduce the charge transfer resistance or enhancing the rate capability. However, for Si-Sn hybrid electrodes, it can be noticed that the R_{CT} remains at a stable level, even when cycled at full capacity. This supports the hypothesis that the synergistic effect of Si and Sn in the electrode composite enhances the cycling longevity, from Sn's metallic nature and ductility.

7.3 HYBRID Si-Sn HETEROSTRUCTURE FILM VIA PLASMA-ENHANCED CHEMICAL VAPOUR DEPOSITION

When considering silicon as the predominant anode active material, the one-dimensional aspect of silicon nanowires (SiNWs) has received widespread attention[102,334]. It reported to be structurally beneficial as an anode active material as it: (i) allows sufficient space between collections of nanowires to accommodate the volume changes brought about by lithiation, and (ii) allows axial/radial stress relaxation of the nanowires[335]. This relaxation is thought to alleviate any progressive pulverisation that is commonly observed in the bulk and thick film Si structures during operational cycling[118,336]. Metal-assisted vapour-liquid-solid (VLS) mechanism is a widely used approach to obtain anisotropic 1D nanowires owing to its simplicity and versatility with regards to semiconductor nanowires[253,337]. This method represents an alternative manufacturing route beyond conventional composite electrode fabrication methodology and could constitute an economically viable, less energy-intense production route within energy storage manufacturing[253].

The crystalline properties of nanowires grown this way is considered to be of good quality and sometimes referred to as “defect-free”, with the exception of multiple twin defects that can cut across the nanowires[336]. Si is a commonly used alloying element in several grades of aluminium and steel[338] but does not alloy to a high degree with Sn since the solubility of Sn in Si is very low ($\approx 5 \times 10^{19}$ cm^{-3})[339] as illustrated by the binary phase diagram for the silicon-tin alloy system (see Figure 4.2). The reader is requested to refer to section 4.1.3 (Figure 4.3) for heterostructure synthesis details.

7.3 RESULTS AND DISCUSSION

7.3.1 MORPHOLOGY

The morphology and vertical cross-section microstructure of the vapour deposited Sn-SiNWs film is shown in Figure 7.8a and 7.8b. The Pt layer seen in the cross-section Figure 7.8b is used to protect the sample from any damage induced by the ion beam. Identification of the phase composition of the intermetallic Cu-Sn layer by X-ray diffraction was challenging due to the thickness of the films making detection of the intermetallics very difficult. The Sn catalyst layer in Figure 7.8c deposited prior to any Si alloying and precipitation can be seen to appear as quite a uniformly self-assembled series of spherical deposits that are crystalline. The catalyst is subsequently treated under a H_2-plasma before the growth of SiNWs following the introduction of the silane gas.

The assembly of layered thin films relies on interfacial integrity has been found to have a profound effect on the resulting function[340]. The formation of intermetallics between Si, Sn and the underlying Cu substrate may significantly affect the stability of the interface – this could promote the adhesion quality of the active anode film and warrants more in-depth investigation beyond the experimental scope of this study.

The SiNWs have a very high aspect ratio, as can be seen in Figure 7.8a, with diameters typically around 100 – 150 nm and lengths of up to 10 µm, incorporating a significant mass of SiO_2 shell. This cannot be directly or very easily quantified as the nanowires are combined with a Sn layer that will have its own associated oxide layer. With higher magnification, it is evident that many of the NWs have kinks in their 2D morphology as shown in Figure 7.8a. The zig-zag morphology found in some of the nanowires is due to stacking-fault energy of Si (50 mJ m^{-2}) – this generates twins during crystallisation[336] as shown in Figure 7.9b. Twin defects are a special type of grain boundary occurring commonly in many different minerals and are perpendicular to the growth direction of the nanowire. Likely crystalline parameters are illustrated: single crystalline wires are connected by a 120^{o} angle joint.

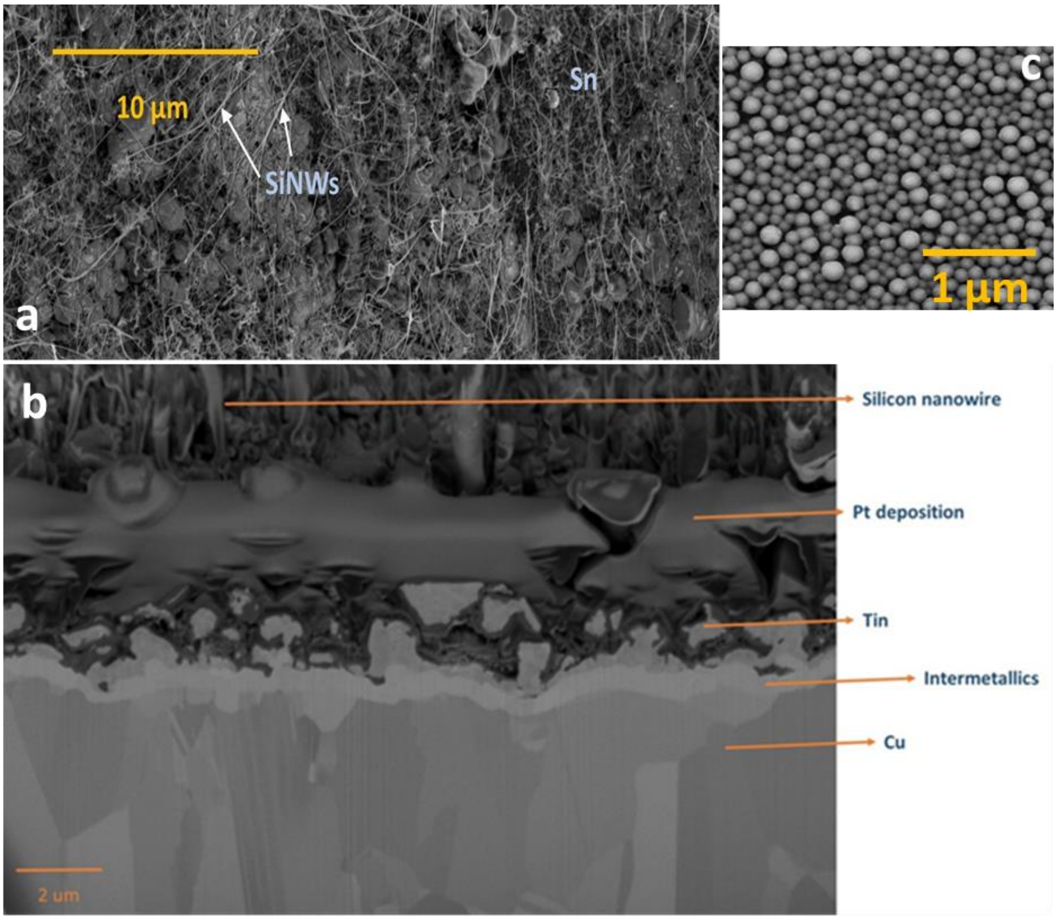

Figure 7.8: (a) Morphology of vapour deposited Sn-SiNWs film (top-view). (b) FIB cross-section of SiNW-Sn hybrid film deposited over copper foil. (c) Self-assembled spherical Sn catalyst nanoparticles layer.

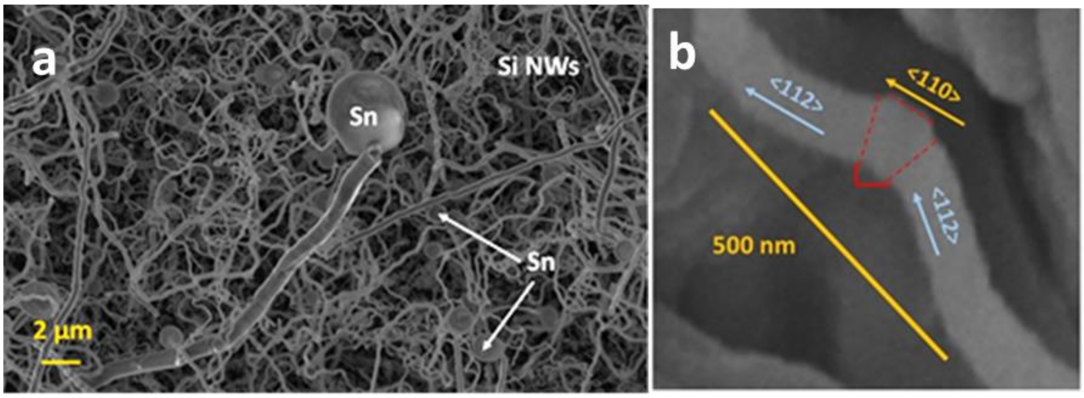

Figure 7.9: SEM image of Si-Sn showing (a) The Sn catalyst particles at the tip of SiNWs grown on a copper foil substrate and (b) Single SiNW with angular kinks with crystalline phase identification of twinning regions.

7.3.2 MATERIAL CHARACTERISATION

7.3.2.1 TRANSMISSION ELECTRON MICROSCOPY (TEM) ANALYSIS

From the selected area electron diffraction (SAED) patterns in Figure 7.10a and 7.10b, there is evidence of both crystalline and amorphous phases within the hybrid films deposited in this work. This will have implications in the lithiation behaviour of the anode active materials during charging, this being attributable to charge transfer kinetics in amorphous – compared with crystalline – silicon[341]. The complex two-phase lithiation of crystalline Si, subsequent lithiation phases that evolve in amorphous Si[42] and the recrystallization of Si[23] has received much attention, and are still yet some way from being definitively concluded.

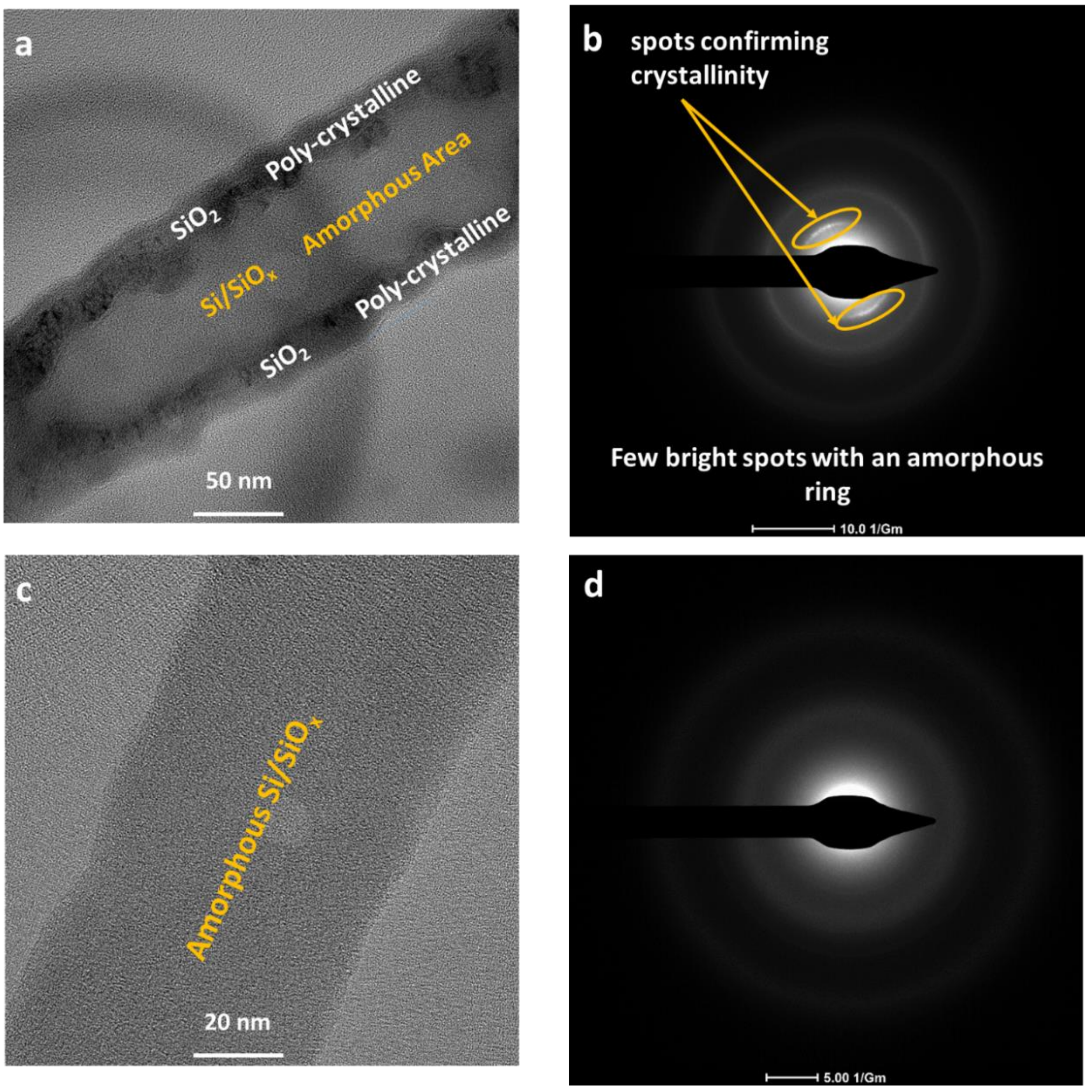

Figure 7.10: HRTEM and Selected Area Electron Diffraction Imaging of SiNW with both crystalline and amorphous regions (a,b) and purely amorphous SiNW (c,d).

7.3.2.2 X-RAY POWDER DIFFRACTION (XRD) ANALYSIS

The crystallinity of these films are further analysed by XRD as shown in Figure 7.11. Characteristic peaks that correspond to diffraction planes of Si (blue) and Sn (red) are identified. The diffraction patterns of the deposited composite is purely composed of elemental state of Si and Sn. Similar patterns corresponding to pure elements have been observed for Si-Sn composites[333]. The diffraction peak of Si indicates the cubic phase of SiNWs. These nanowires grown with Sn at the temperatures used here show increased lattice constants that are attributed to the bending of SiNWs, kinks in the nanowire and incorporation of Sn in the nanowire during the low temperature growth process. The lattice constant of Sn is approximately 20 % larger than silicon[342]. The tetragonal Sn phase structure is evidenced by the peaks appearing at: 30.6°, 32.0°, 43.9°, 55.3°, 62.5° and 79.5° (JCPDS Card No. 04-0673).

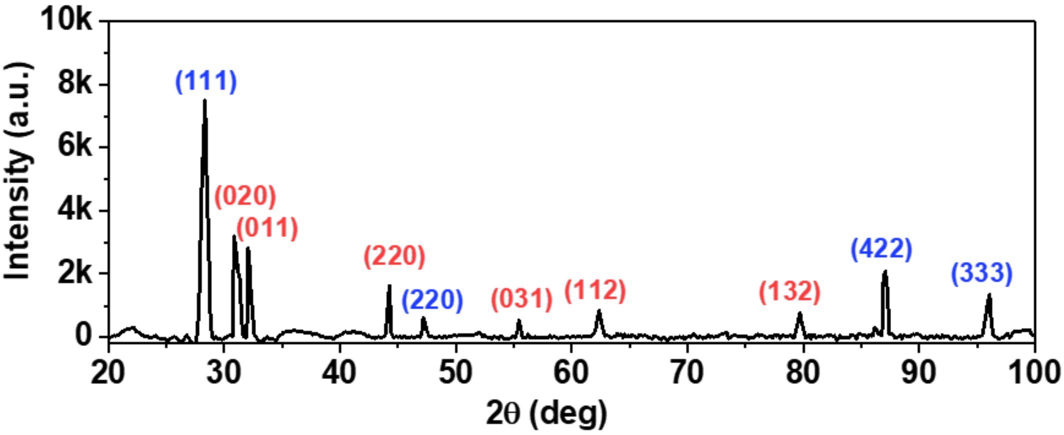

Figure 7.11: X-ray Diffraction pattern of Sn-SiNW film. Characteristic peaks that correspond to diffraction planes of Si (blue) and Sn (red) are highlighted.

7.3.3 ELECTROCHEMICAL CYCLING PERFORMANCE

The reversible lithiation characteristics of amorphous silicon have been shown to retain more extended structural stability than the crystalline material, attributable to increased tolerance to intrinsic stress and strain[341]. Specifically, the amorphous advantage lies in the ability to facilitate the isotropic stress, and strain moments during the lithiation and delithiation processes[341].

The discharge capacity as a function of cycle number is shown in Figure 7.12 and there is a relatively good cycling performance to 100 cycles. However, this electrochemical testing was performed in half-cells against Li foil and this can compensate for the low coulombic efficiency (CE) by supplying excessive Li^+ ions as needed (which would not be the case in a full cell that has a finite Li inventory). In commercial cells, to achieve industry-relevant cycling performance the CE needs to be ≥ 99.93 % to achieve a target number of charge-discharge cycles (at least 300) before it reaches 80 % capacity retention.

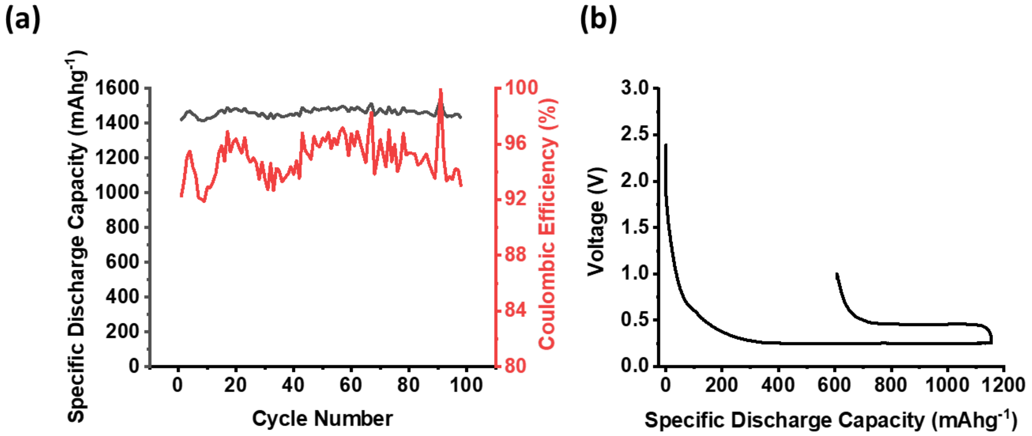

Figure 7.12: (a) Specific discharge capacity and columbic efficiency vs. cycle Number and (b) first lithiation-delithiation voltage profiles for Sn-SiNWs Anode vs Li/Li^{+}.

7.4 SUMMARY

Herein, a hybrid composite material was made from two high capacity materials, silicon and Sn, via conventional composite material mixing and advanced manufacturing technique. The high rate performance and high reversibility of the hybrid Si-Sn electrode was significantly improved by electrochemically active Sn additive. By pairing two high capacity materials, silicon and Sn, the hybrid electrode prepared via conventional mixing exhibits a stable specific discharge capacity about 1122 mAh g^{-1} under a current density of 289 mA g^{-1} after 100 cycles. Sn with a dual purpose of conductive additive as well as an electrochemically active component in the Si-based electrode is advantageous. As Sn lithiates before Si, an internal pressure build-up within the electrode, which is beneficial for the hybrid electrode to achieve high reversible capacity. With the pressure build-up there is an improved contact at the interfaces and thereby decrease in impedance. Also, it in turn enhances the electrode's fatigue property during cycling aging, which is helpful in cell's longevity.

Further, a relatively low temperature PECVD deposition technique was shown to generate a binary anode system composed of both crystalline and amorphous SiNWs with a dense Sn layer and some interfacial copper-tin intermetallic phases. Sn has been shown to be an interesting catalyst for SiNW growth as it is isoelectric with Si thus a neutral "impurity". PECVD of Si in combination with Sn catalyst seeds opens up exciting possibilities at low temperatures. This is facilitated by the dissociation of the precursor gas in a low power plasma, allowing lowering of the substrate temperature whilst maintaining high SiNW growth rate. This non-optimised film was able to endure reversible lithiation for 100 cycles at nearly four times the maximum capacity of graphite. Conventional powder-binder-additive containing electrodes did not achieve this level of performance in a direct cycle life comparison.

Alternative manufacturing routes such as low temperature PECVD do not require indirect materials or energy-intensive processing, and could be a key enabler generating cheaper and long lasting electrode architectures. Their ability to deposit onto three-dimensional structures could present opportunities beyond the capability of conventional coating techniques. This can enable the use of metallic foam or carbon-based current collectors in batteries for very high rate applications. The potential for use in flexible or wearable energy storage could also become increasingly possible by this approach. Further developing the capability to generate wearable energy storage is of much practical interest although it is far from being at a level ready for commercial exploitation. PECVD is an established, scalable technology that is well-suited to depositing functional semiconductor coatings. This strategy presents new possibilities to explore and better understand the approaches to designing and understanding new electrode materials and microstructures, to correlate structure with performance, and how to better optimise energy storage components.

The benefits from Sn in the Si-based electrode largely depends on the microstructure of the composite. In this study, it was demonstrated that the performance synergy between silicon and Sn outperforms the individual contribution of each material alone. Even though further study is required with respect to long-term cyclic ageing, it can be justified that optimising the formulation further could meet the future requirement for anodes in LIBs.

CHAPTER 8. CONCLUSION AND SUGGESTION FOR FUTURE WORK

Understanding the influence of functional additives on electrode microstructures under different current densities is crucial, especially towards the development of high capacity LIBs to meet high energy density requirements. By applying advanced 3D imaging and other associated physicochemical characterisations, this study presents both qualitative and quantitative analysis of various Si-based electrode microstructures with purposefully selected additives. This thesis highlights the importance of flexible and conductive additives for high capacity LIBs. The research found that with cyclic aging, the microstructure of Si-dominant electrode undergoes massive detrimental structural transformations compared to the Si electrodes with flexible additives. Therefore, an understanding of the real geometry for example the distribution and dynamics of the pore phases are essential requirements for studying degradation mechanisms, particularly before, during and at the end of the battery's useful life.

8.1 GENERAL SUMMARY OF MAIN FINDINGS

In this study, a comprehensive literature review of different degradation mechanisms taking place in anodes has been discussed, for a better understanding of materials and the underlying chemical processes that lead to resistance build-up and capacity loss in LIBs. The report also focusses on silicon as the ultimate successor to the commercially used graphite anode for LIBs and the issues that are preventing its commercialisation. Various approaches have been described by researchers to improve state-of-the-art for silicon and the pros and cons of these approaches described therein. From the literature, it can be concluded that microstructural evolution during the lithiation and delithiation processes has a direct influence on the performance of the battery. The batteries performance can be correlated to the battery electrode's microstructure, and various 2D and 3D characterisation techniques have been implemented to understand this relationship. The limitation of understanding of microstructure in 2D is made more complex due to the dynamics of electrochemical reactions and the changes that take place as a result. Geometrical parameters such as porosity, tortuosity, pore size distribution and volumetric pore surface area cannot be established from 2D characterisation techniques, though they provide a great deal of information regarding the particle morphology, material's microstructure and distribution. With the development of tomographic imaging technique, it is possible to observe and characterise a wide range of battery chemistry materials in 3D at multiple length scales.

This report also reviews the application tomography techniques used to probe LIBs. The exceptionally high-resolution image with a pixel size of tens of nanometer from FIB-SEM tomography technique illustrates the microstructural changes in finer detail. Furthermore, vast majority of the microstructural research work that has been carried out in the literature is based on cathodes and only a few studies on the anodes, particularly on silicon-based electrodes. Moreover, according to literature reviews, in studies carried out on silicon-based electrodes, microstructural evolution investigations with different current densities has not been considered.

High capacity LIBs are much needed to address the current energy crisis in real-world applications, such as vehicle electrification, portable consumer electronics, and stationary energy storage systems. This study aims to characterise silicon-based electrodes with additives more suited to resist pulverisation and to interpret any degradation mechanisms that occur that ultimately define battery performance. The geometrical parameterisation of fresh and aged electrodes is crucial to correlate performance to microstructural in combination with other physicochemical characterisations such as tracking impedance build-up during cycling.

This research work aimed to comprehensively understand the influence of different additives on Si-based electrodes for high capacity LIBs, concerning the optimisation of electrode microstructure stability under different current densities. This was accomplished by analysing a galvanostatically cycling dataset. The electrode formulations were at three different silicon capacities, namely, 1200 mAh g^{-1} (corresponding to a current density of 238 mA g^{-1} at C/5), 1800 mAh g^{-1} (corresponding to a current density of 358 mA g^{-1} at C/5) and to the maximum experimental capacity of 3579 $mAhg^{-1}$ (corresponding to a current density of 716 mA g^{-1} at C/5). Cells were cycled at the full capacity of silicon, to compare the effects of these additives towards capacity retention and cycle life under more extreme operational parameters. Also, at 1800 mAh g^{-1} and/or 1200 mAh g^{-1} capacity limits to minimise any pulverization from large volume expansion upon lithiation[42] for improved cycle life. From *Chapters 5*, *6*, and *7* the prime findings are:

(i) It was observed that, as expected, the cells cycling at the full experimental capacity of silicon show noticeable capacity fade effects compared to the cells cycling at the half experimental capacity of silicon. This capacity fade is further delayed as the capacity limit is further reduced to 1200 $mAhg^{-1}$. The main reason for this observation can be attributed to breaking down and continual growth of SEI, which in turn results in pore clogging and increased resistance for Li^+ ion movement.

(ii) It was evident that incorporation of the MOFs in the Si anode has a significant positive effect on stabilising the electrode. The fact that UiO-67 shows superior additive properties in comparison to UiO-66 could be attributed to an increased innate structural flexibility and larger pore size. Whilst the flexibility argument has been documented in literature, further work would be required experimentally to systematically conclude that this property is the main performance enhancer.

(iii) It was observed that the incorporated graphene in the composite improves the mechanical and electrochemical performance of the Si-graphene electrodes. The sandwich-like 3D structure with a homogenous spread of porosity, particularly in Si-FLG_{WJM} composite would provide facile pathways for electrons and lithium ions. This thereby enhances the electrical conductivity and lithium diffusion rate, and also provides empty space surrounding the silicon particles to buffer the volume changes at the electrode level, from silicon particles more elastically.

(iv) It was noticed that the electrochemically active Sn as an additive significantly improves the rate performance and cycling stability. As Sn lithiates at a higher voltage before Si, an internal pressure build-up within the electrode, is considered to be beneficial for the hybrid electrode to achieve high reversible capacity. With the pressure build-up there is an improved contact at the interfaces and thereby decrease in impedance.

The second objective in this research study was to establish the degree of battery degradation with such additives on geometrical parameters. This was accomplished by analysing electrodes before and after cycling using FIB-SEM tomography and image quantification. From *Chapters 5*, *6*, and *7* the prime conclusions are:

(i) A FIB-SEM tomography imaging technique was applied to visualise and quantify geometrical parameters within electrodes such as thickness, pore surface area, phase volume fraction and tortuosity.

(ii) The porosity retention is higher in all the Si-additive electrodes (*i.e.* Si-MOFs, Si-graphene and Si-Sn) in comparison to the Si-dominant control electrodes.

(iii) As foreseen, an incremental change in the thickness of electrodes cycled was observed. Additionally, it can be seen that electrodes cycled at half capacity have a lower increment in the electrode thickness with respect to electrodes cycled at full capacity of silicon.

(iv) Comparing the pore surface areas in contact with the electrolyte for a pristine electrode and a cycled electrode, it can be seen that there is a substantial decrease in specific surface area for the cycled electrode. This means that the surface of the particles has undergone successive reduction reactions, *i.e.* there is continuous formation and growth of SEI.

(v) It was observed that there is segregation of pore-volume distribution upon cyclic aging. Coalescence among the particles in the cycled electrodes is likely from the huge volume expansion and electrochemical fusion of silicon particles.

(vi) There was a significant decrease in the pore size and distribution in cycled electrodes. Upon cyclic aging, there is a shift towards the lower end of the pore volume which may be an indication that the macropores are becoming filled with detached SEI products upon cycling.

(vii) It can be seen that electrode formulations with no additives have a higher volume percent of pores with lower diameter compared to Si-additive electrodes attributing to the Si-fusion and subsequent pulverisation from large volume expansion resulting in microstructure fragility.

The third objective in this research study was to analyse the evolution of impedance characteristics of these electrodes during cycling. This was accomplished by the Nyquist plots obtained from potentiostatic electrochemical impedance spectroscopy. From *Chapters 5*, *6*, and *7* the prime results are:

(i) Nyquist plots obtained from potentiostatic electrochemical impedance spectroscopy provide information on the kinetics of the reaction and diffusion processes corresponding to certain frequency ranges. The two features occurring in the high-frequency range correspond to interfacial phenomena, the first can be attributed to an insulating SEI layer resistance (R_{SEI}), while the second is due to charge transfer resistance (R_{CT}).

(ii) It was observed in all the electrode formulations R_{SEI} gradually increases with the cycle number, which indicates that the SEI layer is continuously growing because of the particle cracking due to large volume changes. During this aging period, where the thick SEI layer breaks off, there is re-formation of a new SEI layer and therefore, an increased series resistance from pore clogging.

(iii) The isolated pores and heterogeneous distribution of the pores hinder the passage of diffusion of Li^+ ions resulting in increased resistance.

(iv) The R_{CT} for cells cycled at full capacity of silicon tends to decreases after a certain number of cycles for all of the formulations and can be explained as a result of large cracks that have resulted in the electrode's structure due to large volume changes from silicon particles. These large voids allow comparatively easy transportation of electrolyte within the electrode and thereby facilitate the availability of Li^+ ions to diffuse through the active particles.

(v) The large cracks also result in a fresh surface for further side reactions, increasing the R_{SEI} which also increases the series resistance as they reduce the electrical conductivity of the electrode as a whole.

The next main objective in this research study was to establish an understanding between the microstructural evolution and electrochemical performance. From *Chapters 5*, *6*, and *7* the prime findings are:

(i) The flexibility from the MOFs, graphene and Sn plays favourably towards the electrode's stability and porosity retention during lithiation/de-lithiation.

(ii) Reduced porosity or increased tortuosity may adversely affect the lithium permeability and diffusion into the active material, resulting in capacity fade and loss of coulombic efficiency.

(iii) The observed changes in porosity are likely to impact the permeability of the electrolyte solvents and be ultimately responsible for the eventual decay in performance of the anode.

(iv) The presence of a cushioning effect in Si-additive electrodes can help to sustain the volume changes and thus restrict the mesopores being filled by fragmented SEI layers. This otherwise could lead to rapid capacity decay with increasing cycle number.

(v) This formation of new SEI results in the consumption of Li^+ ions which should result in capacity loss.

(vi) For the control electrodes with no additives, cycled at half capacity of silicon the impedance gradually increased until certain cycle number and after which there was huge resistance increase: this is likely to be due to the continuum growth of an insulating (SEI) layer and high charge transfer resistance, which is entirely consistent with the cyclic data.

Overall, the knowledge contributions of this study towards the scientific community are:

- The porous zirconium carboxylate MOFs, particularly UiO-67 as additives in Si-based anodes performs the dual purpose of improving and maintaining the porous nature of composite battery materials.

- The uniform layered distribution of silicon particles on the graphene surface forms a highly porous network, providing a facile pathway for unconstrained electrolyte movement and elastic buffer for the volume changes from silicon particles with mitigation of active particle fusion.

- The ductile nature of Sn is assumed to act as a buffer for stress in the silicon composite during the substantial volume changes of silicon and thereby enhancing the electrode's fatigue property during cycling.

- The use of imaging techniques, such as FIB-SEM tomography, alongside other conventional physical characterisations, advances towards a more in-depth understanding of electrode's microstructural evolution at the different operating condition. The multi-scale analysis employed in this research work indicates possible root causes of failure which otherwise would be beyond the scope, particularly from the microscale analysis often coated in the literature. The imaging method contributes to the knowledge that the porosity retention from flexible additives provides "porous networks" and thereby reduces impedance in the Si-based electrodes.

8.2 LIMITAIONS OF THIS WORK

Pragmatic and innovative approaches were considered for improving performance stabilisation for silicon-based anodes via additives. These additives can be conveniently be synthesised or readily commercially available and are chemically compatible with the electrode components. In this study, for each approach, a baseline silicon-dominant electrode was made for studying a comparative performance optimisation with additives. However, there can still be further performance optimisation for Si-additive electrodes, enabling commercialisation through formulation optimisation approach, which represents a lucrative technology transfer opportunity.

With time limitations, the data acquisition during electrochemical cycling (up to 6 months at times), there was no scope to further optimise the current formulation for further performance improvement. For example, in Chapter 5 it remains conclusive that MOFs (especially UiO-67) improves the Si-based electrode's performance dramatically. However, the optimised ratio of MOFs to maintain higher gravimetric and volumetric capacity for high energy density applications is yet to be established. Similarly, in Chapter 6 and Chapter 7 it was determined that graphene and tin as co-lithium hosts, respectively, by 1:1 wt. ratio with Si improves the performance significantly. Hence, further performance improvement for Si electrode from other MOFs, morphologies of graphene and tin with different formulation ratios were not possible to incorporate within the scope of this study.

In this study, all of the electrochemical characterisations were carried out in coin cells vs. Li/Li^+, with lithium as the counter electrode to have a control on varying parameters that might otherwise have been introduced with other cathode materials like $LiCoO_2$, $LiNi_{1/3}Mn_{1/3}Co_{1/3}O_2$. Hence, whether the same formulation ratio can attain similar performance in full coin cell and large cell format is yet to be established. Full cell and large pouch/prismatic cell formats hold a promise for a future possibility of technology development and transfer. However, there can be other challenges for the large format of cells. This can include new requirements for the material synthesis at large volume, gas generation issues due to electrolyte reactions at electrode interface during the formation cycle and other relevant safety considerations.

The representative microstructure was another challenge in this study. A typical reconstructed microstructure volume studied here has the dimensions that cover only a fraction of the entire electrode. There is a possibility for a valid question of whether the analysed microstructure volume is an accurate representation for an electrode as the whole. The electrode's microstructure might slightly vary at a different location, *i.e.* between the centre of the electrode and towards the edges of the electrode. Unfortunately, it is challenging to perform tomography on multiple locations due to time constraint (FIB-SEM tomography takes extensive time to carry out) and limited access to equipment. However, the reconstructed volume is a statistically representable volume of the electrode, and we have now explained this in the research methodology chapter under the representative volume element (RVE) analysis. Additionally, efforts have been made to be consistent in performing tomography on the material at the centre for all the electrodes in the complete study. In-depth research on this microstructural variation could have been an interesting study to be able to quantify any variations observed. However, with limited time and instrument availability constraints, there was no scope for this investigation in this study.

8.3 ONGOING AND SUGGESTIONS FOR FURTHER REASEARCH

In this study, every effort has been made to comprehensively study different additives to Si-based electrodes and their influence on the microstructure and performance at various current density. Still, there remain a few scientific questions unexplored due to the lack of resources and time constraint. To address these questions, some envisaged characterisations are recommended for further study in future work, and are outlined below.

In the study, it is shown that the tomography study of LIB electrodes is a powerful tool to understand the performance-microstructure correlation. With the established tomography and other physicochemical characterisation methods, battery materials can be further investigated in detail via *in-situ* and *in-operando* studies as suggested below.

(i) Developing an electrochemical cell and sample holder for *in-operando* X-ray CT of silicon-based anodes for LIBs.

This envisaged study is aimed at improving the understanding of the degradation processes that are taking place in the complex electrode structures and compare microstructural architecture with performance. By combining electrochemical measurements with quantified microstructural properties achieved from *ex-situ* imaging and *in-situ/in-operando* studies, it is anticipated that this study will elucidate key degradation mechanisms and in turn emphasise optimum operating conditions and particle morphologies. This will lead to major improvements in the design of LIB materials. The understanding of electrode degradation processes will help in substantial electrode design improvements for next-generation automotive and grid storage applications.

4D imaging, *i.e.* continuous tomographic imaging at periodic intervals of lithiation and delithiation of LIB electrodes. This is an important technique to capture particle level micro degradation as well as macro degradation of electrode architectural changes upon repeated cycling. The 3D and 4D tomography imaging study can be performed using both synchrotron and laboratory-based X-ray sources, and at multiple length scales, *i.e.* micrometric to nanometric resolution. Multiple resolution length scales are essential and is required to quantify 3D geometrical parameters, and these quantified analyses would give further insight into the correlation of different physical degradation mechanisms and battery performance.

In *Chapters 5-7*, the 3D morphological evolution of Si-based electrode was captured using FIB-SEM tomography. To develop an understanding of the microstructural evolution non-invasively, an electrochemical cell had to be designed which can be used for regular electrochemical testing as well as transparent to X-rays for analysis under X-ray CT. A custom designed, X-ray transparent cell housing can be used for performing *in-situ* characterisation, which can also be used for further operando studies. With the aid of X-ray CT imaging techniques, it would be interesting to study the dynamic evolution of SEI and Si's particle pulverisation during battery operation, particularly to examine the influence of varying current densities on microstructure. For this study, the proposed cell housing designs can be used for laboratory-based micro X-ray CT with micron resolution to understand the macro degradation of silicon-based electrode materials. For micro degradation analysis using laboratory-based micro X-ray CT with few hundreds of nanometre resolution, initial tests have been performed as discussed below.

Electrochemical cell design (for macro degradation analysis):

A customised functional LIB has been designed which enabled electrochemical testing as well as X-ray tomographic imaging of the electrode materials. The cell used a modified PFA Swagelok tube fitting (PFA-220-6, Union, 1/8 in) to suit the experiment (see Figure 8.1). It is also an effective design protecting the internal material from exposure to the atmosphere to avoid reactions of the Li with oxygen and humidity and allowing 360° free rotation for X-ray access. For this study, the cell assembly consisted of a lithium foil as an anode (0.9 mm), a glass fibre separator (~1 mm) and a cathode made of silicon composite (~1 mm). The electrode preparation for this cell design can be performed either by dip-coating silicon composite slurry onto the tip of the current collector or by cutting a circular disc from the slurry coated electrodes. A stainless steel pin or a copper pin can be used as a current collector. To enhance X-ray transmission, a groove was machined around the circumference of hex nipple tube fitting, thereby leaving a sidewall thickness of 1.5 mm. It was observed that the cell design displayed excellent cycling performance and comparable to the commercial Li-ion cells. The cell was cycled galvanostatically using a battery cycler while acquiring tomographic images after periodic cycles and after failure due to short-circuit. To minimise the artefacts from the imaging the complete cell needed to be kept in the field of view. This *in-situ* imaging study before and after electrochemical testing will provide related information on microstructural parameters in the specific regions of interest of the silicon electrodes.

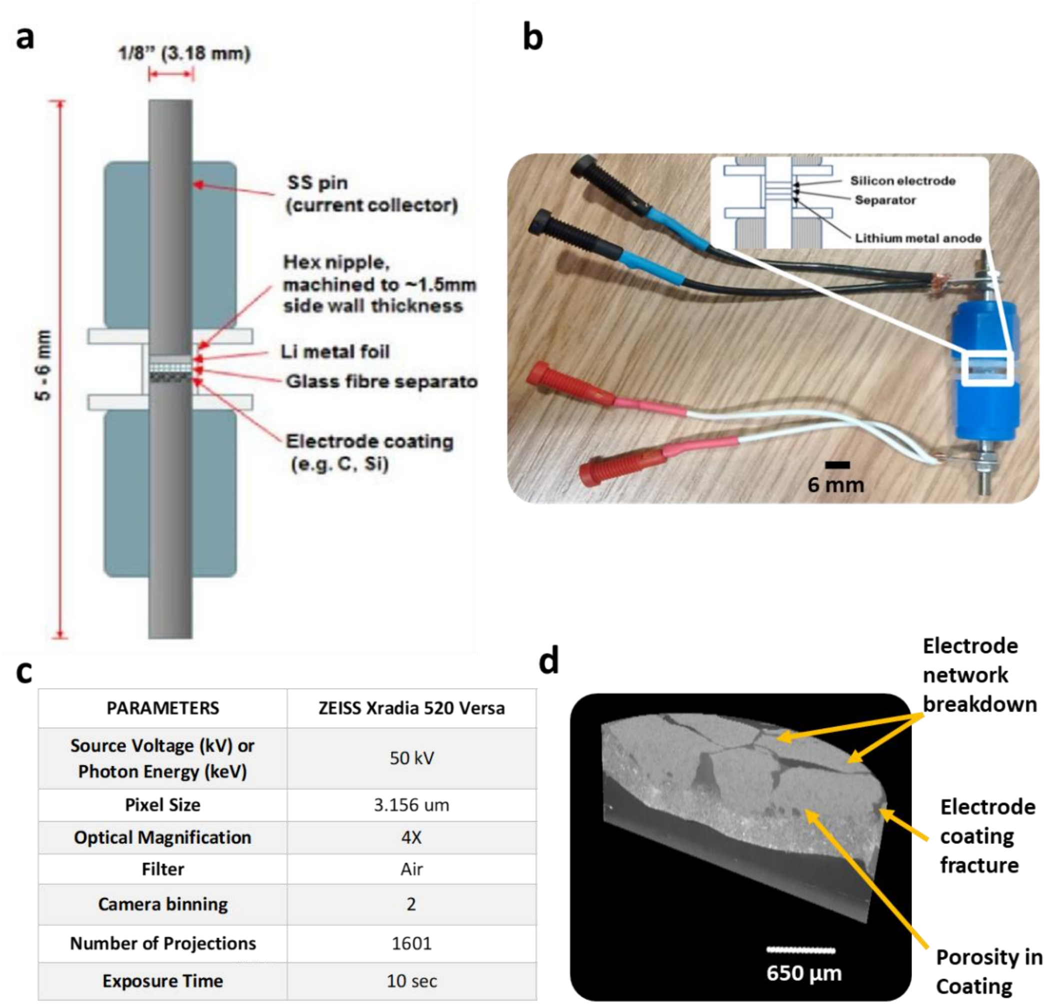

PARAMETERS	ZEISS Xradia 520 Versa
Source Voltage (kV) or Photon Energy (keV)	50 kV
Pixel Size	3.156 um
Optical Magnification	4X
Filter	Air
Camera binning	2
Number of Projections	1601
Exposure Time	10 sec

Figure 8.1: (a) A schematic diagram representation of the electrochemical cell,[343,344] (b) *modified PFA Swagelok tube fitting, (c) scanning parameters used for X-ray CT, and (d) Cross sectional 3D reconstructed tomographic image (using ZEISS Xradia 520 Versa) revealing electrode fracture and electrode network breakdown.*

To obtain higher resolution 3D and 4D information of silicon microstructures, a novel design is proposed in this study (see Figure 8.2). This novel design will give battery researches great flexibility in obtaining any customised design diameter which is very important and inversely related to resolution (*i.e.* lower the cell diameter higher the resolution of the images obtained. Higher resolution images are vital for ease of segmentation process during digital image processing. These designs are going to be 3D printed via Fused Deposition Modelling (FDM) technique under the additive manufacturing technology at the International Institute for Product and Service Innovation (University of Warwick). The additive layer process is also an inexpensive process and also provides flexibility in the choice of material. The design is going to be 3D printed with PPSF (polyphenyl sulfone) thermoplastic as these material has excellent strength, heat and chemical resistance in comparison to other commercially available thermoplastics used in additive layer manufacturing. The proposed design will give a better understanding of micro and macro-degradation simultaneously.

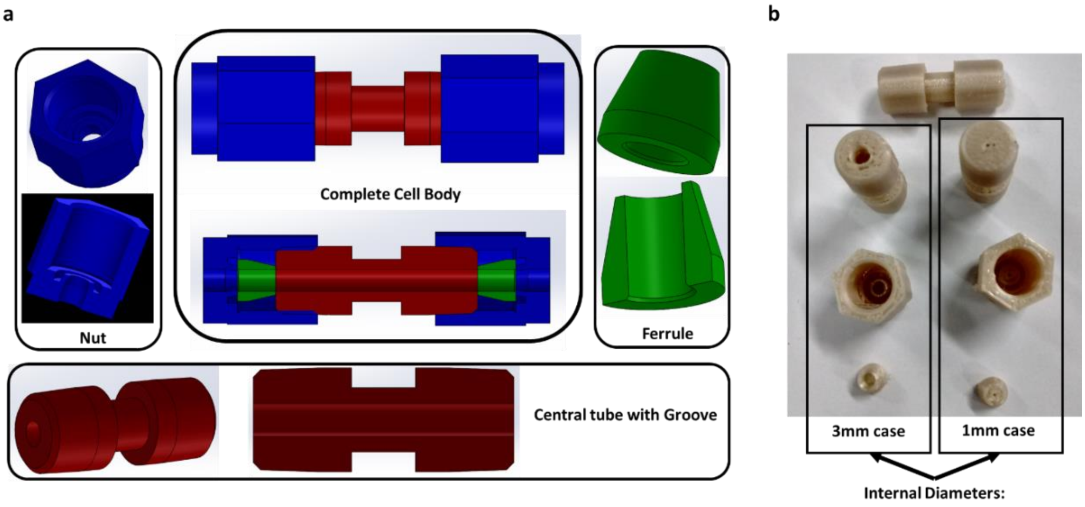

Figure 8.2: (a) Solid works model for proposed electrochemical cell, (b) 3D Printed cell housing with two different diameters.

Few other options that can be explored in the future study are shown in Figure 8.3. These modified cell housings have a similar design as to above-proposed designs but are made from organic thermoplastic polymers. Polytetrafluoroethylene (PTFE) threaded rods and high-performance liquid chromatography (HPLC) tube fitting made of polyether ether ketone (PEEK). PTFE and PEEK are one of the most corrosion resistive materials and would be appropriate as a cell body for electrochemical cell design. The PTFE threaded rod would be bored through at the centre with uniform diameter for containing electrode materials. A central grove would also be made at the centre to allow maximum X-rays to be incident on the materials with least attenuation from the polymer. Whereas for HPLC tube fitting as very similar to PFA Swagelok tube fitting but with an internal diameter of 0.79 mm compared to 3.18 mm for PFA Swagelok tube fitting.

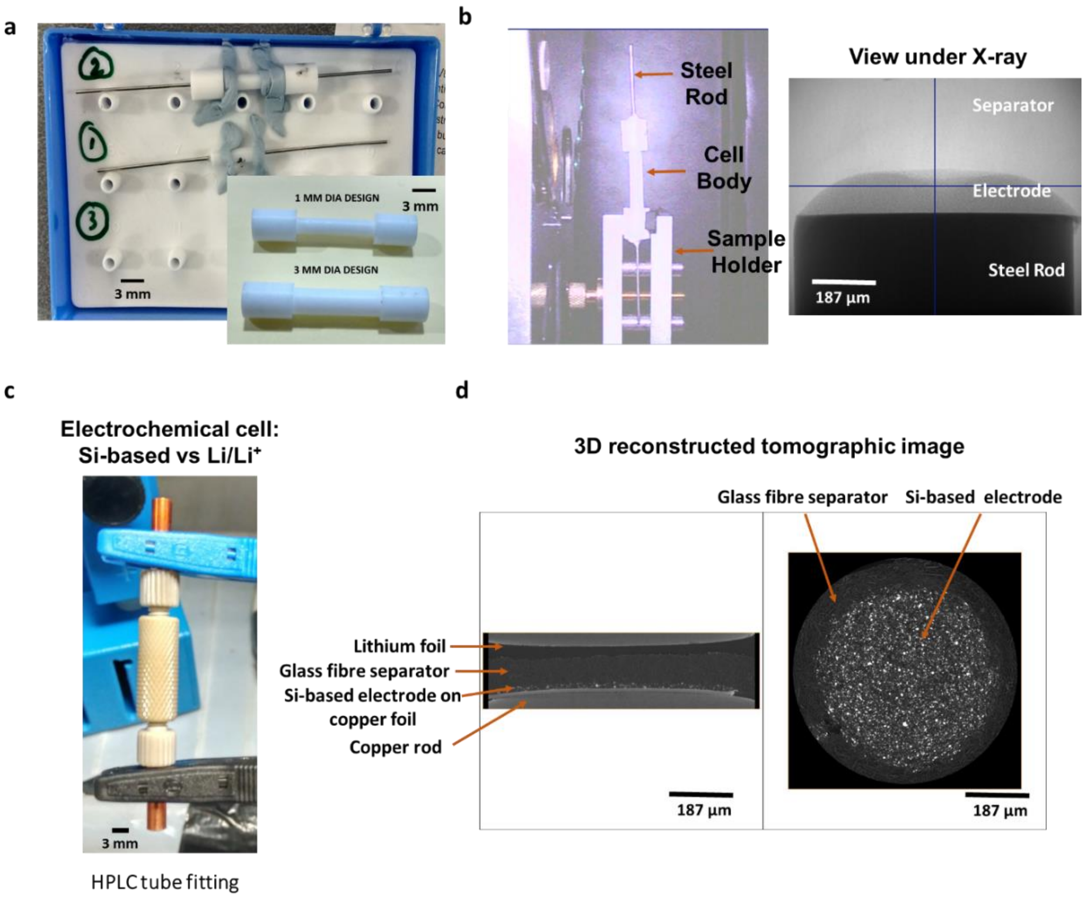

Figure 8.3: (a) PTFE cell housing with two cell housing diameters, (b) a fresh electrochemical cell prepared with 1mm diameter steel rods as current collector in the PTFE cell housing and placed inside ZEISS Xradia 520 Versa for scanning, (c) HPLC tube fitting with copper rods as current collector, (d) 3D reconstructed tomographic image of a fresh cell in HPLC tube fitting with the imaging parameters same as in Figure 8.1c.

Novel sample preparation (for nano-degradation analysis):

Ex-situ X-ray CT imaging method requires cell disassembly. After the cell has been disassembled in a glove box under an argon atmosphere, it must be rinsed with organic solvent (DMC) to remove any traces of electrolyte salts present and dried inside the glovebox. Sample preparation for nano X-ray CT is not at all trivial. Most of the sample preparation carried out for nano X-ray CT is either by scraping material from the current collector or by chipping out material from the coating to visualise transient changes in the electrode material structure as a result from different battery conditioning. However, in the above approaches, any quantitative measurement performed is not accurate as the porosity, tortuosity values become modified from the mechanical damage. In the proposed studies, the current collector can be separated from the electrode coating using a sharp blade and self-closing tweezers under the optical microscope as shown in Figure 8.4. This novel approach separates the highly attenuating copper phase, otherwise there would be artefacts in imaging the lower Z phase(s) adjacent to the high Z phase(s). With this approach, the copper is removed from the interested region of interest in the sample without damaging any geometrical properties of the material. After separating the copper from the sample, it was adhered to a steel pin for positioning in a pin vice sample holder.

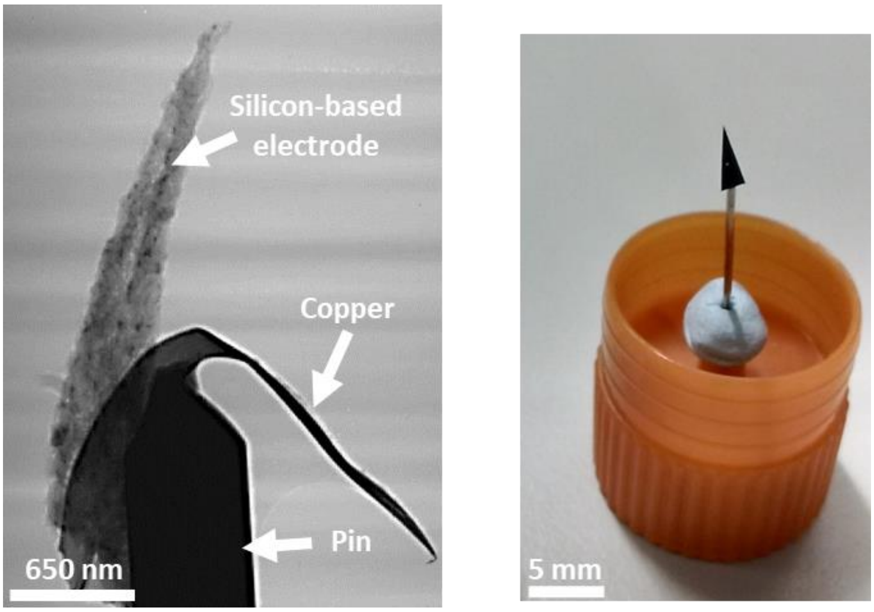

Figure 8.4: Sample preparation for nano X-ray CT.

It should be noted that the *ex-situ* microstructural evolution studies for multiple length scale study requires cell disassembly. The reader should be aware that there are numbers of factors to be considered while designing an electrochemical cell for X-ray CT or preparing a sample for X-ray CT because of the complexity of the tomographic imaging. For example, the X-ray source required, the experimental setup, the material type, parameter under investigation and the region of interest.

Apart from the electrochemical cell designs, an appropriate cell holder is also a significant requirement for excellent imaging. With this specific design of the sample holder will help to achieve a reproducible X-Y position, with sufficient clamping strength so that the electrical connection wires will not move the cell during the *in-operando* study. The design is fitted with a hexagonal hole in the moving bar, which is in relevance to the nut part of the above-proposed cell design for the PFA Swagelok tube fittings and 3D printed cell housings. Figure 8.5 represents a conventional sample holder and the proposed modified sketches for the relevant parts in the holder.

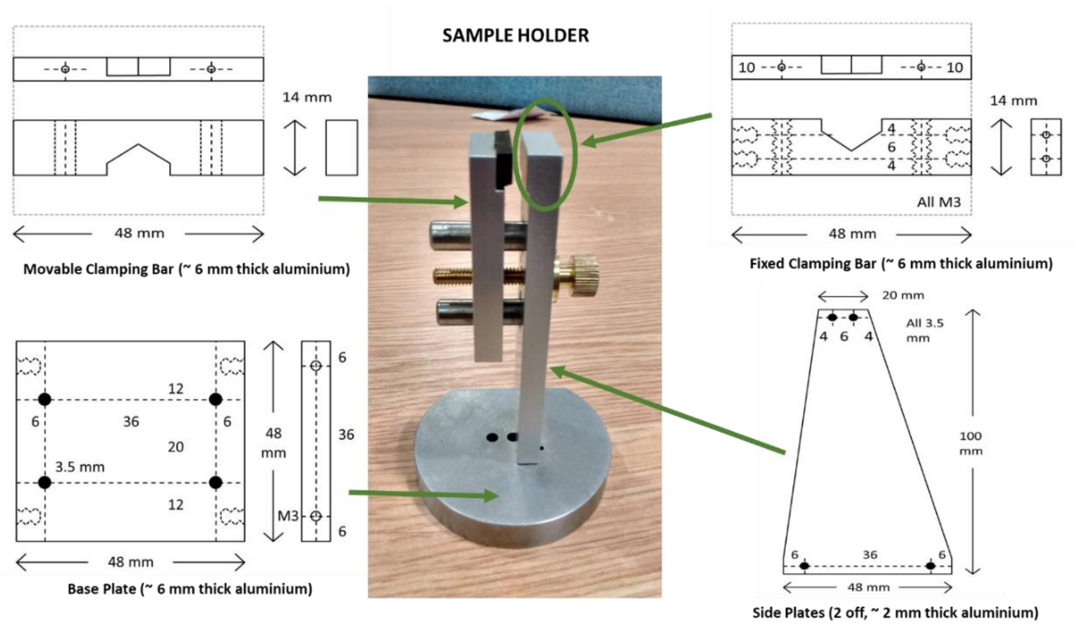

Figure 8.5: New proposed sample holder design for operando tomographic imaging.

(ii) Developing an electrochemical cell and sample holder for *operando* XRD on LIB electrode inks.

In *Chapter 7*, the reversible cyclic stability of the hybrid electrode can be attributed to Sn's presence in the composite, and its expansion over lithiation leads to the application of uniform pressure to silicon particles from its homogenous presence in the electrode. Unfortunately, because of the complexity in this hybrid system, it was challenging to deconvolute this synergy effect from individual components entirely. Therefore, a further detailed study on this hybrid electrode is proposed to expand on the theory in further detail by *in-operando* XRD technique at intermediate steps of lithiation. A modified 2032 coin cell body as shown in Figure 8.6, can be used for *in-*

operando XRD study. The incorporated beryllium (Be) disk is 9.5 mm in diameter and 127 µm thick (American Elements).

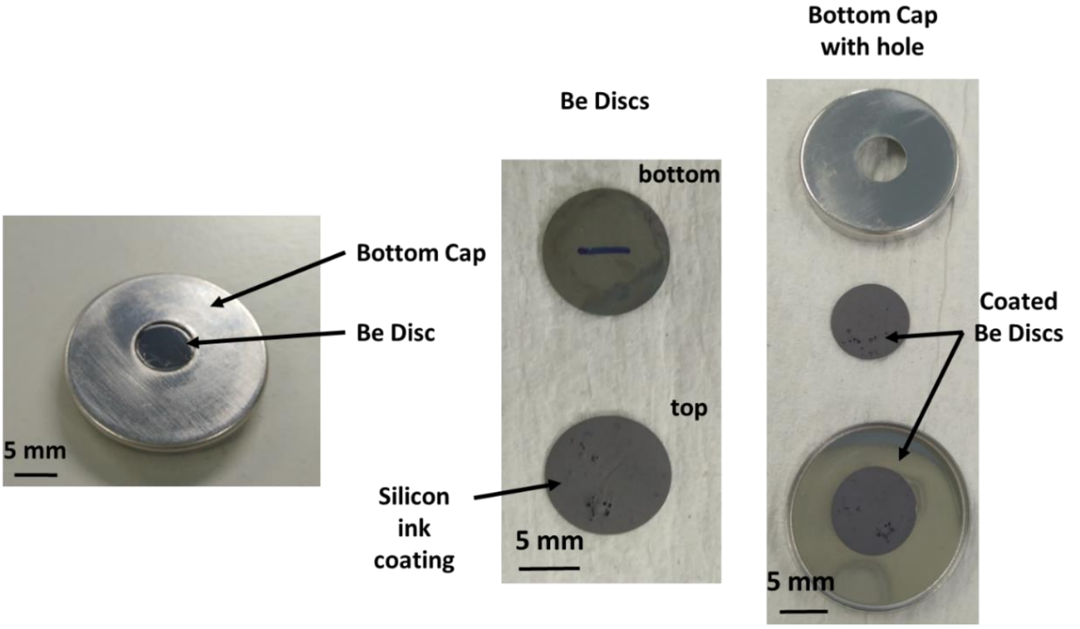

Figure 8.6: Modified 2032 coin cell body for in-operando *XRD studies with beryllium (Be) disk of 9.5 mm in diameter and 127 µm thick (American Elements) as X-ray entrance window.*

(iii) Comparative optimisation study of different MOFs, various graphene morphology and tin particle sizes in silicon-based systems as hybrid anode materials for high capacity LIBs.

In future work, a comparative study with different materials could be considered to study the influence of additives for better understanding of different modes of degradation. Electrochemical characterisation along with *in-situ* and *in-operando* tomographic imaging of silicon hybrid systems can be carried out to study microstructural evolution. In *Chapter 5*, concerning the mechanism of charge transfer between MOFs and electrolyte, further *in-operando* NMR characterisation can be performed, to obtain an accurate lithiation mechanism in MOFs at different state of charge levels. This will help to understand in detail the contribution of electrochemically active MOFs towards the improved performance. Additionally, there are many combinations of organic linkers and metals that the benefit of the MOF could be optimised. Perhaps a redox-active MOF could be used that has some significant Li capacity.

From this research work, the electrode formulations could be further optimised for performance to move towards and commercial development routes. Electrodes could be tested under continuous power or continuous current, and the effects of kinetics involved in both cases would be illustrated visually from the tomographic imaging.

All the above-envisaged studies were, however, beyond the scope of the current research presented in this thesis. These studies are suggested as future work in this research area. Additionally, the current research work has opened up new possible research directions by bringing together a multi-characterisation approach to track the microstructural changes under LIB operation. The ability to qualitatively and quantitatively evaluate the microstructural changes in 3D, provides insights into the prime sources of battery degradation. Furthermore, this approach is not restricted to only Si-based electrodes rather can be applied to any electrode chemistry for comprehensive understanding into microstructural evolution.

REFERENCES

1. Department for Business, E. & I. S. *Climate change explained Contents*. (2018).
2. United States Environmental Protection Agency. *Fast Facts: U.S. Transportation Sector Greenhouse Gas Emissions, 1990-2015 (EPA-420-F-17-013)*. (2017).
3. International Energy Agency. *2018 World Energy Outlook: Executive Summary*. (2018).
4. IIGCC. *COP-21 in Paris – a guide for investors*. (2015).
5. Zanini, M., Basu, S. & Fischer, J. E. Alternate synthesis and reflectivity spectrum of stage 1 lithium-graphite intercalation compound. *Carbon N. Y.* **16,** 211–212 (1978).
6. Whittingham, M. S. & Gamble, F. R. The lithium intercalates of the transition metal dichalcogenides. *Mater. Res. Bull.* **10,** 363–371 (1975).
7. Haering, R. R., Stiles, J. A. R. & Brandt, K. *LITHIUM MOLYBDENUM DISULPHIDE BATTERY CATHODE*. (1979).
8. Julien, C. & Stoynov, Z. *Materials for lithium-ion batteries*. *NATO Science Series* **85,** (Springer Science & Business Media, 2009).
9. Obrovac, M. N. & Chevrier, V. L. Alloy Negative Electrodes for Li-Ion Batteries. *Chem. Rev.* **114,** 11444–11502 (2014).
10. McDowell, M. T., Lee, S. W., Nix, W. D. & Cui, Y. 25th anniversary article: Understanding the lithiation of silicon and other alloying anodes for lithium-ion batteries. *Adv. Mater.* **25,** 4966–4985 (2013).
11. Ziv, B. *et al.* Investigation of the Reasons for Capacity Fading in Li-Ion Battery Cells. *J. Electrochem. Soc.* **161,** A1672–A1680 (2014).
12. Evarts, E. C. To the limits of lithium. *Nature* **526,** S93–S95 (2015).
13. Sekai, K. *et al.* Lithium-ion rechargeable cells with $LiCoO_2$ and carbon electrodes. *J. Power Sources* **43,** 241–244 (1993).
14. Ozawa, K. Lithium-ion rechargeable batteries with $LiCoO_2$ and carbon electrodes: the $LiCoO_2$/C system. *Solid State Ionics* **69,** 212–221 (1994).
15. Birrell, S. A., McGordon, A. & Jennings, P. A. Defining the accuracy of real-world range estimations of an electric vehicle. *17th IEEE Int. Conf. Intell. Transp. Syst.* 2590–2595 (2014). doi:10.1109/ITSC.2014.6958105
16. Cooper, A. & Schefter, K. *Electric Vehicle Sales Forecast and the Charging Infrastructure Required Through 2030. Institute for Electric Innovation, Edison Electric Institute* (2018).
17. US Department of Energy. *USDRIVE - Electrochemical Energy Storage Technical Team Roadmap*. (2017). doi:148
18. Szostech, M. & VanHoek, D. Real World Battery Capacity Loss. *My Electric*

Car Forums (2018). Available at: http://www.electricvehiclewiki.com/Main_Page. (Accessed: 8th April 2019)

19. Harris, S. J., Timmons, A., Baker, D. R. & Monroe, C. Direct in situ measurements of Li transport in Li-ion battery negative electrodes. *Chem. Phys. Lett.* **485,** 265–274 (2009).

20. Orsini, F., Dupont, L., Beaudoin, B., Grugeon, S. & Tarasc, J.-M. Scanning and transmission electron microscopy contributions to the improvement of electrode materials and interfaces in the design of better batteries. *Int. J. Inorg. Mater.* **2,** 701–715 (2000).

21. Dolle Â, M., Grugeon, S., Beaudoin, B., Dupont, L. & Tarascon, J.-M. In situ TEM study of the interface carbon/electrolyte. *J. Power Sources* **97–98,** 104–106 (2001).

22. Koltypin, M., Cohen, Y. S., Markovsky, B., Cohen, Y. & Aurbach, D. The study of lithium insertion–deinsertion processes into composite graphite electrodes by in situ atomic force microscopy (AFM). *Electrochem. commun.* **4,** 17–23 (2002).

23. Ogata, K. *et al.* Revealing lithium–silicide phase transformations in nano-structured silicon-based lithium ion batteries via in situ NMR spectroscopy. *Nat. Commun.* **5,** (2014).

24. Hatchard, T. D. & Dahn, J. R. In Situ XRD and Electrochemical Study of the Reaction of Lithium with Amorphous Silicon. *J. Electrochem. Soc.* **151,** A838–A842 (2004).

25. Ender, M., Joos, J., Carraro, T. & Ivers-Tiffée, E. Three-dimensional reconstruction of a composite cathode for lithium-ion cells. *Electrochem. commun.* **13,** 166–168 (2011).

26. Kubis, A. J., Shiflet, G. J., Hull, R. & Dunn, D. N. Focused ion-beam tomography. *Metall. Mater. Trans. A* **35,** 1935–1943 (2004).

27. Paul R. Shearing *et al.* Exploring electrochemical devices using X-ray microscopy: 3D micro-structure of batteries and fuel cells. *Microsc. Anal.* **1,** 19–22 (2013).

28. Wiedemann, A. H., Goldin, G. M., Barnett, S. A., Zhu, H. & Kee, R. J. Effects of three-dimensional cathode microstructure on the performance of lithium-ion battery cathodes. *Electrochim. Acta* **88,** 580–588 (2013).

29. Wilson, J. R., Cronin, J. S., Barnett, S. A. & Harris, S. J. Measurement of three-dimensional microstructure in a $LiCoO_2$ positive electrode. *J. Power Sources* **196,** 3443–3447 (2011).

30. Wilson, J. R. *et al.* Three-dimensional reconstruction of a solid-oxide fuel-cell anode. *Nat. Mater.* **5,** 541–4 (2006).

31. Zaefferer, S., Wright, S. I. & Raabe, D. Three-dimensional orientation microscopy in a focused ion beam-scanning electron microscope: A new dimension of microstructure characterization. *Metall. Mater. Trans. A Phys. Metall. Mater. Sci.* **39,** 374–389 (2008).

32. Shearing, P. R., Brett, D. J. L. & Brandon, N. P. Towards intelligent engineering of SOFC electrodes: a review of advanced microstructural characterisation techniques. *Int. Mater. Rev.* **55,** 347–363 (2010).

33. Shearing, P., Wu, Y., Harris, S. J. & Brandon, N. In Situ X-Ray Spectroscopy and Imaging of Battery Materials. *Electrochem. Soc. Interface* 43–47 (2011).

34. Shearing, P. R., Howard, L. E., Jorgensen, P. S., Brandon, N. P. & Harris, S. J. Characterization of the 3-dimensional microstructure of a graphite negative electrode from a Li-ion battery. *Electrochem. commun.* **12,** 374–377 (2010).

35. Shearing, P. R. *et al.* Multi Length Scale Microstructural Investigations of a Commercially Available Li-Ion Battery Electrode. *J. Electrochem. Soc.* **159,** A1023–A1027 (2012).

36. Newman, J. Optimization of Porosity and Thickness of a Battery Electrode by Means of a Reaction-Zone Model. *J. Electrochem. Soc.* **142,** 97–101 (1995).

37. Doyle, M., Fuller, T. F. & Newman, J. Modelling the Galvanostatic Charge and Discharge of the Lithium/Polymer/Insertion Cell. *J. Electrochem. Soc.* **140,** 1526–1533 (1993).

38. Doyle, M. & Newman, J. Comparison of Modeling Predictions with Experimental Data from Plastic Lithium Ion Cells. *J. Electrochem. Soc.* **143,** 1890–1903 (1996).

39. Zielke, L. *et al.* Three-Phase Multiscale Modeling of a $LiCoO_2$ Cathode: Combining the Advantages of FIB–SEM Imaging and X-Ray Tomography. *Adv. Energy Mater.* **5,** 1401612 (2015).

40. Noh, M., Kwon, Y. & Lee, H. Amorphous Carbon-Coated Tin Anode Material for Lithium Secondary Battery. *Chem. Mater.* **796,** 1926–1929 (2005).

41. Beaulieu, L. Y. *et al.* The Electrochemical Reaction of Li with Amorphous Si-Sn Alloys. *J. Electrochem. Soc.* **150,** A149 (2003).

42. Obrovac, M. N. & Christensen, L. Structural Changes in Silicon Anodes during Lithium Insertion/Extraction. *Electrochem. Solid-State Lett.* **7,** A93–A96 (2004).

43. Gonzalez, J. *et al.* X-ray microtomography characterization of Sn particle evolution during lithiation/delithiation in lithium ion batteries. *J. Power Sources* **285,** 205–209 (2015).

44. Zhang, W.-J. A review of the electrochemical performance of alloy anodes for lithium-ion batteries. *J. Power Sources* **196,** 13–24 (2011).

45. Pecquenard, B., Le Cras, F., Martinez, H., Martin, L. & Ulldemolins, M. Evolution of the Si electrode/electrolyte interface in lithium batteries characterized by XPS and AFM techniques: The influence of vinylene carbonate additive. *Solid State Ionics* **215,** 36–44 (2012).

46. Tian, H., Xin, F., Wang, X., He, W. & Han, W. High capacity group-IV elements (Si, Ge, Sn) based anodes for lithium-ion batteries. *J. Mater.* **1,** 153–169 (2015).

47. Rezqita, A., Hamid, R., Schwarz, S., Kronberger, H. & Trifonova, A. Conductive Additive for Si/Mesoporous Carbon Anode for Li-Ion Batteries: Commercial Graphite vs Carbon Black C65. *ECS Trans.* **66,** 17–27 (2015).

48. Safari, M. & Delacourt, C. Aging of a Commercial Graphite/$LiFePO_4$ Cell. *J. Electrochem. Soc.* **158,** A1123–A1135 (2011).

49. Tariq, F. *et al.* Three-dimensional high resolution X-ray imaging and quantification of lithium ion battery mesocarbon microbead anodes. *J. Power Sources* **248,** 1014–1020 (2014).

50. Liu, X. H. & Huang, J. Y. In situ TEM electrochemistry of anode materials in lithium ion batteries. *Energy Environ. Sci.* **4,** 3844–3860 (2011).

51. Bang, B. M., Lee, J.-I., Kim, H., Cho, J. & Park, S. High-Performance Macroporous Bulk Silicon Anodes Synthesized by Template-Free Chemical Etching. *Adv. Energy Mater.* **2,** 878–883 (2012).

52. Ashuri, M., He, Q. & Shaw, L. L. Silicon as a potential anode material for Li-ion batteries: Where size, geometry and structure matter. *Nanoscale* **8,** 74–103 (2016).

53. Yoshio, M. *et al.* Carbon-Coated Si as a Lithium-Ion Battery Anode Material. *J. Electrochem. Soc.* **149,** A1598 (2002).

54. Wang, J., Xu, T., Huang, X., Li, H. & Ma, T. Recent progress of silicon composites as anode materials for secondary batteries. *RSC Adv.* **6,** 87778–87790 (2016).

55. Kasavajjula, U., Wang, C. & Appleby, A. J. Nano- and bulk-silicon-based insertion anodes for lithium-ion secondary cells. *J. Power Sources* **163,** 1003–1039 (2007).

56. Lestriez, B., Bahri, S., Sandu, I., Roué, L. & Guyomard, D. On the binding mechanism of CMC in Si negative electrodes for Li-ion batteries. *Electrochem. commun.* **9,** 2801–2806 (2007).

57. Farooq, U. *et al.* Effect of binder and composition ratio on electrochemical performance of silicon/graphite composite battery electrode. *Mater. Lett.* **136,** 254–257 (2014).

58. Huang, Q., Loveridge, M. J., Genieser, R., Lain, M. J. & Bhagat, R. Electrochemical Evaluation and Phase-related Impedance Studies on Silicon–Few Layer Graphene (FLG) Composite Electrode Systems. *Sci. Rep.* **8,** 1386 (2018).

59. Schroder, K. W., Celio, H., Webb, L. J. & Stevenson, K. J. Examining solid electrolyte interphase formation on crystalline silicon electrodes: Influence of electrochemical preparation and ambient exposure conditions. *J. Phys. Chem. C* **116,** 19737–19747 (2012).

60. MARSHALL BRAIN. How Lithium-ion Batteries Work. *HOWSTUFFWORKS* (2006). Available at: http://electronics.howstuffworks.com/everyday-tech/lithium-ion-battery1.htm. (Accessed: 24th May 2016)

61. Myung, S. T., Hitoshi, Y. & Sun, Y. K. Electrochemical behavior and

passivation of current collectors in lithium-ion batteries. *J. Mater. Chem.* **21,** 9891–9911 (2011).

62. Tarascon, J.-M. & Armand, M. *Issues and challenges facing rechargeable lithium batteries*. *Nature* **414,** (2001).

63. Finegan, D. P. *et al.* Characterising thermal runaway within lithium-ion cells by inducing and monitoring internal short circuits. *Energy Environ. Sci.* **10,** 1377–1388 (2017).

64. Arora, P., White, R. E. & Doyle, M. Capacity Fade Mechanisms and Side Reactions in Lithium-Ion Batteries. *J. Electrochem. Soc.* **145,** 3647–3667 (1998).

65. Vetter, J. *et al.* Ageing mechanisms in lithium-ion batteries. *J. Power Sources* **147,** 269–281 (2005).

66. Kang, I. *et al.* Nanostructured silicon/silicide/carbon composite anodes with controllable voids for Li-ion batteries. *Mater. Des.* **120,** 230–237 (2017).

67. Biton, M., Yufit, V., Tariq, F., Kishimoto, M. & Brandon, N. Enhanced Imaging of Lithium Ion Battery Electrode Materials. *J. Electrochem. Soc.* **164,** 6032–6038 (2017).

68. Etiemble, A. *et al.* Evolution of the 3D Microstructure of a Si-Based Electrode for Li-Ion Batteries Investigated by FIB / SEM Tomography. *J. Electrochem. Soc.* **163,** 1550–1559 (2016).

69. Liu, H. *et al.* Three-dimensional investigation of cycling-induced microstructural changes in lithium-ion battery cathodes using focused ion beam / scanning electron microscopy. *J. Power Sources* **306,** 300–308 (2016).

70. Paz-Garcia, J. M. *et al.* 4D analysis of the microstructural evolution of Si-based electrodes during lithiation: Time-lapse X-ray imaging and digital volume correlation. *J. Power Sources* **320,** 196–203 (2016).

71. Park, M. *et al.* Silicon Nanotube Battery Anodes. *Nano Lett.* **9,** 3844–3847 (2009).

72. Chevrier, V. L. *et al.* Evaluating Si-Based Materials for Li-Ion Batteries in Commercially Relevant Negative Electrodes. *J. Electrochem. Soc.* **161,** A783–A791 (2014).

73. Loveridge, M. J. *et al.* Enhancing cycling durability of Li-ion batteries with hierarchical structured silicon-graphene hybrid anodes. *Phys. Chem. Chem. Phys.* **18,** 30677–30685 (2016).

74. Aurbach, D., Zinigrad, E., Cohen, Y. & Teller, H. A short review of failure mechanisms of lithium metal and lithiated graphite anodes in liquid electrolyte solutions. *Solid State Ionics* **148,** 405–416 (2002).

75. Liu, X. R. *et al.* Single nanowire electrode electrochemistry of silicon anode by in situ atomic force microscopy: Solid electrolyte interphase growth and mechanical properties. *ACS Appl. Mater. Interfaces* **6,** 20317–20323 (2014).

76. Verma, P., Maire, P. & Novák, P. A review of the features and analyses of the

solid electrolyte interphase in Li-ion batteries. *Electrochim. Acta* **55,** 6332–6341 (2010).

77. Ruffo, R., Hong, S. S., Chan, C. K., Huggins, R. A. & Cui, Y. Impedance Analysis of Silicon Nanowire Lithium Ion Battery Anodes. *J. Phys. Chem. C* **113,** 11390–11398 (2009).

78. Chan, C. K., Ruffo, R., Hong, S. S. & Cui, Y. Surface chemistry and morphology of the solid electrolyte interphase on silicon nanowire lithium-ion battery anodes. *J. Power Sources* **189,** 1132–1140 (2009).

79. Radvanyi, E. *et al.* Failure mechanisms of nano-silicon anodes upon cycling: an electrode porosity evolution model. *Phys. Chem. Chem. Phys.* **16,** 17142–17153 (2014).

80. Wu, H. *et al.* Stable cycling of double-walled silicon nanotube battery anodes through solid-electrolyte interphase control. *Nat. Nanotechnol.* **7,** 310–315 (2012).

81. Imhof, R. & Petr, N. In Situ Investigation of the Electrochemical Reduction of Carbonate Electrolyte Solutions at Graphite Electrodes. *J. Electrochem. Soc.* **145,** 1081–1087 (1998).

82. Novák, P. *et al.* The complex electrochemistry of graphite electrodes in lithium-ion batteries. *J. Power Sources* **97–98,** 39–46 (2001).

83. Blomgren, G. E. Electrolytes for advanced batteries. *J. Power Sources* **81,** 112–118 (1999).

84. Ramadass, P., Haran, B., White, R. & Popov, B. N. Capacity fade of Sony 18650 cells cycled at elevated temperatures: Part I. Cycling performance. *J. Power Sources* **112,** 606–613 (2002).

85. Ratnakumar, B. V. & Smart, M. C. Lithium Plating Behavior in Lithium-ion Cells. *ECS Trans.* **25,** 241–252 (2010).

86. Smart, M. C. *et al.* Improved low-temperature performance of lithium-ion cells with quaternary carbonate-based electrolytes. *J. Power Sources* **119–121,** 349–358 (2003).

87. Ren, J. G. *et al.* Silicon-graphene composite anodes for high-energy lithium batteries. *Energy Technol.* **1,** 77–84 (2013).

88. Jo, Y. N. *et al.* Si-graphite composites as anode materials for lithium secondary batteries. *J. Power Sources* **195,** 6031–6036 (2010).

89. Li, X. *et al.* Design of porous Si/C–graphite electrodes with long cycle stability and controlled swelling. *Energy Environ. Sci.* **10,** 1427–1434 (2017).

90. Li, J. *et al.* Research progress regarding Si-based anode materials towards practical application in high energy density Li-ion batteries. *Mater. Chem. Front.* (2017).

91. Obrovac, M. N. & Krause, L. J. Reversible Cycling of Crystalline Silicon Powder. *J. Electrochem. Soc.* **154,** A103 (2007).

92. Wang, W. & Kumta, P. N. Reversible high capacity nanocomposite anodes of

Si/C/SWNTs for rechargeable Li-ion batteries. *J. Power Sources* **172,** 650–658 (2007).

93. Liu, N. *et al.* A Yolk-Shell Design for Stabilized and Scalable. *Nano Lett.* **12,** 3315–3321 (2012).

94. Key, B., Morcrette, M., Tarascon, J.-M. & Grey, C. P. Pair Distribution Function Analysis and Solid State NMR Studies of Silicon Electrodes for Lithium Ion Batteries: Understanding the (De)lithiation Mechanisms. *J. Am. Chem. Soc.* **133,** 503–512 (2011).

95. Key, B. *et al.* Real-Time NMR Investigations of Structural Changes in Silicon Electrodes for Lithium-Ion Batteries. *J. Am. Chem. Soc.* **131,** 9239–9249 (2009).

96. Li, J. & Dahn, J. R. An In Situ X-Ray Diffraction Study of the Reaction of Li with Crystalline Si. *J. Electrochem. Soc.* **154,** A156 (2007).

97. Wen, C. J. & Huggins, R. A. Chemical diffusion in intermediate phases in the lithium-silicon system. *J. Solid State Chem.* **37,** 271–278 (1981).

98. Ohzuku, T. Formation of Lithium-Graphite Intercalation Compounds in Nonaqueous Electrolytes and Their Application as a Negative Electrode for a Lithium Ion (Shuttlecock) Cell. *J. Electrochem. Soc.* **140,** 2490 (1993).

99. Shim, J. & Striebel, K. A. The dependence of natural graphite anode performance on electrode density. *J. Power Sources* **130,** 247–253 (2004).

100. Datta, M. K. & Kumta, P. N. In situ electrochemical synthesis of lithiated silicon-carbon based composites anode materials for lithium ion batteries. *J. Power Sources* **194,** 1043–1052 (2009).

101. Limthongkul, P., Jang, Y.-I., Dudney, N. J. & Chiang, Y.-M. Electrochemically-driven solid-state amorphization in lithium-silicon alloys and implications for lithium storage. *Acta Mater.* **51,** 1103–1113 (2003).

102. Chan, C. K. *et al.* High-performance lithium battery anodes using silicon nanowires. *Nat. Nanotechnol.* **3,** 31–35 (2008).

103. Liu, X. H. *et al.* In situ atomic-scale imaging of electrochemical lithiation in silicon. *Nat. Nanotechnol.* **7,** 749–756 (2012).

104. Braithwaite, J. W. *et al.* Corrosion of Lithium-Ion Battery Current Collectors. *J. Electrochem. Soc.* **146,** 448 (1999).

105. Honbo, H., Takei, K., Ishii, Y. & Nishida, T. Electrochemical properties and Li deposition morphologies of surface modified graphite after grinding. *J. Power Sources* **189,** 337–343 (2009).

106. Dollé, M., Sannier, L., Beaudoin, B., Trentin, M. & Tarascon, J.-M. Live Scanning Electron Microscope Observations of Dendritic Growth in Lithium/Polymer Cells. *Electrochem. Solid-State Lett.* **5,** A286 (2002).

107. Lee, S. W., McDowell, M. T., Choi, J. W. & Cui, Y. Anomalous Shape Changes of Silicon Nanopillars by Electrochemical Lithiation. *Nano Lett.* **11,** 3034–3039 (2011).

108. Rhodes, K., Dudney, N., Lara-Curzio, E. & Daniel, C. Understanding the Degradation of Silicon Electrodes for Lithium-Ion Batteries Using Acoustic Emission. *J. Electrochem. Soc.* **157,** A1354–A1360 (2010).

109. Goldman, J. L., Long, B. R., Gewirth, A. A. & Nuzzo, R. G. Strain Anisotropies and Self-Limiting Capacities in Single-Crystalline 3D Silicon Microstructures: Models for High Energy Density Lithium-Ion Battery Anodes. *Adv. Funct. Mater.* **21,** 2412–2422 (2011).

110. Wu, H. & Cui, Y. Designing nanostructured Si anodes for high energy lithium ion batteries. *Nano Today* **7,** 414–429 (2012).

111. Gonzalez, J. *et al.* Three dimensional studies of particle failure in silicon based composite electrodes for lithium ion batteries. *J. Power Sources* **269,** 334–343 (2014).

112. McDowell, M. T. *et al.* Studying the Kinetics of Crystalline Silicon Nanoparticle Lithiation with In Situ Transmission Electron Microscopy. *Adv. Mater.* **24,** 6034–6041 (2012).

113. Delpuech, N. *et al.* Correlation between irreversible capacity and electrolyte solvents degradation probed by NMR in Si-based negative electrode of Li-ion cell. *Electrochem. commun.* **33,** 72–75 (2013).

114. Fan, X., Zou, L., Zheng, Y.-P., Kang, F.-Y. & Shen, W.-C. Electrospinning Preparation of Nanosilicon/Disordered Carbon Composite as Anode Materials in Li-Ion Battery. *Electrochem. Solid-State Lett.* **12,** A199 (2009).

115. Ryu, J. H., Kim, J. W., Sung, Y.-E. & Oh, S. M. Failure Modes of Silicon Powder Negative Electrode in Lithium Secondary Batteries. *Electrochem. Solid-State Lett.* **7,** A306 (2004).

116. Liu, N. *et al.* A pomegranate-inspired nanoscale design for large-volume-change lithium battery anodes. *Nat. Nanotechnol.* **9,** 187–192 (2014).

117. Song, J. *et al.* Interpenetrated Gel Polymer Binder for High-Performance Silicon Anodes in Lithium-ion Batteries. *Adv. Funct. Mater.* **24,** 5904–5910 (2014).

118. Ryu, I., Wook, J., Cui, Y. & Nix, W. D. Size-dependent fracture of Si nanowire battery anodes. *J. Mech. Phys. Solids* **59,** 1717–1730 (2011).

119. Peng, K., Jie, J., Zhang, W. & Lee, S. T. Silicon nanowires for rechargeable lithium-ion battery anodes. *Appl. Phys. Lett.* **93,** 1–4 (2008).

120. Hwang, T. H., Lee, Y. M., Kong, B.-S., Seo, J.-S. & Choi, J. W. Electrospun Core−Shell Fibers for Robust Silicon Nanoparticle-Based LIB anode.pdf. *Nano Lett.* **12,** 802–807 (2012).

121. Ji, L. & Zhang, X. Electrospun carbon nanofibers containing silicon particles as an energy-storage medium. *Carbon N. Y.* **47,** 3219–3226 (2009).

122. Zhou, Y. *et al.* Novel mesoporous silicon nanorod as an anode material for lithium ion batteries. *Electrochim. Acta* **127,** 252–258 (2014).

123. Yao, Y. *et al.* Interconnected Silicon Hollow Nanospheres for Lithium-ion

Battery Anodes with Long Cycle Life. *Nano Lett.* **11,** 2949–2954 (2011).

124. Gowda, S. R. *et al.* Three-dimensionally engineered porous silicon electrodes for Li Ion batteries. *Nano Lett.* **12,** 6060–6065 (2012).

125. Wang, W. & Kumta, P. N. Nanostructured Hybrid Silicon/Carbon Nanotube Heterostructures: Reversible High-Capacity Lithium-Ion Anodes. *ACS Nano* **4,** 2233–2241 (2010).

126. Maranchi, J. P., Hepp, A. F. & Kumta, P. N. High Capacity, Reversible Silicon Thin-Film Anodes for Lithium-Ion Batteries. *Electrochem. Solid-State Lett.* **6,** A198 (2003).

127. Ohara, S., Suzuki, J., Sekine, K. & Takamura, T. A thin film silicon anode for Li-ion batteries having a very large specific capacity and long cycle life. *J. Power Sources* **136,** 303–306 (2004).

128. Li, J., Dozier, A. K., Li, Y., Yang, F. & Cheng, Y.-T. Crack Pattern Formation in Thin Film Lithium-Ion Battery Electrodes. *J. Electrochem. Soc.* **158,** A689 (2011).

129. Ge, M. *et al.* Large-scale fabrication, 3D tomography, and lithium-ion battery application of porous silicon. *Nano Lett.* **14,** 261–268 (2014).

130. Rahman, A., Choy, Y., Guangsheng, W. & Cuie, S. A review on porous negative electrodes for high performance lithium-ion batteries. *J. Porous Mater.* **22,** 1313–1343 (2015).

131. Li, Z. F. *et al.* Novel pyrolyzed polyaniline-grafted silicon nanoparticles encapsulated in graphene sheets as Li-ion battery anodes. *ACS Appl. Mater. Interfaces* **6,** 5996–6002 (2014).

132. Zhu, J., Wang, T., Fan, F., Mei, L. & Lu, B. Atomic-Scale Control of Silicon Expansion Space as Ultrastable Battery Anodes. *ACS Nano* **10,** 8243–8251 (2016).

133. Wu, Z. H. *et al.* Self-healing alginate–carboxymethyl chitosan porous scaffold as an effective binder for silicon anodes in lithium-ion batteries. *Rare Met.* 1–8 (2016). doi:10.1007/s12598-016-0753-0

134. Mazouzi, D. *et al.* Critical roles of binders and formulation at multiscales of silicon-based composite electrodes. *J. Power Sources* **280,** 533–549 (2015).

135. Li, J., Christensen, L., Obrovac, M. N., Hewitt, K. C. & Dahn, J. R. Effect of Heat Treatment on Si Electrodes Using Polyvinylidene Fluoride Binder. *J. Electrochem. Soc.* **155,** A234 (2008).

136. Magasinski, A. *et al.* Toward Efficient Binders for Li-Ion Battery Si-Based Anodes: Polyacrylic Acid. *ACS Appl. Mater. Interfaces* **2,** 3004–3010 (2010).

137. Epur, R., Ramanathan, M., Beck, F. R., Manivannan, A. & Kumta, P. N. Electrodeposition of amorphous silicon anode for lithium ion batteries. *Mater. Sci. Eng. B-Advanced Funct. Solid-State Mater.* **177,** 1151–1156 (2012).

138. Zhao, J. *et al.* Artificial Solid Electrolyte Interphase-Protected Li_xSi Nanoparticles: An Efficient and Stable Prelithiation Reagent for Lithium-Ion

Batteries. *J. Am. Chem. Soc.* **137,** 8372–8375 (2015).

139. Zhang, Q. *et al.* Synergetic Effects of Inorganic Components in Solid Electrolyte Interphase on High Cycle Efficiency of Lithium Ion Batteries. *Nano Lett.* **16,** 2011–2016 (2016).

140. Yang, Y., Wang, Z., Zhou, R., Guo, H. & Li, X. Effects of lithium fluoride coating on the performance of nano-silicon as anode material for lithium-ion batteries. *Mater. Lett.* **184,** 65–68 (2016).

141. Sasidharachari, K., Na, B. K., Woo, S. G., Yoon, S. & Cho, K. Y. Facile conductive surface modification of Si nanoparticle with nitrogen-doped carbon layers for lithium-ion batteries. *J. Solid State Electrochem.* **20,** 2873–2878 (2016).

142. Jeong, M. G. *et al.* Nitrogen-doped Carbon Coated Porous Silicon as High Performance Anode Material for Lithium-Ion Batteries. *Electrochim. Acta* **209,** 299–307 (2016).

143. Li, J., Dudney, N. J., Nanda, J. & Liang, C. Artificial solid electrolyte interphase to address the electrochemical degradation of silicon electrodes. *ACS Appl. Mater. Interfaces* **6,** 10083–10088 (2014).

144. Franco Gonzalez, A., Yang, N. H. & Liu, R. S. Silicon Anode Design for Lithium-Ion Batteries: Progress and Perspectives. *J. Phys. Chem. C* **121,** 27775–27787 (2017).

145. Korgel, B. A. Nanomaterials developments for higher-performance lithium ion batteries. *J. Phys. Chem. Lett.* **5,** 749–750 (2014).

146. Kohandehghan, A. *et al.* Nanometer-scale Sn coatings improve the performance of silicon nanowire LIB anodes. *J. Mater. Chem. A* **2,** 11261 (2014).

147. Bogart, T. D., Lu, X., Gu, M., Wang, C. & Korgel, B. A. Enhancing the lithiation rate of silicon nanowires by the inclusion of tin. *RSC Adv.* **4,** 42022–42028 (2014).

148. Mori, T. *et al.* High specific capacity retention of graphene/silicon nanosized sandwich structure fabricated by continuous electron beam evaporation as anode for lithium-ion batteries. *Electrochim. Acta* **165,** 166–172 (2015).

149. Feng, K. *et al.* Silicon-Based Anodes for Lithium-Ion Batteries: From Fundamentals to Practical Applications. *Small* **14,** (2018).

150. St. John, M. R. Thermodynamic Studies of Li-Ge Alloys: Application to Negative Electrodes for Molten Salt Batteries. *J. Electrochem. Soc.* **129,** 246 (1982).

151. Abel, P. R. *et al.* Nanostructured Si(1- x)Gex for tunable thin film lithium-ion battery anodes. *ACS Nano* **7,** 2249–2257 (2013).

152. Wu, J. *et al.* A novel nano-structured interpenetrating phase composite of silicon / graphite – tin for lithium-ion rechargeable batteries anode materials. *J. Alloys Compd.* **596,** 86–91 (2014).

153. Whiteley, J. M., Kim, J. W., Piper, D. M. & Lee, S.-H. High-Capacity and

Highly Reversible Silicon-Tin Hybrid Anode for Solid-State Lithium-Ion Batteries. *J. Electrochem. Soc.* **163,** A251–A254 (2016).

154. Ren, W. *et al.* SnO_2@Si core–shell nanowire arrays on carbon cloth as a flexible anode for Li ion batteries. *J. Mater. Chem. A* **1,** 13433 (2013).

155. Zhong, L., Beaudette, C., Guo, J., Bozhilov, K. & Mangolini, L. Tin nanoparticles as an effective conductive additive in silicon anodes. *Nat. Publ. Gr.* **6,** 1–8 (2016).

156. Chockla, A. M., Klavetter, K. C., Mullins, C. B. & Korgel, B. A. Tin-Seeded Silicon Nanowires for High Capacity Li-Ion Batteries. *Chem. Mater.* **24,** 3738–3745 (2012).

157. Guo, J., Sun, A., Chen, X., Wang, C. & Manivannan, A. Cyclability study of silicon-carbon composite anodes for lithium-ion batteries using electrochemical impedance spectroscopy. *Electrochim. Acta* **56,** 3981–3987 (2011).

158. Piper, D. M., Yersak, T. A. & Lee, S.-H. Effect of Compressive Stress on Electrochemical Performance of Silicon Anodes. *J. Electrochem. Soc.* **160,** A77–A81 (2012).

159. Son, S. B. *et al.* A highly reversible nano-si anode enabled by mechanical confi nement in an electrochemically activated $Li_xTi_4Ni_4Si_7$ matrix. *Advanced Energy Materials* **2,** 1226–1231 (2012).

160. Yersak, T. A. *et al.* An All-Solid-State Li-Ion Battery with a Pre-Lithiated Si-Ti-Ni Alloy Anode. *J. Electrochem. Soc.* **160,** A1497–A1501 (2013).

161. Lee, J. I. *et al.* High-performance silicon-based multicomponent battery anodes produced via synergistic coupling of multifunctional coating layers. *Energy Environ. Sci.* **8,** 2075–2084 (2015).

162. Zhang, L., Wu, H. Bin & Lou, X. W. Metal−Organic-Frameworks-Derived General Formation of Hollow Structures with High Complexity. *J. Am. Chem. Soc.* **135,** 10664–10672 (2013).

163. Xia, W., Mahmood, A., Zou, R. & Xu, Q. Metal–organic frameworks and their derived nanostructures for electrochemical energy storage and conversion. *Energy Environ. Sci.* **8,** 1837–1866 (2015).

164. Wang, L. *et al.* Metal-organic frameworks for energy storage: Batteries and supercapacitors. *Coord. Chem. Rev.* **307,** 361–381 (2016).

165. Xu, G. *et al.* Exploring metal organic frameworks for energy storage in batteries and supercapacitors. *Mater. Today* **20,** 191–209 (2017).

166. Li, J.-R., Kuppler, R. J. & Zhou, H.-C. Selective gas adsorption and separation in metal–organic frameworks. *Chem. Soc. Rev.* **38,** 1477 (2009).

167. Takashima, Y. *et al.* Molecular decoding using luminescence from an entangled porous framework. *Nat. Commun.* **2,** 168 (2011).

168. Lee, J. *et al.* Metal–organic framework materials as catalysts. *Chem. Soc. Rev.* **38,** 1450 (2009).

169. Kundu, T. *et al.* Mechanical downsizing of a gadolinium(III)-based metal-

organic framework for anticancer drug delivery. *Chem. - A Eur. J.* **20,** 10514–10518 (2014).

170. Ke, F. S., Wu, Y. S. & Deng, H. Metal-organic frameworks for lithium ion batteries and supercapacitors. *J. Solid State Chem.* **223,** 109–121 (2015).

171. Pan, H., Hu, Y.-S. & Chen, L. Room-temperature stationary sodium-ion batteries for large-scale electric energy storage. *Energy Environ. Sci.* **6,** 2338 (2013).

172. Hu, X., Zhu, Z., Cheng, F., Tao, Z. & Chen, J. Micro-nano structured Ni-MOFs as high-performance cathode catalyst for rechargeable Li–O_2 batteries. *Nanoscale* **7,** 11833–11840 (2015).

173. Demir-Cakan, R. *et al.* Cathode composites for Li-S batteries via the use of oxygenated porous architectures. *J. Am. Chem. Soc.* **133,** 16154–16160 (2011).

174. An, T. *et al.* A flexible ligand-based wavy layered metal-organic framework for lithium-ion storage. *J. Colloid Interface Sci.* **445,** 320–325 (2015).

175. Zhang, L., Wu, H. Bin, Madhavi, S., Hng, H. H. & Lou, X. W. D. Formation of Fe2O3 Microboxes with Hierarchical Shell Structures from Metal–Organic Frameworks and Their Lithium Storage Properties. *J. Am. Chem. Soc.* **134,** 17388–17391 (2012).

176. Cao, X. *et al.* Metal oxide-coated three-dimensional graphene prepared by the use of metal-organic frameworks as precursors. *Angew. Chemie - Int. Ed.* **53,** 1404–1409 (2014).

177. Shin, J. *et al.* MIL-101(Fe) as a lithium-ion battery electrode material: a relaxation and intercalation mechanism during lithium insertion. *J. Mater. Chem. A* **3,** 4738–4744 (2015).

178. Kaveevivitchai, W. & Jacobson, A. J. Exploration of vanadium benzenedicarboxylate as a cathode for rechargeable lithium batteries. *J. Power Sources* **278,** 265–273 (2015).

179. Gou, L. *et al.* One-pot synthesis of a metal-organic framework as an anode for Li-ion batteries with improved capacity and cycling stability. *J. Solid State Chem.* **210,** 121–124 (2014).

180. Maiti, S., Pramanik, A., Manju, U. & Mahanty, S. Reversible Lithium Storage in Manganese 1,3,5- Benzenetricarboxylate Metal−Organic Framework with High Capacity and Rate Performance. *ACS Appl. Mater. Interfaces* **7,** 1–7 (2015).

181. SenthilKumar, R., Nithya, C., Gopukumar, S. & AnbuKulandainathan, M. Diamondoid-Structured Cu-Dicarboxylate-based Metal-Organic Frameworks as High-Capacity Anodes for Lithium-Ion Storage. *Energy Technol.* **2,** 921–927 (2014).

182. Li, X., Cheng, F., Zhang, S. & Chen, J. Shape-controlled synthesis and lithium-storage study of metal-organic frameworks Zn_4O(1,3,5-benzenetribenzoate)2. *J. Power Sources* **160,** 542–547 (2006).

183. Saravanan, K., Nagarathinam, M., Balaya, P. & Vittal, J. J. Lithium storage in

a metal organic framework with diamondoid topology - a case study on metal formates. *J. Mater. Chem.* **20,** 8329–8335 (2010).

184. Katz, M. J. *et al.* A facile synthesis of UiO-66, UiO-67 and their derivatives. *Chem. Commun.* **49,** 9449 (2013).

185. Cavka, J. H., Olsbye, U., Guillou, N., Bordiga, S. & Lillerud, K. P. A New Zirconium Inorganic Building Brick Forming Metal Organic Frameworks with Exceptional Stability. *J. Am. Chem. Soc.* **6,** 1–19 (2008).

186. Zhang, Q., Yu, Z., Du, P. & Su, C. Carbon Nanomaterials Used as Conductive Additives in Lithium Ion Batteries. *Recent Pat. Nanotechnol.* **4,** 100–110 (2010).

187. Chabot, V. *et al.* Graphene wrapped silicon nanocomposites for enhanced electrochemical performance in lithium ion batteries. *Electrochim. Acta* **130,** 127–134 (2014).

188. Xin, X. *et al.* A 3D porous architecture of Si/graphene nanocomposite as high-performance anode materials for Li-ion batteries. *J. Mater. Chem.* **22,** 7724–7730 (2012).

189. Zhao, X., Hayner, C. M., Kung, M. C. & Kung, H. H. In-plane vacancy-enabled high-power Si-graphene composite electrode for lithium-ion batteries. *Adv. Energy Mater.* **1,** 1079–1084 (2011).

190. Zhang, Z. *et al.* Scalable synthesis of interconnected porous silicon/carbon composites by the rochow reaction as high-performance anodes of lithium ion batteries. *Angew. Chemie - Int. Ed.* **53,** 5165–5169 (2014).

191. Mazouzi, D., Lestriez, B., Roué, L. & Guyomard, D. Silicon Composite Electrode with High Capacity and Long Cycle Life. *Electrochem. Solid-State Lett.* **12,** A215 (2009).

192. Bonaccorso, F. *et al.* Graphene, related two-dimensional crystals, and hybrid systems for energy conversion and storage. *Science (80-.).* **347,** 1246501 (2015).

193. Güneş, F. A direct synthesis of Si-nanowires on 3D porous graphene as a high performance anode material for Li-ion batteries. *RSC Adv.* **6,** 1678–1685 (2016).

194. Bai, X., Yu, Y., Kung, H. H., Wang, B. & Jiang, J. Si@SiO_x/graphene hydrogel composite anode for lithium-ion battery. *J. Power Sources* **306,** 42–48 (2016).

195. Ji, J. *et al.* Graphene-encapsulated Si on ultrathin-graphite foam as anode for high capacity lithium-ion batteries. *Adv. Mater.* **25,** 4673–4677 (2013).

196. Park, S. H. *et al.* Self-assembly of Si entrapped graphene architecture for high-performance Li-ion batteries. *Electrochem. commun.* **34,** 117–120 (2013).

197. Tang, H. *et al.* Self-assembly silicon/porous reduced graphene oxide composite film as a binder-free and flexible anode for lithium-ion batteries. *Electrochim. Acta* **156,** 86–93 (2015).

198. Cen, Y., Sisson, R., Qin, Q. & Liang, J. Current Progress of Si/Graphene

Nanocomposites for Lithium-Ion Batteries. *C* **4,** 18 (2018).

199. Lee, J. K., Smith, K. B., Hayner, C. M. & Kung, H. H. Silicon nanoparticles-graphene paper composites for Li ion battery anodes. *Chem. Commun.* **46,** 2025–2027 (2010).

200. Mi, H. *et al.* In situ coating of nitrogen-doped graphene-like nanosheets on silicon as a stable anode for high-performance lithium-ion batteries. *J. Mater. Chem. A* **2,** 11254–11260 (2014).

201. Son, I. H. *et al.* Silicon carbide-free graphene growth on silicon for lithium-ion battery with high volumetric energy density. *Nat. Commun.* **6,** 1–8 (2015).

202. Landi, B. J., Ganter, M. J., Cress, C. D., DiLeo, R. A. & Raffaelle, R. P. Carbon nanotubes for lithium ion batteries. *Energy Environ. Sci.* **2,** 638–654 (2009).

203. Zhang, Y. C. *et al.* Rice husk-derived hierarchical silicon/nitrogen-doped carbon/carbon nanotube spheres as low-cost and high-capacity anodes for lithium-ion batteries. *Nano Energy* **25,** 120–127 (2016).

204. Shu, J., Li, H., Yang, R., Shi, Y. & Huang, X. Cage-like carbon nanotubes/Si composite as anode material for lithium ion batteries. *Electrochem. commun.* **8,** 51–54 (2006).

205. Fan, Y., Zhang, Q., Xiao, Q., Wang, X. & Huang, K. High performance lithium ion battery anodes based on carbon nanotube-silicon core-shell nanowires with controlled morphology. *Carbon N. Y.* **59,** 264–269 (2013).

206. Dai, L., Chang, D. W., Baek, J.-B. & Lu, W. Carbon Nanomaterials for Advanced Energy Conversion and Storage. *Small* **8,** 1130–1166 (2012).

207. Ge, M., Fang, X., Rong, J. & Chongwu Zhou. Review of porous silicon preparation and its application for lithium-ion battery anodes. *Nanotechnology* **24,** 422001 (2013).

208. Su, X. *et al.* Silicon-Based Nanomaterials for Lithium-Ion Batteries: A Review. *Adv. Energy Mater.* **4,** 1–23 (2014).

209. Eastwood, D. S. *et al.* The application of phase contrast X-ray techniques for imaging Li-ion battery electrodes. *Nucl. Instruments Methods Phys. Res. Sect. B Beam Interact. with Mater. Atoms* **324,** 118–123 (2014).

210. Uchic, M. D., Holzer, L., Inkson, B. J., Principe, E. L. & Munroe, P. Three-Dimensional Microstructural Characterization Using Focused Ion Beam Tomography. *MRS Bull.* **32,** 408–416 (2007).

211. Levi, M. D. & Aurbach, D. Diffusion Coefficients of Lithium Ions during Intercalation into Graphite Derived from the Simultaneous Measurements and Modeling of Electrochemical Impedance and Potentiostatic Intermittent Titration Characteristics of Thin Graphite Electrodes. *J. Phys. Chem. B* **101,** 4641–4647 (1997).

212. Hu, Y. S. *et al.* Synthesis of hierarchically porous carbon monoliths with highly ordered microstructure and their application in rechargeable lithium batteries with high-rate capability. *Advanced Functional Materials* **17,** 1873–1878 (2007).

213. Liu, X. H. *et al.* In situ TEM experiments of electrochemical lithiation and delithiation of individual nanostructures. *Adv. Energy Mater.* **2,** 722–741 (2012).

214. Ender, M., Joos, J., Carraro, T. & Ivers-Tiffee, E. Quantitative Characterization of $LiFePO_4$ Cathodes Reconstructed by FIB/SEM Tomography. *J. Electrochem. Soc.* **159,** A972–A980 (2012).

215. Wu, H. *et al.* Focused helium ion beam deposited low resistivity cobalt metal lines with 10 nm resolution: implications for advanced circuit editing. *J. Mater. Sci. Mater. Electron.* **25,** 587–595 (2014).

216. Genieser, R. *et al.* Lithium ion batteries (NMC/graphite) cycling at 80 °C: Different electrolytes and related degradation mechanism. *J. Power Sources* **373,** 172–183 (2018).

217. Volkert, C. A., Minor, A. M., Editors, G. & May, B. Focused Ion Beam and Micromachining. *MRS Bull.* **32,** 389–399 (2007).

218. Zielke, L. *et al.* A Combination of X-Ray Tomography and Carbon Binder Modeling: Reconstructing the Three Phases of $LiCoO_2$ Li-Ion Battery Cathodes. *Adv. Energy Mater.* **4,** 1301617 (2014).

219. Liu, Y., King, H. E., Huis, M. A. van, Drury, M. R. & Plümper, O. Nano-Tomography of Porous Geological Materials Using Focused Ion Beam-Scanning Electron Microscopy. *Minerals* **6,** 104 (2016).

220. Amelinckx, S., Dyck, D. van, Landuyt, J. van & Tendeloo, G. van. *Electron Microscopy: Principles and Fundamentals*. (WILEY-VCH Verlag, 2007).

221. Goldstein, J. I. *et al. Scanning Electron Microscopy and X-Ray Microanalysis*. (Springer, 2008).

222. Jørgensen, P. S. *et al. Quantitative Data Analysis Methods for 3D Microstructure Characterization of Solid Oxide Cells*. (2010). doi:IMM-PHD-2010-231

223. Liu, Z. *et al.* Three-dimensional morphological measurements of LiCoO2 and $LiCoO_2/Li(Ni_{1/3}Mn_{1/3}Co_{1/3})O_2$ lithium-ion battery cathodes. *J. Power Sources* **227,** 267–274 (2013).

224. Chen-Wiegart, Y. K. *et al.* Tortuosity characterization of 3D microstructure at nano-scale for energy storage and conversion materials. *J. Power Sources* **249,** 349–356 (2014).

225. Stephenson, D. E. *et al.* Modeling 3D Microstructure and Ion Transport in Porous Li-Ion Battery Electrodes. *J. Electrochem. Soc.* **158,** A781–A789 (2011).

226. Gully, A. *et al.* Effective Transport Properties of Porous Electrochemical Materials — A Homogenization Approach. *J. Electrochem. Soc.* **161,** E3066–E3077 (2014).

227. Hutzenlaub, T., Thiele, S., Zengerle, R. & Ziegler, C. Three-Dimensional Reconstruction of a LiCoO2 Li-Ion Battery Cathode. *Electrochem. Solid-State Lett.* **15,** A33 (2012).

228. Hutzenlaub, T. *et al.* FIB/SEM-based calculation of tortuosity in a porous LiCoO2cathode for a Li-ion battery. *Electrochem. commun.* **27,** 77–80 (2013).

229. Liu, Z. *et al.* Relating the 3D electrode morphology to Li-ion battery performance; a case for $LiFePO_4$. *J. Power Sources* **324,** 358–367 (2016).

230. Etiemble, A. *et al.* Multiscale morphological characterization of process induced heterogeneities in blended positive electrodes for lithium–ion batteries. *Journal of Materials Science* 1–21 (2016). doi:10.1007/s10853-016-0374-x

231. Vierrath, S. *et al.* Morphology of nanoporous carbon-binder domains in Li-ion batteries - A FIB-SEM study. *Electrochem. commun.* **60,** 176–179 (2015).

232. Chen, Z., Christensen, L. & Dahn, J. R. Mechanical and Electrical Properties of Poly(vinylidene fluoride–tetrafluoroethylene–propylene)/Super-S Carbon Black Swelled in Liquid Solvent as an Electrode Binder for Lithium-Ion Batteries. *J. Appl. Polym. Sci.* **91,** 2958–2965 (2004).

233. Velichko, A., Holzapfel, C. & Mücklich, F. 3D Characterization of Graphite Morphologies in Cast Iron. *Adv. Eng. Mater.* **9,** 39–45 (2007).

234. Stampanoni, M. *et al.* High resolution X-ray detector for synchrotron-based microtomography. *Nucl. Instruments Methods Phys. Res. Sect. A Accel. Spectrometers, Detect. Assoc. Equip.* **491,** 291–301 (2002).

235. Richard Ketcham. X-ray Computed Tomography (CT). (2012). Available at: http://serc.carleton.edu/research_education/geochemsheets/techniques/CT.html. (Accessed: 16th May 2015)

236. Paulus, M. J., Gleason, S. S., Kennel, S. J., Hunsicker, P. R. & Johnson, D. K. High Resolution X-ray Computed Tomography: An Emerging Tool for Small Animal Cancer Research. *Neoplasia* **2,** 62–70 (2000).

237. Flynn, M. J., Hames, S. M., Reimann, D. A. & Wilderman, S. J. Microfocus X-ray sources for 3D microtomography. *Nucl. Instruments Methods Phys. Res. Sect. A Accel. Spectrometers, Detect. Assoc. Equip.* **353,** 312–315 (1994).

238. Spowart, J. E. Automated serial sectioning for 3-D analysis of microstructures. *Scr. Mater.* **55,** 5–10 (2006).

239. Alkemper, J. & Voorhees, P. W. Quantitative serial sectioning analysis. *J. Microsc.* **201,** 388–394 (2001).

240. Kral, M. V, Mangan, M. A., Spanos, G. & Rosenberg, R. O. Three-dimensional analysis of microstructures. *Mater. Charact.* **45,** 17–23 (2000).

241. Weyland, M. Electron tomography of catalysts. *Top. Catal.* **21,** 175–183 (2002).

242. Yan, B., Lim, C., Yin, L. & Zhu, L. Three Dimensional Simulation of Galvanostatic Discharge of $LiCoO_2$ Cathode Based on X-ray Nano-CT Images. *J. Electrochem. Soc.* **159,** A1604–A1614 (2012).

243. Pietsch, P. & Wood, V. X-Ray Tomography for Lithium Ion Battery Research : A Practical Guide. *Annu. Rev. Mater. Res.* **47,** 451–479 (2017).

244. Finegan, D. P. *et al.* In-operando high-speed tomography of lithium-ion

batteries during thermal runaway. *Nat. Commun.* **6,** 6924 (2015).

245. Yufit, V. *et al.* Investigation of lithium-ion polymer battery cell failure using X-ray computed tomography. *Electrochem. commun.* **13,** 608–610 (2011).

246. Stock, S. R. X-ray microtomography of materials. *Int. Mater. Rev.* **44,** 141–164 (1999).

247. Cocco, A. P. *et al.* Three-dimensional microstructural imaging methods for energy materials. *Phys. Chem. Chem. Phys.* **15,** 16377–16407 (2013).

248. Del Rio Castillo, A. E. *et al.* High-yield production of 2D crystals by wet-jet milling. *Mater. Horizons* **5,** 890–904 (2018).

249. Smallman, R. E. & Bishop, R. J. *Modern physical metallurgy and materials engineering*. (Elsevier, 1999).

250. Tang, J. *et al.* Plasma-Assisted Growth of Silicon Nanowires by Sn Catalyst: Step-by-Step Observation. *Nanoscale Res. Lett.* **11,** (2016).

251. Misra, S., Yu, L., Chen, W., Foldyna, M. & Roca I Cabarrocas, P. A review on plasma-assisted VLS synthesis of silicon nanowires and radial junction solar cells. *J. Phys. D. Appl. Phys.* **47,** (2014).

252. Akhtar, S., Usami, K., Tsuchiya, Y., Mizuta, H. & Oda, S. Vapor-Liquid-Solid Growth of Small- and Uniform-Diameter Silicon Nanowires at Low Temperature from Si2H6. *Appl. Phys. Express* 014003 (2008).

253. Choi, H. *Vapor – Liquid – Solid Growth of Semiconductor*. (Springer, 2012).

254. Wagner, R. S. & Ellis, W. C. Vapor-liquid-solid mechanism of crystal growth and its application to silicon. *Trans. Metall. Soc. AIME* **233,** 1053–1064 (1965).

255. Komaba, S. *et al.* Polyacrylate Modifier for Graphite Anode of Lithium-Ion Batteries. *Electrochem. Solid-State Lett.* **12,** A107 (2009).

256. Linden, D. *Handbook Of Batteries*. (2002).

257. Bard, A. J. & Faulkner, L. R. *Electrochemical methods : fundamentals and applications*. (Wiley, 2001).

258. Lain, M. J., Beattie, S. D., Loveridge, M. J., Dashwood, R. & Bhagat, R. Differential Voltage Analysis of Composite Silicon Anodes for Lithium Ion Cells. *Meet. Abstr.* **MA2015-03,** 477–477 (2015).

259. Barsoukov, E. & Macdonald, J. R. *Impedance Spectroscopy*. *John Wiley & Sons, Inc.* (2005).

260. Orazem, M. E. & Tribollet, B. *WILEY*. *Electrochemical Impedance Spectroscopy* (John Wiley & Sons, Inc., 2008).

261. Nobili, F., Tossici, R., Marassi, R., Croce, F. & Scrosati, B. An AC Impedance Spectroscopic Study of Li_xCoO_2 at Different Temperatures. *J. Phys. Chem. B* **106,** 3909–3915 (2002).

262. Zhuang, Q.-C. *et al.* An Electrochemical Impedance Spectroscopic Study of the Electronic and Ionic Transport Properties of Spinel $LiMn_2O_4$. *J. Phys. Chem. C* **114,** 8614–8621 (2010).

263. Barsoukov, E. *et al.* Comparison of kinetic properties of $LiCoO_2$ and $LiTi_{0.05}Mg_{0.05}Ni_{0.7}Co_{0.2}O_2$ by impedance spectroscopy. *Solid State Ionics* **161,** 19–29 (2003).

264. Umeda, M. *et al.* Electrochemical impedance study of Li-ion insertion into mesocarbon microbead single particle electrode Part I. Graphitized carbon. *Electrochim. Acta* **47,** 885–890 (2001).

265. Yamada, Y., Iriyama, Y., Abe, T. & Ogumi, Z. Kinetics of Lithium Ion Transfer at the Interface between Graphite and Liquid Electrolytes: Effects of Solvent and Surface Film. *Langmuir* **25,** 12766–12770 (2009).

266. Mirzaeian, M. & Hall, P. J. Characterizing capacity loss of lithium oxygen batteries by impedance spectroscopy. *J. Power Sources* **195,** 6817–6824 (2010).

267. Sun, X.-G. & Dai, S. Electrochemical and impedance investigation of the effect of lithium malonate on the performance of natural graphite electrodes in lithium-ion batteries. *J. Power Sources* **195,** 4266–4271 (2010).

268. Levi, M. D. & Aurbach, D. Simultaneous Measurements and Modeling of the Electrochemical Impedance and the Cyclic Voltammetric Characteristics of Graphite Electrodes Doped with Lithium. *J. Phys. Chem. B* **101,** 4630–4640 (1997).

269. Zhuang, Q.-C., Qiu, X.-Y., Xu, S.-D., Qiang, Y.-H. & Su, S.-G. in *Lithium Ion Batteries – New Developments* 189–226 (InTech, 2012).

270. Rubanov, S. & Munroe, P. R. Investigation of the structure of damage layers in TEM samples prepared using a focused ion beam. *J. Mater. Sci. Lett.* **20,** 1181–1183 (2001).

271. Winter, D. A. M. DE, Lebbink, M. N., Wiggers de Vries, D. F., Post, J. A. & Drury, M. R. FIB-SEM cathodoluminescence tomography: practical and theoretical considerations. *J. Microsc.* **243,** 315–326 (2011).

272. Koblischka-veneva, A. & Koblischka, M. R. Ion damage during preparation of nanostructures in magnetite by means of focused ion-beam (FIB) milling. *Superlattices Microstruct.* **44,** 468–475 (2008).

273. Schneider, C. A., Rasband, W. S. & Eliceiri, K. W. NIH Image to ImageJ: 25 years of Image Analysis HHS Public Access. *Nat. Methods* **9,** 671–675 (2012).

274. Schindelin, J. *et al.* Fiji - an Open Source platform for biological image analysis. *Nat Methods* **9,** 241 (2012).

275. Cooper, S. J., Bertei, A., Shearing, P. R., Kilner, J. A. & Brandon, N. P. TauFactor: An open-source application for calculating tortuosity factors from tomographic data. *SoftwareX* **5,** 203–210 (2016).

276. Tang, B. *et al.* Mechanism of electrochemical lithiation of a metal-organic framework without redox-active nodes. *J. Chem. Phys.* **144,** 194702 (2016).

277. Han, Y. *et al.* Metal-organic frameworks (MOFs) as sandwich coating cushion for silicon anode in lithium ion batteries. *ACS Appl. Mater. Interfaces* **7,** 26608–26613 (2015).

278. García, R. E. & Chiang, Y.-M. Spatially Resolved Modeling of Microstructurally Complex Battery Architectures. *J. Electrochem. Soc.* **154,** A856 (2007).

279. Øien, S. *et al.* Detailed structure analysis of atomic positions and defects in zirconium metal-organic frameworks. *Cryst. Growth Des.* **14,** 5370–5372 (2014).

280. Wu, H., Yildirim, T. & Zhou, W. Exceptional mechanical stability of highly porous zirconium metal-organic framework UiO-66 and its important implications. *J. Phys. Chem. Lett.* **4,** 925–930 (2013).

281. Shi, F. *et al.* Failure mechanisms of single-crystal silicon electrodes in lithium-ion batteries. *Nat. Commun.* **7,** 1–8 (2016).

282. Philippe, B. *et al.* Role of the LiPF6 salt for the long-term stability of silicon electrodes in Li-ion batteries - A photoelectron spectroscopy study. *Chemistry of Materials* **25,** 394–404 (2013).

283. Radvanyi, E., De Vito, E., Porcher, W. & Jouanneau Si Larbi, S. An XPS/AES comparative study of the surface behaviour of nano-silicon anodes for Li-ion batteries. *J. Anal. At. Spectrom.* **29,** 1120–1131 (2014).

284. Bordes, A., Eom, K. & Fuller, T. F. The effect of fluoroethylene carbonate additive content on the formation of the solid-electrolyte interphase and capacity fade of Li-ion full-cell employing nano Si-graphene composite anodes. *J. Power Sources* **257,** 163–169 (2014).

285. Karki, K. *et al.* Lithium-assisted electrochemical welding in silicon nanowire battery electrodes. *Nano Lett.* **12,** 1392–1397 (2012).

286. Cooper, S. J. *et al.* Image based modelling of microstructural heterogeneity in $LiFePO_4$ electrodes for Li-ion batteries. *J. Power Sources* **247,** 1033–1039 (2014).

287. Zhang, S. S., Xu, K. & Jow, T. R. Electrochemical impedance study on the low temperature of Li-ion batteries. *Electrochim. Acta* **49,** 1057–1061 (2004).

288. Chen, L., Wang, K., Xie, X. & Xie, J. Effect of vinylene carbonate (VC) as electrolyte additive on electrochemical performance of Si film anode for lithium ion batteries. *J. Power Sources* **174,** 538–543 (2007).

289. Eom, K., Joshi, T., Bordes, A., Do, I. & Fuller, T. F. The design of a Li-ion full cell battery using a nano silicon and nano multi-layer graphene composite anode. *J. Power Sources* **249,** 118–124 (2014).

290. Jow, T. R., Delp, S. A., Allen, J. L., Jones, J.-P. & Smart, M. C. Factors Limiting Li+ Charge Transfer Kinetics in Li-Ion Batteries. *J. Electrochem. Soc.* **165,** A361–A367 (2018).

291. Novoselov, K. S. *et al.* Electric Field Effect in Atomically Thin Carbon Films. *Science (80-.).* **306,** 666–669 (2004).

292. Geim, A. K. & Novoselov, K. S. The rise of graphene. *Nat. Mater.* **6,** 183–191 (2007).

293. Greco, E. *et al.* Few-layer graphene improves silicon performance in Li-ion battery anodes. *J. Mater. Chem. A* **5,** 19306–19315 (2017).

294. Palumbo, S. *et al.* Silicon Few-Layer Graphene Nanocomposite as High-Capacity and High-Rate Anode in Lithium-Ion Batteries. *ACS Appl. ENergy Mater.* (2019). doi:10.1021/acsaem.8b01927

295. Tao, Y. *et al.* Towards ultrahigh volumetric capacitance: Graphene derived highly dense but porous carbons for supercapacitors. *Sci. Rep.* **3,** 1–8 (2013).

296. Wong, D. P. *et al.* A stable silicon/graphene composite using solvent exchange method as anode material for lithium ion batteries. *Carbon N. Y.* **63,** 397–403 (2013).

297. Cui, L.-F., Hu, L., Wook, J. & Cui, Y. Light-Weight Free-Standing Carbon Lithium Ion Batteries. *ACS Nano* **4,** 3671–3678 (2010).

298. Xiao, Q., Zhang, Q., Fan, Y., Wang, X. & Susantyoko, R. A. Soft silicon anodes for lithium ion batteries. *Energy Environ. Sci.* **7,** 2261 (2014).

299. Zhang, B., Zheng, Q. Bin, Huang, Z. D., Oh, S. W. & Kim, J. K. SnO_2-graphene-carbon nanotube mixture for anode material with improved rate capacities. *Carbon N. Y.* **49,** 4524–4534 (2011).

300. Wang, B. *et al.* Adaptable silicon-carbon nanocables sandwiched between reduced graphene oxide sheets as lithium ion battery anodes. *ACS Nano* **7,** 1437–1445 (2013).

301. Wang, J. Z., Zhong, C., Chou, S. L. & Liu, H. K. Flexible free-standing graphene-silicon composite film for lithium-ion batteries. *Electrochem. commun.* **12,** 1467–1470 (2010).

302. Chang, J. *et al.* Multilayered Si nanoparticle/reduced graphene oxide hybrid as a high-performance lithium-ion battery anode. *Adv. Mater.* **26,** 758–764 (2014).

303. Liang, G. *et al.* Electrosprayed silicon-embedded porous carbon microspheres as lithium-ion battery anodes with exceptional rate capacities. *Carbon N. Y.* **127,** 424–431 (2018).

304. Wu, J. *et al.* Multilayered silicon embedded porous carbon/graphene hybrid film as a high performance anode. *Carbon N. Y.* **84,** 434–443 (2015).

305. Ferrari, A. C. *et al.* Raman Spectrum of Graphene and Graphene Layers. *Phys. Rev. Lett.* **97,** 187401 (2006).

306. Tuinstra, F. & Koenig, J. L. Raman Spectrum of Graphite Raman Spectrum of Graphite. *J. Chem. Phys.* **53,** 1126–1130 (1970).

307. Gan, L. *et al.* A facile synthesis of graphite/silicon/graphene spherical composite anode for lithium-ion batteries. *Electrochim. Acta* **104,** 117–123 (2013).

308. Vasconcelos, L. S. de, Xu, R., Li, J. & Zhao, K. Grid indentation analysis of mechanical properties of composite electrodes in Li-ion batteries. *Extrem. Mech. Lett.* **9,** 495–502 (2016).

309. Zou, J., Sole, C., Drewett, N. E. & Hardwick, L. J. In Situ Study of Li

Intercalation into Highly Crystalline Graphitic Flakes of Varying Thicknesses. *J. Phys. Chem. Lett.* **7,** 4291–4296 (2016).

310. Cui, L., Yang, Y., Hsu, C. & Cui, Y. Carbon - Silicon Core - Shell Nanowires as High Capacity Electrode for Lithium Ion Batteries 2009. *Nano letters* **9,** 3370–3374 (2009).

311. An, W. *et al.* Scalable synthesis of ant-nest-like bulk porous silicon for high-performance lithium-ion battery anodes. *Nat. Commun.* **10,** (2019).

312. Magasinski, A. *et al.* High-performance lithium-ion anodes using a hierarchical bottom-up approach. *Nat. Mater.* **9,** 353–358 (2010).

313. Li, B. *et al.* Hollow carbon nanospheres/silicon/alumina core-shell film as an anode for lithium-ion batteries. *Sci. Rep.* **5,** 7659 (2015).

314. Chen, X. *et al.* Conductive rigid skeleton supported silicon as high-performance Li-Ion battery anodes. *Nano Lett.* **12,** 4124–4130 (2012).

315. Ko, M. *et al.* Scalable synthesis of silicon-nanolayer-embedded graphite for high-energy lithium-ion batteries. *Nat. Energy* **1,** 16113 (2016).

316. Kim, S. Y. *et al.* Facile Synthesis of Carbon-Coated Silicon/Graphite Spherical Composites for High-Performance Lithium-Ion Batteries. *ACS Appl. Mater. Interfaces* **8,** 12109–12117 (2016).

317. Chae, C., Noh, H. J., Lee, J. K., Scrosati, B. & Sun, Y. K. A high-energy li-ion battery using a silicon-based anode and a nano-structured layered composite cathode. *Adv. Funct. Mater.* **24,** 3036–3042 (2014).

318. Xu, Q. *et al.* Watermelon-Inspired Si/C Microspheres with Hierarchical Buffer Structures for Densely Compacted Lithium-Ion Battery Anodes. *Adv. Energy Mater.* **7,** 1601481 (2017).

319. Zhou, W., Upreti, S. & Whittingham, M. S. High performance Si/MgO/graphite composite as the anode for lithium-ion batteries. *Electrochem. commun.* **13,** 1102–1104 (2011).

320. Tao, H. C., Fan, L. Z., Mei, Y. & Qu, X. Self-supporting Si/Reduced Graphene Oxide nanocomposite films as anode for lithium ion batteries. *Electrochem. commun.* **13,** 1332–1335 (2011).

321. Kehrwald, D., Shearing, P. R., Brandon, N. P., Sinha, P. K. & Harris, S. J. Local Tortuosity Inhomogeneities in a Lithium Battery Composite Electrode. *J. Electrochem. Soc.* **158,** A1393 (2011).

322. Evanoff, K. *et al.* Ultra-Strong Silicon-Coated Carbon Nanotube Nonwoven Fabric as Multifunctional Lithium Ion Battery Anodes. *ACS Nano* 9837–9845 (2012).

323. Wu, H. *et al.* Stable Li-ion battery anodes by in-situ polymerization of conducting hydrogel to conformally coat silicon nanoparticles. *Nat. Commun.* **4,** 1943–1946 (2013).

324. Tian, H., Xin, F., Wang, X., He, W. & Han, W. ScienceDirect High capacity group-IV elements (Si , Ge , Sn) based anodes for lithium-ion batteries. *J.*

Mater. **1,** 153–169 (2015).

325. Serena Gallanti, M. J. L. and R. B. Electrodeposition of Si and Sn-based Amorphous Films for High Energy Novel Electrode Materials. *MRS Adv.* **2,** 3249–3254 (2017).

326. Charlish, A. Silicon eyed as way to boost electric car battery potential. *Reuters* (2018).

327. Major lithium producer patents lithium tin for batteries. *International Tin Association Ltd.* (2018).

328. Jin, Y. *et al.* Scalable Production of the Silicon-Tin Yin-Yang Hybrid Structure with Graphene Coating for High Performance Lithium-Ion Battery Anodes. *ACS Applied Materials and Interfaces* **9,** 15388–15393 (2017).

329. Wang, X., Wen, Z., Liu, Y. & Wu, X. A novel composite containing nanosized silicon and tin as anode material for lithium ion batteries. *Elecrochimica Acta* **54,** 4662–4667 (2009).

330. Whiteley, J. *et al.* High-Capacity and Highly Reversible Silicon- Tin Hybrid Anode for Solid-State Lithium-Ion Batteries for Solid-State Lithium-Ion Batteries. *J. Electrochem. Soc.* **2,** A251–A254 (2016).

331. Antitomaso, P. *et al.* SnSb electrodes for Li-ion batteries: the electrochemical mechanism and capacity fading origins elucidated by using operando techniques. *J. Mater. Chem. A* **5,** 6546–6555 (2017).

332. Rhodes, K. J., Meisner, R., Kirkham, M., Dudney, N. & Daniel, C. In Situ XRD of Thin Film Tin Electrodes for Lithium Ion Batteries. *J. Electrochem. Soc.* **159,** A294 (2012).

333. Wu, J. *et al.* A novel Si/Sn composite with entangled ribbon structure as anode materials for lithium ion battery. *Sci. Rep.* **6,** 1–7 (2016).

334. Liu, N., Hu, L., Mcdowell, M. T., Jackson, A. & Cui, Y. Prelithiated Silicon Nanowires as an Anode for Lithium Ion Batteries. *ACS Nano* **5,** 6487–6493 (2011).

335. Cho, J.-H. & Picraux, S. T. Silicon nanowire degradation and stabilization during lithium cycling by SEI layer formation. *Nano Lett.* **14,** 3088–95 (2014).

336. Korgel, B. A. Twins cause kinks. *Nano Lett.* **5,** 521–522 (2006).

337. Peng, K. *et al.* Silicon nanowire array photoelectrochemical solar cells Silicon nanowire array photoelectrochemical solar cells. *Appl. Phys. Lett* **163103,** 1–4 (2008).

338. Rana, R. S., Purohit, R. & Das, S. Reviews on the Influences of Alloying elements on the Microstructure and Mechanical Properties of Aluminum Alloys and Aluminum Alloy Composites. *Int. J. Sci. Res. Publ.* **2,** 1–7 (2012).

339. Neimash, V. B. & Goushcha, A. O. Self-sustained cyclic tin induced crystallization of amorphous silicon. *J. Mater. Res* **30,** 3116–3124 (2015).

340. Pritchett, M. & Kelber, J. A. Adherence/Diffusion Barrier Layers for Copper Metallization: Amorphous Carbon:Silicon Polymerized Films, University of

North Texas. (2004).

341. Lin, L., Xu, X., Chu, C., Majeed, M. K. & Yang, J. Mesoporous Amorphous Silicon : A Simple Synthesis of a High-Rate and Long-Life Anode Material for Lithium-Ion Batteries. *Ange. Chem. Int. Ed.* **55,** 14063–14066 (2016).

342. Shiryaev, S. Y. *et al.* Pseudomorphic Si1-xSnx alloy films grown by molecular beam epitaxy on Si. *Appl. Phys. Lett.* **16,** 2287 (1995).

343. Ebner, M., Marone, F., Stampanoni, M. & Wood, V. *Visualization and Quantification of Electrochemical and Mechanical Degradation in Li Ion Batteries*. *Science* **342,** (2013).

344. Taiwo, O O, Eastwood, D S, Lee, P D, Paz-garcia, J M, Hall, S A, Brett, D J L, Shearing, P. R. In-Situ Examination of Microstructural Changes within a Lithium-Ion Battery Electrode using Synchrotron X-ray Microtomography. *228th ECS Meet. (October 11-15, 2015)* **69,** 81–85 (2015).